Solar fuels production by photoelectrochemical CO₂ reduction

Dora Alicia Garcia Osorio

Supervisor Professor Alex Cowan

Thesis submitted to the University of Liverpool in partial fulfilment of the degree of Doctor in Philosophy

March 2023

Stephenson Institute for Renewable Energy

Abstract

Using solar energy to meet the world energy demand is one of the greatest challenges in modern society where a photoelectrochemical approach could aid with solar intermittency by storing the energy in chemical bonds.[1] In this thesis, hybrid photocathodes were studied for producing solar fuels either H_2 or to convert CO_2 into syngas ($CO:H_2$), which could be potentially used as a feedstock in the already installed chemical process.

A hybrid photocathode uses a light absorbing material to harvest the sunlight and a catalyst to carry out the reduction reaction. In this work, we focused in the covalent immobilization of the molecular catalyst onto the electrode surface since it could improve the charge transfer at the interface. ZnTe and Sb_2Se_3 were explored, with focus on the latter since by the careful interface tailoring (mainly through the addition of CdS/TiO_2) to improve charge extraction, significant progress was achieved. This work is summarised in chapter 2. Sb_2Se_3 has been mainly used with noble metals for H_2 production as a photocathode,[2] and to the best of our understanding, here it was first time coupled with molecular catalysts.

To accomplish a hybrid photocathode for H_2 production, **NiP** ($[Ni(P_2^{R'}N_2^{R''})_2]^{2+}$ core ($P_2^{R'}N_2^{R''}$ = bis(1,5-R'-diphospha-3,7-R''-diazacyclooctane)) was chosen as model catalyst since it mimics the hydrogenase, ranks among the most active molecular catalyst and can be covalently immobilised on TiO_2 by the phosphonic acid pendant arm in the outer coordination sphere.[3] TiO_2 was incorporated onto Sb_2Se_3/CdS as a protective layer and to provide an anchoring surface. The resultant Sb_2Se_3-**NiP** hybrid device gave rise to -1.3 mA cm^{-2} at 0 V *vs* RHE, representing the highest photocurrent for **NiP** decorated photocathodes. It was only possible accomplished by increasing the surface area through a TiO_2 mesoporous scaffold (TiO_2-*meso*) for increasing the catalyst loading from 7.08 ± 0.43 nmol cm^{-2} on the planar device to 45.76 ± 0.81 nmol cm^{-2}. However, fast deactivation occurred in the minutes scale due to photoelectron accumulation which in turns triggers the failure of the TiO_2 layer. This finding was supported when the Sb_2Se_3-**NiP** hybrid device was benchmarked with Pt as a photoelectron extractor and by transient photocurrent analysis, it was revealed that the TiO_2-*meso*/Pt interface acted as a reservoir of photoelectron accumulation for the HER catalysis to occur on Pt suggesting that **NiP** was not able to consume all the photoelectrons Sb_2Se_3 generated.

Ni and Co based molecular catalyst, which demonstrated high selectivity for CO production, were explored to build a hybrid photocathode for CO_2 reduction.[4] Ni cyclam in solution (**Ni(cyc)$^{2+}$**, **cyc**

=1,4,8,11-tetraazacyclotetradecane), and **Ni(cycP)** with **cycP** = [(1,4,8,11-tetraazacyclotetradecan-1-yl)methyl] phosphonic acid covalently anchored to the planar TiO_2 were explored. Nevertheless, both approaches gave rise to low photocurrents *ca.* 5 μA cm^{-2} at -0.41 V vs RHE for **Ni(cyc)$^{2+}$** in solution, and *ca.* 20 μA cm^{-2} at -0.39 V vs RHE when immobilised. The complete CO_2 hybrid photocathode using Ni-based molecular catalyst was not assembled due to the low **Ni(cycP)** content even when a TiO_2-*meso* was used to increase the surface binding area (∼14 nmol cm^{-2}), this was attributed to the strong interaction with the Ni metal centre. **CoPP** (Co protoporphyrin IX) was covalently anchored to the TiO_2-*meso* but found that the carboxylic acid anchoring group did not provide enough stability to be used in a CO_2R hybrid photocathode. However, the light absorber architecture used for these devices did not have the CdS buffer layer which displayed the best PEC activity. Therefore, to assess the capabilities of Sb_2Se_3/CdS/TiO_2 photocathode for CO_2 reduction, a metal benchmark should be used like Au or Ag followed by the molecular catalyst for CO_2 reduction.

References

1   L. K. Putri, B. J. Ng, W. J. Ong, S. P. Chai and A. R. Mohamed, *Adv Energy Mater*, 2022, **17**, 2201093.

2   S. Chen, T. Liu, Z. Zheng, M. Ishaq, G. Liang, P. Fan, T. Chen and J. Tang, *Journal of Energy Chemistry*, 2022, **67**, 508–523.

3   M. A. Gross, A. Reynal, J. R. Durrant and E. Reisner, *J Am Chem Soc*, 2014, **136**, 356–366.

4   E. Boutin, L. Merakeb, B. Ma, B. Boudy, M. Wang, J. Bonin, E. Anxolabéhère-Mallart and M. Robert, *Chem Soc Rev*, 2020, **49**, 5772–5809.

List of publications

The following papers were published in peer-reviewed journals for this PhD project:

- Dora Alicia Garcia Osorio, Gaia Neri and Alexander J Cowan. "*Hybrid Photocathodes for Carbon Dioxide Reduction: Interfaces for Charge Separation and Selective Catalysis.* ChemPhotoChem, 2021, **5** (7). pp. 595-610. (**Chapter 1**).

- Dora Alicia Garcia-Osorio, Thomas P. Shalvey, Liam Banerji, Khezar Saeed, Gaia Neri, Laurie J. Phillips, Oliver S. Hutter, Carla Casadevall, Daniel Antón-García, Erwin Reisner, Jonathan D Major and Alexander J Cowan. "*Hybrid photocathode based on a Ni molecular catalyst and Sb_2Se_3 for solar H_2 production*" Chemical communications, 2023,**59**, 944-947. (**Chapter 3**).

- Khezar H. Saeed, Dora-Alicia Garcia Osorio, Chao Li, Liam Banerji, Adrian M. Gardner and Alexander J. Cowan. "*Monitoring interfacial electric fields at a hematite electrode during water oxidation*" Chemical Science, 2023,**14**, 3182-3189.

Acknowledgements

This work is by no means a sole achievement, there are a lot of people I would like to thank, without them it would not have been possible to reach this stage. My deepest gratitude to the Mexican government for my scholarship through **SENER-CONACyT** (CVU 556479).

Firstly, my upmost gratitude to **Professor Alex Cowan** for giving me the opportunity to join your group. Thanks so much for all your patience (with my terrible English), invaluable guidance and most importantly for sharing all your knowledge and passion for science. I find myself extremely lucky for having you as a supervisor. **"The World of Alex Cowan"**, the former and new members of the group, it has been such a pleasure to work next to people who also share the same interests even when experiments do not always work, which happens quite often. *Without any doubt, one of the biggest and most important achievements of my PhD was feeling part of the Cowan group and gaining your friendship.*

I feel very grateful to all the people who have contributed scientifically to my PhD project. **Dr Gaia Neri** for making me feel very welcome since the very beginning of my PhD and taught me not only all the lab stuff, but also walked me through the UK life. **Dr Khezar Saeed** for showing me the magic of Raman analysis. **Dr Thomas Shalvey** and **Liam Banerji** for the SEM, EDX, and XRD analysis, and **Dr Bhavin Siritanaratkul** for all you help with the GC. **Dr. Hansaem Jang** for all the electrochemistry discussion/guidance. **Marta Alemanno** for the contact angle analysis. **Dr Thomas Shalvey**, **Dr Bhavin Siritanaratkul**, **Dr Khezar Saeed**, and **Francesca Greenwell**, for taking the time to proof read my thesis chapters and all your feedback. Thank so much also to **Dr Jon Major** and his group for all the advice with the light absorbers and for sharing all the facilities in Lab 1. **Vince Vasey** for all you help in building and fixing stuff in the lab. And to all the people in Stephenson Institute for Renewable Energy (Physicists and chemists) who build such a friendly working place and are always willing to help.

I could not have achieved this goal without friends especially my Daçarinos del Forro: **Bruna Baggio**, **Julia Fernandez-Vidal**, **Robert Batty**, **Alex Wright** & **Nick Cook** having you around kept me sane and most importantly happy (with plenty of 92° coffees and pints) during the last and most difficult part of the PhD. **Bruna** and **Julia** thanks so much for all the vents and girly chats over the years. **Rob** thanks for making the best Yorkshire puddings ever! Showing great interest in learning about other cultures, my English lessons, but most importantly for your friendship. **Alex** thanks for making me feel that I was not alone during the long writing days, our meaningful and riveting chats were my reward after

Abbreviations

The following list contains the commonly abbreviated terms used in this thesis, each one was fully denoted the first time mentioned in each chapter.

ΔG_{ET}	Gibbs free energy change for electron transfer
$\Delta\phi_{sc}$	Potential drop across the space charge region
ε_0	Vacuum permittivity
cyc^{2+}	1,4,8,11-tetraazacyclotetradecane
cycP	[(1,4,8,11-tetraazacyclotetradecan-1-yl)methyl] phosphonic acid
ε_{sc}	Relative permittivity of the semiconductor material
$\tau_{Q_{max}}$	Time at the maximum charge passed
ALD	Atomic layer deposition
ATR-FTIR,	Attenuated total reflectance (ATR)- Fourier transform infrared (FTIR)
AZO	Aluminium-doped zinc oxide
bpy	2,2′-Bipyridine
BC	Back contact
CA	Chronoamperometry
cat	Catalyst
CBM	Conduction band minimum
CE	Counter electrode
CNT	Carbon nanotubes
CO$_2$R	CO$_2$ reduction
CoPc	Co phthalocyanine
CoPcP	Co phthalocyanine modified with a phosphonic anchoring group
CoPP	Co protoporphyrin IX
Co-qPyH	Co quarter pyridine
Co-tpyP	Co bis(terpyridine)
CPP	Control potential photoelectrolysis
CSS	Close-spaced sublimation
CW	Constant wave
dcbpy	4,4′-dicarboxy-2,2′-bipyridine
DMF	Dimethylformamide

DSPEC	Dye sensitised photoelectrochemical cell
DSPEC	Photoelectrosynthesis cells
DSSC	Dye-sensitised solar cell
DTDP	4,40-dithiodipyridine
E_C	Conduction band
E_{cat}	Onset potential of catalysis
EDX	X-ray spectroscopy
E_F	Fermi level
E_g	Band gap
EIS	Electrochemical impedance spectroscopy
E_{onset}	Onset potetential
E_{red}	Redox Fermi level of the electrolyte
ETL	Electron Transport Layer
EtOH	Ethanol
E_V	Valence band
FE	Faradaic efficiency
FEG	Field emission gun
FTO	Fluorine-doped Tin Oxide
GC	Glassy Carbon
HER	Hydrogen Evolution Reaction
HMDE	Hanging Mercury Drop Electrode
HT	Heat treatment
HTL	Hole Transport Layers
IMPS	Intensity-modulated photocurrent
IMVS	Photovoltage-modulated spectroscopy
IPCE	Incident photon-to-current efficiency
LED	Light-emitting diode
LSV	Linear Sweep Voltammetry
MeCN	Acetonitrile
NA	No annealing
N_d	Doping density
$_nE_F^*$	Quasi electron Fermi level
NHE	Normal Hydrogen Electrode
NiP	$[Ni(P_2^RN_2^{R''})_2]^{2+}$ core ($P_2^RN_2^{R''}$ = bis(1,5-R′-diphospha-3,7-R″-diazacyclooctane))
no HT	No heat treatment
OCP	Open circuit potential

PEALD	Plasma Enhance Atomic Layer Deposition
PEC	Photoelectrochemical
$_pE_F^*$	Quasi hole Fermi level
post-CPP	post controlled potential photoelectrolysis
PS	Photosensitiser or dye
PV	Photovoltaic
Q	Elementary charge
qPyH	2,2′:6′,2″:6″,2‴-quaterpyridine
RE	Reference electrode
RHE	Reversible Hydrogen Electrode
RuP	Ru^{II}(2,2'-bipyridine)$_2$(2,2'-bipyridine-4,4'-diylbis(phosphonic acid)),
S:N	Signal:noise ratio
SCLJ	Semiconductor liquid junction
SDD	Silicon drift detector
SEM	Scanning electron microscope
T	Temperature
t	Time
TAS	Transient absorption spectroscopy
TDMAT	Tetrakis (dimethyl-amido) titanium
TE	Transparent electrode
TEM	Transmission electron microscopy
TEOA	Triethanolamine
TON	Turnover number
TPC	Transient photocurrent
tpy	2,2';6',2"-terpyridine
TRPL	Time-resolved photoluminescence
TTIP	Titanium tetraisopropoxide
UV	Ultra violet
UV-VIS	Ultraviolet-visible region in the spectra
VBM	Valence Band Maxima
V$_{ph}$	Photovoltage
WE	working electrode
W_{sc}	Space charge region
XPS	X-ray photoelectron spectroscopy
XRD	X-ray diffraction

Table of Contents

Chapter 1

Hybrid photocathodes
Inorganic semiconductors-molecular catalyst

Text and figures of this chapter were based on the review *ChemPhotoChem* 2021,5, 595–61.

1. Introduction

Enabling the use of solar energy to meet the world's energy demands is one of the greatest challenges of modern society. However, the intermittent nature of sunlight means that efficient ways to store and transport the captured energy need to be found. Using solar energy to produce high value chemicals and feedstock is regarded as one such way.[1] In particular, the light-driven conversion of water and CO_2 into hydrogen and/or carbon-based fuels and feedstocks is particularly attractive, as the products like syngas can be readily introduced into existing chemicals and energy infrastructure *e.g.* the Fischer–Tropsch process.[2–5] Some of the most common light-driven approaches for producing solar fuels are shown in Figure 1: (a) photocatalysis, (b) photoelectrochemistry, and (c) photovoltaics coupled with electrochemical devices (PV-PEC).[6]

The PV-PEC approach has progressed significantly in the last 10 years, and is reviewed extensively elsewhere.[7–9] Although significant challenges remain and concerns persist about the overall system cost, attempts are being made to commercialise CO_2 electrolysis.[10] Photoelectrochemical (PEC) conversion (Figure 2b) represents an alternative approach where the electrodes apart from transferring the charge for a reduction or oxidation reaction are also able to absorb the light, in a photocathode and photoanode,

respectively without any bias applied ideally. Analyses indicate that the PEC approach may offer a balance between cost/complexity of system and efficiency.[11–16]
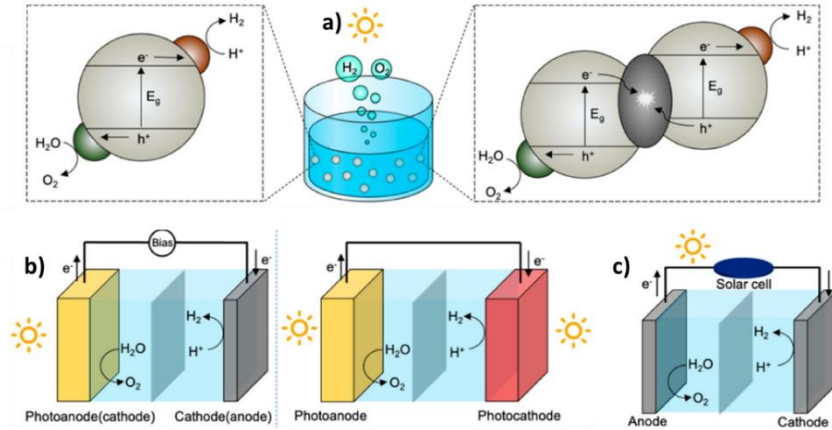
Figure 1. *Solar fuel production by (a) photocatalysis, (b) photoelectrochemistry and (c) photovoltaics coupled with an electrolyser.[6]*

Significant progress has been made in the field of PEC devices using metal-based catalysts,[17] but in this work we focus on molecular catalysts since they exhibit high selectivity and turnover frequencies representing an alternative when coupled with inorganic semiconductors to build a hybrid photocathode (Figure 2a). A range of light absorber/catalyst interfaces have now been explored, specifically for CO_2R, and some of the typical devices are shown in Figure 2b-e.

Regarding H_2 hybrid photocathodes, Meyer and collaborators reviewed in detail the mechanism of photoelectrochemical water splitting, the different ways to interface a H_2 molecular catalyst with an inorganic semiconductor and summarised the state-of-the-art devices.[22] Given the similarities between H_2 and CO_2R hybrid photocathodes, here the introduction is focussed mainly on the latter since it represents additional technological challenges, in both the energetic requirements and the product selectivity, compared to H_2 production from water splitting. In section 5, a brief summary of the most representative devices will be presented to provide context for the H_2 hybrid photocathode developed in chapter 2.
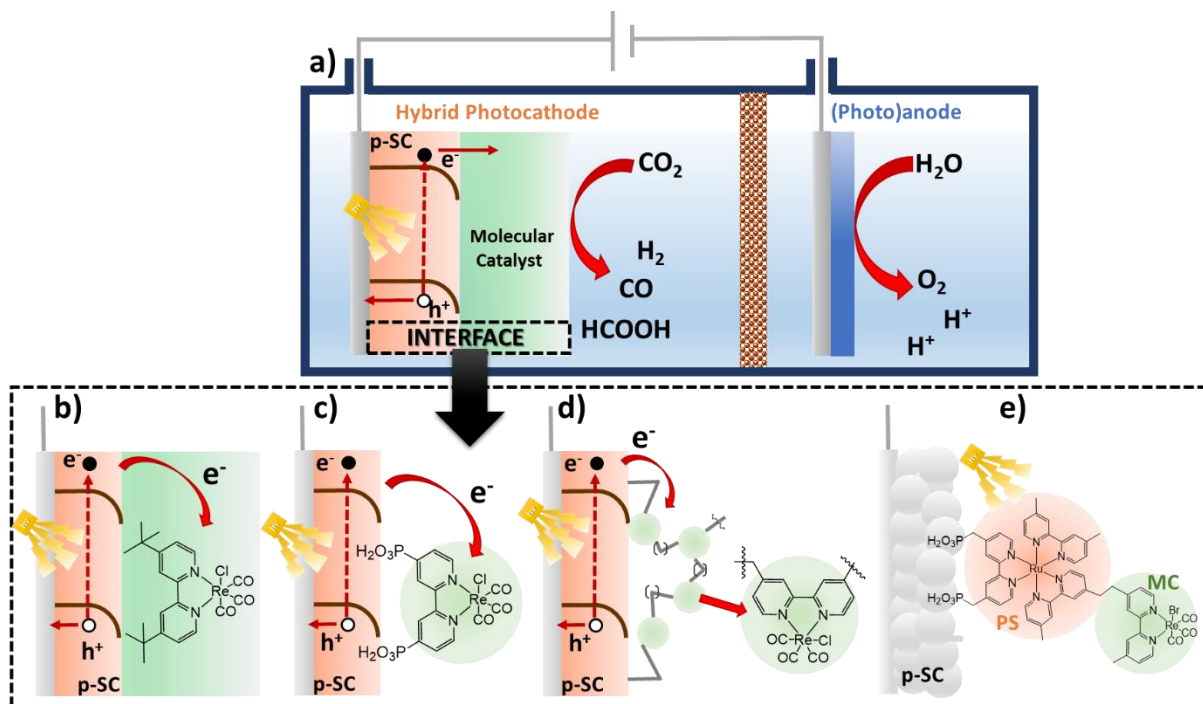
Figure 2. *(a) Schematic illustration of a hybrid p-semiconductor (p-SC) photocathode and a (photo)anode in a photoelectrochemical cell for CO₂ reduction.[13] Types of interfaces between the molecular catalyst (green) with the light absorber material (orange) discussed: (b) molecular catalyst in solution,[18] (c) covalently bound to the semiconductor,[19] (d) electropolymerised,[20] (e) and supramolecular catalyst composed by a photosensitiser (PS) and catalyst (cat).[21]*

First, the photoelectrochemistry is briefly reviewed in the following section, followed by the challenges in the CO₂R reduction reaction, and finally the different approaches to build a CO₂R hybrid photocathode will be discussed, (shown in Figure 2 b-d), highlighting the advantages and disadvantages of the different structures for the state-of-the-art materials.

1.2. Semiconductors as photocathodes

Prior discussing the operational principle of hybrid photocathodes, the ideal semiconductor/electrolyte interface is presented before addressing non-ideal behaviour often observed in many semiconductors.[23,24] This is followed by the effect of the applied potential on the band-banding and a brief description of the *p-n* junction, a widely-used strategy in some of the state-of-the-art photocathodes.

1.2.1 Ideal *p*-type semiconductor-electrolyte interface

In a *p*-type semiconductor, the Fermi level (E_F) is located just above the valence band edge, Figure 3a. When the semiconductor is immersed in an electrolyte with a redox Fermi level (E_{red}) that lies above E_F, the difference between E_F and E_{red} leads to a transfer of charge from solution to the semiconductor until equilibrium is achieved ($E_F = E_{red}$), Figure 3b. The accumulation of electrons in the semiconductor generates a negatively charged region close to the semiconductor liquid junction (SCLJ), and the negative charge in the semiconductor is balanced by a rearrangement of electrolyte ions within the double layer structure. This charge redistribution generates an electric field that varies linearly with distance from the interface in an ideal semiconductor. Hence a parabolic variation in potential across the space charge region occurs and the energy of the electrons and holes is modified giving rise to bending of the valence (E_V) and conduction bands (E_C) on the energy level diagrams, Figure 3b.[25,26]
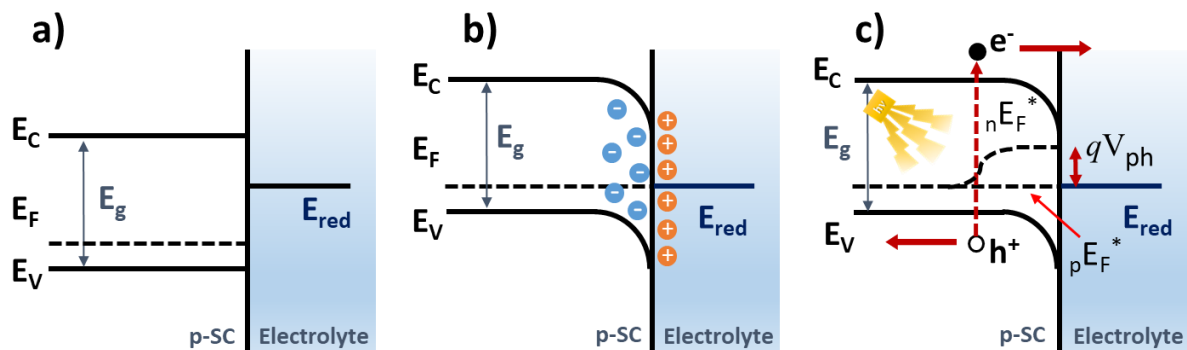
Figure 3 *Band diagrams of a p-type semiconductor (a) before, (b) after the equilibrium with the electrolyte, and (c) under illumination.[25–27] $_nE_F{}^*$ and $_pE_F{}^*$ are the quasi electron and quasi hole Fermi levels, respectively.*

Under illumination with photons of higher energy than the band gap (E_g), a hole-electron pair is created within the semiconductor. When photon absorption occurs within the space charge region, the electric field present facilitates charge separation[28] with the migration of electrons towards the semiconductor surface and holes being moved into the bulk of the semiconductor (Figure 3c). Additionally, the decreased majority charge carrier (hole) concentration close to the SCLJ lowers recombination rates,

further increasing the probability of charge carrier separation. As a result, charge separation is often assumed to occur with unity efficiency within space charge region.[24] In contrast, within the bulk of the semiconductor where the hole concentration is high, recombination rates of photogenerated charges will be significantly greater. The subsequent low levels of charge separation within the bulk means that only photoelectrons generated within the distance of the minority carrier diffusion length of the space charge region are likely to reach the semiconductor surface. Once at the electrode/electrolyte interface, the ability of the electrons to drive the desired reduction (*e.g.* H^+ or CO_2 reduction) in a net forward manner is given by the electron quasi-Fermi level ($_nE_F{}^*$), illustrated in Figure 3c where $_pE_F{}^*$ is the hole quasi-Fermi level and V_{ph} the available photovoltage for the overall electrochemical reaction.[25]

The probability of electron-hole separation is far greater in the space charge region than in the bulk. Nominal widths of the space charge region (W_{sc}) of ~10-100's nm are often reported, but equation 1 (where ε_0 is the vacuum permittivity and q the elementary charge) shows that W_{sc} depends on the doping density (N_d), potential drop across the space charge region ($\Delta\phi_{sc}$) and the relative permittivity of the semiconductor material (ε).

$$W_{sc} = \left(\frac{2\Delta\phi_{sc}\varepsilon\varepsilon_0}{qN_d}\right)^{1/2} \qquad \text{Eq. (1)}$$

Therefore, through tuning of the dopant concentration and modification of the potential drop across the semiconductor, typically by applying a bias to the electrode, it is possible to vary W_{sc} and hence the overall efficiency of charge separation under illumination.

1.2.2 Non-ideality of the semiconductor-electrolyte interface

For an ideal semiconductor-electrolyte interface, the incident photon to current efficiency for a photocathode and its dependence on applied potential is determined only by W_{sc}, the electron diffusion length and the absorption coefficient for the incoming photons, according to a model by Gärtner.[29] In reality, large deviations from such ideal behaviour are often observed. Amongst the assumptions of the

Gärtner model is that electron transfer across the interface is fast, preventing build-up of charge at the SCLJ. As will be discussed in more detail in section 1.3.1, the rate of electron transfer during a reduction reaction is likely to be slow in the absence of a catalyst, producing charge accumulation which leads to a change in band bending, thus increasing recombination losses at the interface.

A further complication are the surface states arising from the termination of the semiconductor lattice that causes Fermi level pinning, leading to lower band bending than the ideal case. Materials with redox active surface states, *i.e.* those able to undergo electron transfer to/from the bulk semiconductor or to/from species in solution will change the charge distribution at the interface. The occupancy of the states will depend upon E_F, with states filled at values above the energy of the surface states (E_{SS}) and emptied as E_F is lowered. The changing occupancy of these surface states changes the surface charge of the semiconductor and hence the potential drop across the Helmholtz layer of the electrolyte. As a result, when E_F is at ~E_{SS} changes in potential primarily occur across the Helmholtz layer and the change in band bending with applied potential is significantly lower than ideal behaviour would predict. Until the surface states are either completely populated or depopulated with electrons, the Fermi level effectively becomes pinned and largely insensitive to applied voltage.[24] In cases where the density of surface states is high enough the potential across the space charge region, and hence the band bending within the semiconductor, is essentially fixed by these surface states and becomes independent of the E_{red} of species in solution, Figure 4. It has been shown in photoelectrochemical studies with many common photocathodes including *p*-GaAs, *p*-Si that Fermi level pinning occurs. Although this limits the achievable photovoltage, it does enable photoelectron transfer to a wider range of redox couples in solution including those that may be at a more negative potential than the conduction band edge in the absence of the redox couple.[30] Surface states can also play an important role in the trapping of photogenerated charges. Trap states lying in energy between the conduction and valence band edges, modify the driving force for charge transfer across the semiconductor/(catalyst)/electrolyte interface and they can also act as recombination centres.[26]

It is therefore clear that the result of non-ideal behaviour brought about through nanostructuring and the presence of surface states, including those induced by the formation of the semiconductor/catalyst

interface, can be hard to predict. This makes measurements to determine the mechanisms and kinetics

of key processes including charge separation, transport and transfer vital in enabling rational design of

hybrid photoelectrodes.
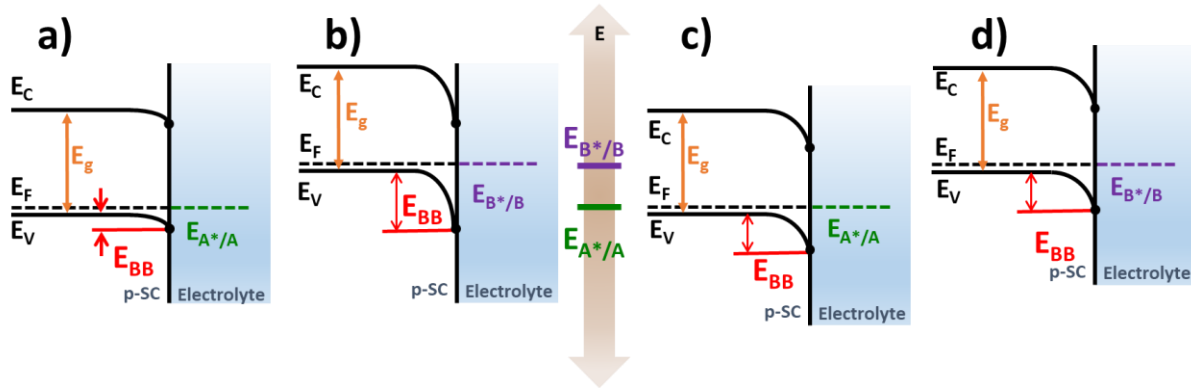
Figure 4. *Interface energetics of a p-SC: (a, b) Band Bending (E_{BB}) dependent on the E_{red}: $E_{A*/A}$, $E_{B*/B}$, and (c, d) Fermi Level Pinning, where E_{BB} is independent of E_{red}. Adapted for a p-type semiconductor from [30].*

1.2.3 Effect of the applied potential

The previous section discussed the semiconductor/electrolyte interface and highlighted the non-ideal

behaviour of some *p*-type semiconductors. However, often after illumination, the $_nE_F^*$ does not have

enough energy to overcome the cathodic overpotential (η_c, Figure 5g) to drive a reduction reaction

either for HER or CO_2R, therefore an additional applied potential is usually required. Figure 5a shows

a "map", represented in a linear sweep voltammetry, of how the applied potential changes the band

bending in the semiconductor providing the extra energy to carry out the reaction. Applying a positive

potential in an *p*-type semiconductor promotes an accumulation layer (indicated as red region in Figure

5a, d) where the holes are transferred to the electrolyte and minimal contribution to the current is

observed after illuminating the semiconductor (shown as a red trace in Figure 5). Contrary, applying a

negative potential increases the $_nE_F^*$ until it reaches the potential required to drive the reaction (E_{onset})

then there is an increase in the photocurrent, as shown in Figure 5f. When applying a more negative

potential, the band bending increases even further promoting the photoelectron extraction towards the electrolyte and the holes moved towards the back contact (Figure 5e).[27,33] An ideal *p*-type semiconductor would exhibit a more positive E_{onset} meaning that less extra energy is required to drive the reaction since catalysis is efficient and the recombination processes are minimal.[17]
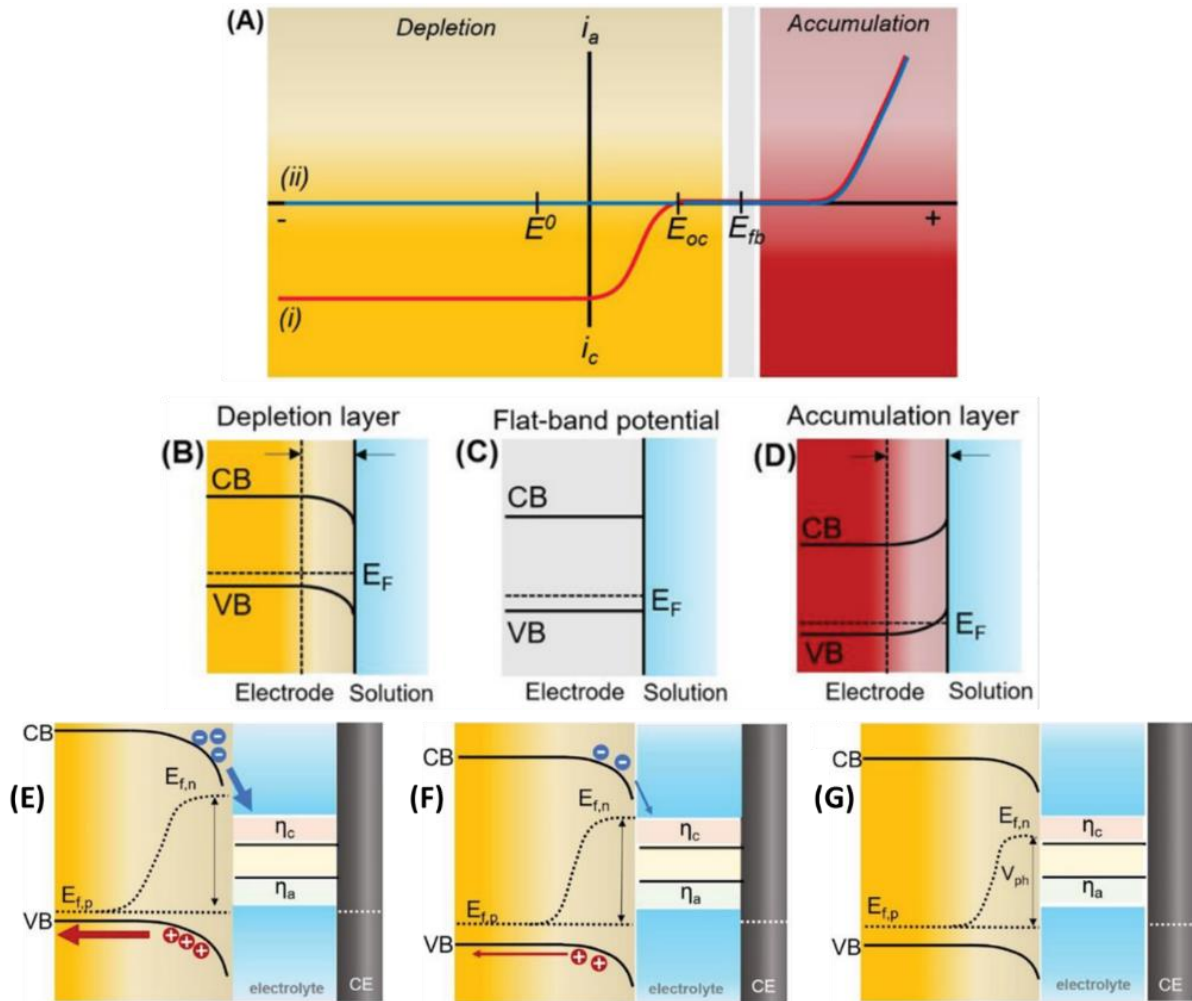
Figure 5 *Influence of the applied potential to the band bending in an p-type semiconductors (a) linear sweep voltammetry indicating the (b) depletion and (c) accumulation region occurring at negative and positive applied bias, respectively. Flat band potential (c). (e-g) indicate the change in the energetics of the $_nE_F^*$ level when it is not enough to drive the reaction (g), at the E_{onset} potential (f) and when it is increased even further to the E_{onset} by the applied bias. η_c and η_b indicate the overpotentials to drive the reduction and oxidation reaction, respectively. Figure adapted from[17]*

An important metric at the SCLJ is the flat band potential (E_{fb}) which represents the potential where the E_F of the semiconductor is aligned to the redox potential of the electrolyte and no net charge transfer

occurs at the interface due to the lack of electric field, as indicated in Figure 5c. The difference between the E_{FB} and the E_{red} of the electrolyte determines the maximum photovoltage at the SCLJ, which is located within the E_C and E_V.[34] A semiconductor with a small band gap is desired to harvest most of the solar spectrum, but consequently it will provide a low photovoltage, which in the actual PEC device is even lower due to the charge accumulation and recombination process that modify the energetics of the $_nE_F*$.[17]

Note that effect of the applied potential on the band bending was only described qualitatively, the exact band position was not indicated in Figure 5 and not drawn to scale.

1.2.4 *p-n* junction-electrolyte interface

An applied potential to promote the reduction reaction and therefore increasing the photocurrent adds an energy cost to the device. Another strategy that the PEC community has explored to improve the photovoltage is adding a buried junction when a *p-* and *n*-type semiconductors are overlaid, as shown in Figure 6a.[34] The equilibrium is reached when the Fermi level of the semiconductors is aligned caused by the rearrangement of charges at the *p-n* semiconductor interface (Figure 6b). In the *p*-type semiconductor, the holes are transferred to the *n*-type creating a depletion layer of the majority charge carriers, then this interface becomes negatively charged. Meanwhile in the *n*-type semiconductor, the electrons are transferred to the *p-* type leaving a positively charged interface, where an electric field is generated aiding the charge separation. After photon absorption, the $_nE_F*$ arises from the large population of photoelectrons and the photovoltage in this device is dictated by the difference between the electron $_nE_F*$ and the $_pE_F*$ at the *p-n* junction as shown in Figure 6c.[35] The mismatch in the band alignment between the *p-* and *n-* type junction lowers photovoltage as indicated in Figure 6d.

Adding a transparent *n*-type semiconductor such as TiO_2 also provides a protection layer against photocorrosion which occurs when the *p*-type semiconductor is in direct contact with the electrolyte.

This approach has been extensively studied with a large number of semiconductors including silicon, chalcogenides, CuO, among others.[17,35]

An alternative approach to induce band-bending in the semiconductor is by adding a molecule with a large dipole moment at the surface, either carboxylic or phosphonic acids are often added. Nevertheless, the low stability and the shielding effect caused by the electrolyte are the main drawbacks. [28,36,37] Recently, the introduction of a phosphonic acid layer of 2 nm of thickness at the interface of p-Si and TiO$_2$ created a stable "buried junction" protecting the dipole and shifting the onset potential ($\Delta E = 400$ mV) to more positive potentials for H$_2$ evolution reaction in the LSV, when compared with the p-Si/TiO$_2$ device.[37]
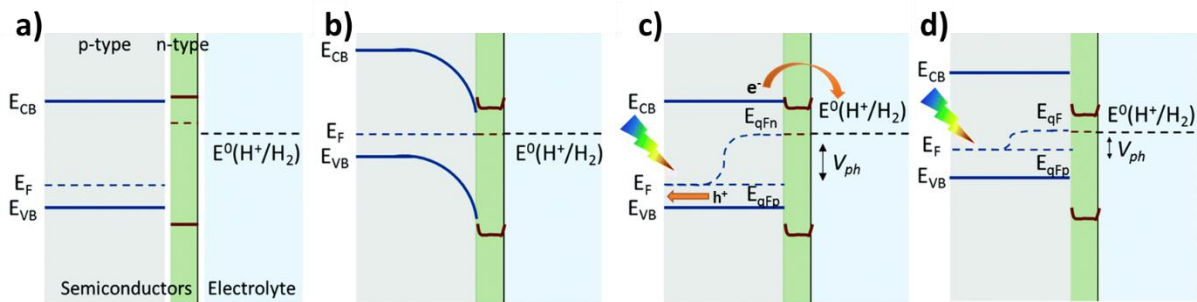
Figure 6 *Buried p-n junction for a photocathode (a) before, (b) after equilibrium, (c) after photon absorption and (d) mismatching band alignment. Note that the energetics of the band bending was only described qualitatively, the exact band position was not indicated. Adapted from*[35]

1.3. Photoelectrochemical reduction reaction

Charge separation at the semiconductor/electrolyte interface is necessary for achieving efficient PEC devices. However, the slow kinetics of photoelectron transfer for either for HER or CO$_2$R leads to charge accumulation at the interface, increasing the recombination rate and the likelihood of trapping of charges in deep-lying states (see section 1.2.2).

Specifically for CO$_2$R, the low CO$_2$ solubility in aqueous electrolytes (~33 mM),[38] and the thermodynamic stability of CO$_2$ to reduction[39] present a great challenge to achieve efficient PEC CO$_2$

conversion.[40–43] The standard potential for the one-electron reduction of CO_2 ($CO_2/CO_2^{\cdot-}$) is -1.9 V *vs*

RHE, a very negative value.[38] In contrast, a range of multi-electron, multi-proton reductions of CO_2 are

achieved at significantly more positive potentials. The various C_1 products that can be obtained from

the reduction of CO_2 in aqueous solutions at pH 7 are shown in the Latimer-Frost diagram in Figure 7.[44]

An effective way to enabling the multi-electron and -proton reduction of CO_2 and to avoid the formation

of $CO_2^{\cdot-}$ is therefore to first transfer the photoelectrons to a known CO_2 reduction electrocatalyst which

can accumulate multiple electrons. A further advantage is that by judicious choice of electrocatalyst it

should be possible to target specific CO_2 reduction products and avoid competitive hydrogen

evolution.[39]
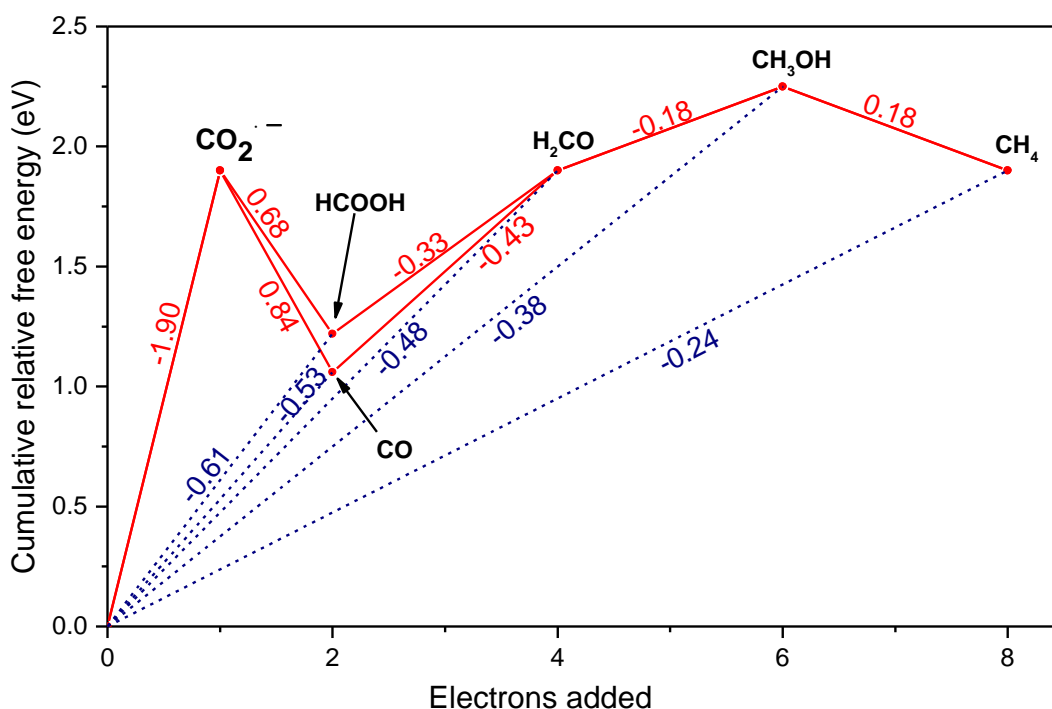
Figure 7. *Latimer-Frost diagram for the possible reduction reactions of CO_2 in water at pH 7 with showing the relative stability for each species (red, eV). Values taken from ref.* [44] *and references therein. The blue lines show the equilibrium potential for the electrochemical reaction to achieve the indicated products (vs NHE).*

A range of metals have been shown to be effective as electrocatalysts for CO_2 reduction and examples

of semiconductor photoelectrodes decorated with metal nanoparticles such as Au, Ag, Ru, In, and Pb

have been reported.[17,45–48] However the ability of molecular catalysts to accumulate multiple charge equivalents, [49–53] the capability to achieve extremely high turnover frequencies (~10^6 s^{-1}) and high selectivity make them an attractive target for use in PEC devices.[54,55] Furthermore, the synthetic tunability of molecular catalysts also offers control over the electrode/catalyst interface making it feasible to develop structures that facilitate fast electron transfer from the semiconductor to the catalyst to prevent charge accumulation within the space charge layer to lower recombination losses.

The following discussion is based on the representative molecular catalysts shown in Figure 8 that were coupled with inorganic semiconductors to build hybrid photocathodes.

1.3.1 Molecular electrocatalysts for PEC CO$_2$ reduction

For a hybrid electrode to operate effectively a negative change in Gibbs free energy for electron transfer (ΔG_{ET}) from the semiconductor to the molecular catalyst is necessary. Therefore, semiconductors with particularly negative conduction band potentials *e.g.*, InP:Zn (-0.92 V$_{RHE}$),[56] GaP (-1.77 V$_{RHE}$),[56,57] *N*-Ta$_2$O$_5$ (-1.17 V$_{RHE}$),[57] Cu$_2$ZnSnS$_4$ (-0.87 V$_{RHE}$),[58] Cu$_2$O (-1.2 V$_{RHE}$)[59] have been investigated as photocathodes (shown in Figure 14). Most of these are expected to be able to undergo electron transfer to the commonly used molecular electrocatalysts shown in Figure 8, based on the onset potential for CO$_2$ catalysis (E_{cat}) with the electrocatalyst either in solution or when immobilised onto an electroactive support (*e.g.* [Ru(bpy-R)$_2$(CO)$_2$]$^{2+}$ (**1-4**) ~ -0.7 to -0.9 V$_{NHE}$,[60] [Ni(cyclam-R)]$^{2+}$ (**5, 9, 10**) ~ -0.9 V$_{NHE}$,[61,62] [Mn(bpy-R)(CO)$_3$X] (**15**) ~ -0.9 V$_{NHE}$,[63,64] [Re(bpy-R)(CO)$_3$X] (**11, 12, 14**) ~ -0.9 to -1.2 (typically),[19,65] V$_{NHE}$, [Co(tpy-R)$_2$]$^{2+}$ (**13**) ~ -0.8 V$_{NHE}$[66]).

(1)

R = -H **(2)**
-PO₃H₂ **(3)**
-COOH **(4)**

(5)

R =
(6)
-PO₃H₂ **(7)**
-COOH **(8)**

(9-10)

R = -t-Bu **(11)**
-PO₃H₂ **(12)**

(13)

(14)

(15)

X = N, C
(16, 17)

(18)

(19)

(20)

Figure 8 *Structures/classes of molecular electrocatalysts coupled to semiconductor photoabsorbers for PEC CO₂R discussed in this chapter.*

1.3.2. Driving force of electron transfer at the semiconductor-molecular catalyst

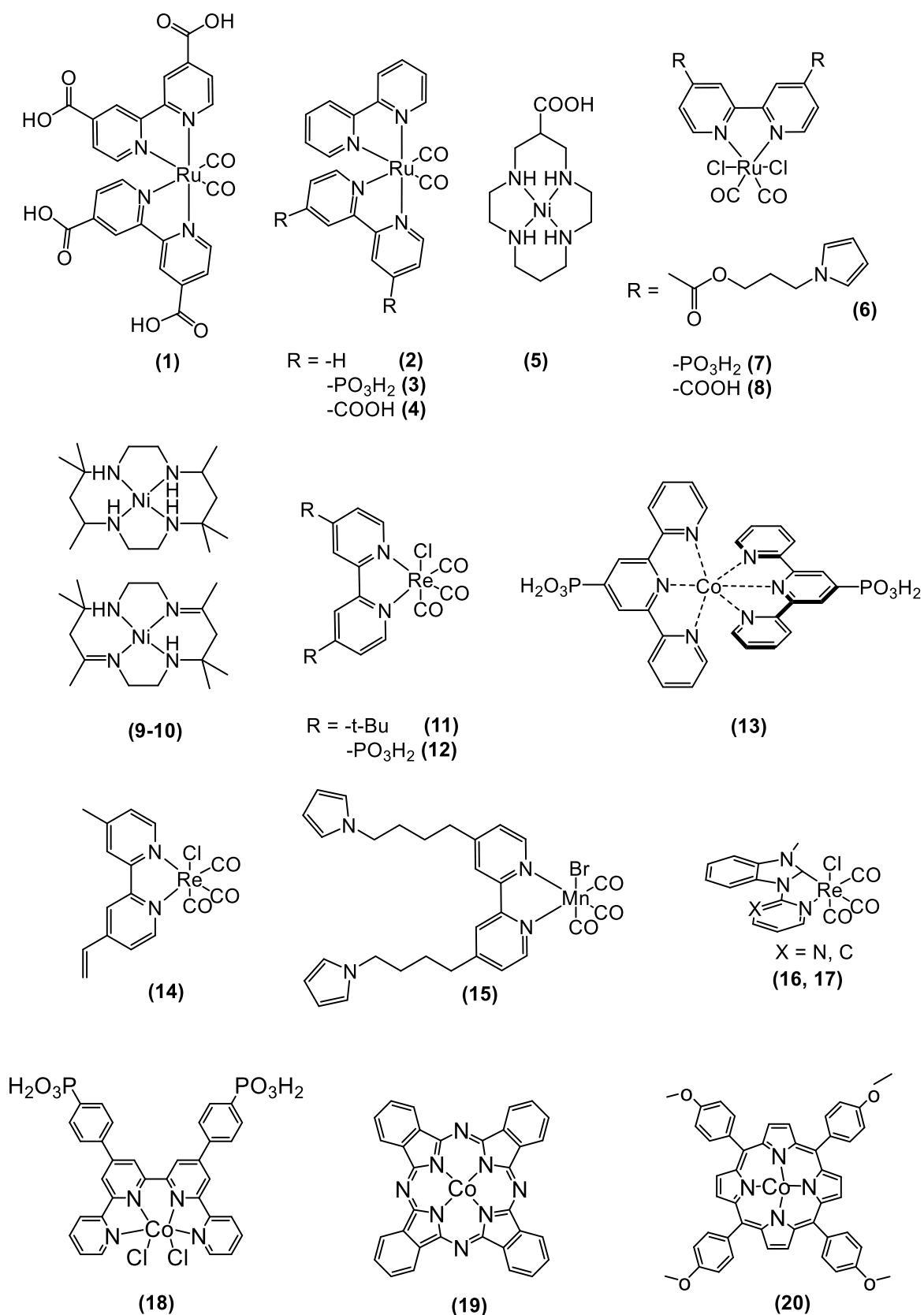As electron-hole recombination within the absorber material is in kinetic competition with electron transfer to the catalyst,[73] it is important to optimise the rate of electron transfer to (and minimise or ideally avoid the back-electron transfer from) the catalyst. In systems where Fermi-level pinning of the semiconductor is not occurring, control of the driving force for electron transfer can be achieved through synthetic modification of the molecular catalyst to change its onset potential for CO_2. Motohiro *et al.*[74] studied a series of Ru polypyridyl molecular catalysts modified with differing types of binding groups (**2-4**) on p-type N doped Ta_2O_5 for CO_2 reduction to HCOOH and CO. A correlation between the catalyst reduction potential and the overall activity of the hybrid photocathode was observed, where the catalysts with the most positive E_{cat} gave rise to the highest turnover numbers (TONs). (**3**) modified with the phosphonic acid binding group was found to be catalytically active in solution at potentials +0.1 V positive of those with carboxylic acid groups (**4**), with the increased driving force for charge transfer being proposed for the increase in TONs from 24 (HCOOH) and 17 (CO) with **4**, to 118 (HCOOH) and 76 (CO) with **3**.[74]

The electron transfer can also be tuned through modification of the energetics in the conduction band of the semiconductor. The negative shift in E_C for $Ti_{1-x}Zr_xO_2$ (*ca.* 150 mV) compared to TiO_2 led to a ~50% increase in the rate of electron transfer and enhanced charge separation lifetimes, when modified with **Ni(cyclam)$^{2+}$** (**cyclam** = 1,4,8,11-tetraazacyclotetradecane) catalyst (**5**).[75]

Multiple reports have shown no correlation between PEC activity and predicted ΔG_{ET} based on isolated measurements of the catalyst and semiconductor. The PEC activity of Cr_2O_3/N,Z*n*-Fe_2O_3/TiO_2 was dominated by the binding mode and its strength between the molecular catalyst and the TiO_2 layer,[76] similarly studies on Ru catalysts (**6-8**) with *N*-Ta_2O_5, GaP, and InP indicated that PEC activity was controlled by the nature of the interface formed such as geometry of components and the electronic structure.[57] These studies demonstrated that factors such as catalyst immobilisation method, orientation at the surface, presence of charge transfer pathways, and the role of immobilisation on the catalytic mechanism can instead dominate the overall activity of photoelectrodes.

1.4. Interfacing the catalyst and light absorber

In the following section some of the common approaches for catalyst immobilization on inorganic semiconductors (shown in Figure 2) are described, highlighting the advantages and disadvantages of each the system.

1.4.1 Early studies of hybrid electrodes - catalysts in solution

Within 5 years of the first reports of PEC CO_2 reduction, studies using molecular catalysts in solution began to appear (Figure 2b).[48,69,70] A common feature of early works was an improved selectivity towards a specific CO_2 reduction product, for example using a CdTe absorber with a cobalt phthalocyanine complex, Bockris achieved ~100% Faradaic efficiency (FE) for CO production. [48] A particular focus of early studies was the use of **Ni(cyclam)$^{2+}$** and derivatives (**9-10**), catalysts known to be highly selective for CO_2 reduction in water to CO,[77] with a range of *p*-type semiconductor such as *p*-Si[69,70] *p*-GaP, *p*-GaAs.[78] Experiments with *p*-Si were initially carried out in acetonitrile-water mixes,[69,70] but soon studies with *p*-GaAs in water were also reported.[78,79] In all cases addition of **9-10** led to a significant change in product distribution confirming their catalytic role, with CO the dominant product formed, while in the absence of the catalysts only H_2 was produced. Notably the total charge passed also increased in the presence of the Ni catalysts, and photocurrent onset potentials shifted positive. The ease of use of a photoelectrode and catalyst in solution is still relatively widespread with recent examples including the use of *p*-Si with both Re(bpy)(CO)$_3$Cl derivatives[18] and iron porphyrin complexes (**21**)[80] (both for CO production) and *p*-GaP with pyridine for methanol production in water.[81]

The approach of using the catalyst in solution does have several disadvantages: (1) the high concentration of catalyst in solution can cause parasitic light absorption, (2) large portions of the catalyst are not in contact with the semiconductor surface at any one-time decreasing the probability of charge transfer if multiple charges are required,[82,83] (3) the nature/orientation of the catalyst-electrode interaction is hard to control and highly dependent on the electrolyte,[84] light intensity and applied

potential,[69,85] with some molecular catalyst maybe be photodecomposed during long illumination periods.[86] For example, in a recent study of Re-*N*-heterocyclic carbene complexes (**16** and **17**) with a *p*-Si photocathode, addition of 5% water to an acetonitrile electrolyte was found to be sufficient to prevent one of the two catalysts studied adsorbing onto the photocathode.[87] Finally, **(4)** under conditions where the photoelectron flux is relatively low, it is also feasible that diffusion of partially reduced species away from the electrode surface may occur prior to completion of the catalytic cycle.

1.4.2 Polymerised catalysts – generating charge transport pathways and imparting stability

Immobilisation of molecular catalysts (Figure 2c-e) onto the semiconductor surface aids separation of liquid products from the catalyst materials, decreases the amounts of catalyst needed, and in some studies it has also been shown to improve the rate of interfacial electron transfer from the semiconductor to the catalyst.[75,83,88] One of the most effective methods to adhere catalysts to semiconductors surfaces is through electropolymerisation (Figure 2d).[57,58,72]

Over 30 years ago [Re(vinyl-bpy)(CO)$_3$Cl] (**14**), a derivative of a widely studied class of Re carbonyl electrocatalysts, was reductively (photoelectrochemically) polymerised onto both *p*-Si and *p*-WSe$_2$ photocathodes in MeCN-based electrolytes.[89] In this study, a photovoltage of ~0.6 V (with *p*-Si) was achieved leading to CO$_2$ catalysis occurring at more positive applied potentials when compared to the complex deposited onto Pt.

More recently, the polymerisation of Mn bipyridine complex (**15**) onto light absorbing semiconductors has also been reported for photoelectrochemical reduction of CO$_2$.[72] In this study *p*-type H-terminated Si nanowires were used as the light absorber, and although product analysis was not carried out for the hybrid photocathode, the cyclic voltammograms under CO$_2$ and light illumination (MeCN, 5% water) showed a significant increase of the current density compared to Ar and dark curves.

Polymerisation does offer several advantages over the other methods of catalyst immobilisation described below. Morikawa and coworkers[56] demonstrated that electron transfer pathways between the

semiconductor surface and the catalyst (and in between catalytic centres) were formed using a Ru catalyst that generates a conductive polypyrrole polymer (**6**). Furthermore, it offers the possibility to generate thick polymer coatings with high concentration of catalytic sites on the semiconductor. A 110 nm thick layer based on a Ru(**6**) precursor was deposited on a Cr_2O_3/N,Zn-Fe_2O_3/TiO_2/**6** photoelctrode.[76] A further benefit of the thick polymer catalyst layer was that it provided a protective layer over the absorber with the polymerised catalyst photoelectrode achieving a stable photocurrent (150 μA cm^{-2}) over a 13 hour period to produce HCOOH and CO with a high Faradic efficiency (63% and 30%, respectively). In contrast rapid (minutes) degradation of the Cr_2O_3/N,Zn-Fe_2O_3/TiO_2 structure occurred with similar Ru complexes when -PO_3H_2 and -COOH anchoring groups (**7-8**) were used.[76]

In addition to these works, a number of other photocathodes have now been studied with polymerised Ru catalysts for CO_2 reduction with highlights including the use of **6** electropolymerised on a *p*-type InP:Zn wafer[56] which was able to produce formate in water with a FE of 62.3% when bulk electrolysis was carried out at -0.6 V_{NHE} under visible illumination.

Although control of the catalyst orientation at the electrode surface is not usually possible through polymerisation, an interesting approach to control and build a more defined interface for charge transfer is through functionalities that enable covalent binding to the semiconductor surface alongside a polymerisable catalyst. In studies using Cu_2ZnSnS_4 (CZTS)[58] and InP[57] photoelectrodes, mixtures of **6** and **7** lead to higher rates of CO_2R to formate compared to each catalyst in isolation. It was then proposed that the phosphonate groups of **7** enabled binding to the surface of the sulphide and phosphide semiconductors while **7** acted as an electron transfer facilitator to the conductive polymer network generated by **6**.

In some cases, it has been proposed that the polymer chain commonly used to link molecular catalysts either acted as the catalyst itself or facilitated the catalytic CO_2R. A polypyrrole based photoelectrodes exhibited a FE of 62% for CH_3COOH production,[90] while polyaniline based photoelectrodes achieved a FE of 78% for the same reaction.[91]

Recent advances making use of multifunctional coatings consisting of redox active centres with functionalities to covalently bind to the electrode surface in a controllable manner and catalytic centres with polymerizable groups are of great interest. [57,58] Reisner and co-workers[92] synthesized a polymer containing 3 different functionalities: (i) phosphonic acid groups to enable binding to the p-Si/TiO$_2$ absorber, (ii) terpyridine ligands for coordinating Co^{2+} in a similar derivative complex than **13** and (iii) hydrophobic functional groups in the second coordination sphere of the molecular catalyst which improve CO$_2$ diffusion across the polymer. This approach significantly increase the CO:H$_2$ selectivity from 2:1 to 6:1 compared to the Co-based monomer.

Despite being used in some of the very earliest studies,[89] polymerised catalysts have consistently led to the formation of layers with some of the highest stabilities, however this is often at the cost of control of catalyst orientation making it hard to design effective charge transfer interfaces.[21]

1.4.3 Covalent immobilisation of catalysts
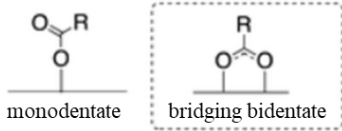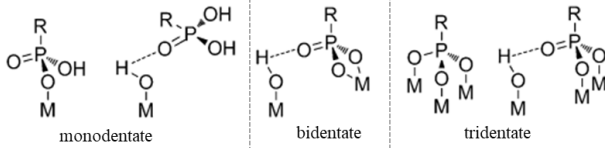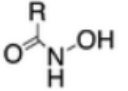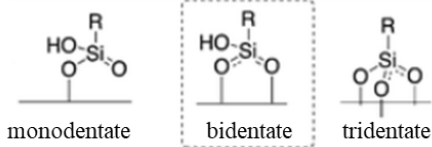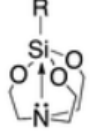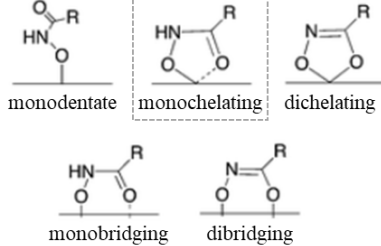
The covalently binding the of molecular catalyst onto the light absorber, or onto a protective coating, provides a way to generate well-defined photoelectrode-catalyst interfaces. In principle such control enables the fine tuning of the charge transfer efficiency through modification of the chemical functionality of the anchoring group and by controlling the catalyst binding angle. A range of possible binding groups to metal oxides are known,[93–95] with the majority of the literature coming from the dye-sensitised solar cell (DSSC) community.[96] However, most DSSCs work was carried out in organic solvents, and the stability of the anchoring groups can change in aqueous electrolytes or in organic solvents containing an acid source required for CO$_2$R in a PEC cell.[97]

In general, a good anchoring group should react to form a functionality resistant to detachment from the surface, promote charge transfer, be able to withstand the reducing environment during catalysis and be stable to long-term light exposure. These requirements apply to both the catalyst in a PEC or catalyst and dyes for Dye Sensitised Photoelectrochemical Cell (DSPEC, see section 1.4.4). Table 1

summarises some of the most reported anchoring groups, the stability across different pHs, the electron injection after being anchored to a metal oxide, and the possible binding modes highting the most favourable binding.[97,131]

Historically carboxylates and phosphonates are the most widely studied and employed anchoring groups as they bind well to oxide semiconductors.[96] Although in aqueous solvents phosphonic acid binding groups offer greater stability than carboxylic acids, the rate of charge transfer to/from the surface bound molecules is significantly slower with phosphonic acid groups.[98] In studies of DSSC, this change in rate of charge transfer has been ascribed to the nature of the sp^2 hybridised –COOH group which enables electron delocalisation, in contrast the sp^3 phosphonic group effectively acting as an insulator between the semiconductor and bound molecule.[96] Theoretical studies of the rate of electron transfer from *N*-Ta_2O_5 to $Ru(bpy-R_2)(CO)_2Cl_2$ (R = PO_3H_2 (**7**) and CO_2H (**8**)) have also assigned the faster electron transfer to **8** to be due to increased nonadiabatic coupling between the donor and acceptor sites.[99]

Table 1 *Molecular structure of some of the most common anchoring groups used for binding catalyst/dye molecules to metal oxides surfaces, pH stability and possible binding modes, the most favourable binding is also indicated.* [97,131]

Anchoring group	Molecular structure	pH stability	Electron injection	Possible binding modes
Carboxylic acid		pH < 4	Efficient	
Phosphonic acid		pH < 7	Moderate	
Hydroxamatic acid		pH 2 – 10.25	Efficient	
Silantrane		pH 2 – 11	Unknown	

A large number of molecular electrocatalysts have now been modified with phosphonic and carboxylic acids for immobilisation, and used in photocatalytic CO_2 reduction, with examples including derivatives of Ni(cyclam)$^{2+}$,[75,100] Ru(bpy)(CO)$_2$Cl$_2$,[60] Re(bpy)(CO)$_3$Cl,[19] Co(II) bis(terpyridine)[66,101] with covalent immobilisation being shown by TAS to facilitate electron transfer to the catalysts, when compared to the same catalyst in solution.[100,101] An important breakthrough study was on Re(bpy-PO$_3$H$_2$)(CO)$_3$Cl (**12**) bound to a mesoporous TiO_2 layer coated on Cu$_2$O/AZO/ALD-TiO$_2$ (ALD, atomic layer deposition; AZO aluminium-doped zinc oxide).[19] In a previous work by Grätzel, where an unbound Re catalyst (**11**) was used with a Cu$_2$O absorber, the electrostatic repulsion between the reduced catalyst intermediates and the polarised photoelectrode prevented multiple charge transfer and subsequent CO$_2$R.[82] Immobilisation of **12** onto the light absorber overcomes the repulsion of the catalyst from the electrode surface.[19] Initial studies where the catalyst was bound directly onto the smooth ALD TiO_2 layer (used with AZO to both protect, and form a charge separation junction with the Cu$_2$O)[59,102] resulted in very low catalyst loadings. Under 1 sun the catalyst on ALD TiO_2 was unable to turnover at a sufficiently high rate to keep up with the photogenerated electron flux from the Cu$_2$O. Once a high surface area mesoporous TiO_2 layer was added, catalyst loadings of ~85 nmol cm^{-2} (geometric) were achieved and a large increase in photocurrent occurred. Although this result was an important step for the field, activity decreased within 2 hours under illumination, proposed to be due a combination of catalyst desorption and structural change of the bipyridine ligand of the anchored catalyst. The covalent immobilisation does bring advantages by facilitating the multi-electron transfers to the catalyst required for CO$_2$R, but if the catalyst becomes inactive, it may remain fixed on to the electrode surface blocking regeneration.[19,66]

Recently, Robert and coworkers developed a hybrid photocathode using a photovoltaic solar cell based on CIGS/CdS/AZO/ZnO and a Co quarpyridine modified with phosphonic groups (Co-qPyH, **18**) anchored onto an ALD TiO$_2$.[103] The molecular catalyst loading was 3 ± 1 nmol cm^{-2} and after 2 hours of electrolysis at -0.06 V vs NHE the photocurrent decresed from -3 to ~-0.5 mA cm^{-2}, however a remarkable selectivity of 97% towards CO was attained and only 3% for H$_2$ despite the hybrid photocathode operated only in aqueos electrolyte (0.1 M KHCO$_3$ saturated with CO$_2$, pH 6.8). The

decrease in the photocurrent was associated either to the desorption of the molecular catalyst or to the degradation of the photovotaic solar cell if the electolyte reached the AZO layer, concluding that an increase of TiO_2 surface area could add extra protection to the solar cell and allow higher loadings of **18** to improve the performace.

In section 1.4.2, the application of a cobalt bis(terpyridine) catalyst in a polymer matrix on p-Si/TiO_2 was discussed,[92] and a similar system without the conductive polymer where a phosphonated cobalt bis(terpyridine) (**13**) was bound directly to the p-Si/TiO_2 has also been reported.[66] In addition to using entirely earth abundant elements and operating in water, this work was notable for the stability achieved, with > 8 hrs of activity reported without significance loss in activity. Following *in-situ* spectroelectrochemical studies, the stability (and improved onset potential) of **13** was associated with the change in CO_2R mechanism of the catalyst upon immobilisation, Figure 9. In contrast to solution studies where cobalt bis(terpyridine) catalysts undergo loss of one terpyridine ligand prior to CO_2 binding, which can be irreversible if the ligand diffuses away, the **13**-catalyst immobilised onto the TiO_2 scaffold was thought to retain its bis(terpyridine) ligation with only a single Co-N site detached to enable CO_2 binding.

Catalyst desorption has been reported to occur even when phosphonic acid binding groups are used, and to reach a level of stability where devices are of practical use orders of magnitude increases in stability are required.[19,103–105] Recently, within the PEC water splitting community, hydroxamates and silatrane groups have been explored as alternative. Carboxylates and phosphonates hydrolise at moderate pH values (pH >4 for carboxylates, pH > 7 for phosphonates). Hydroxamates and silatranes are stable across a much greater pH range (2-10 and 2-11, respectively). Silatranes have similar injection rates than phosphonates when the anchors were used to bind a porphyrin dye onto TiO_2 in a DSSC cell. Furthermore, hydroxamates have shown faster charge injection rates compared to even carboxylic acids when equivalent dye centres and semiconductors are used.[106] They have been applied to PEC devices for hydrogen evolution and Table 1 summarises some of the key features. Gong and co-workers modified a cobaloxime with carboxylic, phosphonic and hydroxamates anchoring groups and studied the effect of the anchoring group on the surface of p-Si/TiO_2.[107] This study demonstrated that

hydroxamates moieties displayed superior capabilities in aqueous electrolytes, generating higher photocurrents, achieving faster electron transfer and better stabilities when compared with carboxylic and phosphonic anchoring derivatives. However, this is the less explored functionality used as anchoring group.
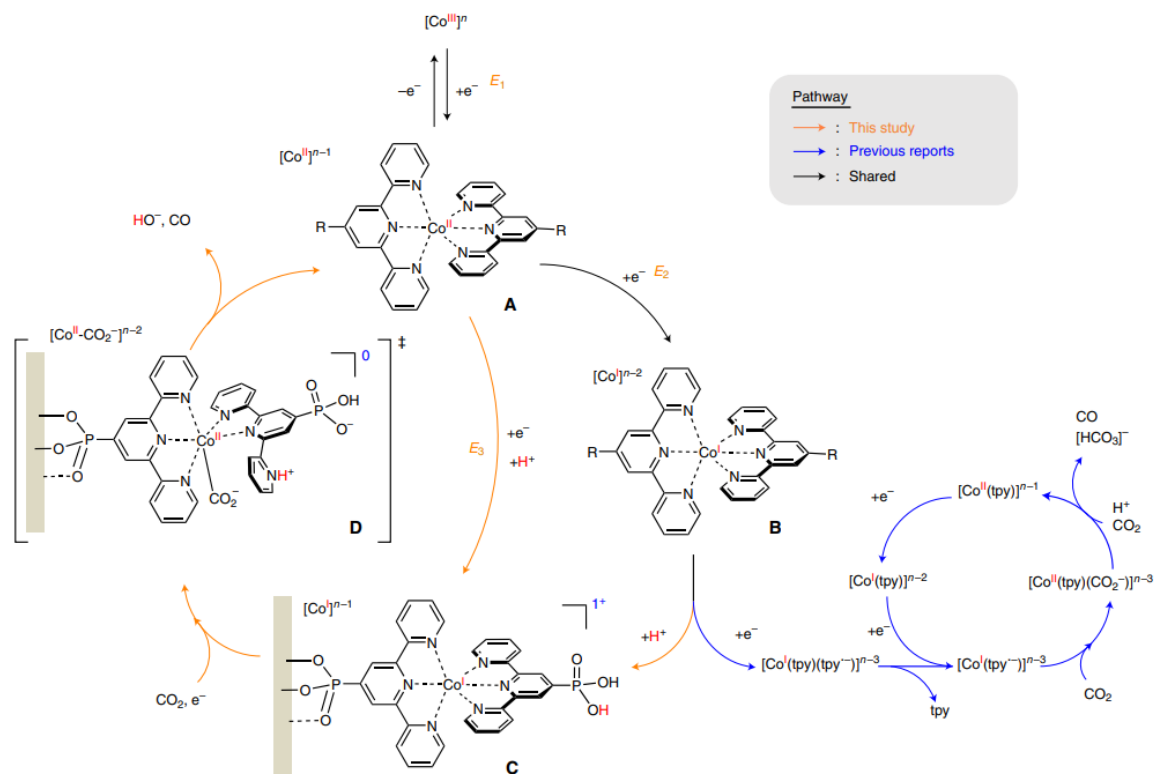
Figure 9 *Proposed mechanism for CO_2 reduction by 13 anchored to TiO_2-meso (orange pathway), in contrast to catalyst in solution (blue pathway).*[66]

1.4.4 Dye and supramolecular constructs

Turnover frequencies as high as 10^6 s^{-1} for CO_2 reduction to CO have been reported for some Fe porphyrin electrocatalysts under idealised conditions,[55] however the kinetics of the CO_2R of many molecular catalysts under practical operating conditions can be much slower (*e.g.* Re(bpy)(CO)$_3$Cl k_{cat} ~150 s^{-1}, CH$_3$CN[108]). Therefore kinetic competition between back electron transfer from the catalyst to the semiconductor can become limiting.[66,68,83,109] In part, this can be overcome through the use of a greater number of catalysts immobilised on high-surface area supports, in the manner described above

for Cu_2O/AZO/ALD-TiO_2/m-TiO_2/**12**[19] and Si/m-TiO_2/**13** electrodes.[66] Alternatively the lifetime of the charge-separated state can be increased through modulation of the internal electric field of the semiconductor,[75] the use of multi-layer solid-state structures[103,110] or by the design of supramolecular constructs for energetic and longer range (spatial) charge separation.[111]

A different approach to building photocathodes for CO_2R has emerged based on the field of dye-sensitised solar cells, which makes use of supramolecular structures to generate long-range charge separated states (Figure 2e).[112–115] Here, rather than using a narrow band-gap semiconductor as the light absorber, a wide band-gap material is used as a hole transporting layer (HTL) with a molecular photosensitiser for light harvesting.[88,116] The cascade of events that leads to CO_2 reduction is: (1) the photosensitiser or dye (PS) absorbs the light, (2) the wide band-gap semiconductor, usually NiO extracts the holes from the excited photosensitiser (3) electron transfer from the reduced photosensitiser to the catalyst (cat) occurs and finally (4) CO_2 reduction takes place at the molecular catalyst, as indicated in Figure 10.[116] The resultant charge separated state is with the electron residing on the catalyst and the hole on the semiconductor, with the neutral dye molecule between them.

The group of Meyer have recently reported the use of silane binding groups to link a vinyl group-containing Ru absorber (poly(Ru^{II})) on the surface of *p*-type NiO photoelectrodes *via* electropolymerisation in order to build a DSPEC.[117] The CO_2 reduction centre, a Re polypyridyl complex (poly(Re^I)) was then bound to the poly(Ru^{II}) also by electropolymerisation. The photocathode was able to reduce CO_2 to CO under 100 mW cm^{-2}, $\lambda \geq 400$ nm at -0.7 V *vs* Ag/AgCl with more than 80% of the initial photocurrent (*ca.* 15 μA cm^{-2}) being maintained after 10 hours. The prolonged PEC activity was a result of the strong Si-O bonds compared with equivalent phosphonated catalysts which showed rapid loss in activity. TAS analysis on the ns-μs scale indicated that the recombination rate of the catalytically active state (NiO(h^+)-poly(Ru^I)-poly(Re^0)) was in the μs-ms scale, suggesting that the presence of the aliphatic chains connecting the metal complexes to the NiO surface may be an important factor in achieving a long-lived charge separated states improving the PEC activity.
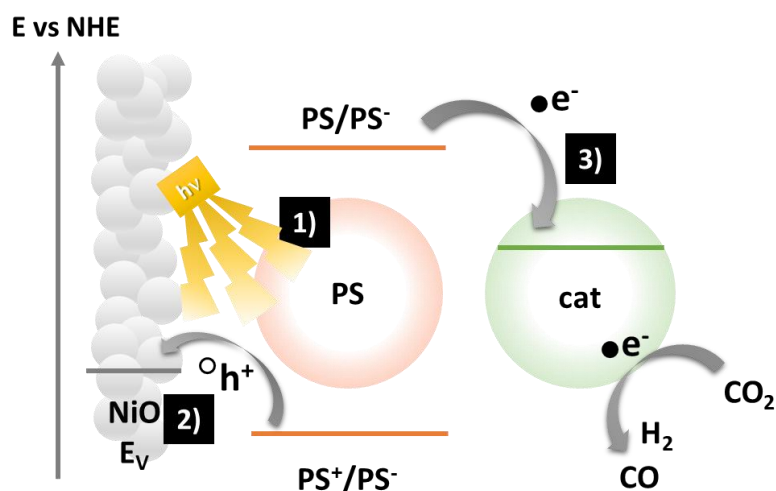
Figure 10 *Working principle of a DSPEC (1) the photosensitiser or dye (PS) absorbs the light, (2) NiO extract holes from the excited photosensitiser (3) electron transfer from the reduced photosensitiser to the molecular catalyst (cat) and (4) CO$_2$R at the cat. Adapted from*[88].

The difficulty of synthesis of the complex molecular architectures is potentially a major drawback which may limit the emergence of more complex structures for use in DSPEC. A simple method to construct a dye-catalyst supramolecule was recently reported, where each component (electron donor, dye, catalyst) was added in a layer-by-layer approach using Zr-phosphonate bridges onto mesoporous NiO.[111] The phosphonated dianiline donor between the NiO and the dye ([Ru((4,4′-(PO$_3$H$_2$CH$_2$)$_2$-2,2′-bipyridine)(2,2′-bipyridine))$_2$]$^{2+}$)[96] played a critical role leading to *ca.* 8 times higher photocurrents (at -0.54 V$_{NHE}$) compared to photoelectrodes where only the dye and the catalyst ([Re(I)((4,4'-PO$_3$H$_2$CH$_2$)$_2$-2,2'-bipyridine)(CO)$_3$Cl]) were present. While the stability of the photoelectrodes was in this example quite low, further studies by the same research group[110] showed a marked increase in stability when using a binary *p-n* junction with a protective coating. Here *n*-type GaN nanowires were deposited on *n$^+$-p-p$^+$* silicon wafer (Si/*n*-GaN) with a sub nm thick NiO or Al$_2$O$_3$ overlayer to stabilise the phosphonate linkage to the surface were interfaced with a range of phenylene diamine donors, as shown in Figure 11. Remarkable photocurrents of −1 mA cm^{-2} at −0.25 V *vs* RHE were achieved for 20 h with HCOOH as CO$_2$R product. TAS and emission spectroscopy revealed the highest PEC activity was achieved on photocathodes where the donor exhibited the most positive reduction potential,

confirming that a high driving force between the photoelectrode components was highly desirable.[110] This work also represents the state-of-the-art DSPEC device.
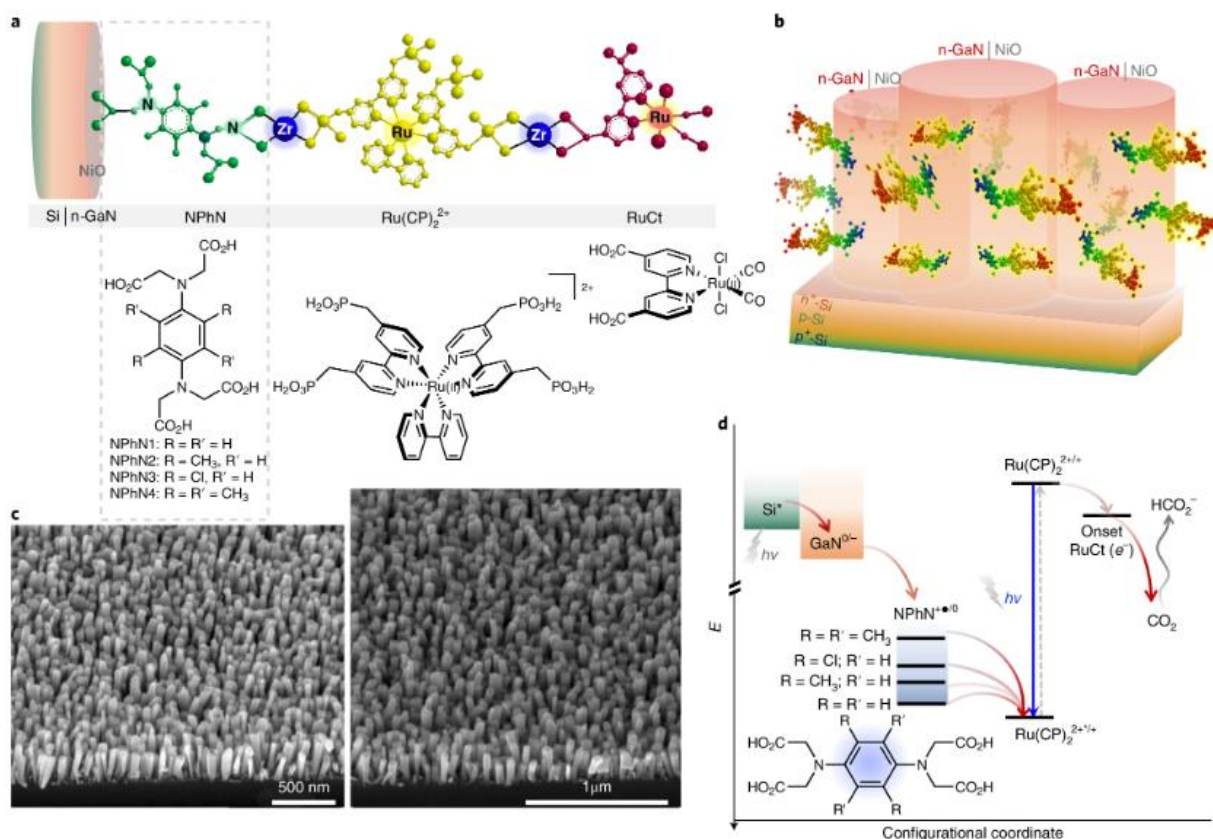
Figure 11. *(a, b) Photocathode structure of a supramolecular dye build by Zr bridges on Si/n-GaN where NPhN, Ru(CP)$_2$$^{2+}$, RuCt act as electron donor, dye and catalyst, respectively. (c) SEM image of the on Si/n-GaN nanowires and (d) Energy level diagram of the different redox process occurring at the photocathode, the red arrows indicated the direction of photoelectron transfer.*

Some of the most representative hybrid photocathodes have been described highlighting the advantages brought about by each immobilization method. As a general trend, still most of the hybrid photocathodes achieved photocurrents in the microamperes scale. Recently, the PEC community has also explored immobilising molecular catalysts on conductive carbon supports such as carbon nanotubes (CNT) or graphene by non-covalently π-π stacking, which significantly enhanced the PEC activity and will be discussed in the following section.

1.4.5 Molecular catalyst immobilised on carbon materials

The immobilization of molecular catalysts by π-π stacking on carbon supports has been extensively studied and demonstrated clear improvement in the CO_2R catalytic activity with lower catalyst content.[118,119] Furthermore, this approach does not require the modification of the catalyst with an anchoring group which sometimes could hamper the electrocatalytic activity, and opens a wide range of opportunities for studying molecular catalyst immobilised on carbon substrates alongside light absorbers.

Recently, the catalytic activity of a group of Co-based molecular catalyst supported on CNT was studied onto p-nSi/TiO$_2$, including cobalt bis(terpyridine)[120] and Cobalt phthalocyanine (**CoPc, 19**).[121] The CNT@**Co^{II}(BrqPy)**, (with **BrqPy** = 4',4''-bis(4-bromophenyl)-2,2':6',2'':6'',2'''-qua-terpyridine) displayed the largest photocurrent −1.5 mA cm^{-2} at −0.11 V *vs* RHE in aqueous electrolyte (0.1 M KHCO$_3$ pH=6.8) with notably 100% FE for CO during 2 h.[120] Using the same light absorber (p-type Si/TiO$_2$), the production of methanol was demonstrated at −0.36 V *vs* RHE with FE$_{MeOH}$ of 8% when **CoPc** was immobilised on graphene oxide (GO), representing the first hybrid photocathode that achieves 6 electron transfer for CO_2R. Linking the active material (GO@**CoPc**) onto p-type Si/TiO$_2$ was accomplished by adding 3-aminopropyl) triethoxysilane which reacted *via* silanization with the TiO$_2$ and anchored the GO@**CoPc** through hydrogen bonds of the linker amines.[121]

Using carbon-based supports for molecular catalyst in photocathodes with front illumination involves a trade-off between light harvesting and active dark composite loading, therefore careful tailoring is required to achieve high PEC activity. Furthermore, for this approach the interface TiO$_2$/carbon@molecular catalyst demonstrated to be the most vulnerable region in the device since the deactivation was associated to the detachment of the CNT@**Co^{II}(BrqPy)**[120] and the linker failure in p-type Si/TiO$_2$/GO@**CoPc**.[121]

Another remarkable photocathode architecture was accomplished by using (**19**) immobilised on CNT alongside a perovskite based solar cell ((Cs$_{0.15}$FA$_{0.85}$)Pb(I$_{0.9}$Br$_{0.1}$)$_3$), shown in Figure 12. The pero*vs*kite instability in water was successful avoided by carbon encapsulation giving rise to −15.5 mA cm^{-2} at

−0.11 in V *vs* RHE in CO_2-saturated 0.5 M $KHCO_3$ demonstrating to be stable upon 25 h with a FE_{CO} of 80%.[122] A similar approach was also reported by Reisner and collaborators with a perovskite solar cell alongside cobalt(II) meso-tetrakis(4-methoxyphenyl) **(20)** on CNT, this device exhibited a photocurrent of −5.67 mA cm^{-2} at 0 V *vs* RHE at 1 sun illumination with low selectivity towards CO ($CO:H_2$ was only 0.22 ± 0.10), the CO selectivity was improved only after decreasing the applied potential and/or light intensity, suggesting that even high molecular catalyst loadings on the CNT, its turnover frequency was not enough to keep up with photoelectron flux, therefore H_2 was the main product.[123]

Figure 12 *(a) Carbon encapsulated perovskite (($Cs_{0.15}FA_{0.85}$)$Pb(I_{0.9}Br_{0.1})_3$) photocathode and (b) energy level diagram of the perovskite solar cell.*[122]

These examples demonstrated the possibility to incorporate all the knowledge about grafting molecular catalyst on carbon materials in the field of hybrid photocathodes. In addition, these devices were back illuminated allowing higher CNT@molecular catalyst loadings without compromising the solar cell light harvesting. On the other hand, the use of perovskite solar cell-based devices indeed enhanced the PEC activity for CO_2R photocathodes at the cost of the complexity of the sophisticated multilayer architecture and careful encapsulation, as shown in Figure 12.

1.5. State-of-the-art of hybrid photocathodes for H_2

Some of the most representative hybrid photocathodes for CO_2R have been discussed in the previous section and significant progress in the field has been accomplished based on devices for hydrogen production summarised by Meyer[22] and more recently by Moore.[124] These HER hybrid photocathodes share the same operational principle in light absorption than devices for CO_2R, furthermore similar immobilisation strategies have been explored.

In this section only the most representative HER hybrid photocathodes, covalently immobilised on metal oxides are summarised in Table 2 to provide context for our device presented in Chapter 3. It also contains the stability, which was defined as the photocurrent at the beginning of the control potential photoelectrolyis (CPPE, $J_0 \ @ \ t = 0$) against the photocurrent measured at certain time ($J \ @ \ t \ (h)$) at 0 V *vs* RHE, according to Eq. (2). Aditionally, Table 3 contains the hydrogen evolution catalysts studied in those devices.

$$\% \text{ Stability} = \frac{J \ @ \ t \ (h)}{J_0 \ @ \ t=0} \qquad\qquad \text{Eq. (2)}$$

A notable device was reported by Turner.[125] It coupled the efficient *p*-type light absorber ($GaInP_2$) with 35 nm thick ALD TiO_2, which provides a suitable surface for the cobaloxime molecular catalyst to be anchored through carboxylic acid groups. The 20 h stability was attributed to the ~0.4 nm thick ALD TiO_2 layer deposited afterwards to protect the carboxylic acid anchoring group. The hybrid photocathode with the cobaloxime displayed similar performance in terms of photocurrent and stability that the platinized device

Similar to CO_2R hybrid photocathodes, these devices have also limited stability at the milliampere scale, therefore extended stability is imperative to achieve large-scale usage.

The examples of photoelectrodes described previously demonstrate the dual role of the hybrid structure in enabling both catalysis and charge separation, however both processes take place at completely different time scales as shown in Figure 13.[126] For a photocathode to operate effectively, charge transfer

at the molecular catalyst should meet photocharge generation and molecular electrocatalysts could be in principle be designed to bind to the surface in a manner to meet optimal charge transfer.
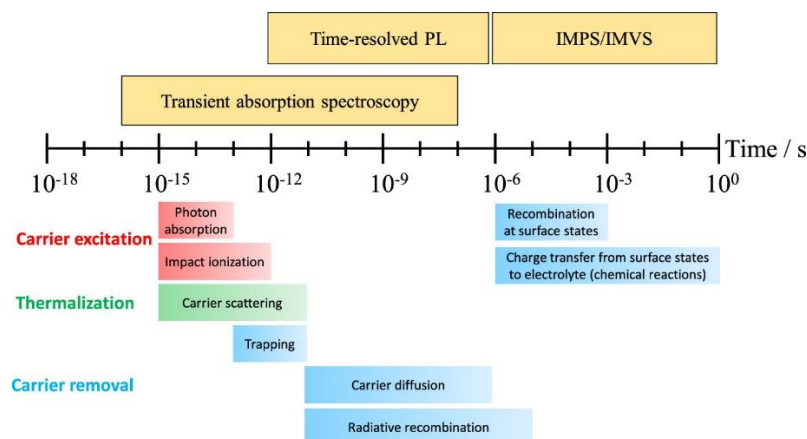
Figure 13 *Typical time scales of the different process occurring in a photocathode compared with the time scale resolution of the techniques that can be used to study them PL: photoluminescence, IMPS: intensity modulated photovoltage and photocurrent spectroscopy.* [126]

In Figure 13 some of the experimental techniques like time resolved photoluminesce (TRPL), transient absorption spectroscopy (TAS), intensity modulated photovoltage and photocurrent (IMPS/IMP*VS*) could be used in combination with *in-situ* spectroscopic techniques to provide information regarding to the catalyst mechanism at the interface for the designing of more efficient photocathodes to meet important criteria in achieving solar to fuel production at large scale such as efficiency, cost and scalability.
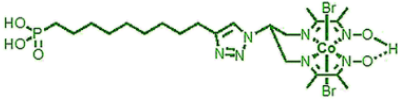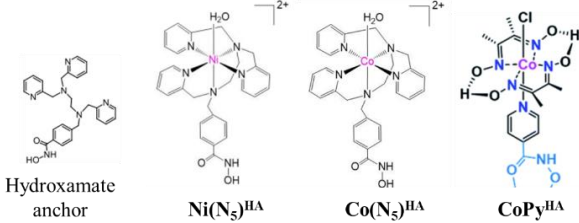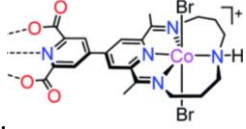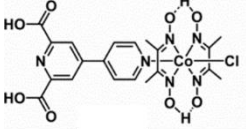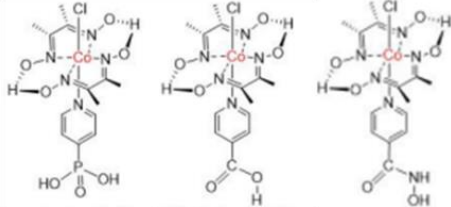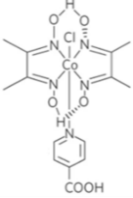
Finally, from the literature survey carried out from the introduction a general trend is observed, the first examples of hybrid photocathodes used the molecular catalyst in solution alongside a *p*-type semiconductor. After, synthetic modifications on the molecular catalyst to be immobilized in the electrode either by polymerization or covalently linking were dominant, and most recently the complexity of the device has increased significantly from the *p-n* junction to the complete solar cell approach, or the p+ or n- modifications in the semiconductors to improve charge separation. Nevertheless, even if efficient light harvesting devices are achieved, the TON of molecular catalyst need to improve otherwise the stability of the device could be compromise.

Table 2 *Hybrid photocathodes for H$_2$ production*

Photocathode	$-j$ (mA cm^{-2}) @ 0 V *vs* RHE	Stability (%) t (h)	Electrolyte	Light source	Ref.
p-Si/TiO$_2$/**NiP**	0.35	28%; 24	0.1 M Acetic Acid, pH 4.5	AM 1.5G, 100 mW cm^{-2} λ> 400 nm	[104]
Au/LTCA/TiO$_2$/**NiP**	0.5	8%; 6	0.1 M Na$_2$SO$_4$, pH 3	AM 1.5G, 100 mW cm^{-2}	[105]
p-Si/ALD-TiO$_2$/SC-TiO$_2$/**Co$_{C11P}$**/ALD-TiO$_2$	1.3	77%; 1	1 M PBS, pH 7	AM 1.5G, 100 mW cm^{-2}	[127]
p-Si/TiO$_{2(ALD/DB)}$/**Ni(N$_5$)^{HA}**	1	100%	0.1 M PBS, pH 7	AM 1.5G, 100 mW cm^{-2}	[128]
p-Si/TiO$_{2(ALD/DB)}$/**Co(N$_5$)^{HA}**	0.7	100%	0.1 M PBS, pH 7	AM 1.5G, 100 mW cm^{-2}	[128]
p-Si/TiO$_{2(ALD/DB)}$/**CoPy^{HA}**	0.4	84%; 6	0.1 M PBS, pH 7	AM 1.5G, 100 mW cm^{-2}	[128]
Si/TiO$_2$/**Co(CR-DCP)**	0.68	100%; 10	0.1 M ABS, pH 4.5	AM 1.5G, 100 mW cm^{-2} λ> 400 nm	[129]
CuFe$_x$O$_y$/TiO$_2$/**CoHEC**	4.5 0.4 V *vs* RHE	67%; 20 min	0.2 M PBS, pH 6.7	1 sun, (400–780 nm)	[130]
p-Si/TiO$_2$/**CoPy-4-CONH(OH)**	0.32	≈100%; 2	0.1 M BBS, pH 9	AM 1.5G, 100 mW cm^{-2} λ> 400 nm	[107]
p-Si/TiO$_2$/**CoPy-4-PO$_3$H$_2$**	0.18	75%; 2	0.1 M BBS, pH 9	AM 1.5G, 100 mW cm^{-2} λ> 400 nm	[107]
p-Si/TiO$_2$/**CoPy-4-COOH**	0.16	66%; 2	0.1 M BBS, pH 9	AM 1.5G, 100 mW cm^{-2} λ> 400 nm	[107]
GaInP$_2$/TiO$_2$/ **(OOCpy)Co(dmgH)$_2$(Cl)**/TiO$_2$	9	56%; 20	0.1M NaOH, pH 13	1-sun, 100 mW cm^{-2}	[125]

LTCA- La$_5$Ti$_2$Cu$_{0.9}$Ag$_{0.1}$S$_5$O$_7$ **SC**- Spin coating, **ALD**-Atomic Layer Deposition, **DB**-Doctor-blading, **ABS**: Acetic buffer solution, **PBS**: Phosphate buffer solution, **BBS**: Borate buffer solution

Table 3 *Molecular structure of metal complexes listed in Table 2*

Molecular catalyst		Molecular structure	Ref.
Co$_{C11P}$	Diimine–dioxime cobalt complex		127
Ni(N$_5$)^{HA} **Co(N$_5$)^{HA}** **CoPy^{HA}**	diamine-tripyridine ligand with an hydroxamate anchor	Hydroxamate anchor **Ni(N$_5$)^{HA}** **Co(N$_5$)^{HA}** **CoPy^{HA}**	128
Co(CR-DCP)	cobalt tetraazamacrocyclic catalyst with 2,6-dicarboxypyridin-4-yl		129
CoHEC	chloro([4,4′-bipyridine]-2,6-dicarboxylic acid)bis(dimethylglyoximato)cobalt(III))		130
CoPy-4-X	cobaloxime catalysts (Py = pyridine, X = PO$_3$H$_2$, COOH, and CONH(OH)	X=PO$_3$H$_2$ X=COOH X=CONH(OH)	107
(OOCpy)Co (dmgH)$_2$(Cl)	(dmgH)$_2$ = bis-glyoxime and isonictonic acid		125

1.6. References

1   J. Barber, *Chem. Soc. Rev.*, 2009, **38**, 185–196.

2   L. Hammarström, *Acc. Chem. Res.*, 2009, **42**, 1859–1860.

3   M. Aresta, A. Dibenedetto and A. Angelini, *Chem. Rev.*, 2014, **114**, 1709–1742.

4   S. C. Roy, O. K. Varghese, M. Paulose and C. A. Grimes, *ACS Nano*, 2010, **4**, 1259–1278.

5   D. U. Nielsen, X. M. Hu, K. Daasbjerg and T. Skrydstrup, *Nat. Catal.*, 2018, **1**, 244–254.

6   H. Song, S. Luo, H. Huang, B. Deng and J. Ye, *ACS Energy Lett.*, 2022, **7**, 1043–1065.

7   T. Jesper Jacobsson, V. FjällströmFj, M. Edoff and T. Edvinsson, *Energy Environ. Sci.*, **7**, 2056–2070.

8   W. Je Chang, K.-H. Lee, H. Ha, K. Jin, G. Kim, S.-T. Hwang, H. Lee, S.-W. Ahn, W. Yoon, H. Seo, J. Sug Hong, Y. Kyung Go, J.-I. Ha and K. Tae Nam, *ACS Omega*, 2017, **2**, 20.

9   I. Garcia, I. Rey-Stolle, C. Algora, W. Stolz, K. Volz, S. Essig, S. Ward, M. A. Steiner, D. J. Friedman, J. F. Geisz, P. Stradins, D. L. Young, J. Jia, L. C. Seitz, J. D. Benck, Y. Huo, Y. Chen, J. W. D. Ng, T. Bilir, J. S. Harris and T. F. Jaramillo, *Energy Procedia*, 2016, **77**, 13237.

10   T. Haas, R. Krause, R. Weber, M. Demler and G. Schmid, *Nat. Catal.*, 2018, **1**, 32–39.

11   L. Zhang, Z. J. Zhao, T. Wang and J. Gong, *Chem. Soc. Rev.*, 2018, **47**, 5423–5443.

12   X. Chang, T. Wang, P. Yang, G. Zhang and J. Gong, *Adv. Mater.*, 2018, **1804710**, 1–13.

13   S. Xie, Q. Zhang, G. Liu and Y. Wang, *Chem. Commun.*, 2016, **52**, 35–59.

14   V. Kumaravel, J. Bartlett and S. C. Pillai, *ACS Energy Lett.*, 2020, **5**, 486–519.

15   P. Ding, T. Jiang, N. Han and Y. Li, *Mater Today Nano*, 2020, 10, 1–11.

16   S. Haussener, *Solar Energy*, 2022, **246**, 294–300.

17   L. K. Putri, B. J. Ng, W. J. Ong, S. P. Chai and A. R. Mohamed, *Adv. Energy Mater.*, 2022, **17**, 2201093.

18   B. Kumar, J. M. Smieja and C. P. Kubiak, *J. Phys. Chem. C.*, 2010, **114**, 14220–14223.

19   M. Schreier, J. Luo, P. Gao, T. Moehl, M. T. Mayer and M. Grätzel, *J. Am. Chem. Soc.*, 2016, **138**, 1938–1946.

20   J. A. Esterhuizen, N. M. Orchanian, L. E. Hong, S. C. Marinescu, D. A. Popov and J. A. Skrainka, *ACS Appl. Energy Mater.*, 2018, **2**, 110–123.

21   R. Kamata, H. Kumagai, Y. Yamazaki, G. Sahara, O. Ishitani, R. Abe, M. Higashi, T. Morikawa, K. Maeda, Y. Ueda and O. Ishitani, *ACS Appl. Mater. Interfaces*, 2018, **11**, 5632–5641.

22   F. Niu, D. Wang, F. Li, Y. Liu, S. Shen and T. J. Meyer, *Adv. Energy Mater.*, 2019, **1900399**, 1–24.

23   L. M. Peter, in *RSC Energy and Environment Series*, Royal Society of Chemistry, 2016, vol. 2016-Janua, pp. 3–28.

24   Z. Zhang and J. T. Yates, *Chem. Rev.*, 2012, **112**, 5520–5551.

25   A. J. Nozik, *Annu. Rev. Phys. Chem.*, 1978, **29**, 189–222.

26   J. L. White, M. F. Baruch, J. E. Pander, Y. Hu, I. C. Fortmeyer, J. E. Park, T. Zhang, K. Liao, J. Gu, Y. Yan, T. W. Shaw, E. Abelev and A. B. Bocarsly, *Chem. Rev.*, 2015, **115**, 12888–12935.

27   H. Gerischer, *J. Electroanal. Chem.*, 1977, **82**, 133–143.

28   W. A. Smith, I. D. Sharp, N. C. Strandwitz and J. Bisquert, *Energy. Environ. Sci.*, 2015, **8**, 2851–2862.

29   W. W. Gartner, *Phys. Rev.*, 1959, **116**, 84–87.

30   A. J. Bard, A. B. Bocarsly, F. R. F. Fan, E. G. Walton and M. S. Wrighton, *J. Am. Chem. Soc.*, 1980, **102**, 3671–3677.

31   J. Bisquert, G. Garcia-Belmonte and F. Fabregat-Santiago, *J. Solid State Electrochem.*, 1999, **3**, 337–347.

32   W. J. Albery and P. N. Bartlett, *J. Electrochem. Soc.*, 1984, **131**, 315–325.

33   A. J. Nozik and R. Memming, *J. Phys. Chem.*, 1996, **100**, 13061–13078.

34   M. G. Walter, E. L. Warren, J. R. McKone, S. W. Boettcher, Q. Mi, E. A. Santori and N. S. Lewis, *Chem. Rev.*, 2010, **110**, 6446–6473.

35   W. Yang, R. R. Prabhakar, J. Tan, S. D. Tilley and J. Moon, *Chem. Soc. Rev.*, 2019, **48**, 4979–5015.

36   J. M. Gurrentz and M. J. Rose, *J. Am. Chem. Soc.*, 2020, **142**, 5657–5667.

37   R. Wick-Joliat, T. Musso, R. R. Prabhakar, J. Löckinger, S. Siol, W. Cui, L. Sévery, T. Moehl, J. Suh, J. Hutter, M. Iannuzzi and S. D. Tilley, *Energy Environ Sci.*, 2019, 9–12.

38   B. P. Sullivan, K. Krist and H. E. Guard, *Electrochemical and electrocatalytic reactions of carbon dioxide*, Elsevier, 1993.

39   B. Kumar, M. Llorente, J. Froehlich, T. Dang, A. Sathrum and C. P. Kubiak, *Annu. Rev. Phys. Chem.*, 2012, **63**, 541–69.

40   L. Junfu and C. Y. Baozhu, *J. Electroanal. Chem.*, 1992, **324**, 191–200.

41   H. Yoneyama, K. Sugimura and S. Kuwabata, *J. Electroanal. Chem.*, 1988, **249**, 143–153.

42   B. Aurian-Blajeni, M. Halmann and J. Manassen, *Sol. Energy Mater.*, 1983, **8**, 425–440.

43   M. Halmann, *Nature,* 1978, **275**, 115–116.

44   J. Schneider, H. Jia, J. T. Muckerman and E. Fujita, *Chem. Soc. Rev.*, 2012, **41**, 2036–2051.

45   I. Taniguchi, B. Aurian-Blajeni and J. O. Bockris, *Electrochim Acta*, 1984, **29**, 923–932.

46   Y. J. Jang, J. W. Jang, J. Lee, J. H. Kim, H. Kumagai, J. Lee, T. Minegishi, J. Kubota, K. Domen and J. S. Lee, *Energy Environ. Sci.*, 2015, **8**, 3597–3604.

47   J. S. Duchene, G. Tagliabue, A. J. Welch, W. H. Cheng and H. A. Atwater, *Nano Lett.*, 2018, **18**, 2545–2550.

48   J. O. Bockris and J. C. Wass, *Mater. Chem. Phys.*, 1989, **22**, 249–280.

49   K. A. Grice, *Coord. Chem. Rev.*, 2017, **336**, 78–95.

50   Y. Wang, D. He, H. Chen and D. Wang, *J. Photochem. Photobiol.*, 2019, **40**, 1–33.

51   M. Stanbury, J.-D. Compain and S. Chardon-Noblat, *Coord. Chem. Rev.*, 2018, **361**, 120–137.

52   R. Francke, B. Schille and M. Roemelt, *Chem. Rev.*, 2018, 118, 4631–4701.

53   K. Elouarzaki, V. Kannan, V. Jose, H. S. Sabharwal and J. M. Lee, *Adv. Energy. Mater.*, 2019, **9**, 1–33.

54   S. Ren, D. Joulié, D. Salvatore, K. Torbensen, M. Wang, M. Robert and C. P. Berlinguette, *Science*, 2019, **365**, 367–369.

55   C. Costentin, M. Robert, J.-M. M. Savéant and A. Tatin, *Proc. Natl. Acad. Sci. U S A*, 2015, **112**, 6882–6886.

56   T. Arai, S. Sato, K. Uemura, T. Morikawa, T. Kajino and T. Motohiro, *Chem. Comm.*, 2010, **46**, 6944–6946.

57   S. Sato, T. Arai, T. Morikawa, K. Uemura, T. M. Suzuki, H. Tanaka and T. Kajino, *J. Am. Chem. Soc.*, 2011, **133**, 15240–15243.

58   T. Arai, S. Tajima, S. Sato, K. Uemura, T. Morikawa and T. Kajino, *Chem. Comm.*, 2011, **47**, 12664–12666.

59   A. Paracchino, N. Mathews, T. Hisatomi, M. Stefik, S. D. Tilley and M. Grätzel, *Energy Environ. Sci.*, 2012, **5**, 8673–8681.

60   S. Sato, T. Morikawa, S. Saeki, T. Kajino and T. Motohiro, *Angew. Chem. Int. Ed.*, 2010, **49**, 5101–5105.

61   Marc. Beley, J. Paul. Collin, Romain. Ruppert and J. Pierre. Sauvage, *J. Am. Chem. Soc.*, 1986, **108**, 7461–7467.

62   G. Neri, I. M. Aldous, J. J. Walsh, L. J. Hardwick and A. J. Cowan, *Chem. Sci.*, 2016, **7**, 1521–1526.

63   M. Bourrez, F. Molton, S. Chardon-Noblat and A. Deronzier, *Angew. Chem. Int. Ed. Engl.*, 2011, **50**, 9903–9906.

64   J. J. Walsh, G. Neri, C. L. Smith and A. J. Cowan, *Chem. Comm.*, 2014, **50**, 12698–12701.

65   J. Hawecker, J.-M. Lehn and R. Ziessel, *J. Chem. Soc. Chem. Commun.*, 1984, **0**, 328–330.

66   J. J. Leung, J. Warnan, K. H. Ly, N. Heidary, D. H. Nam, M. F. Kuehnel, E. Reisner, V. Kumaravel, J. Bartlett, S. C. Pillai, J. J. Leung, J. Warnan, K. H. Ly, N. Heidary, D. H. Nam, M. F. Kuehnel and E. Reisner, *Nat. Catal.*, 2019, **2**, 354–365.

67   C. J. Kaminsky, S. Weng, J. Wright and Y. Surendranath, *Nat. Catal.*, 2022, **5**, 430–442.

68   K. Yamanaka, S. Sato, M. Iwaki, T. Kajino and T. Morikawa, *J. Phys. Chem. C*, 2011, **115**, 18348–18353.

69   M. G. Bradley, T. Tysak, D. J. Graves, N. A. Vlachopoulos and N. A. Vlachopoulosc, *J. Chem. Soc., Chem. Commun.*, 1983, **116**, 349–350.

70   M. G. Bradley and T. Tysak, *J. Electroanal. Chem.*, 1982, **135**, 153–157.

71   D. He, T. Jin, W. Li, S. Pantovich, D. Wang and G. Li, *Chem. Eur. J.*, 2016, **22**, 13064–13067.

72   E. Torralba-Penalver, Y. Luo, J. D. Compain, S. Chardon-Noblat and B. Fabre, *ACS Catal.*, 2015, **5**, 6138–6147.

73   A. J. Cowan and J. R. Durrant, *Chem. Soc. Rev.*, 2013, **42**, 2281–2293.

74   T. M. Suzuki, H. Tanaka, T. Morikawa, M. Iwaki, S. Sato, S. Saeki, M. Inoue, T. Kajino and T. Motohiro, *Chem. Comm.*, 2011, **47**, 8673.

75   G. Neri, J. J. Walsh, C. Wilson, A. Reynal, J. Y. C. Lim, X. Li, A. J. P. White, N. J. Long, J. R. Durrant and A. J. Cowan, *Phys. Chem. Chem. Phys.*, 2015, **17**, 1562–1566.

76   K. Sekizawa, S. Sato, T. Arai and T. Morikawa, *ACS Catal.*, 2018, **8**, 1405–1416.

77   M. Beley, J.-P. Collin, R. Ruppert and J.-P. Sauvage, *J. Chem. Soc. Chem. Commun.*, 1984, **2**, 1315–1316.

78   J.-P. Petit, P. Chartier, M. Beley and J.-P. Deville, *J. Electroanal. Chem.*, 1989, **269**, 267–281.

79   M. Beley, J. P. Collin, J. P. Sauvage, J. P. Petit and P. Chartier, *J. Electroanal. Chem.*, 1986, **206**, 333–339.

80   K. Alenezi, S. K. Ibrahim, P. Li and C. J. Pickett, *Chem. Eur. J.*, 2013, **19**, 13522–13527.

81   E. E. Barton, D. M. Rampulla and A. B. Bocarsly, *J. Am. Chem. Soc.*, 2008, **130**, 6342-+.

82   M. Schreier, P. Gao, M. T. Mayer, J. Luo, T. Moehl, M. K. Nazeeruddin, S. D. Tilley and M. Grätzel, *Energy Environ. Sci.*, 2015, **8**, 855–861.

83   C. D. Windle, E. Pastor, A. Reynal, A. C. Whitwood, Y. Vaynzof, J. R. Durrant, R. N. Perutz and E. Reisner, *Chem. Eur. J.*, 2015, **21**, 3746–3754.

84   A. Wagner, C. D. Sahm and E. Reisner, *Nat. Catal.*, 2020, **3**, 775–786.

85   B. Zhao, H. Lei, N. Wang, G. Xu, W. Zhang and R. Cao, *Chem. Eur. J.*, 2019, 1–7.

86   E. Boutin, L. Merakeb, B. Ma, B. Boudy, M. Wang, J. Bonin, E. Anxolabéhère-Mallart and M. Robert, *Chem. Soc. Rev.*, 2020, **49**, 5772–5809.

87   T. Jin, D. He, W. Li, C. J. Stanton, S. A. Pantovich, G. F. Majetich, H. F. Schaefer, J. Agarwal, D. Wang and G. Li, *Chem. Comm.*, 2016, **52**, 14258–14261.

88   H. Tian, *ChemSusChem*, 2015, **8**, 3746–3759.

89   C. R. Cabrera and H. D. Abruña, *J. Electroanal. Chem.*, 1986, **209**, 101–107.

90   R. Aydin and F. Köleli, *Synth. Met.*, 2004, **144**, 75–80.

91   F. Koleli, T. Ropke and C. Hamann, *Synth. Met.*, 2004, **140**, 65–68.

92   J. J. Leung, J. A. Vigil, J. Warnan, E. Edwardes Moore and E. Reisner, *Angew. Chem. Int. Ed.*, 2019, **58**, 7697–7701.

93   M. F. Kuehnel, C. D. Sahm, G. Neri, J. R. Lee, K. L. Orchard, A. J. Cowan and E. Reisner, *Chem. Sci.*, 2018, **9**, 2501–2509.

94   M. F. Kuehnel, K. L. Orchard, K. E. Dalle and E. Reisner, *J. Am. Chem. Soc.*, 2017, **139**, 7217–7223.

95   J. Huang, K. L. Mulfort, P. Du and L. X. Chen, *J. Am. Chem. Soc.*, 2012, **134**, 16472–16475.

96   L. Zhang and J. M. Cole, *ACS Appl. Mater. Interfaces*, 2015, 7, 3427–3455.

97   K. L. Materna, R. H. Crabtree and G. W. Brudvig, *Chem. Soc. Rev.*, 2017, 46, 6099–6110.

98   R. Ernstorfer, L. Gundlach, S. Felber, W. Storck, R. Eichberger and F. Willig, *J. Phys. Chem. B*, 2006, **110**, 25383–25391.

99   A. V. Akimov, R. Asahi, R. Jinnouchi and O. V. Prezhdo, *J. Am. Chem. Soc.*, 2015, **137**, 11517–11525.

100   G. Neri, M. Forster, J. J. Walsh, C. M. Robertson, T. J. Whittles, P. Farrás and A. J. Cowan, *Chem. Commun.*, 2016, **52**, 14200–14203.

101   C. Bozal-Ginesta, C. A. Mesa, A. Eisenschmidt, L. Francàs, R. B. Shankar, D. Antón-García, J. Warnan, J. Willkomm, A. Reynal, E. Reisner, J. R. Durrant, L. Francas, R. B. Shankar, D. Anton-Garcia, J. Warnan, J. Willkomm, A. Reynal, E. Reisner and J. R. Durrant, *Chem. Sci.*, 2020, **12**, 946–959.

102   A. Paracchino, V. Laporte, K. Sivula, M. Graetzel and E. Thimsen, *Nat. Mater.*, 2011, **10**, 456–461.

103   P. B. Pati, R. Wang, E. Boutin, S. Diring, S. Jobic, N. Barreau, F. Odobel and M. Robert, *Nat. Commun.*, 2020, **11**, 1–9.

104   J. J. Leung, J. Warnan, D. H. Nam, J. Z. Zhang, J. Willkomm and E. Reisner, *Chem. Sci.*, 2017, **8**, 5172–5180.

105   T. E. Rosser, T. Hisatomi, S. Sun, D. Antón-García, T. Minegishi, E. Reisner and K. Domen, *Chem. Eur. J.*, 2018, **24**, 18393–18397.

106   W. R. McNamara, R. L. Milot, H. E. Song, R. C. Snoeberger, V. S. Batista, C. A. Schmuttenmaer, G. W. Brudvig and R. H. Crabtree, *Energy Environ. Sci.*, 2010, **3**, 917–923.

107   L. Gong, H. Yin, C. Nie, X. Sun, X. Wang and M. Wang, *ACS Appl. Mater. Interfaces*, 2019, **11**, 34010−34019.

108   M. L. Clark, P. L. Cheung, M. Lessio, E. A. Carter and C. P. Kubiak, *ACS Catal.*, 2018, **8**, 2021–2029.

109   X. Xiong, M. Forster, J. D. Major, Y. Xu and A. J. Cowan, *J. Phys. Chem. C*, 2017, **121**, 22073–22080.

110   B. Shan, S. Vanka, T.-T. Li, L. Troian-Gautier, M. K. Brennaman, Z. Mi and T. J. Meyer, *Nat. Energy*, 2019, **4**, 290–299.

111   D. Wang, Y. Wang, M. D. Brady, M. v. Sheridan, B. D. Sherman, B. H. Farnum, Y. Liu, S. L. Marquard, G. J. Meyer, C. J. Dares and T. J. Meyer, *Chem. Sci.*, 2019, **10**, 4436–4444.

112   Y. Kou, S. Nakatani, G. Sunagawa, Y. Tachikawa, D. Masui, T. Shimada, S. Takagi, D. A. Tryk, Y. Nabetani, H. Tachibana and H. Inoue, *J. Catal.*, 2014, **310**, 57–66.

113   G. Sahara, R. Abe, M. Higashi, T. Morikawa, K. Maeda, Y. Ueda and O. Ishitani, *Chem. Comm.*, 2015, **51**, 10722–10725.

114   G. Sahara, H. Kumagai, K. Maeda, N. Kaeffer, V. Artero, M. Higashi, R. Abe and O. Ishitani, *J. Am. Chem. Soc.*, 2016, **138**, 14152–14158.

115   H. Kumagai, G. Sahara, K. Maeda, M. Higashi, R. Abe and O. Ishitani, *Chem. Sci.*, 2017, **8**, 4242–4249.

116   M. K. Brennaman, R. J. Dillon, L. Alibabaei, M. K. Gish, C. J. Dares, D. L. Ashford, R. L. House, G. J. Meyer, J. M. Papanikolas and T. J. Meyer, *J. Am. Chem. Soc.*, 2016, **138**, 13085–13102.

117   T.-T. Li, B. Shan and T. J. Meyer, *ACS Energy Lett.*, 2019, **4**, 629–636.

118   L. Sun, V. Reddu, A. C. Fisher and X. Wang, *Energy Environ Sci.*, 2020, **13**, 374–403.

119   D. Nam, P. de Luna, A. Rosas-hernández, A. Thevenon, F. Li, T. Agapie, J. C. Peters, O. Shekhah, M. Eddaoudi and E. H. Sargent, *Nat. Mater.*, 2020, **19**, 266–276.

120   Z. Wen, S. Xu, Y. Zhu, G. Liu, H. Gao, L. Sun and F. Li, *Angew. Chem. Int. Ed.*, 2022, **61**, e2022010 (1 of 7).

121   A. Krayev, H. Shema, O. Leitner and J. Nia, *Angew. Chem. Int. Ed*, 2023, **62**, (1 of 7).

122   H. Zhang, Y. Chen, H. Wang, H. Wang, W. Ma, X. Zong and C. Li, *Adv. Energy Mater.*, 2020, **10**, 2002105, 1–9.

123   V. Andrei, B. Reuillard and E. Reisner, *Nat. Mater.*, 2020, **19**, 189–194.

124   E. A. Reyes-Cruz, D. Nishiori, B. L. Wadsworth, N. P. Nguyen, L. K. Hensleigh, D. Khusnutdinova, A. M. Beiler and G. F. Moore, *Chem. Rev.,* 2022, **122**, 21, 16051–16109.

125   J. Gu, Y. Yan, J. L. Young, K. X. Steirer, N. R. Neale and J. A. Turner, *Nat. Mater.*, 2016, **15**, 456–462.

126   J. He and C. Janáky, *ACS Energy Lett.*, 2020, **5**, 1996–2014.

127   S. Chandrasekaran, N. Kaeffer, L. Cagnon, D. Aldakov, J. Fize, G. Nonglaton, F. Baleras, P. Mailley and V. Artero, *Chem. Sci.*, 2019, **10**, 4469–4475.

128   L. Gong, P. Zhang, G. Liu, Y. Shan and M. Wang, *J. Mater. Chem. A.*, 2021, **9**, 12140–12151.

129   C. Nie, C. Liu, L. Gong and M. Wang, *J. Mater. Chem. A.*, 2021, **9**, 234–238.

130   C. Tapia, E. Bellet-Amalric, D. Aldakov, F. Boudoire, K. Sivula, L. Cagnon and V. Artero, *Green Chem.*, 2020, **22**, 3141–3149.

131   C. C. Queffeíec, M. Petit, P. Janvier, D. A. Knight, B., Bujoli, *Chem. Rev.,* 2012, **112**, 7, 3777–3807.

Chapter 2

Finding the light absorber

Scope of the chapter

In this chapter, the process followed to find a suitable photocathode light absorber is described. ZnTe was proposed as a starting material since the position of the Conduction Band Minimum (CBM) at -1.48 V vs RHE lies among the most negative values of p-type semiconductors,[1] suggesting the photoelectrons generated have enough driving force to carry reduction reactions, such as CO_2 reduction towards CO at -0.11 V vs RHE or H^+ reduction for producing H_2 at 0.0 V vs RHE.[2] The simplest approach, whereby the bare ZnTe is deposited on FTO was first studied. Soon after, the need for a protective layer and/or passivating layer to improve charge separation and to avoid photocorrosion was identified. The main criteria to select a suitable capping layer was based on the position of the metal oxides CBM and Al_2O_3, ZrO_2, ZnO:Al (AZO) and Ta_2O_5, were studied. Promising combinations such as $ZnTe/ZrO_2$ and $ZnTe/Ta_2O_5$ were identified, as well as the need of catalysts for promoting photoelectron extraction and supressing recombination. Pt was used as benchmarking catalyst for the Hydrogen Evolution Reaction (HER), and although this device structure is not new in the literature, it allowed to find the bottlenecks of the device and provide insights for further optimization. In this way, improvements in the semiconductor deposition process were identified as a necessity to increase film quality. This would be expected to improve the photocurrent, since only -20 μA cm^{-2} was obtained at 0 V vs RHE for $FTO/ZnTe/Ta_2O_5/Pt$, which lies well behind the ZnTe state-of-the-art photocathodes (-1.5 mA cm^{-2} at 0 V vs RHE).[3]

For the second part of this chapter, Sb_2Se_3 was studied as an alternative light absorber since its deposition conditions had been already optimised.[4] Several factors such as the semiconductor crystalline structure, size and surface states, *p-n* junction, selective contacts and catalyst determine how the photocarriers are efficiently (or not) extracted from the device, defining the photoelectrochemical (PEC) performance (photocurrent and onset potential). Whilst the Sb_2Se_3 CBM provides less driving force for a reduction reaction (-0.5 V *vs* RHE), the state-of-the-art materials exhibit photocurrents -30 mA cm^{-2} at 0 V *vs* RHE[5] which is significantly higher compared with the ZnTe champion photocathode, indeed highlighting the importance in tailoring all the components. Sb_2Se_3/TiO_2 and $Sb_2Se_3/CdS/TiO_2$ interfaces were studied and identified that the TiO_2 crystalline structure played a key role in the PEC performance of the device. Although photocurrents lower to the state-of-the-art photocathodes were recorded, the devices demonstrated to be suitable platform for hybrid photocathodes which usually achieve photocurrents in the micro-milliampere scale as summarised in Chapter 1, when used alongside Earth abundant molecular catalyst for H_2, and CO_2 reduction reaction (CO_2R) for the following chapters.

The ZnTe and Sb_2Se_3 absorbers studied in this chapter were made in collaboration with Dr Jon Major's group (Dr Thomas Shalvey, Dr Laurie Philips and Dr Oliver Hutter) from the Stephenson Institute for Renewable Energy at University of Liverpool. The ALD capping layers (thermal Al_2O_3, and PEALD TiO_2) were made in collaboration with Dr Richard Potter from the School of Engineering at University of Liverpool.

2.1 Introduction

2.1.1 State-of-the-art of ZnTe photocathodes

In general, there are many requirements for a semiconductor to be considered as suitable photocathode light absorber. Some of the most important characteristics are listed below:

(a) Small band gap to absorb a wide range of the solar spectrum.

(b) Suitable band alignment to drive a reduction reaction such as H_2 production (HER) or CO_2 reduction (CO_2R). The difference between the CBM and the redox potential for a particular reaction determines the driving force.

(c) To provide facile transport of the photogenerated charges across the light absorber before recombination, properties such as high charge carrier mobility, long charge-carrier lifetime, long diffusion length of charge carriers are needed.

(d) Stability in aqueous solution, although as will be shown protective layers can be used.

(e) Based on earth abundant materials to be economically feasible[6]

(f) High absorption coefficient, since a larger absorption coefficient allows thinner layers for effectively photon absorption with larger energy than the band gap to generate the hole-electron pairs. [7]

For reduction reactions like CO_2R and HER, a large number of metal oxides and chalcogenides exhibit the required light absorption characteristics to be used in PEC cells.[2,8] Figure 14 shows the CBM and the Valence Band Maxima (VBM) of some semiconductors commonly used for CO_2R.[9]

The CBM of ZnTe is particularly notable for its large driving force for interfacial electron transfer from the semiconductor to electron acceptors in the electrolyte. Furthermore, its band gap of 2.26 eV enables to use most of the visible region from the solar spectrum. ZnTe has been used as a photocathode for HER and CO_2R, however the bare semiconductor ZnTe exhibited low stability maintaining the 68.5% of the initial photocurrent after 3 h of control potential photoelectrolysis (CPP) at -0.7 V *vs* RHE and only the 25.4% selectivity to CO.[1] Table 4 contains a summary of the state-of the-art photocathodes

based on ZnTe, the stability was defined as the photocurrent measured at the beginning of the CPP (J_0 @ $t = 0$) against the photocurrent measured at certain time (J @ t (h)) as indicated in equation 2.
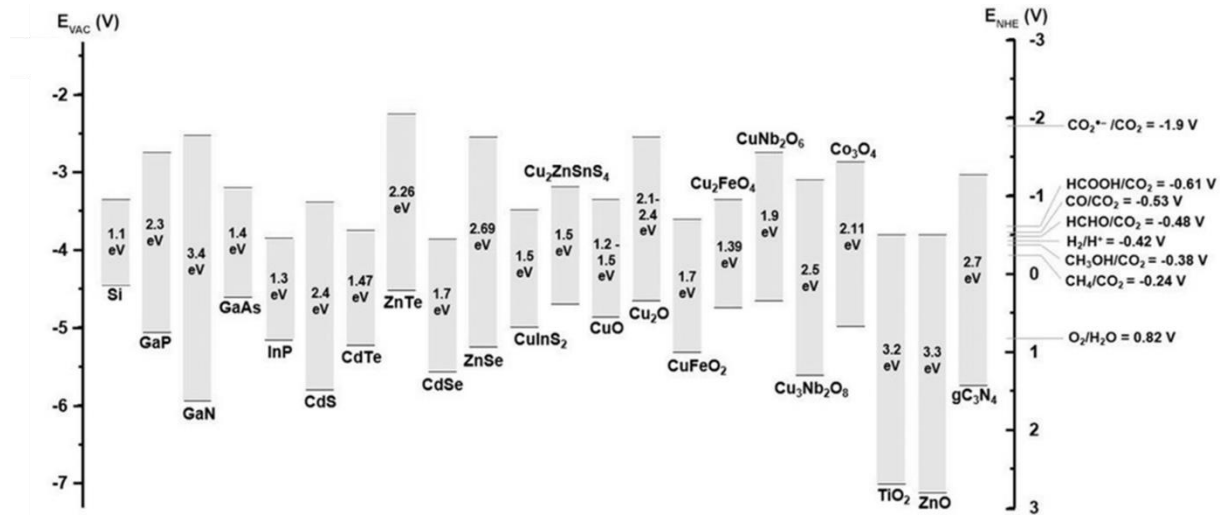

Figure 14 *CBM, VBM and Eg of commonly used semiconductors used for CO$_2$R. The thermodynamic potentials of CO$_2$R are also indicated at pH 7.*[10]

Other attempts to improve the photoelectrocatalytic performance of the ZnTe involve modifying the semiconductor itself; by incorporation of N in the lattice of ZnTe, the charge mobility improved due to the increase in the h$^+$ density, since the N replaced Te leaving an electron deficient site.[15] Another strategy was the addition of a *p-n* junction between the *p*-type ZnTe and an *n*-type semiconductor such as CdTe[13] or CdS,[3] creating a buried heterojunction, which is further discussed below. The addition of thin layer of carbon to protect the semiconductor against photocorrosion, increased the stability from 40% to 80% and photocurrent from −10 to −18 mA cm^{-2} at −0.7 V *vs* NHE. It is worthy to note that for this stability test only 20 min were considered.[14] The thin carbon layer was added by soaking the ZnTe photoelectrode in aqueous glucose followed by N$_2$ annealing at 350 °C for 5 h. If this carbon thin layer is then doped with N, it also acted as an electrocatalyst for CO$_2$R due to the basic nature of the N sites.[15] Recently, Ag$_3$Cu was also used as catalyst in ZnTe based photocathodes, it promoted CO$_2$R towards CO giving rise to 6.8 syngas production ratio (CO:H$_2$) under AM 1.5G. This ZnTe based photocathode stands the highest photocurrent and stability of −5.1 mA cm^{-2} at −0.2 V RHE for 24 h in CO$_2$-saturated 0.1 M KHCO$_3$.[16]

Table 4 *State-of-the-art photocathodes based on ZnTe*

Photoelectrode	−J (mA cm^{-2}) at E *vs* RHE	Faradaic Efficiency (%)	% Stability Time (h)	Electrolyte	Ref.
Zn/ZnO/ZnTe	15 −0.7 V	CO – 18.1 H$_2$ – 53.2 Total – 71.3	68.5 % 3	0.5 M KHCO$_3$ pH 7.5	[1]
Zn/ZnO/ZnTe/Au	20 −0.7 V	CO – 58.0 H$_2$ – 31.8 Total – 89.9	50 % 3	0.5 M KHCO$_3$ pH 7.5	[11]
FTO/ZnTe/PPy	*Charge 0.58 C −0.3 V	CO – 10.1 HCOOH – 26.1 H$_2$ – 21.5 Total – 57.7	6	0.5 M KHCO$_3$	[12]
FTO/ZnO/ZnTe/ CdTe/Au	4 −0.11 V	CO – 65.82 H$_2$ – 15.95 Total – 81.77	37 % 1.5	0.5 M KHCO$_3$	[13]
Zn/ZnO/ZnTe/C/MoS$_2$	1.1 0.0 V	H$_2$ ≈ 90%	45.5 % 3	0.5 M Na$_2$SO$_4$	[14]
Zn/ZnO/N:ZnTe/N:C	≈ 1.5 −0.11	CO – 71.65 H$_2$ –20.01 Total – 91.66	** 3	0.5 M KHCO$_3$	[15]
ITO/ZnTe:Cu/CdS/Ti/ Mo/Pt	1.5 0 V	---	73.7 % 1	1M KPi pH 6.7	[3]
FTO/ZnTe/TiO$_2$/Ag$_3$Cu	4 −0.2 V	CO ≈ 85 H$_2$ ≈13 Total ≈ 100	≈ 95 % 24	0.1 M KHCO$_3$ pH 6.8	[16]

* Only the charge after 6 h of CPP was reported not the current, therefore it was not possible to determine the stability of the device.
** The Chronoamperometry (CA) test was not reported

Although significant progress has been made using ZnTe as light absorber, from Table 4 it is clear that stability remains an issue, especially when compared with the Si/TiO$_2$/Pt based photocathodes that reached −20 mA cm^{-2} at 0.3 V *vs* RHE for 72h for HER.[17] Meanwhile for CO$_2$R, the ZnTe state-of-the-art photocathode has reached similar performance than Si/TiO$_2$/Au displaying −5 mA cm^{-2} for 10 h and CO:H$_2$ selectivity of 1:1 at −0.1 V *vs* RHE.[18]

From Table 4, it is evident that most of the ZnTe photocathodes shared the same basic structure (Zn/ZnO/ZnTe), which has been modified with different catalyst for either HER and CO$_2$R in aqueous

electrolytes.[1,11,13–15] For a better understanding of the basic structure, Figure 15 shows the band diagram (before equilibrium) based on work function, CBM and VBM and Fermi Level (E_F). [1,3,11,13–15,19]
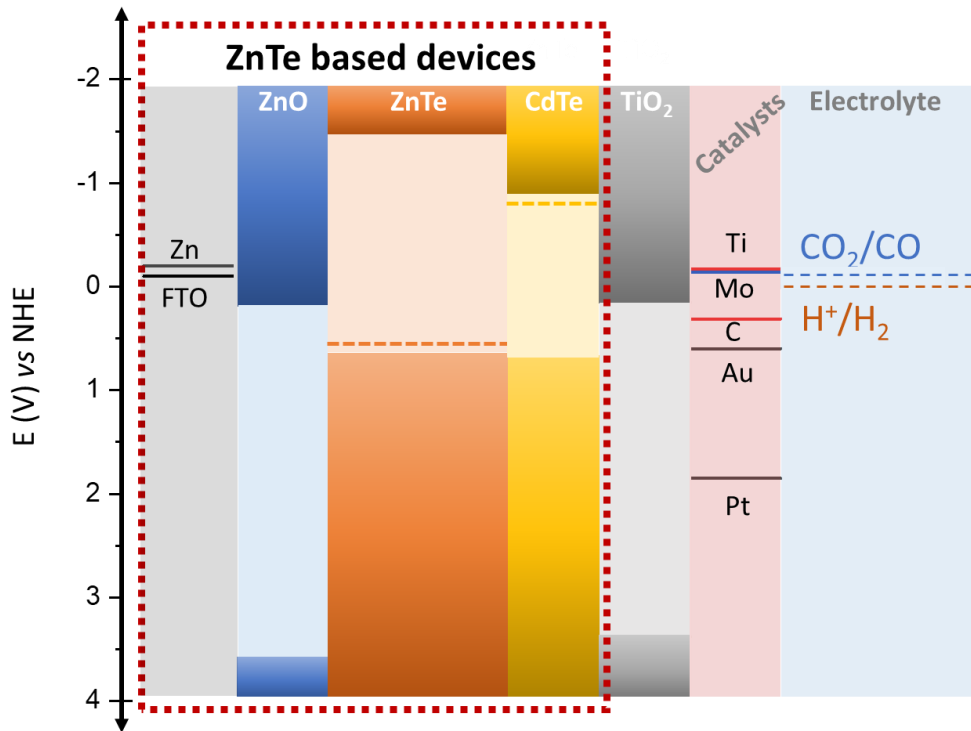
Figure 15 *Band diagram (before equilibrium) based on work function, CBM and VBM of the most common ZnTe photocathodes structure modified with different catalyst for HER or CO_2R in aqueous electrolytes.[1,3,11,13–15,19]*

In the Zn/ZnO/ZnTe based devices, the electric field for charge separation is generated between semiconductor and the electrolyte considering an ideal flat double layer capacitor model.[20] For an effective charge separation in a photocathode, the hole extraction from the semiconductor towards the metallic contact plays an important role, and an ohmic contact is required.[21,22] Specifically for a *p*-type semiconductor, a metal which work function is larger than the E_F of the semiconductor (more negative value in the absolute scale) establishes an ohmic contact. The resultant charge transfer due to the difference in E_F causes holes to gather at this interface forming an accumulation layer, thereby causing upward band bending in the semiconductor and allowing efficient hole extraction as shown in Figure 16a.[21] Au is commonly used to form an ohmic contact[21] as well as NiO_X, and they are considered as

Hole Transport Layers (HTL). For metal oxides, two criteria should be met. The first is that the CBM of the metal oxide should lay above from the light absorber CBM to avoid electron back recombination from the semiconductor, and second that the VBM of the metal oxide and the semiconductor needs to be closer to the work function of the metallic contact,[23] which for the basic structure is Zn.[1,11,14,15] From the band diagram in Figure 2, it is evident that ZnO does not meet the requirements to be considered as an HTL. Instead, we hypothesized that the ZnO played a key role during the synthesis. Briefly, the synthesis of Zn/ZnO/ZnTe based devices started with a Zn plate, after the ZnO is formed, and by a substitution reaction, Te ions replaced O to generate ZnTe at the top. Furthermore, it was found that ZnO was necessary as template for the ZnTe to grow, even after the substrate was swapped from Zn to FTO.[13]
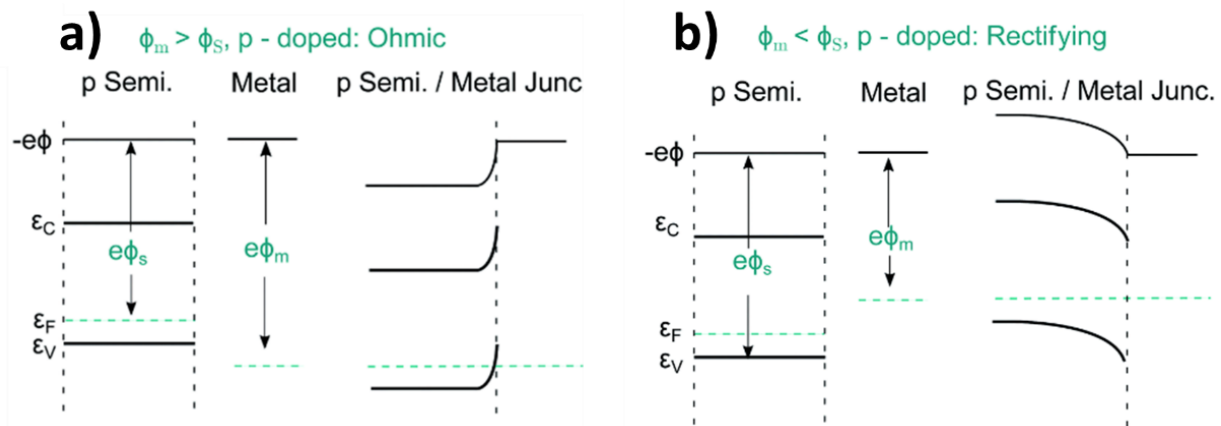
Figure 16 *(a) Ohmic contact and (b) Schottky contact at the junction between a p-type semiconductor and metal.[22]*

The addition of Au at the top of Zn/ZnO/ZnTe devices not only provided the active centres for CO_2R and changed the selectivity of the reaction as discussed previously,[11] but also improved the charge separation at the ZnTe/Au interface by forming a Schottky barrier with the semiconductor. Considering the carbon work function at -0.31 V *vs* NHE,[14] it is likely that the same rectifying effect improved charge separation at the interface ZnTe/C, since the depletion layer at the interface contains electron excess creating a concentration gradient and forcing the holes to move in opposite direction, as shown in Figure 16b.[22]

Another attempt to improve the performance of the Zn/ZnO/ZnTe based photocathodes was done by creating a buried junction with an *n*-type type semiconductor.[3,13] In this way, the electric field created at the *p-n* junction improved the hole-electron separation and provided a photovoltage that reduces the applied potential required to carry out a reduction reaction.[24] Note that a meaningful comparison can be made between Zn/ZnO/ZnTe/Au[11] and Zn/ZnO/ZnTe/CdTe/Au[13] since both of the devices were synthesised in a similar way. The photocathode without the buried junction reached a photocurrent of -1.25 mA cm^{-2} at -0.11 V *vs* RHE (thermodynamic potential for CO2R to CO),[11] meanwhile the device with the buried junction exhibited -2.5 mA cm^{-2} at the same potential (-0.11 V *vs* RHE). The Faradaic efficiency was also shifted, an applied potential of -0.7 V *vs* RHE was required to favour CO$_2$R over H$_2$ production (FE$_{CO}$ 58%, FE$_{H2}$ 31.8%) without the *p-n* buried junction,[11] and similar selectivity was achieved at lower overpotential (-0.11 V *vs* RHE) after adding an *n*-type CdTe (FE$_{CO}$ 65.82%, FE$_{H2}$ 15.95%).[13] Note that the synthesis protocol was kept the same for making these devices,[11, 13] including the chemicals (apart from CdTe precursors), however changes during the semiconductor deposition time conducted to more homogeneous coatings with lower voids at the ZnO/ZnTe interface. The first photocathodes had large ZnTe crystals at the top of ZnO nanowires (as shown in Figure 17a), meanwhile the latest (also more efficient) devices a conformation ZnTe coating was achieved on the top of the ZnO nanoroad as illustrated by the cross-sectional image in panel (b) of Figure 17. The improved contact between each layer in the device also could be related to the improvement of the PEC performance as well as the *p-n* junction.

Minegishi, et al also included a *p-n* junction by adding an *n*-type CdS layer in ITO/ZnTe:Cu/CdS/Ti/Mo/Pt,[3] Close-spaced sublimation (CSS) was used as deposition technique of the ZnTe. Even with the best deposition conditions, whereby the temperature, time and two-step deposition were optimised to favour large ZnTe crystals, the authors pointed out the photocurrent was almost negligible without the buried junction.
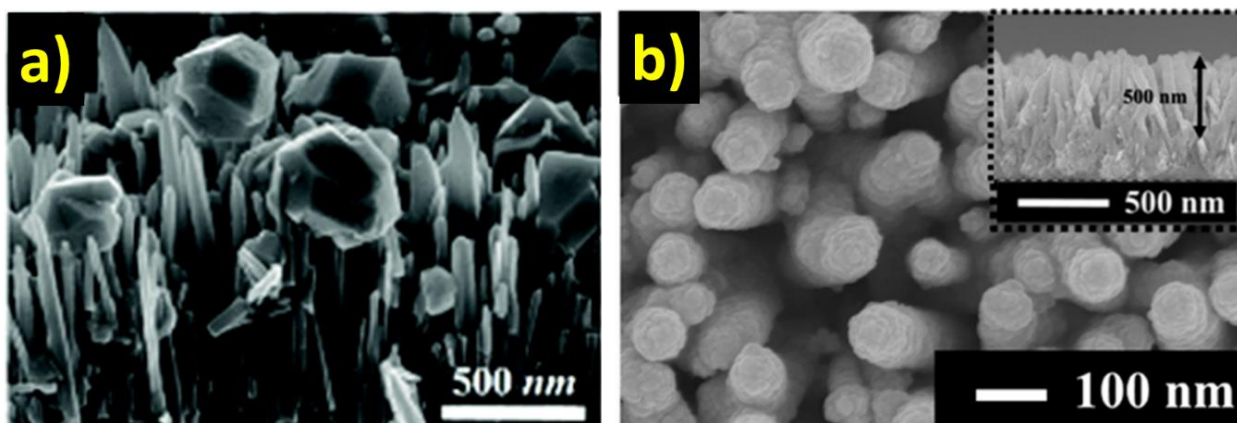
Figure 17 *SEM images of the ZnO/ZnTe structures demonstrating the improvement of conformational layers at the ZnO/ZnTe interface. Panel (a) was reproduced from[11], and panel (b) from[13]*

Finally, the ZnTe state-of-the-art CO_2R photocathode was made by depositing ZnTe quantum dots on FTO. After a thin (~5 nm) amorphous TiO_2 layer was added on the top of the ZnTe, carrier recombination was significantly reduced by the passivation of surface defects.[16] The second role of the TiO_2 layer was avoiding contact between the electrolyte and the light absorber. It also important to highlight, that this photocathode operated in 0.1 M $KHCO_3$ solution at pH 6.8. Considering that TiO_2 CBM follows a Nerstian behaviour with the pH as shown in Figure 18,[25,26] and assuming it is heavily doped, then the E_F locates close to the CBM. At pH 7, the TiO_2 CBM is located at -0.6 V *vs* NHE,[26] and the required potential for producing CO is -0.521 V *vs* NHE.[2] The driving force to carried out CO_2R to CO is then reduced to 0.079 V, and based on the photocurrent and the high selectivity achieved in the ZnTe based photocathode,[16] it is likely that that the TiO_2 does not hinder CO_2R and it stands only as an electron shuttle between the light absorber and the catalyst. Another successful example of using TiO_2 (40 nm) as capping layer was demonstrated alongside amorphous Si for PEC CO_2R.[18] The careful optimization of Au catalyst layer thickness to keep the balance between catalysis activity and avoiding blocking the incident light towards the semiconductor by reflection, enabled a steady photocurrent of -5 mA cm^{-2} during 10 h at constant 1 sun illumination. The CO:H_2 selectivity was 1:1 at lower overpotentials (-0.1 V *vs*

RHE), suggesting that TiO_2 is a suitable candidate to be used as a protective layer that enables electron transfer for CO_2R in aqueous electrolytes.
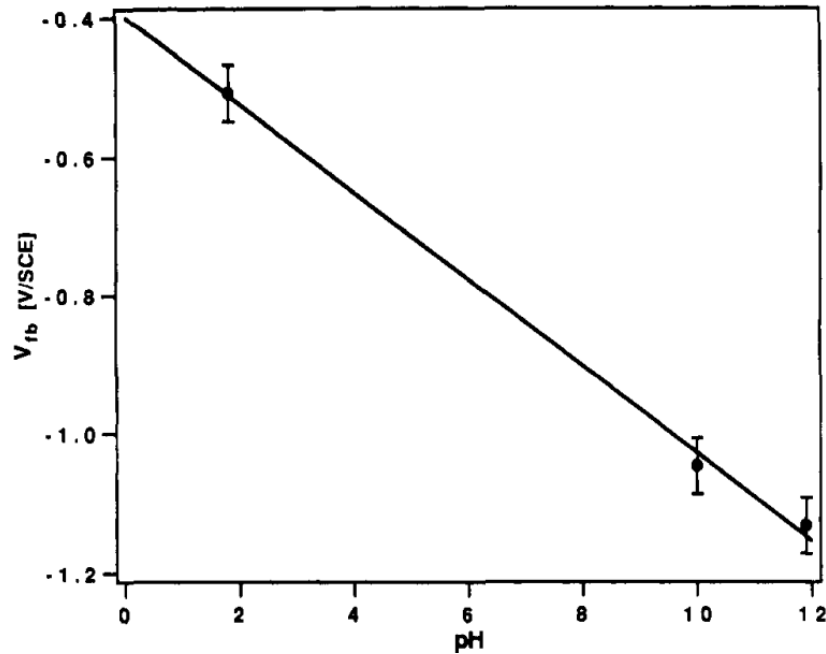

Figure 18 *Flat-band potential of TiO_2 as a function of the pH of the solution.*[26]

2.1.2 State-of-the-art of the Sb_2Se_3 photocathodes

Chalcogenides have gained interest from the photovoltaic community (PV), especially Sb_2Se_3 which has suitable properties like small band gap (direct 1.17 and indirect 1.03 eV), only one stable crystalline structure at room temperature, Earth abundancy (Sb $2x10^{-5}$% and Se 5 $x10^{-6}$% in Earth-crust), inexpensive and low-toxicity to be used in large scale devices. Improvements in material processability, and the careful tailing in capping layers have led to the increase in power conversion efficiency passing from less than 1% in 2008 to 10.12% in 2022 for Sb_2Se_3 based solar cells.[7,27]

Sb_2Se_3 has also gained interest from the PEC community since the CBM at -0.5 V *vs* RHE lies more negative than the potential required for HER, providing enough driving force to carry out the reaction.[5,28–31] The photocurrent and stability of Sb_2Se_3 photocathodes have significantly increased for PEC devices for HER in the last couple of years as shown in Figure 19, and Table 5 contains the

experimental details of these studies.[5,32] Here, it is also highlighted that efficient Sb_2Se_3 photocathodes have different layers added for improving photocarriers extraction from light absorber. Note also the resemblance of the state of the art Sb_2Se_3 photocathodes to a thin-film solar cell in(glass/BC/HTL/Absorber/CdS/TE/Antireflective coating/Grid, BC = back contact, TE transparent electrodes).[7]
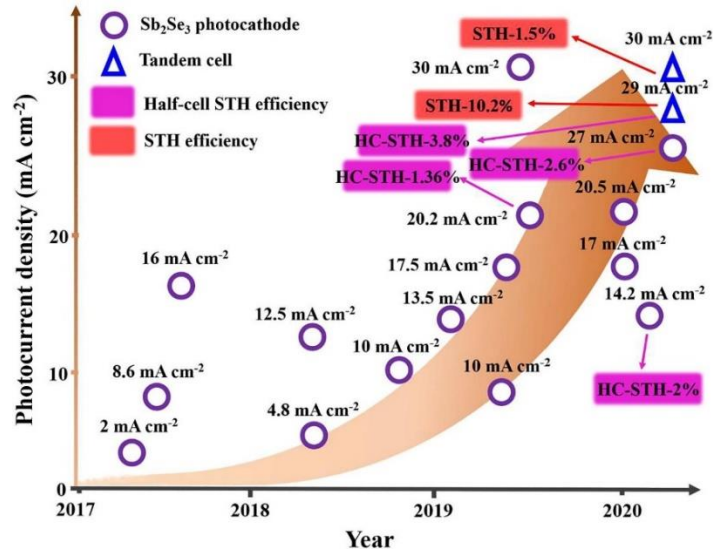

Figure 19 *Sb_2Se_3 state-of-the-art photocathodes for H_2 production, image reproduced from.[5]*

The Sb_2Se_3 bare semiconductor exhibits low PEC performance for HER.[28,29,40] The photocurrent, onset potential and stability were significantly improved by adding an *n*-type semiconductor in a buried junction creating an electric field that improves charge separation. The commonly used *n*-type semiconductors are CdS,[28,35,38,41,42], CdS doped with In,[43] In_2S_3,[44] and TiO_2. The latter is a special case since it could provide the *p-n* junction directly,[23,33–35,37,39,45–48] and act as a physical barrier to avoid the semiconductor contacting the electrolyte.[28,35,38,41–44] As discussed in section 2.1.1, hole extraction is also important at the back contact, and for Sb_2Se_3 photocathodes the common hole transport layers (HTL) are Au,[29,38,41] Cu;NiO_x,[23], NiO,[23,48] and Mo.[28,42,43,47,48] From Figure 19, it is also clear that a H_2 production catalyst is required, with Pt,[23,28,31,33,34,37,42,43] RuO_2,[36,41] and MoS_x[29,35,47] being the most common.

A detailed review of the Sb_2Se_3 state-of-the-art photocathodes was recently published on 2022.[5] It highlights the importance of controlling the morphology of the Sb_2Se_3 crystals, such as large crystals to

avoid recombination and the promotion of crystal growth in the [hk1] crystalline plane to efficiently transport the photocarriers across the ribbons (as will be shown in Figure 34d).

The earlier Sb_2Se_3 photocathodes started with chemical wet synthesis such as electrodeposition and spin coating,[29,32] soon after a milestone in the field was achieved by physical deposition methods such as close space sublimation (CSS),[38,41] and most recently the record devices have been made by sputtering.[43] After the holes and electrons are generated, the photoelectrons need to be efficiently extracted by the careful tailoring of the layer(s) above the Sb_2Se_3 to promote void-free interfaces, avoid lattice mismatch at window layer, and ideally without blocking the Sb_2Se_3 light harvesting.

Table 5 *State of art Sb_2Se_3-based photocathodes.*

#	Photoelectrode	$-J_0$ @ 0 V *vs* RHE (mA cm^{-2})	% Stability $\left[\dfrac{J}{J_0}\right]$	Time (h)	Electrolyte	Ref.
1	FTO/Au/Sb_2Se_3/TiO_2/Pt	2	10	3	0.5 M H_2SO_4	33
2	FTO/Au/Sb_2Se_3/MoS_{x-S}	16	50	5	1 M H_2SO_4	29
3	Glass/Mo/Sb_2Se_3/CdS/TiO_2/Pt	8.6	85	10	0.5 M Na_2SO_4 + 0.25 M Na_2HPO_4 + 0.25M NaH_2PO_4	28
4	FTO/Au/Sb_2Se_3/TiO_2/Pt	12.5	55	2	0.1 M H_2SO_4	34
5	FTO/Au/Sb_2Se_3/TiO_2/MoS_x	4.8	12	0.25	0.5 M H_2SO_4	35
6	FTO/Au/Sb_2Se_3/TiO_2/RuO_x	10	95	2	0.1 M H_2SO_4	36
7	FTO/Au/Sb_2Se_3/CdS/TiO_2/Pt	11	73	3	0.5 M Na_2SO_4 + 0.25 M Na_2HPO_4 + 0.25M NaH_2PO_4	31
8	FTO/Au/Sb_2Se_3/TiO_2/C_{60}/Pt	17	98	10	0.1 M H_2SO_4	37
9	FTO/Cu:NiO_x/Sb_2Se_3/TiO_2/Pt	17.5	75	4	0.1 M H_2SO_4	23
10	FTO/Au/Sb_2Se_3(CSS)/TiO_2/RuO_x	20	93	10	Phosphate buffer pH ~ 6.25	38
	FTO/Au/Sb_2Se_3(CSS)/TiO_2/Pt	30	Not reported		0.1 M H_2SO_4	
11	FTO/Au/Sb_2Se_3/TiO_2/Pt	30	83	2	0.1 M H_2SO_4	39
	FTO/Au/Sb_2Se_3/TiO_2/C_{60}/Pt/TiO_2	30	100	5	0.1 M H_2SO_4	

Finally, is also important to point out that almost all of the devices have a TiO_2 capping layer with the exception of very few studies,[29,42] and the interface TiO_2/catalyst also plays an important role in the long- term stability of devices. By adding C_{60} or swapping from Pt to RuO_2 the stability was significantly improved,[5] but this interface will be discussed in detail in the following chapter 3.[28,3241,4244] To the best of our knowledge, the review done by Liang et al. summarised the most relevant Sb_2Se_3 photocathodes, apart from the most recent study which sets the new record of -35.7 mA cm^{-2} at 0 V vs RHE.[43] The record device was made by a sputtered layer of Sb on the top of Mo, followed by a selenization process, here also the CdS buffer layer was homogeneously doped with In to make it more n-type for better band alignment.[43] This photocurrent now is getting closer the maximum theoretical of -40.9 mA cm^{-2} under AM 1.5 G solar light illumination with 100% photon-to-current conversion. It represents a milestone in Sb_2Se_3 based photocathodes development, even though the stability of this device was not reported.

In this chapter ZnTe and Sb_2Se_3 were studied as ligh absorbers in photocathodes for H_2 production. Using a low band gap semiconductor brings about the possibility of harvesting most of the solar spectrum as is depicted in Figure 20. For ZnTe, the theoretial photocurrent is 8.95 mA cm^{-2}, while for the Sb_2Se_3 it is 40.9 mA cm^{-2}, under ideal conditions where the semiconductor absorbs all higher energy photons than the E_g, each photon generates only one hole-electron pair, and there are no optical losess nor internal recombination. However as previosly discussed in section 1.2.3, having a low band gap semiconductor also limits the maximun photovoltage in the device. In a p-n junction under illumination, the quasifermi level of the electrons ($_nE_F^*$) in the p-type semiconductor allign with the E_C of the n-type semiconductor and these in turn are determined by the Fermi level of the solution, which is the standard potential for HER.[10] Therefore, the photovoltage will be dictated by the difference between the Fermi level of the solution ($E^0_{H^+/H_2}$, in thi case) and the quasi Femi level of the holes ($_pE_F^*$) in the p-type semiconductor (Figure 6). Therefore, the maximum photovoltage generated at the Sb_2Se_3 is 0.5 V,[41] meanwhile for ZnTe 0.67 V,[1,3,11] considering that the $_pE_F^* \approx E_V$ in the p-type semiconductor.
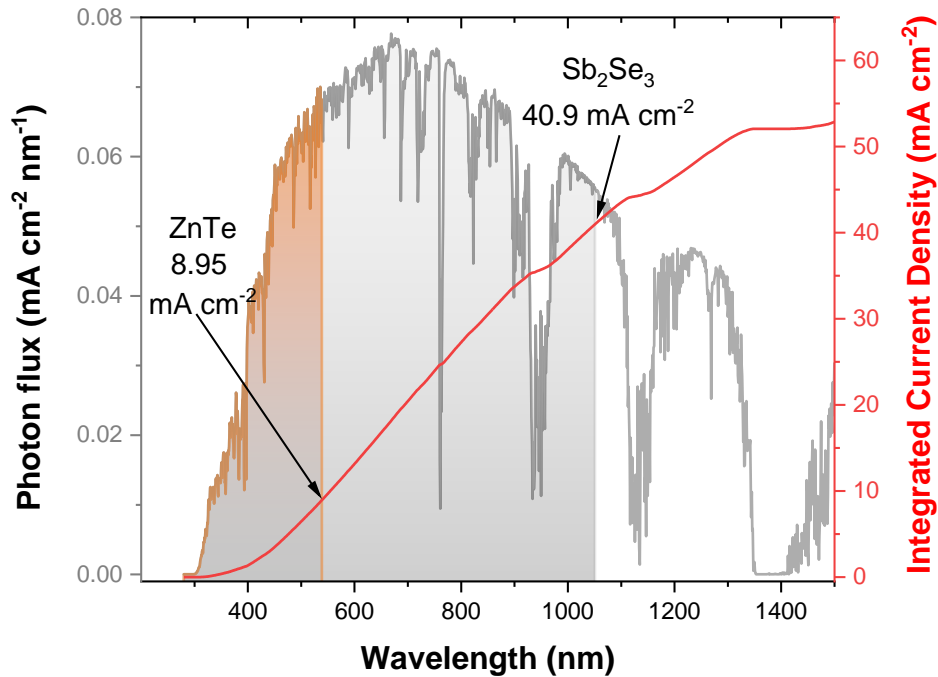
Figure 20 *Solar spectrum and theoretical photocurrent of Sb₂Se₃ and ZnTe.*

2.2 Experimental results

2.2.1 ZnTe

In this section, the experimental results for ZnTe as light absorber in a photocathode are described. All the experimental details like the specific conditions for ZnTe deposition, metal oxides synthesis and the electrochemical setup is fully described in Section 6.1.1. Briefly, ZnTe was thermally evaporated on FTO slides previously cleaned. The XRD pattern is shown in Figure 21a, the [111], [220], [311] and [331] peaks were identified for the zinc-blende ZnTe structure, as well as the FTO peaks of the substrate. The direct bandgap of the 150 nm thick brownish-red ZnTe film was 2.27 eV determined in the Tauc plot (Figure 21b), in line with previous reports in the literature.[1,49]
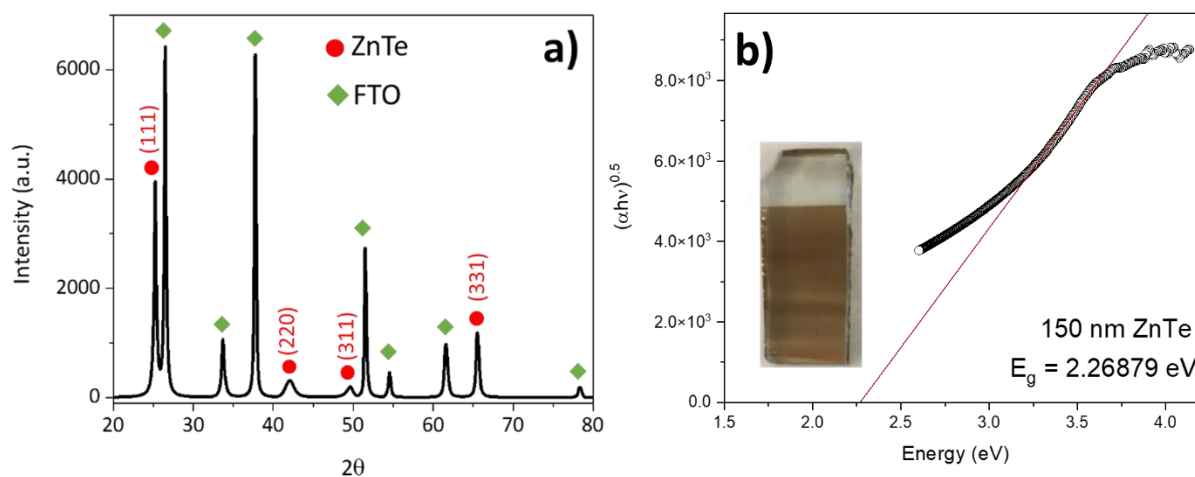
Figure 21 *(a) XRD pattern and (b) Tauc plot of FTO/ZnTe.*

The SEM analysis of the FTO/ZnTe films is shown in Figure 22 panel b and b' where it is observed that the ZnTe crystal size is *ca.* 100 nm and its morphology is completely different to the underlying FTO glass coated. Note the FTO was coated with Au to improve the resolution at higher magnifications, therefore cracks are observed in panel a'.

After the films were characterized by SEM, UV-vis and XRD, the PEC analysis was carried out in 0.1 M $NaClO_4$ pH 4 at 10 mV s^{-1}. Figure 23 shows the Linear Sweep Voltammetry (LSV) of FTO/ZnTe under (a) N_2 and (b) CO_2. The current in the LSV is lower than in literatrure,[2,9,49,50] and no significant difference under CO_2 and N_2 indicates the bare ZnTe does not favour CO$_2$RR without catalyst addition.[1,14,51] Furthermore, a notable feature are the spikes after the light is turned on and off, which are associated to recombination process when the photocharges are not effectively extracted in the device.[75]
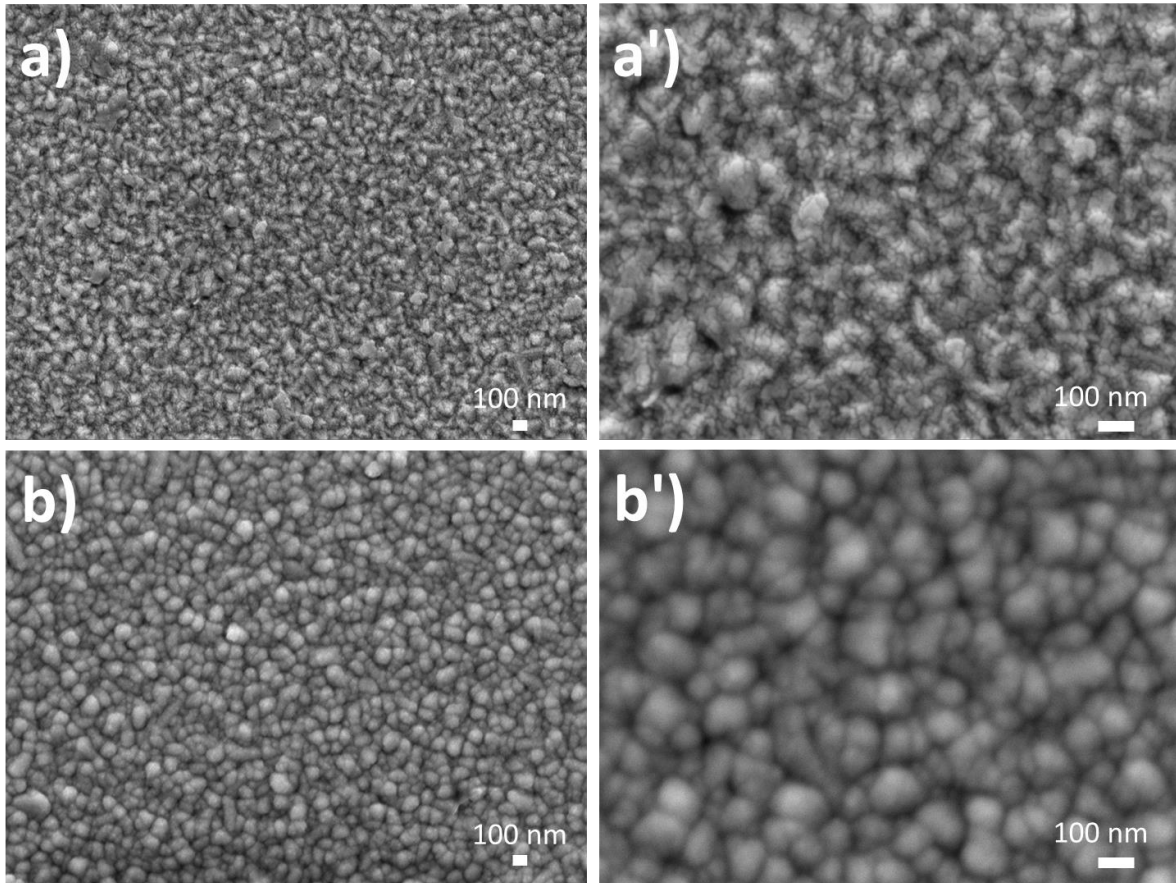
Figure 22 *SEM analysis of FTO (a and a') and FTO/ZnTe (b and b') at two different magnifications (a, b x 30 K, and c, d x 75 K).*
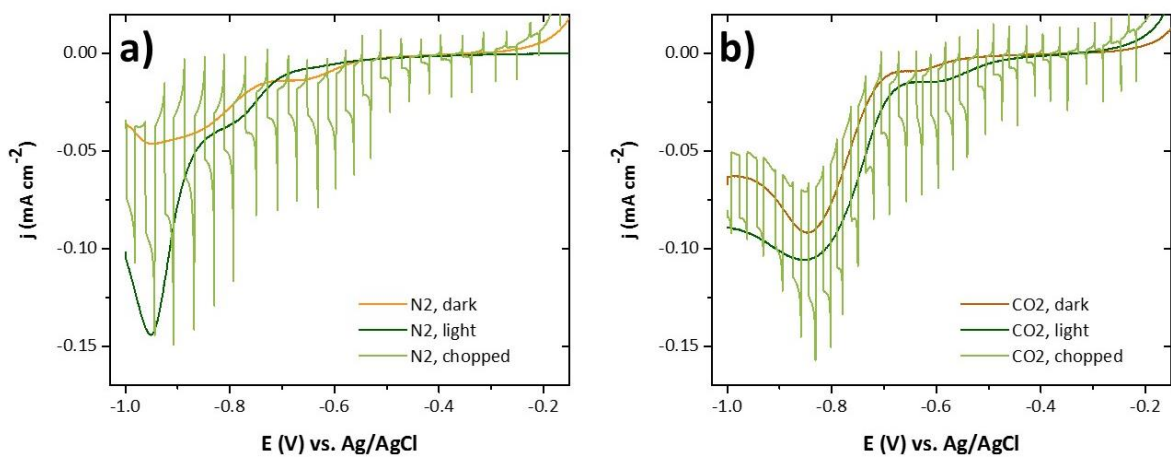

Figure 23 *Chopped, light and dark, LSV of FTO/ZnTe at 60 mW cm^{-2},340≤ λ ≤ 900 nm, in 0.1 M NaClO$_4$ pH 4 at 10 mV s^{-1} under (a) N$_2$ and (b) CO$_2$.*

The high dark current in Figure 23 (under N_2 and CO_2) at potentials more negative of -0.65 V *vs* Ag/AgCl (-0.205 V *vs* RHE) indicates that additional reduction reactions occurred on the surface of the photoelectrode. J. W. Jang *et al* studied the effect of the applied potential on ZnTe by XPS.[1] An amorphous TeO_x layer was identified in a pristine ZnTe photocathode since the Te^{4+} $3d_{5/2}$ and Te^{4+} $3d_{3/2}$ of TeO_2 were found, and the atomic Zn/Te ratio was below 1 (0.73). At -0.2 V vs RHE, the Zn/Te atomic ratio slightly decreased to 0.65, while at more negative potentials (-0.7 V vs RHE) this ratio increased up to 1.19 due to the photocorrosion of ZnTe to Te and Zn^{2+}, as indicated in equation (3). Note that for this study, the ZnTe deactivation mechanism was assessed in a CO_2-saturated 0.5 M $KHCO_3$ pH 7, and in our particular case pH 4 was chosen due the optimal operating pH of the **Ni(cycP)** molecular catalyst (**cycP** = [(1,4,8,11-tetraazacyclotetradecan-1-yl)methylene]phosphonic acid, see discussion below).

$$ZnTe \rightarrow Zn^{2+} + Te + 2e^- \qquad \text{Eq (3)}$$
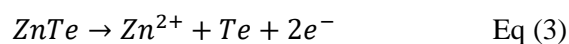
In 1977, Bockris *et al* studied ZnTe as photocathode for H_2 production and highlighted the semiconductor instability in acidic conditions according to the Pourbaix diagram (Figure 24a).[50] Panel b of Figure 24 presents an updated version with focus on the pH-E range used in the chopped light LSV from Figure 23.[90] It is likely that our ZnTe had an oxide/hydroxide Te layer and those species were reduced at more negative potentials than -0.44 V *vs* Ag/AgCl in line with the increase in reductive current. However, at potentials more negative than -0.64V *vs* Ag/AgCl, the Pourbaix diagram does not provide information related to the reaction observed at -0.9 V *vs* Ag/AgCl, it only suggests that ZnTe is solid up to -1.3 V *vs* Ag/AgCl.

The stability of FTO/ZnTe films without catalyst at open circuit potential (OCP) was investigated by soaking the films in 0.1 M $NaClO_4$ for 2 hours in darkness to rule out the light and the negative applied potential in the corrision mechanis of ZnTe. After soaking, LSV was carried out again and the results are presented in Figure 25. Almost no difference is observed under dark and illumitaion, indicating that all the light absorbing capabilities of ZnTe were lost, additionally the colour of the film changed completely from light brown to black, likely due to the partial reduction of the Zn according to the

Pourbaix Diagram (Figure 24). This diagram also highlights that the equilibrium potential of HER is close of ZnTe decomposition in neutral and alkaline media, and for ZnTe to be used as a photocathode coupled with a photoanode in a standing alone device with no membrane, neutral conditions are preferred not to hinder H_2 and O_2 evolution reaction.[24]
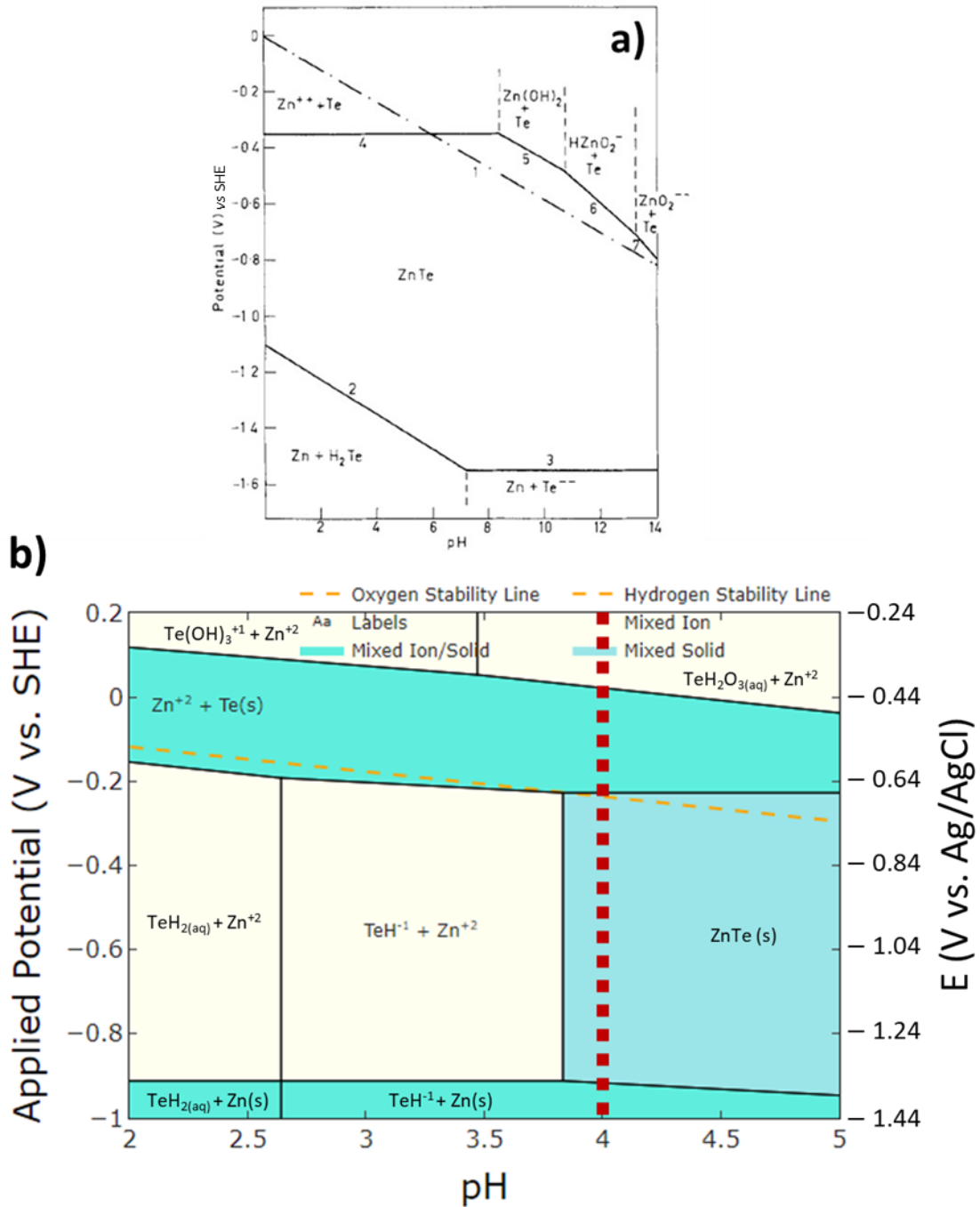

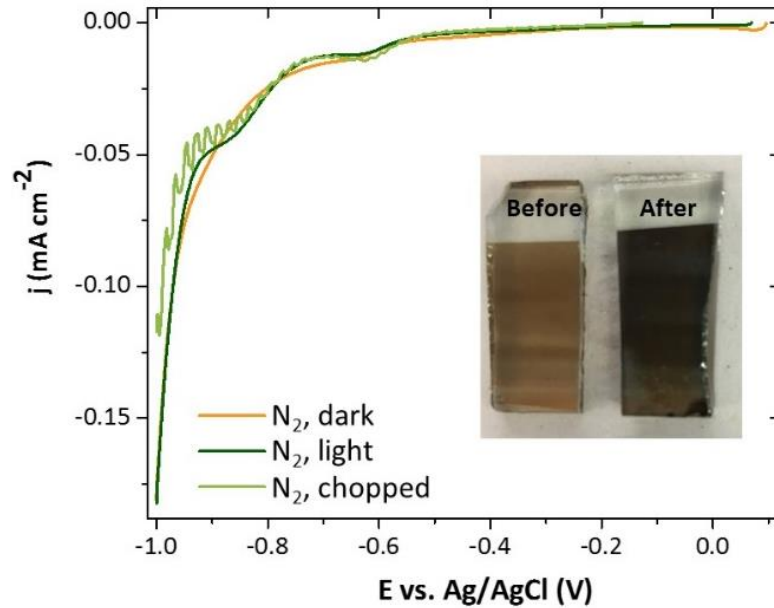**Figure 24** *Pourbaix diagrams for ZnTe water at 25 °C. Panel (a) reproduced from,[50] and b from.[90]*

Figure 25 *Chopped, light and dark, LSV of FTO/ZnTe at 60 mW cm^{-2}, 340$\leq \lambda \leq$ 900 nm, in 0.1 M NaClO$_4$ pH 4 at 10 mV s^{-1} under N$_2$, before and after 2 hours of being soaked in 0.1 M NaClO$_4$ pH 4. The insert presents the colour change of the film.*

Passivation and stabilisation layers have been shown to improve the charge-separation and transfer processes across semiconductor–liquid interfaces, and thereby increasing overall solar energy conversion efficiencies.[52] Usually thin metal oxide layers are added since they can reduce charge recombination at surface states, increase the reaction kinetics, and protect the semiconductor from chemical corrosion.[53,54] In this work, a passivation layer was proposed as a strategy to improve ZnTe photocathodes. Al$_2$O$_3$ was used as first approach since the protective coating is optically transparent and chemically stable, it also has a wide band gap (7.0 and 7.6 eV for amorphous and crystalline phase respectively)[55] and it is stable between pH 4 - 9 according to the Pourbaix diagram.[52,56–60] Although Al$_2$O$_3$ is electrically insulating, it has been demonstrated that if deposited as a thin layer (~1-2 nm) electron tunnelling through the material can still occur. We investigated Al$_2$O$_3$ deposition by several methods including dip coating,[56,61] spin coating, sputtering and ALD.

The dip coating method is fully described in section 6.1.1. Briefly, the FTO/ZnTe samples were dipped in 0.15 M Aluminium tri-sec-butoxide in dry 2-propanol, after the sample was expose to air and the top layer undergoes a hydrolysis reaction to give Al$_2$O$_3$. Although it was reported that rinsing the electrode

with clean water after each "dip-layer" improved Al_2O_3 formation (by hydrolysis of the Aluminium tri-sec-butoxide), a sintering process was required (450 °C for 20 min) to enhance the crystallinity of the metal oxide.[56,61] Therefore, initially control experiments were carried out to determine ZnTe thermal stability, with samples undergoing heat treatments at different temperatures: 300, 200, 120 °C for 20 min. Figure 26 shows the LSV after annealing process, the sample treated at 300 °C (Figure 26a) went black and lost all the photocurrent. Only the lower annealing temperatures at 120° and 200 °C retained the photocurrent similar to Figure 23b, despite ZnTe decomposition occurring above 437 °C. [62] The thermal instability of ZnTe represents a significant drawback that hinders the use of any sintering process to improve the metal oxide crystallinity, which has been directly attributed for long-lasting photocathodes compared with amorphous layers.[63,64] Even without the annealing process, it was found that dip coating was not suitable for making Al_2O_3 films since the samples went black after the immersion in 0.15 M Aluminium tri-sec-butoxide in dry 2-propanol.
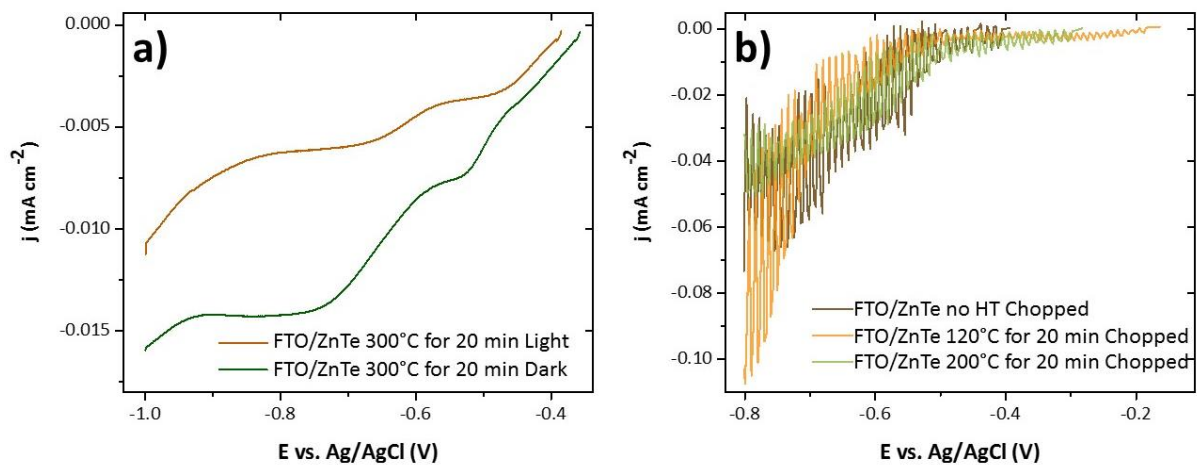
Figure 26. *Chopped, light and dark, LSV at 10 mV s^{-1} of FTO/ZnTe with different heat treatments at (a) 300°C, (b) 200°, 120° C for 20 min, and no heat treatment (no HT), under N$_2$ in 0.1 M NaClO$_4$ pH 4 at 60 mW cm^{-2}, 340≤ λ ≤ 900 nm.*

Spin coating typically produces more homogenous films than dip coating. Different loadings on top of FTO/ZnTe were explored (1, 3, 5, and 10 layers) using 75 μL of 0.15 M metal precursor for each layer at 4000 rpm for 34 s, all the experimental details are indicated in section 6.1.1. Following by a mild thermal treatment at 200 °C for 20 min in air. The chopped

light LSV of these films is presented in the Figure 27a, after the Al_2O_3 deposition the photocurrent decreased. To assess the quality of the capping layer, the samples were dipped in 0.1 M $NaClO_4$ pH 4 for 2 h, after the chopped LSV was measured again (Figure 27b). The photocurrent decreased significantly for all different loadings (including the FTO/ZnTe pristine sample) suggesting that spin coating Al_2O_3 did not form a high-quality barrier or act as a passivating layer. Note that the electrolyte and pH were selected based on the optimal operating conditions of the CO_2R catalyst **NiCycP**, which had been successfully modified with a phosphonic anchoring group to be anchored to metal oxides previously in the group[70] and further studied here in section 4.1.3.

Sputtered Al_2O_3 passivation layers were also studied with different thicknesses: 1, 5, 10, 15, 20 nm onto FTO/ZnTe. The chopped light LSV without any further thermal treatment, and after the stability test is presented in Figure 27 panel (c) and (d), respectively. The photocurrent decreased again after 2 h, even with a relatively thick Al_2O_3 overlayers (15 and 20 nm).

As it was hypothesised before, sputtered films could also have pin holes allowing the electrolyte to get in contact with the ZnTe and decomposed in the same way than spin coating, then (Atomic Layer Deposition) ALD coating was explored. The chopped light LSV of 2 nm ALD Al_2O_3 overlayer is presented in Figure 27e. The same behaviour was observed as previously, the photocurrent decreased following of 2 h immersion in the electrolyte in dark. Consequently, it is proposed that the inability to carry out a thermal treatment to convert what is anticipated to be amorphous Al_2O_3 films (including spin coated, sputtered and ALD) into a crystalline form made it a poor passivation layer on the top of ZnTe, in comparison with other inorganic semiconductors where the photocurrent and the overpotential were significantly improved.[53,54]
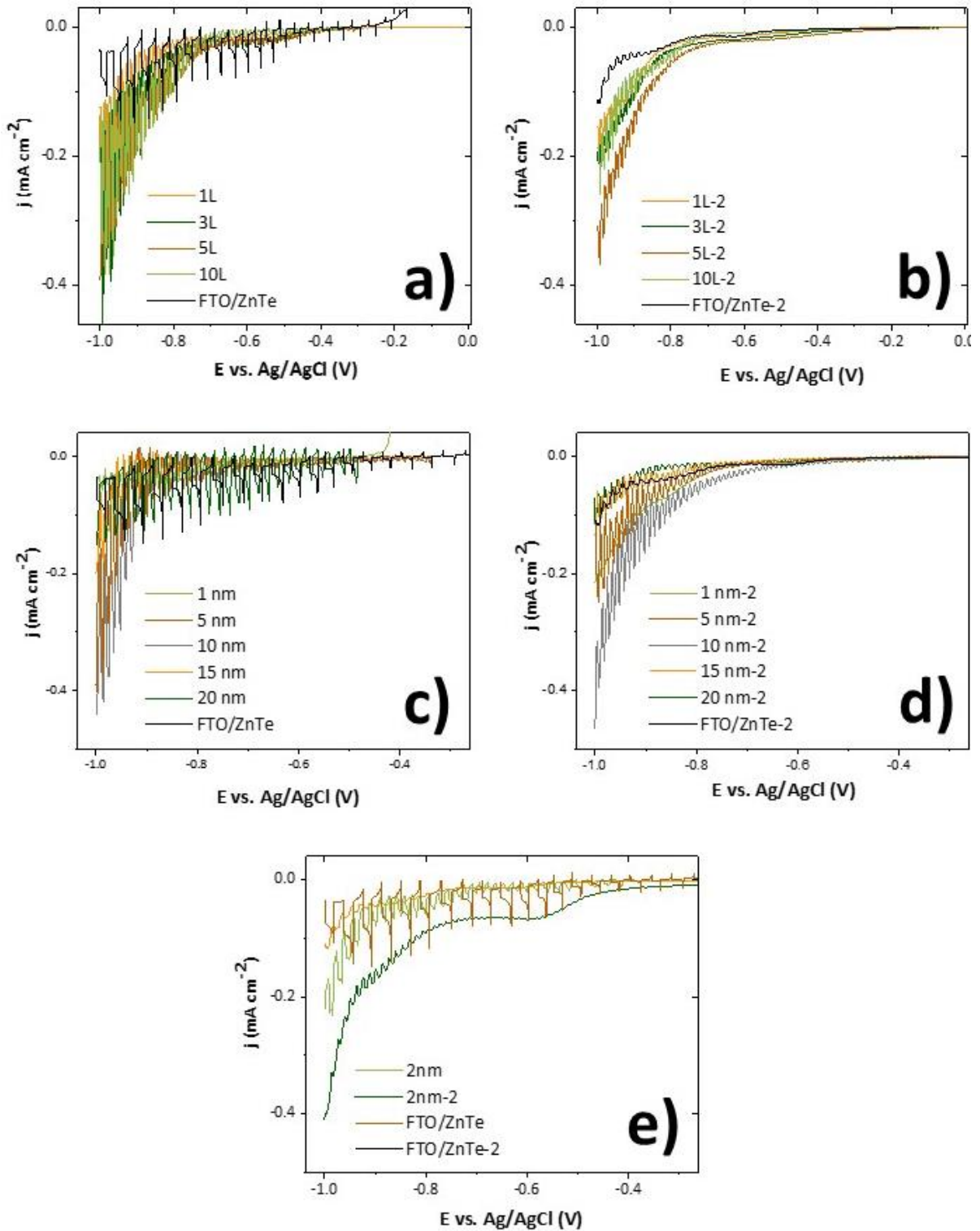
Figure 27 *Chopped light LSV of FTO/ZnTe with Al_2O_3 as passivating layer deposited by: (a, b) spin coating, (c, d) sputtering, (e) ALD at 60 mW cm^{-2}, $340 \leq \lambda \leq 900$ nm, in 0.1 M $NaClO_4$ pH 4 under N_2. The LSVs after the stability test are label as (-2) in the figures b, d and e.*

Since Al_2O_3 was found to be an unsuitable passivating coating, another approach was explored to improve the photoelectrochemical properties of ZnTe. By adding a buried junction, the hole-electron separation is improved.[13,22,24,65] According to the position of the ZnTe CBM,[1,12,51,66,67] ZrO_2 and Ta_2O_5[68] have a suitable band alignment to build a *p-n* junction with the ZnTe (Figure 28). The smaller CBM offset from the metal oxides still provides sufficient driving force to enable electron transfer for CO_2R. Table 6 contains a summary of the different metal oxides studied and their deposition technique. The experimental details are fully described in section 6.1.1.
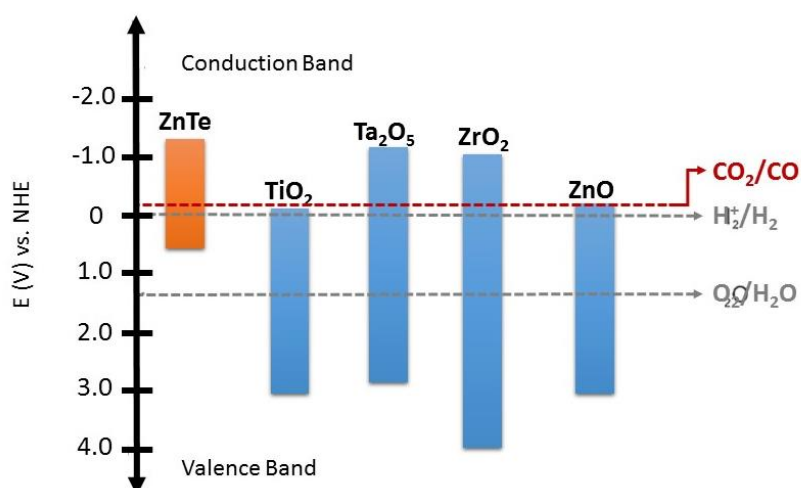
Figure 28 *CBM and VBM of the ZnTe and some suitable metal oxides to carry out CO₂R to CO.*[1,12,51,66–68]

Table 6 *Summary of the metal oxides deposition techniques explored to form a p-n junction on the top of ZnTe.*

Deposition technique	ZrO_2	AZO	Ta_2O_5
Dip Coating	X		
Spin Coating	X		
Spray Coating	X		
Sputtering		X	X

ZrO_2 was first explored using a 0.15 M solution of Zirconium (IV) propoxide in dry 2-propanol.[56,61] Following dipping, the films were rinsed with water to remove the excess of Zr(IV) not chemisorbed on the surface and to promote the hydrolysis to form ZrO_2. Although a thermal treatment is required,

only a slightly heat treatment was applied (200 °C for 20 min) due to the thermal instability of ZnTe. However, this protocol did not produce homogenous films, and therefore a spin coating method was attempted instead. Different layers were deposited (5, 10 and 15) of the Zirconium (IV) propoxide in dry 2-propanol at 0.15 M solution, and the samples were left in air and thermally treated in air at 200 °C for 20 min. The chopped light LSV is presented in the Figure 29. The photocurrents of 10 and 15 layers FTO/ZnTe/ZrO$_2$ samples exceed those of the pristine FTO/ZnTe samples suggesting that a *p-n* junction may be formed, however the photocurrent decreased significantly during stability testing for 2 hours in the dark (Figure 29b). The lack of stability may be due to the presence of pin holes in the ZrO$_2$ allowing the ZnTe to interact with the electrolyte, alternatively it may be due to the poor mechanical stability of the ZrO$_2$/ZnTe interface. It was noted that during the stability test the ZrO$_2$ films (white overlayer) came off from the electrode (insert of the Figure 29b).

Figure 29 *Chopped light LSV of FTO/ZnTe/ZrO$_2$ at 60 mW cm^{-2}, 340≤ λ ≤ 900 nm, in 0.1 M NaClO$_4$ pH 4 under N$_2$. (a) Before and (b) after the stability test.*

The junction ZnTe-ZrO$_2$ represents a promising combination for a CO$_2$R hybrid photocathode, since **Ni(cycP)** molecular catalyst has been successfully immobilized on ZrO$_2$ demonstrating high activity for CO production. In this study, a photocatalytic approach was used where a [Ru(bpy)$_3$]$^{2+}$ (bpy = 2,20 -bipyridine) worked as a dye-sensitizer to collect the photons, and for a hybrid photocathode the [Ru(bpy)$_3$]$^{2+}$ could be replace for ZnTe.[69] For **Ni(cycP)**, the reduction of the Ni$^{II/I}$ catalytic centre

occurred at -0.8 V *vs* NHE under CO_2,[70] and the $ZnTe/ZrO_2$ interface provides a photocurrent ~ -200 $\mu A\ cm^{-2}$ at (-0.8 V *vs* Ag/AgCl, -0.595 V *vs* NHE). Hence, $ZnTe/ZrO_2$ could work as CO_2R photocathode. However, an extended cathodic potential in the chopped light LSV is required to ensure no increase in dark current, and the stability of the $ZnTe/ZrO_2$ junction needs to be improved before using as CO_2R photocathode.

AZO (Aluminium doped ZnO (2%)) was also assessed as an overlayer for ZnTe. AZO is of particular interest as it is anticipated to be able to form a significant depletion layer at the *p-n* junction, even when present as a thin film (*e.g.* 20 nm) due to the higher donor density which will aid charge separation.[71,72] However, the chopped light LSV of a sputtered FTO/ZnTe/AZO film (Figure 30) displayed lower photocurrents than ZrO_2, and no ZnTe stabilisation was achieved despite the 20 nm thick AZO film. We hypothesized that AZO also needs an extra annealing to improve the crystallinity and it might also require a different concentration of Aluminium as a doping metal, using AZO as a protective layer required further optimization beyond the scope of this work. Consequently, we moved to Ta_2O_5 which also has demonstrated good performance in photoanodes as a passivation layer.[73]
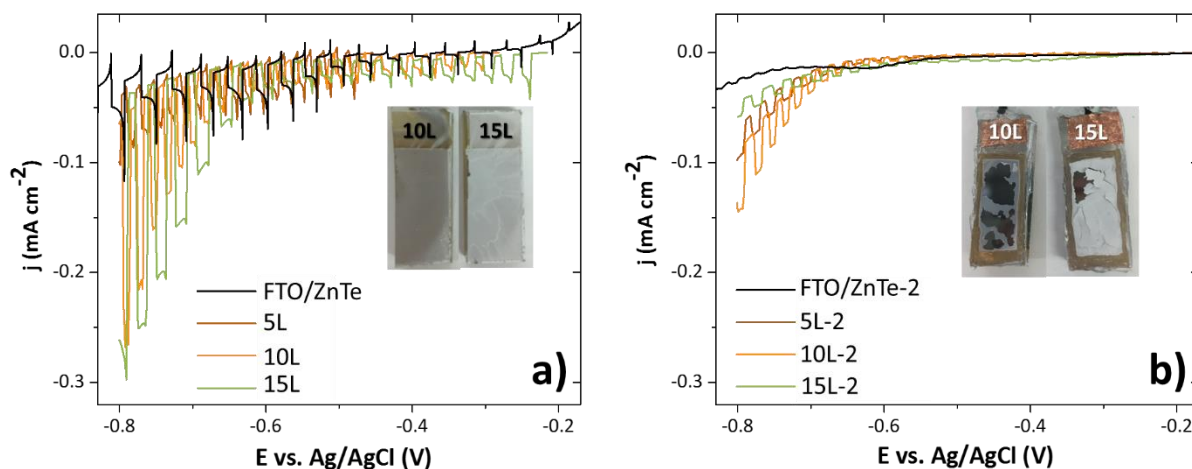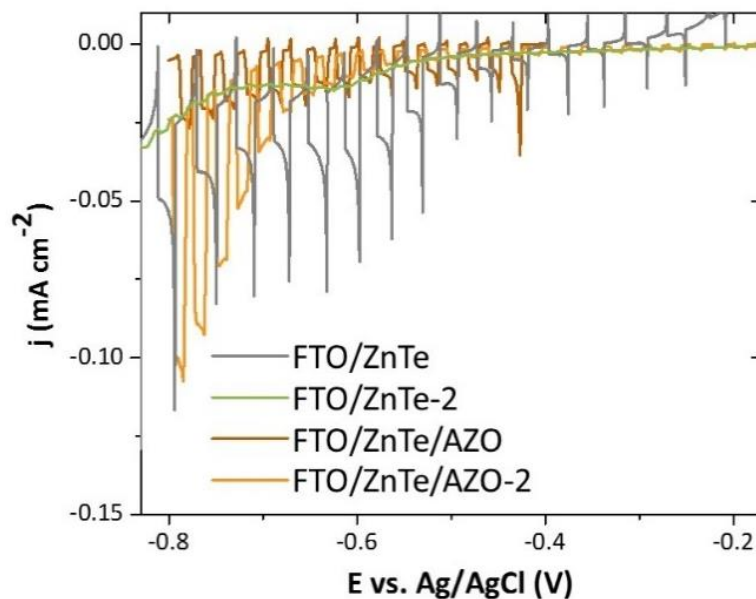

Figure 30 *Chopped light LSV of FTO/ZnTe/AZO at 60 mW cm⁻², 340≤ λ ≤ 900 nm, in 0.1M NaClO₄ pH 4 under N₂. (a) Before and (b) after the stability test.*

Ta_2O_5 has a large band gap (4.2 eV) which does not absorb like TiO_2.[74] To ensure that pin-holes cannot be formed, studies immediately targeted 150 nm thick sputtered Ta_2O_5 on the top of FTO/ZnTe. Chopped light LSV before and after the stability test are shown in Figure 31a. In spite of the low photocurrent, the sample did not decrease in activity after two and four hours of being immersed in 0.1 M $NaClO_4$. The stability of the Ta_2O_5 samples (Figure 31b) allowed further meaningful tests on electrode modifications. Then, a potential cause for the low photocurrents could be the charge accumulation in the buffer layer due to the photocurrent "spikes" as the light is turned on and off in Figure 31a.[75] Therefore, to promote electron extraction from the electrode, two strategies were used: HER catalyst and the addition an electron scavenger.
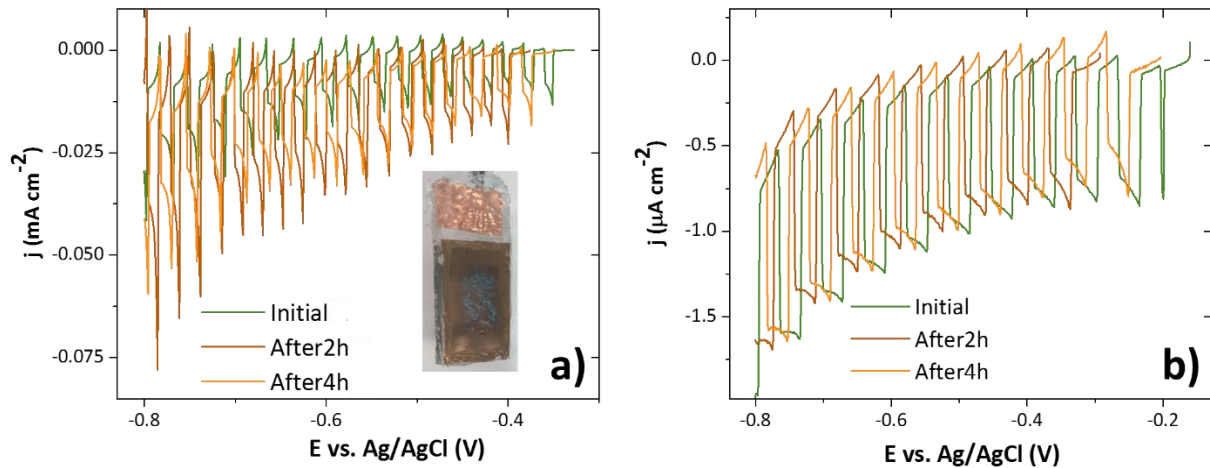
Figure 31 *Chopped light LSV of (a) FTO/ZnTe/Ta$_2$O$_5$ and (b) FTO/Ta$_2$O$_5$ in 0.1 M NaClO$_4$ pH 4 at 10 mV s^{-1}, 60 mW cm^{-2}, 340≤ λ ≤ 900 nm, under N$_2$.*

Platinum is a widely used catalyst for HER in photocathodes,[14,28,29,63,71] several attempts to deposit Pt were made by cyclic voltammetry, chronoamperometry and chronopotentiometry. The best results were obtained with light assisted chronopotentiometry at low current densities (-30 μA cm^{-2}).[29] It is worthy to note that, if a higher current density (and hence more negative potential) was applied the ZnTe decomposed. The chopped light LSV of the FTO/ZnTe/Ta$_2$O$_5$/Pt is shown in Figure 32. The spikes of the LSV with the catalyst disappeared, suggesting that charge separation was improved.[75] However, the photocurrent did not increase significantly. Pt addition allowed the direct comparison between this

FTO/ZnTe/Ta$_2$O$_5$/Pt device with the state-of-art ZnTe photocathodes for HER, which reached up to ~ -1.5 mA cm^{-2} at 0 V *vs* RHE under 1 sun illumination.[3,14]
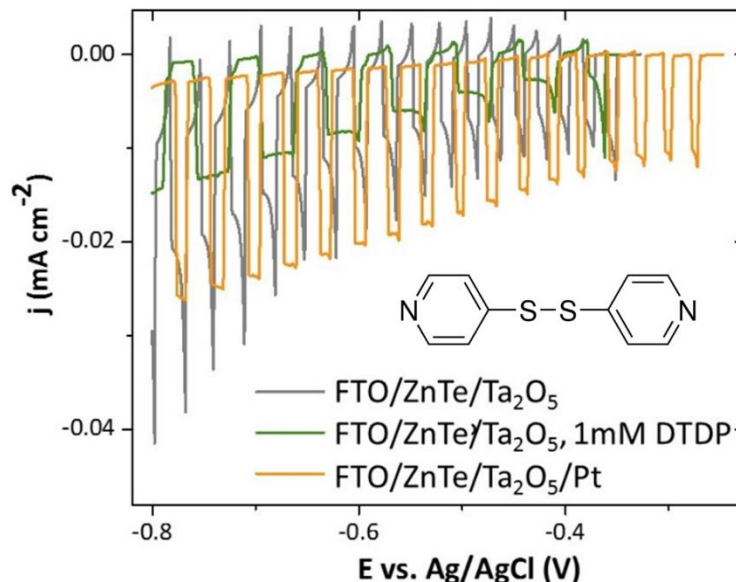
Figure 32 *Chopped light LSV of FTO/ZnTe/Ta$_2$O$_5$ in 0.1 M NaClO$_4$ pH 4 at 10 mV s^{-1}, 60 mW cm^{-2}, 340$\leq \lambda \leq$ 900 nm, under N$_2$. Electron extraction by Pt (FTO/ZnTe/Ta$_2$O$_5$/Pt) as HER catalyst or by 1 mM DPDP as electron scavenger, DPDT molecular structure is shown in the insert.*

The second approach to improve electron extraction is by adding an electron scavenger in the electrolyte. Adding 4,40-dithiodipyridine (DTDP, molecular structure shown in the insert of Figure 32) increased the photocurrent up to 10 times when used as an electron scavenger alongside dye sensitized photocathodes.[76,77] The light chopped LSV using FTO/ZnTe/Ta$_2$O$_5$ with 1 mM DTDP is shown in Figure 32, lower photocurrent was obtained in comparison with FTO/ZnTe/Ta$_2$O$_5$/Pt. This behaviour could be attributed to the thiol pyridine binding to surface of the metal oxide hindering the charge transfer at the surface.[78]

As previously discussed in the introduction of this chapter, having a Hole Transport Layer (HTL) between the light absorber and the current collector (in his case FTO), usually improves the PEC activity. Therefore, a 60 nm thick Au was deposited between the FTO and ZnTe by thermal evaporation. Figure 33 shows the Au effect on ZnTe devices, the spikes increased slightly for the Au sample

compared without HTL. However, the meaningful comparison to determine the Au effect as HTL requires the addition of either Pt or an electron scavenger.
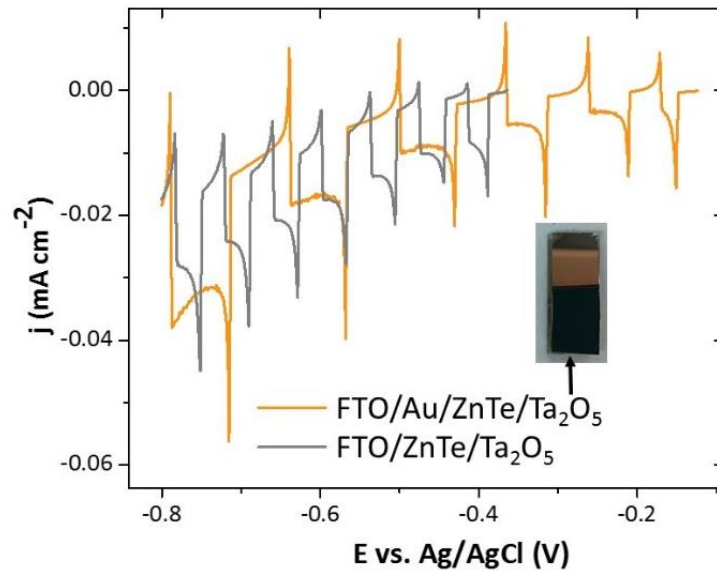
Figure 33 *Chopped Light LSV of FTO/(Au/)ZnTe/ Ta$_2$O$_5$ in 0.1 M NaClO$_4$ pH 4 at 10 mV s^{-1}, 60 mW cm^{-2}, 340$\leq$ $\lambda \leq$ 900 nm under N$_2$.*

Although ZnTe may be considered a promising light absorber for PEC devices owing to its high driving force for reduction reactions, the photo-electro activity of an efficient photocathode is not solely determined by the CBM. This is because even if the photogenerated charges have enough energy to drive the reduction reaction, the photogenerated charge carries (holes and electrons) will recombine if the semiconductor has plenty of surface states or grain boundaries, resulting in a low carrier lifetime. Therefore, the PEC activity is highly dependent on the morphology of the crystal, size, the amount of surface states, the right crystalline orientation of the light absorber material. To develop ZnTe based photocathodes, passivation of the surface states by a thin layer of Al$_2$O$_3$ was studied as well as forming a *p-n* junction alongside several metal oxides; neither the photocurrent not the stability increased significantly. ZnTe/Ta$_2$O$_5$ and ZnTe/ZrO$_2$ were identified as promising combinations in terms of protective overlayers, however the metal oxides crystallinity needed to be improved, since sputtered films are usually amorphous capping layers as well as spin coated ZrO$_2$ films due to the Zr precursor (Zirconium (IV) propoxide) used for the synthesis.

Adding an electron extractor in the form of Pt as HER catalyst, or an electron scavenger in solution such as DTDP, is required to favour a reduction reaction and to reduce recombination process in the device, evidenced by the spikes bleached after the catalyst addition during the chopped light LSV. Considering one of the goals of the thesis was to build a photocathode for CO_2R, initial attempts starting with H_2 production (which only requires two electrons and two protons) provides useful information to find the bottlenecks of the device.

The results of the first section of this chapter by any means implied that thermally evaporated ZnTe is not a suitable candidate to be used as light absorber in PEC devices. Instead, it highlights the need for careful optimization of the deposition process for ZnTe (by thermal evaporation or any other technique) to produce larger crystals with reduced grain boundaries which acted as recombination centres as shown in Figure 22 where the ZnTe crystals are *ca.* 100 nm.

2.2 Sb₂Se₃

2.2.1 Physical characterization of Sb₂Se₃ (XRD, SEM, Eg)

One of the main advantages of Sb₂Se₃ is the fact that has only one orthorhombic crystalline structure stable at room temperature. A 4x4x4 cell is shown in Figure 34a, the atoms inside the Sb₄Se₆ unit cell (Figure 34b) are covalently bound forming nanoribbons (Figure 34c), and the interaction between these structures is by Van der Waals forces.[7,48] The bonds at the edge of the ribbons are saturated inducing a self-passivation effect where recombination loses at grain boundaries are minimised.[7] Since Sb₂Se₃ is an anisotropic material, the charge transport depends on the direction being the highest charge carrier mobility in the [001] plane alongside the covalent bonds in the unit cell. The scheme in Figure 34d depicts charge transport at different nanoribbon orientation being the worst the ribbons oriented parallel to the substrate plane[hk0].[47,48]

Another advantage of Sb₂Se₃ for being used as a light absorber in photocathodes, is the small band gap[7] which allow to collect most of the solar spectrum. Figure 35 shows the TAUC plot for indirect transition in the E_g, being 1.14 eV the band gap of FTO/Sb₂Se₃(1μm).

Considering that high temperatures are needed for Sb₂Se₃ deposition (*ca.* 300 °C) by spin coating or CSS, the HTL needs to meet several requirements. First, an ohmic contact between the metal and the *p*-type semiconductor (a metal with a larger work function than the Fermi level of the semiconductor) is required.[22] Second, it needs to be thermally stable to avoid interdiffusion with the Sb₂Se₃ or if it intermixes, in a way to enhance charge carrier and decreasing the back-contact barrier. Recently, Mo was used as substrate and HTL, after a Sb film was sputtered followed by selenization at temperatures above 360 °C to promote the [001] Sb₂Se₃ crystal growth, then found out that a MoSe₂ phase was formed improving the charge transfer.[42]

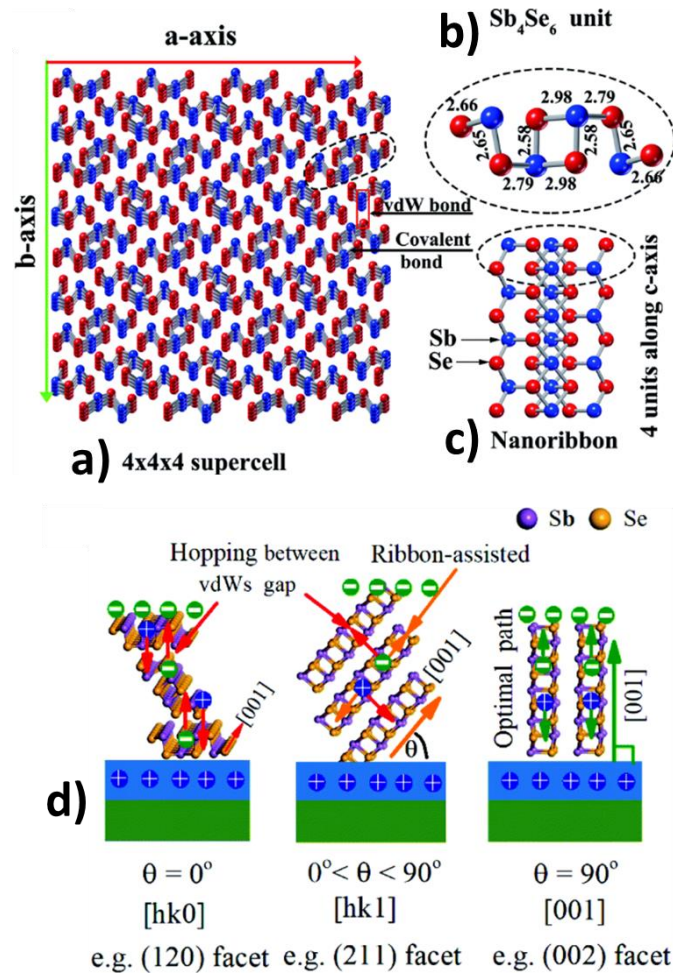***Figure 34*** *(a) Top view of Sb₂Se₃ 4x4x4 supercell, (b) Sb₄Se₆ unit cell, the distance between the bonds is also included, (c) nanoribbon structure of 4 units alongside the c-axis. Image reproduce from[48] (d) Photocarriers transport scheme across the Sb₂Se₃ nanoribbons at different crystal orientation. [001] improves the transport and avoid recombination.[47]*
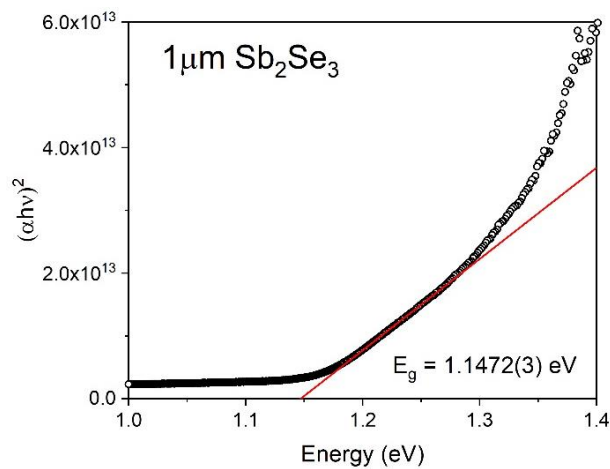

Figure 35 *Tauc plot of Sb₂Se₃ on FTO.*

The early Sb_2Se_3 photocathodes were made by spin coating followed by annealing, but this technique favoured ribbons parallel to the substrate [hk0] with many recombination centres as shown in Figure 34d. Once the [001] orientation was favoured by changing the solvents and deposition time, the photocurrent increased significantly for the same device architecture.[32] Since the Sb_2Se_3 has 1D crystalline structure, avoiding pinholes where the HTL and the Electron Transport Layer (ETL) could be in direct contact, has been challenging. These sites may act as a recombination centres and short circuit the solar cell diminishing the PEC performance of the photocathode. A milestone in photocurrent was achieved by incorporating a compact layer of Sb_2Se_3 which potentially reduce the likelihood of pinholes.[38,39,79], in the first step a compact thin layer was formed at low temperature (350 °C), which acted as a "seed" for the crystal growth during the second stage at higher temperature (450 °C). Finally, a fast cooling process favoured the correct ribbon orientation to promote hole transport in the [001], giving rise to -30 mA cm^{-2} at 0 V *vs* RHE with 10 h stabilty.[38,41] The same approach of having a seed first to promote larger crystals was also implemented by spin coating and similarly, a photocurrent *ca.* -30 mA cm^{-2} at 0 V *vs* RHE was obtained.[39] In this study, Sb_2Se_3 was made by two-stage CSS and all the experimental details are included in section 6.1.2. The SEM images of these samples are shown in Figure 36, where compact homogeneous films are observed with large grain structure in the order of microns. The XRD pattern is shown in Figure 37, where the [211], [221], [301], [321], [141] peaks correspond to the vertically orientated (albeit tilted) nanoribbons.
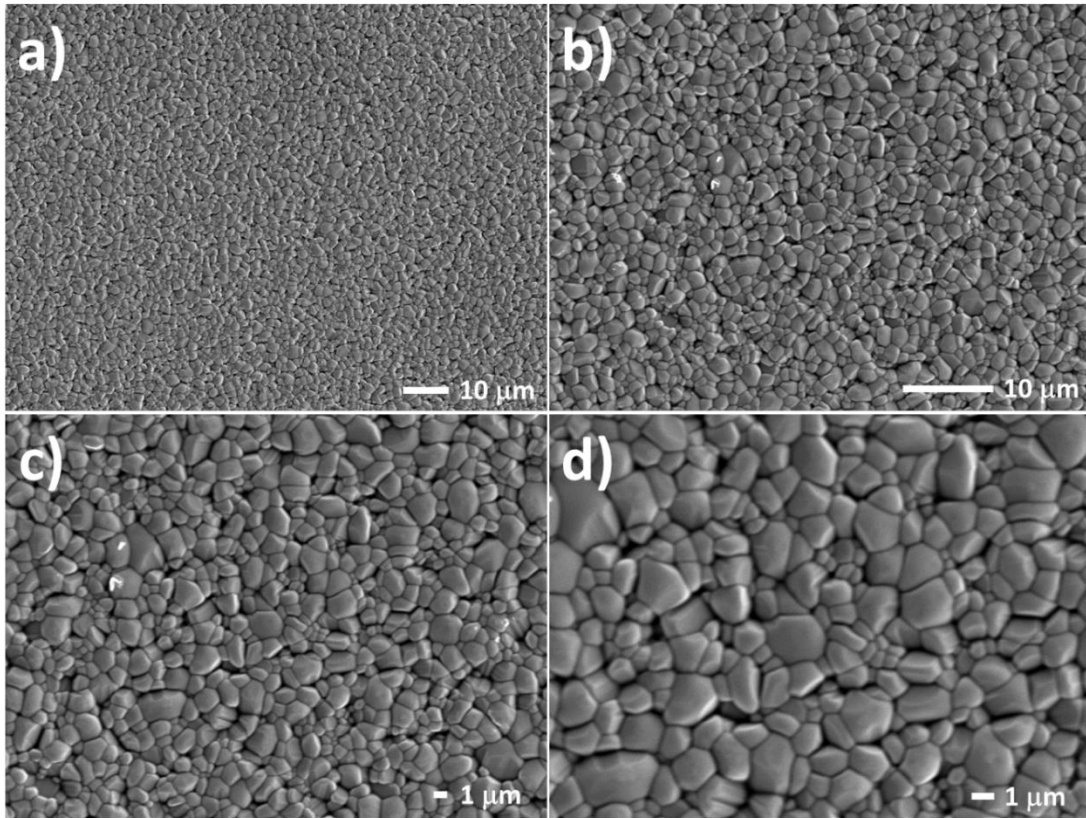
Figure 36 *SEM images at different magnifications (a x1K, b x 2K, c x 3K and d x 5K) of Sb$_2$Se$_3$ grown on FTO using two-stage CSS.*
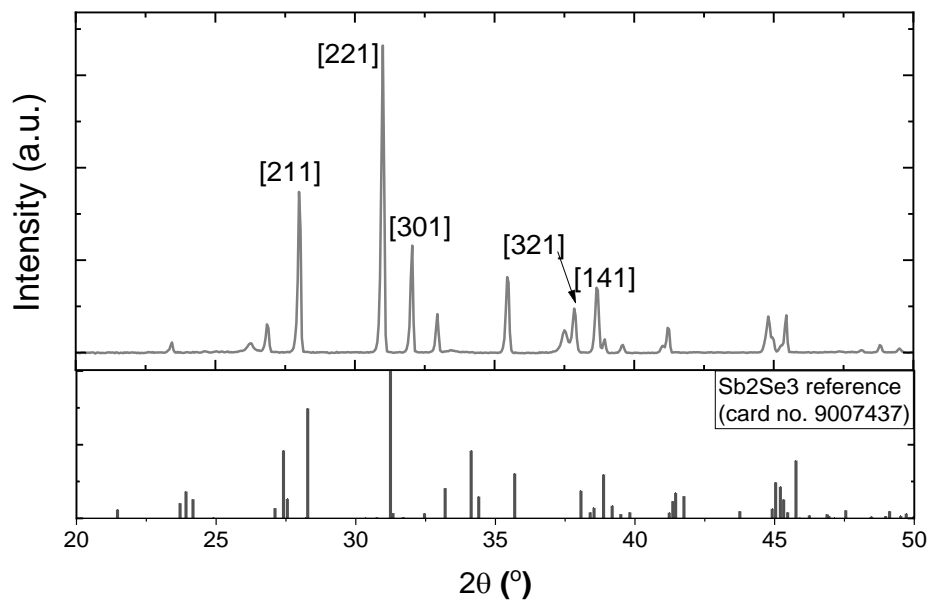
Figure 37 *XRD pattern of FTO/Sb$_2$Se$_3$ made by two steps CSS.*

2.2.2 Optimization Sb₂Se₃/(CdS)/TiO₂ interface

Once the morphology, crystal orientation and the E_g were determined, PEC analysis was carried out in a 3-neck flat cell with no membrane between the catholyte and the anolyte, and all the experimental details are included in Section 6.3.7. However, it is also worthy to point out that TiO_2 contribution was ruled out by the use of a 340 nm long-pass filter in all the PEC experiments.

Figure 38 shows two consecutives chopped light LSV of FTO/Sb_2Se_3 at 10 mV s^{-1} in 0.1 M $NaClO_4$ pH 4 with 60 mW cm^{-2} and $\lambda > 340$nm. The bare semiconductor exhibits low PEC activity for HER for the first LSV and almost all the photocurrent was lost in the second LSV, in-line with previous reports where the pristine Sb_2Se_3 displayed poor PEC activity.[28,29,40] Note, that the pH was chosen based on the best performance of Ni cyclam (and derivatives) for further addition as catalyst alongside Sb_2Se_3 photocathodes for CO_2R.[70]
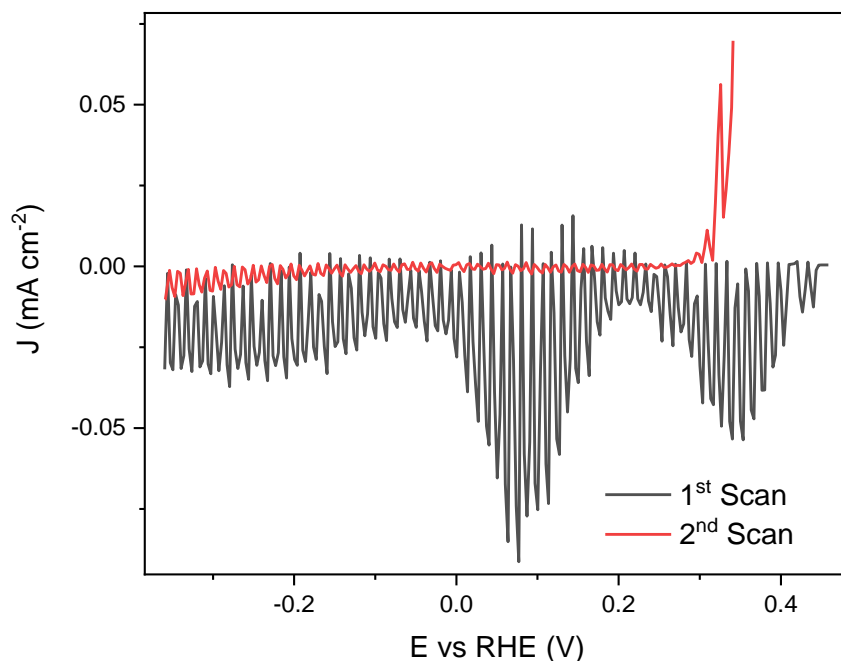
Figure 38 *Two consecutive chopped light LSV of FTO/Sb₂Se₃ at 10 mV s⁻¹ in 0.1 M NaClO₄ pH 4, at 60 mW cm⁻² and λ > 340nm under N₂.*

Sb$_2$Se$_3$ usually is deposited between the HTL and ETL to improve the PEC activity. For subsequent experiments, Au was selected as HTL and TiO$_2$ as an ETL as initial approach. TiO$_2$ was deposited by sputtering, ALD and Plasma Enhance Atomic Layer Deposition (PEALD) and all the experimental details are included in section 6.1.2. Different experimental conditions and deposition techniques were explored to deposit TiO$_2$, and although all the samples included Au as HTL on FTO, this is omitted from the sample labels in the following sections for the sake of conciseness.

2.2.2.1 Sb$_2$Se$_3$/TiO$_2$

Adding a TiO$_2$ layer provides a suitable *p-n* heterojunction with Sb$_2$Se$_3$ to enhance hole-electron pair separation. Furthermore, it prevents chemical corrosion of the light absorber.[23,33–35,37,39,45–48] The TiO$_2$ layer deposited by ALD was identified as the most effective capping layer for Sb$_2$Se$_3$ based photoelectrodes, therefore ALD TiO$_2$ was studied first.

ALD-20nm

It is well-known that ALD provides high quality and almost pinhole-free surfaces for TiO$_2$ protective layers with thickness over 40 nm.[53,54,80] However, 20 nm was found to be the most common thickness in literature, hence a 20 nm ALD TiO$_2$ capping layer was deposited on the top of Sb$_2$Se$_3$. All the experimental details of the ALD deposition are included in section 6.1.2.2, and these samples are label as Sb$_2$Se$_3$/TiO$_2$-ALD(20 nm) from now on. Producing a highly crystalline ALD TiO$_2$ films involves annealing at high temperatures (T $\geq$ 350 °C),[75] but generally the thermal instability of the light absorber restricts its implementation. To guarantee the Sb$_2$Se$_3$ stability/integrity, ALD was performed at a lower temperature of 160 °C. The integrity of the Sb$_2$Se$_3$ after the thermal TiO$_2$ ALD deposition was followed by Raman Spectroscopy to rule out Sb$_2$O$_3$ formation during deposition, since one of the deactivation mechanisms of Sb$_2$Se$_3$ photocathodes has been associated to the Sb$_2$O$_3$ at the Sb$_2$Se$_3$/TiO$_2$ interface.[38]

Sb$_2$O$_3$ has distinct Raman features at 82, 189, 254, 373 and 450 cm^{-1}, but the main peak is located at 254 cm^{-1}.[81] The Raman analysis was conducted after 50 cycles of thermal ALD TiO$_2$ ($\approx$2 nm thick) at 160 °C, and Figure 39 shows the Raman spectra in two different areas of the sample (1, 2) as well as

the control area which was masked during the ALD deposition (defined as 3). Only the peaks associated to S_2bSe_3 were identified at 189 as main peak and the shoulder at 214 cm^{-1}.[81,82] The peaks associated to Sb_2O_3 (Figure 39b for the region close to 254 cm^{-1}) or TiO_2 were not identified.
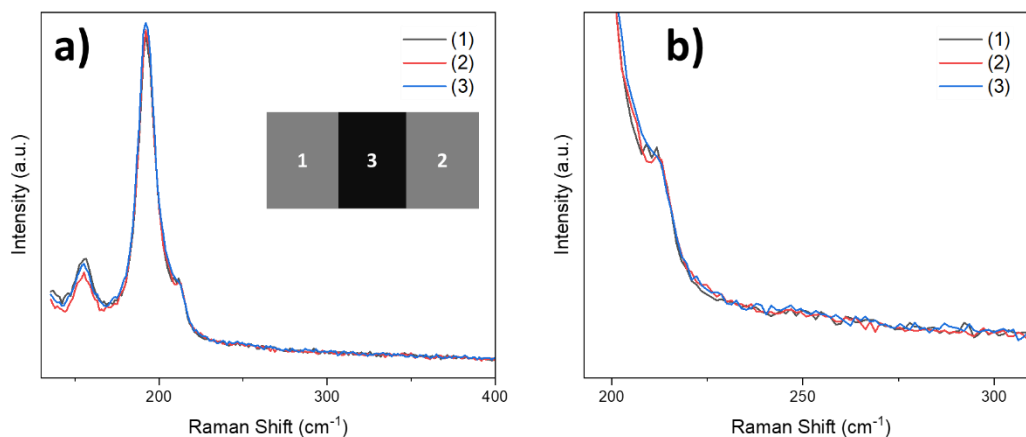
Figure 39 *(a) Raman Spectra after thermal ALD TiO$_2$ on the top of Sb$_2$Se$_3$ (1 and 2) and (3) the control region masked during the ALD deposition. (b) Zoom for the region close to 254 cm^{-1} related to Sb$_2$O$_3$.*

Once the Sb_2O_3 formation was ruled out, the same ALD protocol was used for 20 nm thick ALD TiO_2, and without any further annealing (Sb$_2$Se$_3$/TiO$_2$-ALD(NA)), the chopped light LSV was carried out in in 0.1 M H_2SO_4 at 10 mV s^{-1} and shown in Figure 40. The electrolyte was chosen to benchmark the Sb_2Se_3 photocathodes against reports in the literature. The photocurrent reached only $\approx$20 µA cm^{-2} at 0 V *vs* RHE with large spikes associated to recombination.[75] The Grätzel group pointed out that the crystallinity and thickness of the TiO_2 films are the key parameters in developing long-lasting protective TiO_2 layers deposited by ALD for Cu_2O photocathodes.[63,64,71,83–85] The crystallinity of the metal oxide was mainly governed by the deposition temperature, the titanium precursor (Tetrakis (dimethylamido) titanium, TDMAT or Titanium tetraisopropoxide, TTIP) and the oxygen source either H_2O or H_2O_2 during the synthesis.[80] By transmission electron microscopy (TEM) analysis, it was found out that ALD TiO_2 thin films were largely amorphous with only a few crystalline domains, causing electron trapping.[64] To improve the crystallinity, a mild heat[63] or steam[64] treatment were applied, and the

photoelectrode stability significantly increased from minutes to hours. Therefore, a low temperature heat treatment was applied: 150, 200, 250, 300 °C for 1 h in air. However, the sample annealed at 300 °C went white most likely due to the formation of Sb_2O_3 (white powder), then this sample was not used for further studies. Figure 40a shows the chopped light LSV of the samples annealed at 150, 200, 250 °C in 0.1 M H_2SO_4 at 10 mV/s; the photocurrent was slightly improved after the annealing compared to the control sample (grey trace, Sb_2Se_3/TiO_2-ALD(NA)). The spikes decrease the intensity and according to Gratzel studies after the annealing the amount of Ti^{3+} states decreased, which act as electron trapping and recombination centers.[71,84] However, the HER rate is sufficiently slow that recombination of electron-hole pairs dominates and minimal photocurrent is observed, thus Pt was used as an electron extractor.
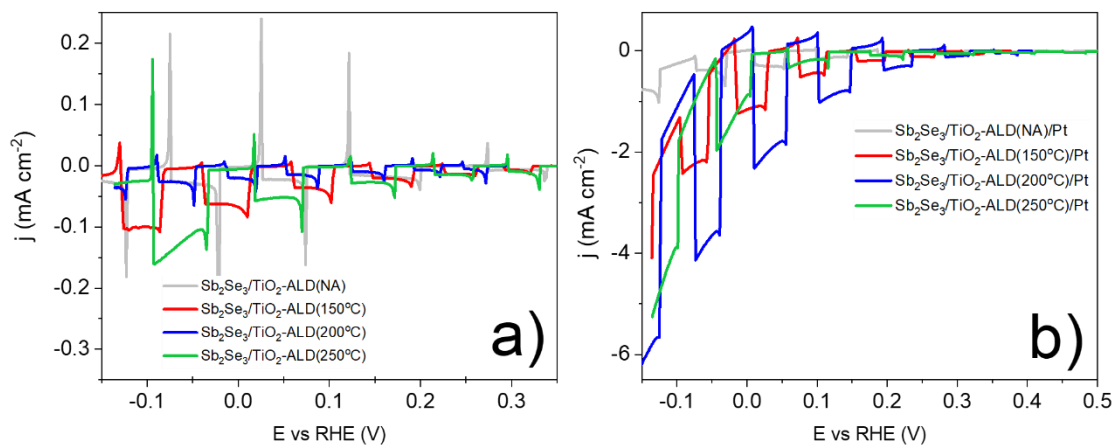
Figure 40 *Chopped light LSV in 0.1 M H_2SO_4 under N_2 at 10 mV s^{-1} of Sb_2Se_3/TiO_2-ALD (a) without (b) with Pt as HER catalyst. The samples were annealed at different temperatures: 150, 200, 250 °C and the control experiment with no annealing (NA), at 60 mW cm^{-2} and λ > 340nm.*

The Pt photoelectrodeposition was carried out according to past studies,[29] at -30 µA cm^{-2} for 15 min at 100 mW cm^{-2}, λ ≥ 340 nm and a water filter, in 1 mM H_2PtCl_6 and 0.1 M Na_2SO_4, after the films were annealed at different temperatures (the experimental details are described in section 6.2.5). Figure 40b shows a clear difference in the LSV after adding Pt since it enables faster photoelectron extraction from the light absorber. The highest photocurrent of −3 mA cm^{-2} at 0 V *vs* RHE was recorded for the samples

annealed at 200°C, however this value is still well below of the state-of-the-art Sb_2Se_3 photocathodes. The different PEC behaviour could be attributed to several reasons, first related to the catalyst loading since most of the Sb_2Se_3 studies rely on Pt e-beam deposition or sputtering. Second, lower light intensity of 60 mW cm^{-2} was used for these experiments, compared to previous reports at 100 mW cm^{-2}.[38,39] Finally, it is likely that after the mild annealing, the ALD TiO_2 capping layer was not completely crystalline. Sb_2Se_3 and ZnTe share the same thermal instability drawback, which hinders any further annealing to improve the crystallinity of metal oxide capping layer.

The most used Ti precursor for ALD TiO_2 protective layer is TDMAT. The Gratzel group measured reduced photocurrent when TTIP and H_2O were used as ALD precursors for Cu_2O photocathodes protective layers, even for thin TiO_2 layers (20 nm).[63] By changing to TDMAT and H_2O_2 as precursors, up to 100nm thick ALD TiO_2 layers were achieved without hindering the photocurrent plateau.[83] This behaviour was attributed to the "TiO_2 photodoping" effect where the conductivity of the metal oxide increases several orders of magnitude after the electron injection during the CPP.[86] Therefore, having thicker ALD TiO_2 significantly improves the stability of the photocathode without introducing large resistance in the device. The impact of the oxygen source using H_2O_2 or H_2O as precursors for ALD were also studied and found out that H_2O_2 produced less oxygen deficiencies (measured by Electrochemical Impedance Spectroscopy, EIS and the donor density), since the Ti^{4+} states were favoured instead of Ti^{3+} states.[63,83] However, this synthesis protocol was not accessible during the study, instead Plasma Enhance Atomic Layer Deposition (PEALD) was used to improve the crystallinity of the TiO_2 capping layer.

PEALD

For this setup, the oxygen source is replaced by O_2 plasma which is a stronger oxidant than H_2O and H_2O_2, and TTIP was used as Ti precursor. PEALD produces denser crystalline films.[87,88] However, it is likely that during the PEALD, the O_2 plasma could oxidize the Sb_2Se_3 surface and form Sb_2O_3, then Raman Spectroscopy was used to rule out this effect. A 2μm

thick Sb_2Se_3 was deposited on a 2x2 cm^2 FTO substrate, and a silicon wafer (0.5 x 1 cm) was placed on the FTO/Sb_2Se_3 to mask a control area during the 10 min O_2 plasma beam at 50 W and 24 W Ar:O_2, pictures shown in the inserts of Figure 41a and c respectively, as the area where the Raman spectra were collected. At higher power (50 W Figure 41a), the area next to the silicon wafer shows a clear difference in colour and became black, and the Raman spectra collected in this region showed the characteristic Sb_2O_3 Raman shifts at 254 cm^{-1}. The control area (indicated as 1) shows no contribution of Sb_2O_3, meanwhile the spectra collected in area 4 and 5 exhibited a small Sb_2O_3 contribution (Figure 41 b). The same behaviour was found using lower intensity 24 W Ar:O_2 (Figure 41c,d), however the black region was smaller but showing the Sb_2O_3 Raman shift at 254 cm^{-1}, and small Sb_2O_3 contribution was also found in the rest of the sample (spectra 4 to 7 shown in Figure 41d) apart from the masked region. From Figure 41 is evident that even with a lower power, there was a Sb_2O_3 formation after the samples were exposed to the O_2 plasma.

To avoid Sb_2O_3 formation, a ≈ 1 nm thick Al_2O_3 was deposited by thermal ALD on the top of FTO/Sb_2Se_3(2µm). It could act as passivation layer of Sb_2Se_3 defects, blocking layer to prevent back electron recombination and to avoid the Sb_2O_3 formation. Furthermore, having a thin Al_2O_3 layer acts as a template for TiO_2 ALD growth produces more homogeneous coatings.[71] The sample was divided in 4 different areas, shown in Figure 42: (1) was used as a blank without any further layer on the top and masked during the ALD, in (2) 10 cycles of thermal Al_2O_3 ALD were applied to give rise to ≈ 1 nm, followed by 10 min of O_2 plasma at 24 W of Ar:O_2 shown in area (3), and in (4) there was no protective Al_2O_3 layer before the O_2 plasma exposure. A Sb_2O_3 Raman peak at 254 cm^{-1} was only observed for the sample directly exposed to the O_2 plasma beam and for the protected area, this peak at was not identified indicating that 1 nm thick Al_2O_3 is a suitable approach to avoid Sb_2O_3 oxide formation.
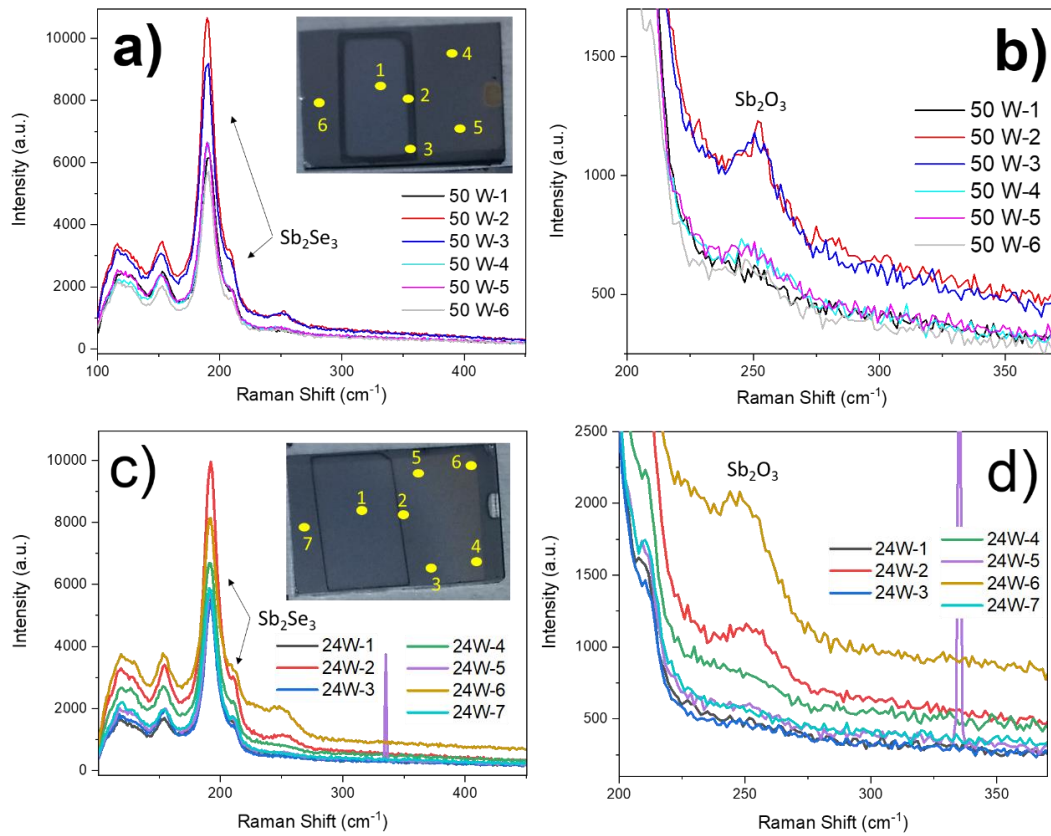
Figure 41 *Raman Spectra of FTO/Sb₂Se₃(2μm) exposed to O₂ plasma at (a, b) 50 W, (c, d) 24 W Ar:O₂ for 10 min and the region where the Raman spectra was collected is shown in the inserts (a, c). Panel (c, d) show the Raman shift of the region close to the Sb₂O₃.*
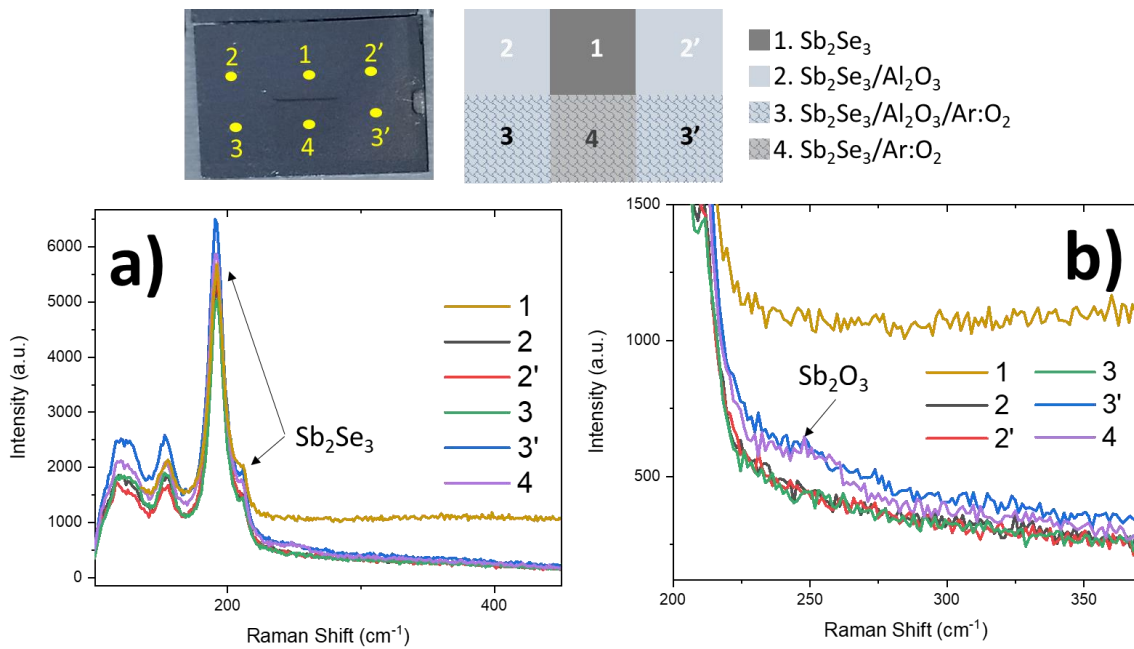
Figure 42 *Raman spectra of FTO/Sb₂Se₃(2μm) protected with 1 nm thick Al₂O₃ followed by 24 W of Ar:O₂*

Once the Sb_2O_3 was ruled out by using a thin Al_2O_3 layer, thermal ALD TiO_2 was conducted and followed by PEALD ($Sb_2Se_3/Al_2O_3/TiO_2$-ALD/TiO_2-PEALD). Two different TiO_2 thickness were studied 20 nm and 100 nm, and the experimental details are included in section 6.1.2.2. The Raman analysis was conducted in the pristine samples prior to the PEC test and the results are shown in Figure 43. Anatase TiO_2 Raman peaks were identified only for 100 nm thick TiO_2 sample, suggesting that the PEALD strategy successfully improved the crystallinity of the samples.
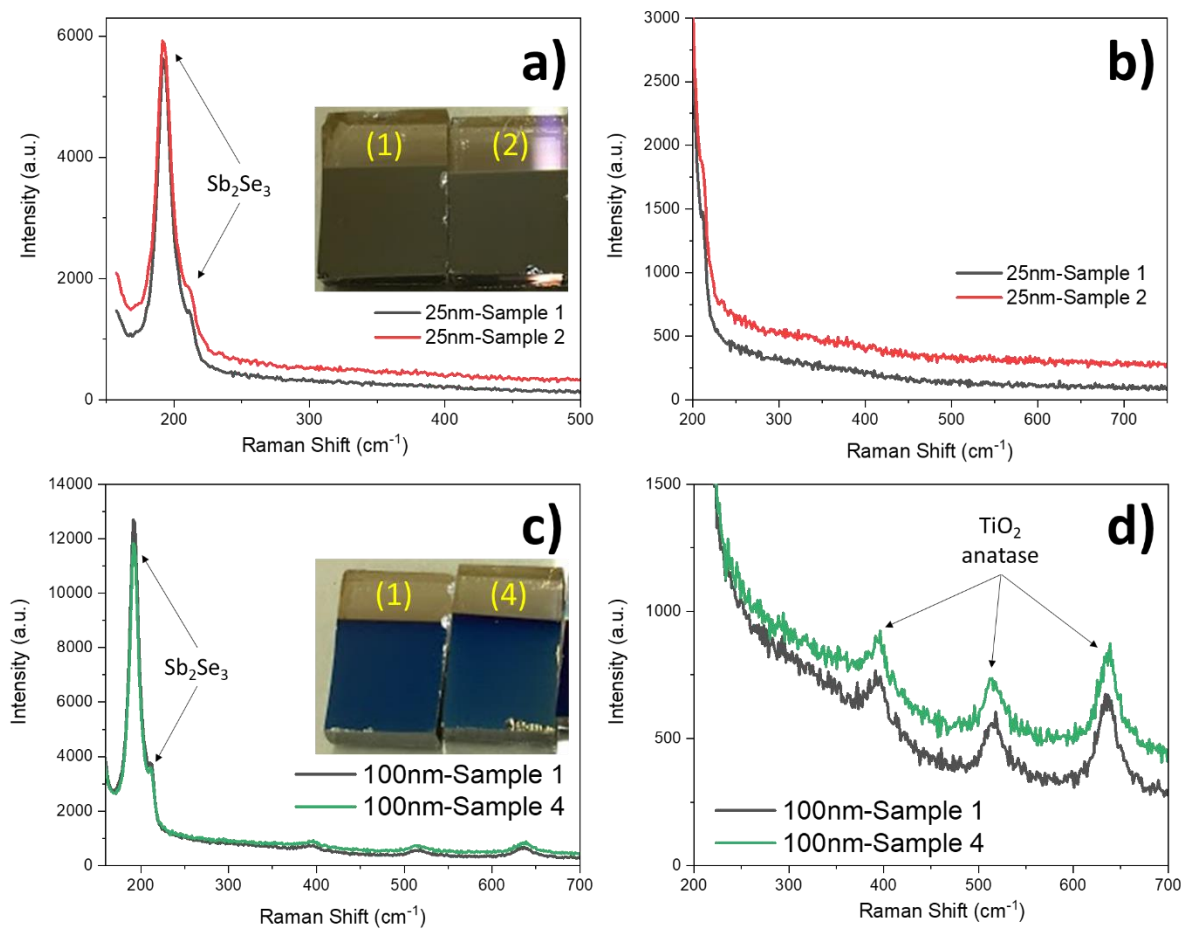
Figure 43 *Raman spectra of the pristine samples (a, c) 20 and (c, d) 100 nm thick PEALD TiO_2 on the top of FTO FTO/Sb_2Se_3(2 μm).*

Without any further annealing, Pt was photoelectrodeposited using the same experimental protocol (section 6.2.5), and Figure 44 shows the chopped light LSV of Sb_2Se_3/TiO_2-PEALD/Pt with the thicknesses indicated in brackets at 10 mV s^{-1} in 0.1 M H_2SO_4. The photocurrent of the 100 nm TiO_2

sample is higher than the one achieved using 25 nm thick TiO_2, ≈ -11 mA cm^{-2} and ≈ -9 mA cm^{-2} at 0 V RHE, respectively likely to the imporved crystallinity of TiO_2. Furthermore, this photocurrent is close to the state of the art Sb_2Se_3/TiO_2 interfaces (Table 3) suggesting that Al_2O_3 ALD could act as electron blocking layer and avoid Sb_2O_3 oxide formation during PEALD TiO_2 whilst not significantly limiting current despite its resistivity. TiO_2 provides a reasonable band alignment with Sb_2Se_3 but is not ideal, since the Sb_2Se_3 VBM and the TiO_2 CBM did not have a significant offset, and interface recombination between the holes in the Sb_2Se_3 VBM and the electrons in the TiO_2 CBM could happen.[89] This could be the reason why, as a general trend, the photocurrent of most of the devices with the Sb_2Se_3/TiO_2 interface is generally lower compared with the state-of-the-art photocathodes that include a CdS as a buffer layer.
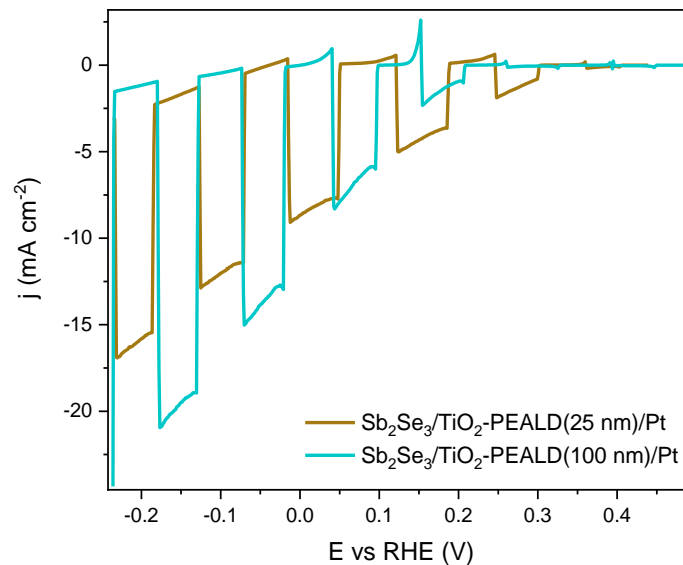
Figure 44 *Chopped light LSV of Sb$_2$Se$_3$/TiO$_2$-PEALD with 25 and 100 nm TiO$_2$ thickness in 0.1 M H$_2$SO$_4$ under N$_2$ using 100 mW cm^{-2}, λ≥340 nm.*

Even though Sb_2Se_3/TiO_2-PEALD(100nm)/Pt was a very promising photocathode architecture for further analysis alongside CO_2R catalysts, technical difficulties related to ALD chamber did not allow more access to PEALD TiO_2 samples. Instead, sputtered TiO_2 was explored as an alternative and more accessible approach.

Sputtering

TiO_2 films were deposited by sputtering at low temperature with two different thicknesses: 20 and 120 nm, the experimental details are contained in the Section 6.1.2.2. Since low crystallinity TiO_2 films were anticipated, a mild heat treatment (200 °C for 1 h in air) was conducted before Pt photo-electrodeposition. Figure 45 shows the chopped light LSV of Sb_2Se_3/TiO_2-S(X nm)/Pt samples with and without annealing (NA) at 10 mV s^{-1} in 0.1 M H_2SO_4. For the 20 nm TiO_2-S layer (Figure 45a), no change in photocurrent was observed before and after the annealing. However, the annealing step significantly increased the photocurrent of the 120 nm TiO_2-S sample (Figure 45b). Having thicker TiO_2 layers in the photoelectrode may also offer an advantage by adding a physical barrier to prevent direct contact of the electrolyte with the light absorber without decreasing the PEC performance.[64,83]
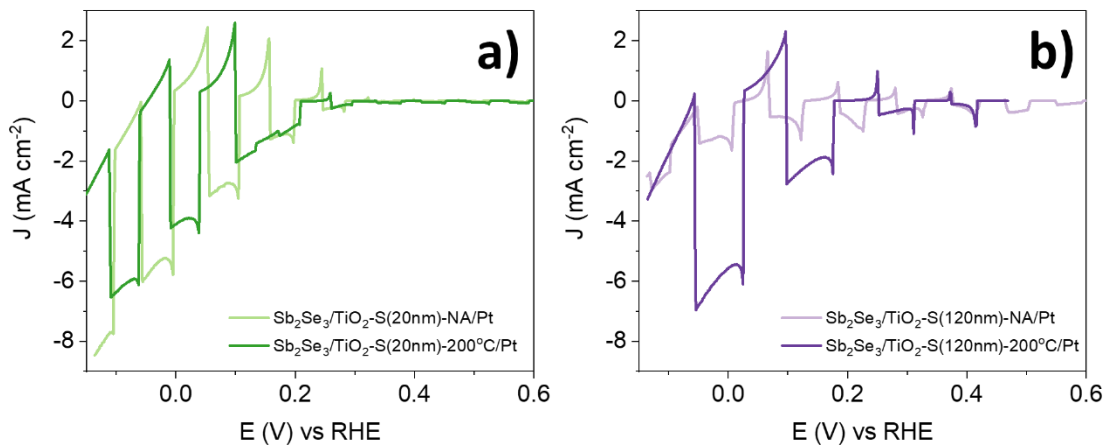
Figure 45 *Chopped Light LSV of Sb_2Se_3/TiO_2-S(X nm)/Pt with X = 25 and 120 nm TiO_2 thickness in 0.1 M H_2SO_4 under N_2 at 10 mV s^{-1} using 100 mW cm^{-2}, $\lambda \geq 340$. NA indicates no annealing before Pt deposition.*

The Sb_2Se_3/TiO_2-S interface produces a photocurrent around -6 mA cm^{-2} at 0 V *vs* RHE after the annealing, independently of the thicknesses. This value lies below the state-of-the-art photocurrent, and for the better understanding of this lower photocurrent, a control set of samples of 100 nm sputtered TiO_2 (FTO/TiO_2-S) were annealed at 200° and 450 °C in air for 1 h. Figure 46 shows the Raman spectra, and no significant difference was observed with no annealing and 200 °C. Only after increasing the

temperature up to 450 °C, the Raman peaks associated to anatase TiO_2 were identified at 144, 195, 393, 517 and 638 cm^{-1} Raman shifts. From Figure 46, it is clear that sputtered TiO_2 produces low crystallinity which is likely associated to the low photocurrent compared to the Sb_2Se_3/TiO_2 PEALD samples. However, the Sb_2Se_3 thermal instability does not allow annealing at higher temperature. Instead, a Sb_2Se_3/CdS junction alongside sputtered TiO_2 was studied as an alternative to improve the PEC performance of the Sb_2Se_3 based photocathodes.
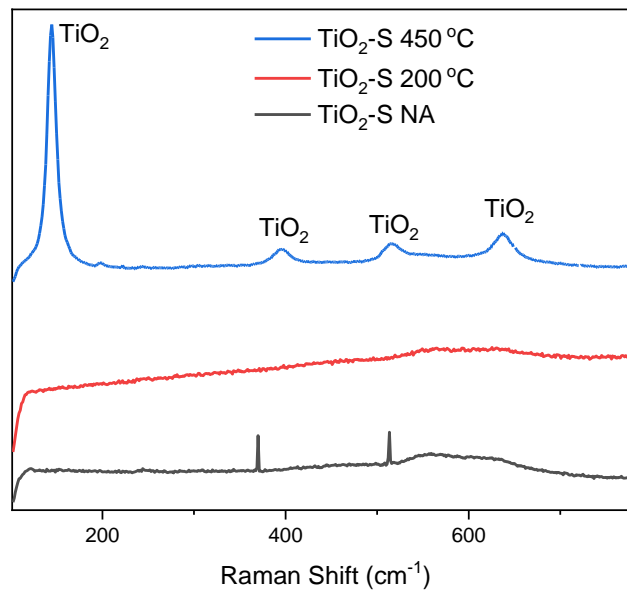
Figure 46 *Raman spectra of 100 nm sputtered TiO_2 (TiO_2-S) annealed at 200 and 450 °C in air, compared with the control without annealing (NA).*

2.2.2.2 $Sb_2Se_3/CdS/TiO_2$

CdS provides a better band alignment than TiO_2[89] as shown in Figure 47a for the isolated semiconductors before equilibrium. The diagram was based on the VBM[41] and the Eg was determined independently for 100 nm isolated films on FTO. The E_g was 2.33 and 3.39 eV for CdS and TiO_2 respectively (Figure 47 b and c respectively).

Most of the Sb_2Se_3 based photocathodes used chemical bath deposition for CdS, and recently some further treatments have been successfully improved the charge extraction at the Sb_2Se_3/CdS junction.[42,43] The first approach reported involved annealing at 280 °C for 5 min under Ar after the addition of the CdS onto Sb_2Se_3.[42] In this way, a void free interface was favoured by the slight Cd^{2+} interdiffusion in the Sb_2Se_3 lattice replacing Sb^{3+}. Consequently, considering that Cd provides 2 electrons to lattice, meanwhile the Sb provides 3 electrons, the substitution of Cd by Sb gives rise a more p-type Sb_2Se_3, which also increases electric field at the Sb_2Se_3/CdS junction. Furthermore, the onset potential is significantly shifted from 0.27 to 0.52 V vs RHE suggesting a better band alignment. By EIS analysis, it was also found that the resistance and capacitance associated to the Sb_2Se_3/CdS interface disappeared, and the time constant for charge transfer associated to HER reaction was shifted towards lower frequencies suggesting that the process was faster, and the photocurrent increased from -6.18 up to -16.25 mA cm^{-2} after the annealing. It is important to note that this study was one of the very few which did not include the TiO_2 capping layer, therefore a meaningful understanding of the Sb_2Se_3/CdS interface was achieved.[42] The second approach explored a CdS n-type doping by introducing In^{3+} cations and once the optimal concentrations was found, the conduction band offset was tuned form "cliff like" to "spike like" with a difference of 0.15 eV, which corresponds to a high-quality semiconductor heterojunction. This careful tailoring of the CdS layer, alongside to the appropriate junction between the HTL (Mo) and the light absorber through a MoSe interface, led to -35.7 mA cm^{-2} at 0 V vs RHE which now stands as the record Sb_2Se_3 photocathodes for HER.[43] This device is only -5.2 mA cm^{-2} away from the theoretical maximum photocurrent density of Sb_2Se_3 as light absorber.[5]

In this study, a 20 nm sputtered CdS buffer layer was incorporated on Sb_2Se_3 followed by 20 nm sputtered TiO_2 capping layer (the experimental details are fully described in section 6.1.2.1). Without any further annealing prior Pt photoelectrodeposition, the light chopped LSV was carried out in 0.1 M H_2SO_4 at 10 mV s^{-1}, and Figure 48 shows that Sb_2Se_3/CdS/TiO_2-S(20nm)/Pt reached up to $ca.$ -20 mA cm^{-2} at 0 V vs RHE, being close to the state-of-the-art Sb_2Se_3 photocathodes. The increase in the photocurrent is likely associated to the better band alignment the CdS provides instead of TiO_2-S.

Figure 47 *(a) Band diagram of the isolated semiconductors Sb₂Se₃, CdS, and TiO₂, based on VBM[41] and Eg measured separately for each component. Tauc plot of (b) CdS and (c) TiO₂ on FTO.*

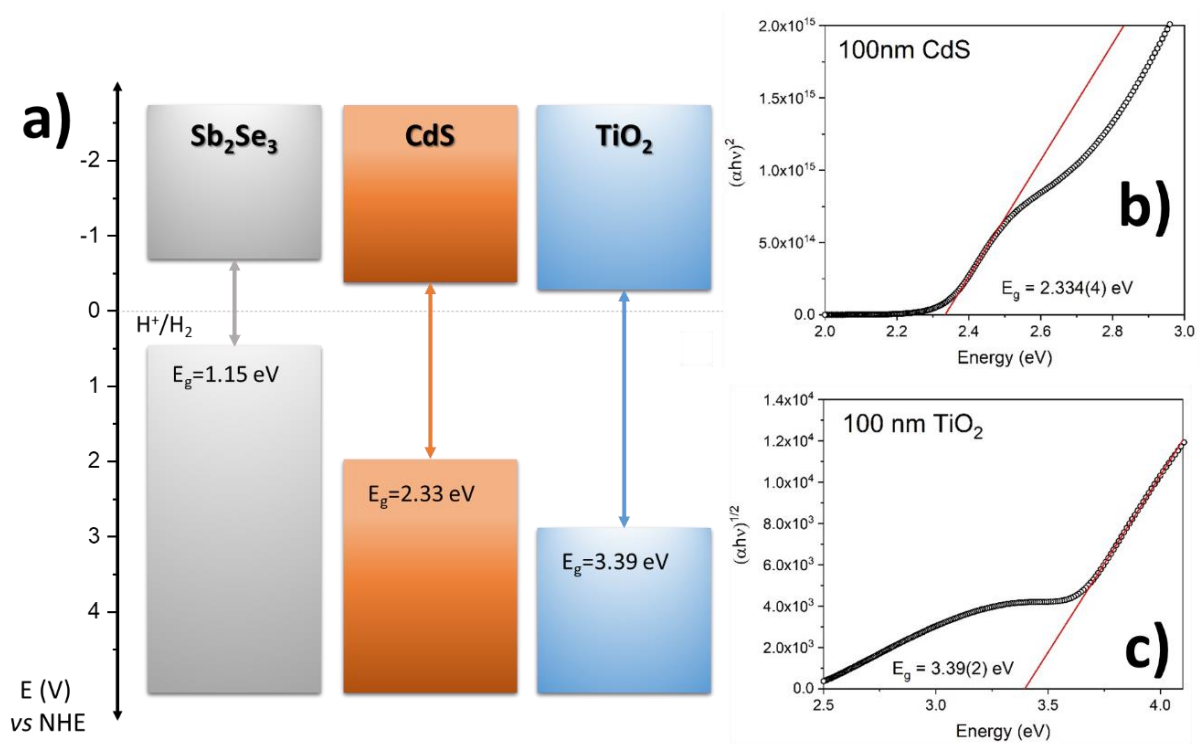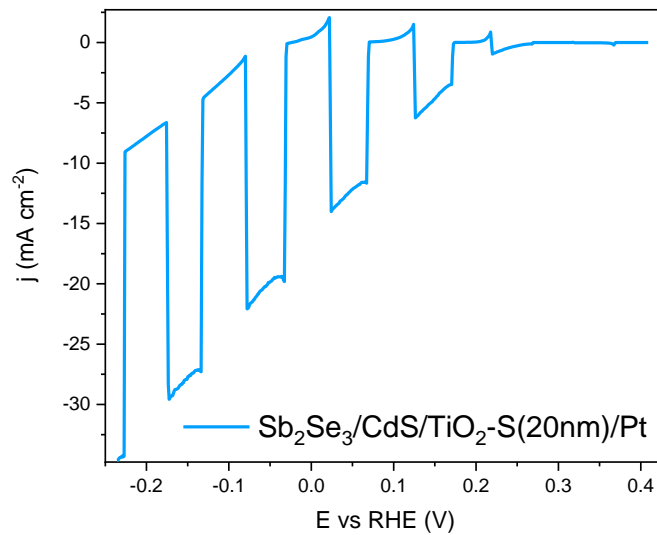**Figure 48** *Chopped light LSV Sb₂Se₃/CdS/TiO₂-S(20nm)/Pt in 0.1 M H₂SO₄ at 10 mV s⁻¹ under N₂ using 100 mW cm⁻², λ≥340.*

As it was discussed previously, a better band alignment at the p-n junction usually gives rise to an improvement of the onset potential, therefore it was expected that the addition of CdS as a buffer layer enhance this parameter.[38] However the opposite effect was observed, a more positive onset potential was observed on Sb_2Se_3/TiO_2-S(X nm)/Pt at *ca.* 0.6 V vs RHE (Figure 45) than Sb_2Se_3/CdS/TiO_2-S(20nm)/Pt at *ca.* 0.4 V *vs* RHE (Figure 48). This behaviour could be related to the reproducibility issues in the onset potential and photocurrent observed during the development of the basic Sb_2Se_3 structure, discussed in detail in section 6.1.2.5. Another possibility could be associated to the heat treatment, the PEC response of Sb_2Se_3/CdS/TiO_2-S(20nm)/Pt was recorded without any thermal treatment and it has been reported that annealing at 280 °C for 5 min promotes a void free interface.[42] Figure 58 (see below, section 3.3.3) supports this hypothesis since after the annealing at 250° and 350 °C under N_2, the onset potential at was shifted up to *ca.* 0.6 V vs RHE even low photocurrents were recorded at this potential.

Yang and collaborators noticed that the photons at ≈516 nm associated to CdS absorption did not contribute to the total photocurrent from IPCE (Incident Photon-to-Current Efficiency) analysis, and determined that a careful tailoring of the CdS layer is required to improve the fill factor and onset potential without the significant decrease in photocurrent.[38] Still, a slight decrease in photocurrent was observed from −24 to −19 mA cm^{-2} compared with the device without the CdS layer at 0 V *vs* RHE at pH 1 H_2SO_4. For this particular study, the Sb_2Se_3 was made by CSS and the ALD TiO_2 capping used TDMAT as Ti precursor,[38] therefore a significant difference in photocurrent is expecting compared to this device. Considering that all the PEC experiments were carried out using front illumination (facing the catalyst side), a possible CdS interference with the Sb_2Se_3 light absorption is already expected and this interface as well as the IPCE analysis will be further discussed in section 3.4. Having 20nm CdS sputtered buffer layer demonstrated to have a positive effect in the PEC performance, even though it does not display the highest photocurrent for Sb_2Se_3 based photocathodes, it provided a flexible platform for further studies for HER and CO_2R using precious metal free molecular catalysts.

2.3 Conclusion

In this chapter, two different semiconductors were assessed as light absorbers for hybrid photocathodes: ZnTe and Sb_2Se_3. Even though progress was made in the development of ZnTe based photocathodes, the highest photocurrent achieved with FTO/ZnTe/Ta_2O_5/Pt was lower than 20 μA cm^{-2} at 0 V vs RHE, which lies well below the state-of-the-art structure: ITO/ZnTe:Cu/CdS/Ti/Mo/Pt, that displayed -1.5 mA cm^{-2} at 0 V vs RHE. Note that for this particular study, the ZnTe was deposited via CSS, a high temperature deposition process which typically results in large grain sizes on the order of microns, compared to the nanometre sized grains of thermal evaporation without further annealing used here. Furthermore, the use of CSS allowed for the deposition to be optimised using two consecutive steps, where the photocurrent increased significantly from -0.05 mA cm^{-2} at 0 V RHE to -0.43 mA cm^{-2} at 0 V vs RHE.[3] The growth of films with large grain sizes and therefore few grain boundaries is expected to favour efficient charge extraction due to lower carrier recombination. Such grain structure is much more feasible with two-step CSS process compared to thermal evaporation, and PEC performance has been improved significantly using CSS in two steps for other semiconductors like Sb_2Se_3.[79]

The experimental results of Sb_2Se_3 demonstrated that even when the light absorber has suitable properties for PEC devices in terms of grain structure and orientation achieved by the optimised CSS deposition, the careful tailoring of the neighbour interfaces was required to properly extract the photogenerated holes and electrons. It was found that the TiO_2 crystallinity played a key role in the PEC performance and this property was highly dependent on the experimental conditions and deposition method (ALD, PEALD or sputtering). The improved band alignment in Sb_2Se_3 based photocathodes by CdS addition, gave rise to higher photocurrents ($ca.$ -20 mA cm^{-2} at 0 V vs RHE, being close to the state-of-the-art Sb_2Se_3 photocathodes) compared with the Sb_2Se_3/TiO_2 interface. Pt was used as benchmark catalyst to promote photoelectron extraction from the light absorber in the photocathode. This strategy also allowed to find the bottlenecks of the device for further improvement. In this way, a suitable architecture was found to be couple with a molecular catalyst either for H_2 production or CO_2R. In the next chapter we study the architecture developed here alongside one of the most active noble metal free molecular catalyst for H_2 production **NiP**.

2.4 References

1   J. W. Jang, S. Cho, G. Magesh, Y. J. Jang, J. Y. Kim, W. Y. Kim, J. K. Seo, S. Kim, K.-H. Lee and J. S. Lee, *Angew. Chem. Int. Ed.*, 2014, **126**, 5852–5857.

2   J. L. White, M. F. Baruch, J. E. Pander, Y. Hu, I. C. Fortmeyer, J. E. Park, T. Zhang, K. Liao, J. Gu, Y. Yan, T. W. Shaw, E. Abelev and A. B. Bocarsly, *Chem. Rev.*, 2015, **115**, 12888–12935.

3   T. Minegishi, A. Ohnishi, Y. Pihosh, K. Hatagami, T. Higashi, M. Katayama, K. Domen and M. Sugiyama, *J. Chem. Phys.*, 2020, **8**, 41101.

4   L. Wang, D. B. Li, K. Li, C. Chen, H. X. Deng, L. Gao, Y. Zhao, F. Jiang, L. Li, F. Huang, Y. He, H. Song, G. Niu and J. Tang, *Nat. Energy*, 2017, **2**, 1–9.

5   S. Chen, T. Liu, Z. Zheng, M. Ishaq, G. Liang, P. Fan, T. Chen and J. Tang, *J. Energy Chem.*, 2022, **67**, 508–523.

6   L. Zhang, Z. J. Zhao, T. Wang and J. Gong, *Chem. Soc. Rev.*, 2018, **47**, 5423–5443.

7   A. Mavlonov, T. Razykov, F. Raziq, J. Gan, J. Chantana, Y. Kawano, T. Nishimura, H. Wei, A. Zakutayev, T. Minemoto, X. Zu, S. Li and L. Qiao, *Sol. Energy*, 2020, **201**, 227–246.

8   S. Xie, Q. Zhang, G. Liu and Y. Wang, *Chem. Commun.*, 2016, **52**, 35–59.

9   H. Pang, T. Masuda and J. Ye, *Chem. Asian J.*, 2018, **13**, 127–142.

10 L. K. Putri, B. J. Ng, W. J. Ong, S. P. Chai and A. R. Mohamed, *Adv. Energy Mater.*, 2022, **17**, 2201093.

11 Y. J. Jang, J. W. Jang, J. Lee, J. H. Kim, H. Kumagai, J. Lee, T. Minegishi, J. Kubota, K. Domen and J. S. Lee, *Energy Environ. Sci.*, 2015, **8**, 3597–3604.

12 D. H. Won, J. Chung, S. H. Park, E. H. Kim and S. I. Woo, *J. Mater. Chem. A*, 2015, **3**, 1089–1095.

13 Y. J. Jang, I. Jeong, J. Lee, J. Lee, M. J. Ko and J. S. Lee, *ACS Nano*, 2016, **10**, 6980–6987.

14 Y. J. Jang, J. Lee, J. Lee and J. S. Lee, *ACS Appl. Mater. Interfaces*, 2016, **8**, 7748–7755.

15 Y. J. Jang, M. D. Bhatt, J. Lee, S. H. Choi, B. J. Lee and J. S. Lee, *Adv. Energy Mater.*, 2018, **8**, 1–8.

16 P. Wen, H. Li, X. Ma, R. Lei, X. Wang, S. M. Geyer and Y. Qiu, *J. Mater. Chem. A*, 2021, **9**, 3589–3596.

17 B. Seger, T. Pedersen, A. B. Laursen, P. C. K. Vesborg, O. Hansen and I. Chorkendorff, *J. Am. Chem. Soc.*, 2013, **135**, 3, 1057–1064.

18 C. Li, T. Wang, B. Liu, M. Chen, A. Li, J. Gong, G. Zhang, M. Du, H. Wang, S. Frank Liu, J. Gong, S. F. Liu and J. Gong, *Energy Environ. Sci.*, 2019, **12**, 923–928.

19 S. Chen and L.-W. Wang, *Chem. Mater.*, 2012, **24**, 3659–3666.

20 A. J. Nozik and R. Memming, *J. Phys. Chem.*, 1996, **100**, 13061–13078.

21 Z. Chen, H. N. Dinh and E. Miller, Photoelectrochemical Water Splitting - Standards, Experimental Methods, and Protocols, 2013.

22   M. Schleuning, I. Y. Ahmet, R. van de Krol Ab and M. M. May, *Sustain. Energy Fuels*, 2022, **6**, 3701.

23   H. Lee, W. Yang, J. Tan, Y. Oh, J. Park and J. Moon, *ACS Energy Lett.*, 2019, **4**, 995–1003.

24   W. Yang, R. R. Prabhakar, J. Tan, S. D. Tilley and J. Moon, *Chem. Soc. Rev.*, 2019, **48**, 4979–5015.

25   J. M. Bolts, *J. Phys. Chem.*, 1976, **80**, 2641–2645.

26   G. Rothenberger, D. Fitzmaurice and M. Gratzel, *J. Phys. Chem.*, 1992, **96**, 5983–5986.

27   Z. Duan, X. Liang, Y. Feng, H. Ma, B. Liang, Y. Wang, S. Luo, S. Wang, R. E. I. Schropp, Y. Mai, Z. Li, Z. Duan, Y. Feng, H. Ma, B. Liang, Y. Wang, S. Luo, S. Wang, Z. Li, X. Liang, R. E. I. Schropp and Y. Mai, *Adv. Mater.*, 2022, **34**, 2202969.

28   L. Zhang, Y. Li, C. Li, Q. Chen, Z. Zhen, X. Jiang, M. Zhong, F. Zhang and H. Zhu, *ACS Nano*, 2017, **11**, 12753–12763.

29   R. R. Prabhakar, W. Septina, S. Siol, T. Moehl, R. Wick-Joliat and S. D. Tilley, *J. Mater. Chem. A*, 2017, **5**, 23139–23145.

30   X. Liu, J. Chen, M. Luo, M. Leng, Z. Xia, Y. Zhou, S. Qin, D. J. Xue, L. Lv, H. Huang, D. Niu and J. Tang, *ACS Appl. Mater. Interfaces*, 2014, **6**, 10687–10695.

31   J. Park, W. Yang, Y. Oh, J. Tan, H. Lee, R. Boppella and J. Moon, *ACS Energy Lett.*, 2019, **4**, 2 517–526.

32   W. Yang and J. Moon, *J. Mater. Chem. A*, 2019, **7**, 20467–20477.

33   J. Kim, W. Yang, Y. Oh, H. Lee, S. Lee, H. Shin, J. Kim and J. Moon, *J. Mater. Chem. A*, 2017, **5**, 2180–2187.

34   W. Yang, J. Ahn, Y. Oh, J. Tan, H. Lee, J. Park, H. C. Kwon, J. Kim, W. Jo, J. Kim and J. Moon, *Adv. Energy Mater.*, 2018, **8**, 1–11.

35   J. Tan, W. Yang, Y. Oh, H. Lee, J. Park and J. Moon, *ACS Appl. Mater. Interfaces*, 2018, **10**, 10898–10908.

36   W. Yang, S. Lee, H.-C. Kwon, J. Tan, H. Lee, J. Park, Y. Oh, H. Choi and J. Moon, *ACS Nano*, 2018, **12**, 11, 11088–11097.

37   J. Tan, W. Yang, Y. Oh, H. Lee, J. Park, R. Boppella, J. Kim and J. Moon, *Adv. Energy Mater.*, 2019, **9**, 1900179, 1–12.

38   W. Yang, J. H. Kim, O. S. Hutter, L. J. Phillips, J. Tan, J. Park, H. Lee, J. D. Major, J. S. Lee and J. Moon, *Nat. Commun.*, 2020, **11**, 1–10.

39   J. Park, W. Yang, J. Tan, H. Lee, J. W. Yun, S. G. Shim, Y. S. Park and J. Moon, *ACS Energy Lett.*, 2020, **5**, 136–145.

40   J. Yang, Y. Lai, Y. Fan, Y. Jiang, D. Tang, L. Jiang, F. Liu and J. Li, *RSC Adv.*, 2015, **5**, 85592–85597.

41   W. Yang, J. Park, H.-C. C. Kwon, O. S. Hutter, L. J. Phillips, J. Tan, H. Lee, J. Lee, S. D. Tilley, J. D. Major and J. Moon, *Energy Environ. Sci.*, 2020, **13**, 4362–4370.

42   G. Liang, T. Liu, M. Ishaq, Z. Chen, R. Tang, Z. Zheng, Z. Su, P. Fan, X. Zhang and S. Chen, *J. Chem. Eng.*, 2022, **431**, 133359.

43   S. Chen, T. Liu, M. Chen, M. Ishaq, R. Tang, Z. Zheng, Z. Su, X. Li, X. Qiao, P. Fan and G. Liang, *Nano Energy*, 2022, **99**, 107417.

44   C. Liu, T. Liu, Y. Li, Z. Zhao, D. Zhou, W. Li, Y. Zhao, H. Yang, L. Sun, F. Li and Z. Li, *J. Mater. Chem. A*, 2020, **8**, 23385–23394.

45   J. Tan, W. Yang, H. Lee, J. Park, K. Kim, O. S. Hutter, L. J. Phillips, S. Shim, J. Yun, Y. Park, J. Lee, J. D. Major and J. Moon, *Appl. Catal. B*, 2021, **286**, 119890.

46   W. Yang, T. Moehl, E. Service and S. D. Tilley, *Adv. Energy Mater.*, 2021, 2003569, 1–10.

47   H. Zhou, M. Feng, K. Song, B. Liao, Y. Wang, R. Liu, X. Gong, D. Zhang, L. Cao and S. Chen, *Nanoscale*, 2019, **11**, 22871–22879.

48   H. Zhou, M. Feng, P. Li, X. Gong, D. Zhang and S. Chen, *Sustain. Energy Fuels*, 2020, **4**, 3943–3950.

49   X. Xiong, M. Forster, J. D. Major, Y. Xu and A. J. Cowan, *J. Phys. Chem. C.*, 2017, **121**, 22073–22080.

50   J. O. Bockris and K. Uosaki, *J. Electrochem. Soc.*, 1977, **124**, 1348–1355.

51   M. Iqbal, Y. Wang, H. Hu, M. He, A. H. Shah, P. Li, L. Lin, A. R. Woldu and T. He, *Electrochim. Acta*, 2018, **272**, 203–211.

52   R. Liu, Z. Zheng, J. Spurgeon and X. Yang, *Energy Environ. Sci.*, 2014, **7**, 2504–2517.

53   S. Hu, N. S. Lewis, J. W. Ager, J. Yang, J. R. McKone and N. C. Strandwitz, *J. Phys. Chem. C.*, 2015, **119**, 24201–24228.

54   M. F. Lichterman, K. Sun, S. Hu, X. Zhou, M. T. McDowell, M. R. Shaner, M. H. Richter, E. J. Crumlin, A. I. Carim, F. H. Saadi, B. S. Brunschwig and N. S. Lewis, *Catal. Today*, 2016, **262**, 11–23.

55   E. O. Filatova and A. S. Konashuk, *J. Phys. Chem. C.*, 2015, 119, 20755–20761.

56   E. Palomares, J. N. Clifford, S. A. Haque, T. Lutz and J. R. Durrant, *J. Am. Chem. Soc.*, 2003, **125**, 475–482.

57   Q. Cheng, M. K. Be**NiP**al, Q. Liu, X. Wang, P. A. Crozier, C. K. Chan and R. J. Nemanich, *ACS Appl. Mater. Interfaces*, 2017, **9**, 16138–16147.

58   R. Fan, J. Min, Y. Li, X. Su, S. Zou, X. Wang and M. Shen, *Appl. Phys. Lett.*, 2015, **106**, 213901–5.

59   M. L. Huang, Y. C. Chang, C. H. Chang, Y. J. Lee, P. Chang, J. Kwo, T. B. Wu and M. Hong, *Appl. Phys. Lett.*, 2005, **87**, 1–3.

60   R. Fan, W. Dong, L. Fang, F. Zheng, X. Su, S. Zou, J. Huang, X. Wang and M. Shen, *Appl. Phys. Lett.*, 2015, **106**, 2–6.

61   I. Ichinose, H. Senzu and T. Kunitake, *Chem. Mater.*, 1997, **9**, 1296–1298.

62   A. R. Balu, V. S. Nagarethinam, A. Thayumanavan, K. R. Murali, C. Sanjeeviraja and M. Jayachandran, *J. Alloys Compd.*, 2010, **502**, 434–438.

63   A. Paracchino, N. Mathews, T. Hisatomi, M. Stefik, S. D. Tilley and M. Grätzel, *Energy Environ. Sci.*, 2012, **5**, 8673–8681.

64   J. Azevedo, L. Steier, P. Dias, M. Stefik, C. T. Sousa, J. P. Araújo, A. Mendes, M. Graetzel and S. D. Tilley, *Energy Environ. Sci.*, 2014, **7**, 4044–4052.

65   B. Shan, S. Vanka, T. T. Li, L. Troian-Gautier, M. K. Brennaman, Z. Mi and T. J. Meyer, *Nat. Energy*, **4**, 2019, 290–299.

66   M. F. Ehsan and T. He, *Appl. Catal. B*, 2015, **166–167**, 345–352.

67   M. F. Ehsan, M. N. Ashiq and T. He, *RSC Adv.*, 2015, **5**, 6186–6194.

68   Y. Yang, S. Niu, D. Han, T. Liu, G. Wang and Y. Li, *Adv. Energy Mater.*, 2017, **7**, 1–26.

69   G. Neri, M. Forster, J. J. Walsh, C. M. Robertson, T. J. Whittles, P. Farrás and A. J. Cowan, *Chem. Commun.*, 2016, **52**, 14200–14203.

70   G. Neri, Thesis, University of Liverpool, 2016.

71   A. Paracchino, V. Laporte, K. Sivula, M. Grätzel and E. Thimsen, *Nat. Mater.*, 2011, **10**, 456–461.

72   L. Pan, J. H. Kim, M. T. Mayer, M.-K. Son, A. Ummadisingu, J. S. Lee, A. Hagfeldt, J. Luo and M. Grätzel, *Nat. Catal.*, 2018, **1**, 412–420.

73   M. Forster, R. J. Potter, Y. Yang, Y. Li and A. J. Cowan, *ChemPhotoChem*, 2018, **2**, 183–189.

74   T. Wang, S. Liu, H. Li, C. Li, Z. Luo and J. Gong, *Ind. Eng. Chem. Res.*, 2019, **58**, 5510–5515.

75   T. Berger, D. Monllor-Satoca, M. Jankulo*vs*ka, T. Lana-Villarreal and R. Gomez, *ChemPhysChem*, 2012, **13**, 2824–2875.

76   M. A. Gross, C. E. Creissen, K. L. Orchard and E. Reisner, *Chem. Sci.*, 2016, **7**, 5537–5546.

77   T.-T. Li, B. Shan and T. J. J. Meyer, *ACS Energy Lett.*, 2019, **4**, 629–636.

78   J. A. Keith and E. A. Carter, *J. Phys. Chem. Lett.*, 2013, **4**, 23, 4058–4063.

79   O. S. Hutter, L. J. Phillips, K. Durose and J. D. Major, *Sol. Energy Mater. Sol. Cells*, 2018, **188**, 177–181.

80   T. Moehl, J. Suh, L. Sévery, R. Wick-Joliat and S. D. Tilley, *ACS Appl. Mater. Interfaces*, 2017, **9**, 43614–43622.

81   A. Shongalova, M. R. Correia, B. Vermang, J. M. V. Cunha, P. M. P. Salomé and P. A. Fernandes, *MRS Commun.*, 2018, **8**, 865–870.

82   A. Kumar, V. Kumar, A. Romeo, C. Wiemer and G. Mariotto, *J. Phys. Chem. C*, 2021, **125**, 19858–19865.

83   S. D. Tilley, M. Schreier, J. Azevedo, M. Stefik and M. Gratzel, *Adv. Funct. Mater.*, 2014, **24**, 303–311.

84   M. Schreier, P. Gao, M. T. T. Mayer, J. Luo, T. Moehl, M. K. K. Nazeeruddin, S. D. D. Tilley and M. Grätzel, *Energy Environ. Sci.*, 2015, **8**, 855–861.

85   M. Schreier, J. Luo, P. Gao, T. Moehl, M. T. Mayer and M. Grätzel, *J. Am. Chem. Soc.*, 2016, **138**, 1938–1946.

86   M. Grätzel, *Inorg. Chem.*, 2005, **44**, 6841–6851.

87   Q. Xie, J. Musschoot, D. Deduytsche, R. L. van Meirhaeghe, C. Detavernier, S. van den Berghe, Y.-L. Jiang, G.-P. Ru, B.-Z. Li and X.-P. Qu, *J. Electrochem. Soc.*, 2008, **155**, H688.

88   J. W. Lim, S. J. Yun and J. H. Lee, *Electrochem. Solid-State Lett.*, 2004, **7**, F73.

89   H. Shiel, O. S. Hutter, L. J. Phillips, J. E. N. Swallow, L. A. H. Jones, T. J. Featherstone, M. J. Smiles, P. K. Thakur, T. L. Lee, V. R. Dhanak, J. D. Major and T. D. Veal, *ACS Appl. Energy Mater.*, 2020, **3**, 11617–11626.

90   ZnTe Pourbaix Diagram (https://materialsproject.org/pourbaix).

Chapter 3

Hybrid photocathode for H$_2$ production

Scope of the Chapter

In this chapter H$_2$ production was successfully achieved by coupling the Sb$_2$Se$_3$/CdS/TiO$_2$ (architecture developed in chapter 2) for light harvesting, alongside the hydrogenase-inspired molecular catalyst **NiP** with [Ni(P$_2^{R'}$N$_2^{R''}$)$_2$]$^{2+}$ core (P$_2^{R'}$N$_2^{R''}$ = bis(1,5-R′-diphospha-3,7-R″-diazacyclooctane)), modified with a phosphonic acid pendant arms in the outer coordination sphere to be covalently anchored to TiO$_2$.

First the planar device Sb$_2$Se$_3$/CdS/TiO$_2$/**NiP** gave rise to 16 μA cm^{-2} at 0 V *vs* RHE, this photocurrent was attributed to the low catalyst content (7.08 ± 0.43 nmol cm^{-2}). To increase the **NiP** loading, an alternative experimental protocol for a high surface area TiO$_2$ layer was developed to meet the thermal stability requirements of the Sb$_2$Se$_3$/CdS junction. The TiO$_2$-*meso* structure was achieved by using 68 h of UV curing to remove the binder, followed by N$_2$ annealing at 350 °C to improve the TiO$_2$ particle interconnectivity. TiCl$_4$ treatment was also explored, however it was found to hinder the PEC activity. The resultant UV cured-N$_2$ annealed (350 °C) films exhibited similar electrochemical properties than the typical slot coated air annealed films. The final Sb$_2$Se$_3$/CdS/TiO$_2$(S-100nm)/TiO$_2$-*meso*/**NiP** gave rise to −1.3 mA cm^{-2} at 0 V *vs* RHE with a catalyst loading of 45.76 ± 0.81 nmol cm^{-2}. This device represented the highest photocurrent reported using the **NiP** molecular catalyst. However, it was found that the Sb$_2$Se$_3$/CdS/TiO$_2$-*meso*/**NiP** deactivates faster than previous reports due to the mismatch between photoelectron generation at the Sb$_2$Se$_3$ and consumption at the **NiP** catalyst associated with lower turn-over frequencies achievable than Pt, when used as a benchmark HER catalyst.

The onset potential at 0.5 V *vs* RHE for the benchmark photocathode Sb$_2$Se$_3$/CdS/TiO$_2$(S-100nm)/TiO$_2$-*meso*/Pt suggested improved charge transfer across the device after the TiO$_2$-*meso* addition. A transient photocurrent (TPC) study was subsequently carried out and results suggested that back recombination in the millisecond scale occured at low applied bias (0.4 V *vs* RHE) without the TiO$_2$-*meso* structure. The slow recombination could be removed by increasing the bias to 0.06V *vs* RHE. Notably, the TiO$_2$(-*meso*)/HER catalyst structure (either Pt or **NiP**) did not show any evidence of back-hole transfer even at low applied bias (0.4 V *vs* RHE) rationalising the shift in onset potential, indicating that the TiO$_2$-*meso* can act as an electron reservoir.

The Sb$_2$Se$_3$ based photocathodes studied in this chapter were made in collaboration with Dr Jon Major's group (Dr Thomas Shalvey) from the Stephenson Institute for Renewable Energy at University of Liverpool. The **NiP** molecular catalyst was kindly provided by Professor Erwin Reisner's group (Dr. Carla Casadevall and Dr. Daniel Antón-García) from the Yusuf Hamied Department of Chemistry at University of Cambridge. Text and figures in this chapter are in part based on ***Chem. Commun.***, 2023,**59**, 944-947, which I am the primary author of.

3.1 Introduction

As pointed out in the previous chapter, Sb$_2$Se$_3$ has recently gained interest from the photovoltaic (PV) community due to its unique properties such as (i) near-direct band gap of 1.18 eV, (ii) a high absorption coefficient across the visible region,[1] and (iii) an unusual 1D nanoribbon structure that enables effective charge transport.[2] These properties, combined with improvements in material processability and the use of earth-abundant elements, have led to the suggestion that Sb$_2$Se$_3$ could be a viable thin film PV material for use on a global scale.[3]

Sb$_2$Se$_3$ has also been studied as a photocathode for HER, the CBM at -0.5 V *vs* RHE provides enough driving force for producing H$_2$,[4] and its band gap (E_g) is close to the optimal calculated for the bottom electrode in dual absorber standalone device for water splitting.[5] Reported solar to hydrogen efficiencies have now exceeded 10% with state-of-the-art Sb$_2$Se$_3$ photocathode.[6,7] With these photocathodes a Sb$_2$Se$_3$/CdS buried junction is coated in a protective TiO$_2$ capping layer. The planar TiO$_2$ is then modified with a HER catalyst like Pt,[8,9] RuO$_2$,[7,10] and MoS$_x$.[11] Notably, even with state-of-the-art devices (Table 5), reductive dissolution of TiO$_2$ is caused by photoelectron accumulation.[6,8] C$_{60}$ between TiO$_2$ and the H$_2$ catalyst can alleviate charge accumulation promoting the photoelectron transfer at the TiO$_2$/Pt interface, but device stabilities are still low.[6,8]

Earth abundant molecular electrocatalysts have not previously been explored on Sb$_2$Se$_3$ photocathodes, even though they are an alternative to precious metal electrocatalysts and could potentially offer improved rates of charge transfer at the semiconductor/molecular catalyst interface.[12,13] Among the several strategies to immobilize molecular catalysts on the surface of semiconductors, covalent linkage provides the strongest interaction through a chemical bond, which determines the catalyst orientation and could improve the charge transfer at the semiconductor/molecular catalyst interface.[14,15]

In this chapter, **NiP** with a [Ni(P$_2^{R'}$N$_2^{R''}$)$_2$]$^{2+}$ core (P$_2^{R'}$N$_2^{R''}$ = bis(1,5-R'-diphospha-3,7-R''-diazacyclooctane), shown in Figure 49b was chosen as model molecular catalyst since it ranks among the most active precious metal free catalyst for H$_2$ production.[16] The **NiP** bio-inspired catalyst mimics the hydrogenase intramolecular proton transfer to the Ni centre through the pendant amine groups in

the second coordination sphere.[17] Furthermore, it has been modified by phosphonic acid groups in the outer coordination sphere to be covalently anchored to TiO_2.[18] The planar hybrid photocathode $FTO/Au/Sb_2Se_3/CdS/TiO_2$(S-100nm)/**NiP** is shown in Figure 49a.
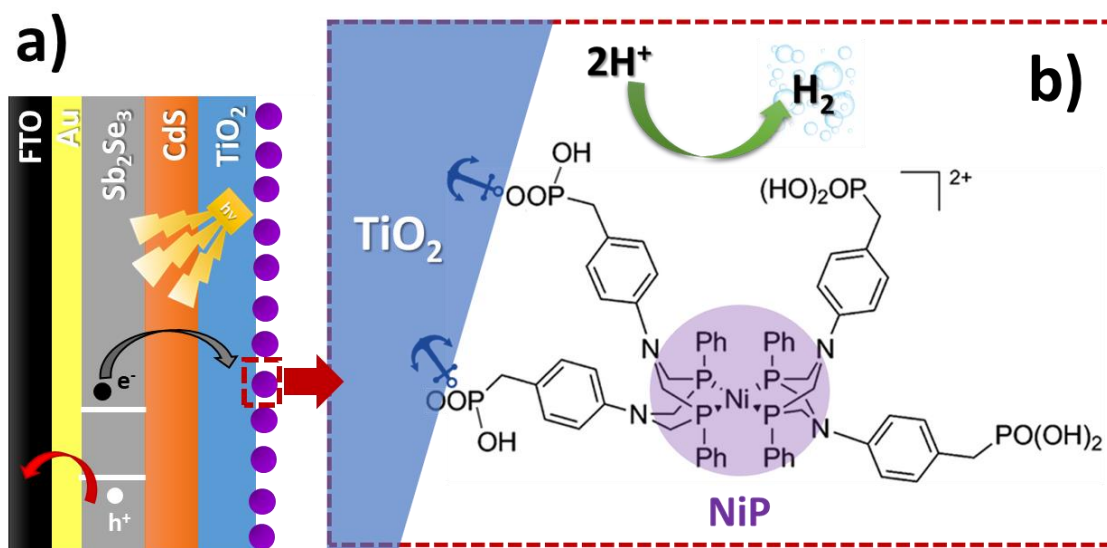

Figure 49 *(a) Schematic diagram of $Sb_2Se_3/CdS/TiO_2$(S-100nm)/**NiP** hybrid photocathode (b) chemical structure of **NiP** catalyst.[18] Note that panel a and b are not drawn to scale.*

Briefly, the photocathode was deposited on previously cleaned FTO, followed by 70 nm thick Au made by thermal evaporation. Sb_2Se_3 (1.5 μm) was deposited by two-step fast-cooling close space sublimation process, which generates a compact preferentially orientated nanoribbon crystal structure that facilitates rapid hole transfer to the Au contact.[2,6,7] Then, a thin sputtered CdS buffer layer (20 nm) was added, which forms a Sb_2Se_3 heterojunction with a negligible conduction band offset, thereby allowing efficient charge separation and electron transfer towards the TiO_2.[1] By adding a CdS buffer layer, the onset potential and fill factor of the Sb_2Se_3 photocathodes are significantly improved despite the parasitic absorption of photons below $\lambda < 500$ nm in the CdS, which decrease the photocurrent (the Sb_2Se_3/CdS junction was discussed in detail in section 2.2.2.2, as well as the equilibria band alignment shown in Figure 47, Chapter 2).[6,7] After, a 100 nm capping TiO_2 layer was sputtered to provide a physical barrier preventing contact between the light absorber and the electrolyte.[19] Note that all the Sb_2Se_3 devices presented in this chapter have the architecture previously described. The detailed experimental conditions for each deposition layer can be found in section 6.1.2.

Prior to **NiP** immobilization onto the sputtered TiO₂ at the top of Sb₂Se₃/CdS, the samples were UV-cleaned using a 365 nm UV LED (2.9 W, 2.2 mm x 2.2 mm) for 4 h, since the wettability of the film improved (from 44.65° to 11.07° measured in the contact angle analysis, shown in section 6.2.1). Then the molecular catalyst was immobilized by soaking the photoelectrode in dry methanol (0.5 mM **NiP)** overnight at room temperature in a dark flask.[16,20,21] After the overnight immobilization, the sample was thoroughly washed in dry methanol to remove the non-chemisorbed catalyst and dried under vacuum for 2 h at 60 °C, and from now on this device was labelled as Sb₂Se₃/CdS/TiO₂(S-100nm)/**NiP**, note that FTO/Au were omitted for clarity.

NiP loadings were determined by stripping the catalyst off in 0.1 M NaOH and quantified by UV-Vis spectroscopy. Figure 50a shows the **NiP** UV-vis spectra at different concentrations: 50, 30, 10, 5, 1 μM in 0.1 M NaOH, and the calibration curve used for the catalyst quantification considering the maximum absorbance peak at 254.8 nm (Figure 50b). In this way, the **NiP** loading on Sb₂Se₃/CdS/TiO₂/**NiP** was 7.08 ± 0.43 nmol cm⁻². Full details of the synthetic procedures for **NiP** immobilization and stripping are provided in Section 6.2.1.
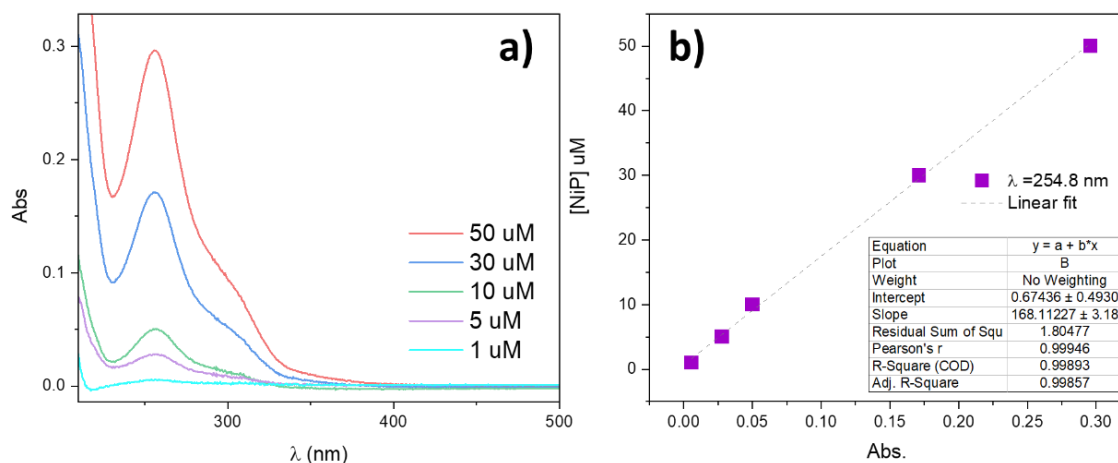

Figure 50 *UV-vis spectra of different **NiP** concentrations using a 2 mm path length cuvette, and (b) **NiP** the calibration curve in 0.1 M NaOH at λ = 254 nm.*

The the pH of the electrolyte for photoelectrochemical studies was selected based on a literature survey. It was reported that the **NiP** maximum catalytic turnover frequency occurs at pH 3 when used as a

homogeneous catalyst in solution.[18] After immobilised on TiO_2, pH 2, 3 and 4 were also studied and the highest activity was found at pH 3, furthermore stable electrocatalysis for 8 hours was achieved at this pH. At lower (2) and higher (4) pHs, the rate of hydrogen production decreased by > 50%, as well as the Faradic Efficiency.[22]

Figure 51 shows the chopped light LSV of $Sb_2Se_3/CdS/TiO_2/$**NiP** in 0.1 M Na_2SO_4 at pH 3, and all the photoelectrochemical tests were done at 100 mW cm^{-2} illumination (unless otherwise stated) and with $\lambda > 340$ nm. The $Sb_2Se_3/CdS/TiO_2/$**NiP** exhibited a photocurrent of only -16 µA cm^{-2} at 0 V *vs* RHE, which exceeds only slightly the current in the absence of any catalyst (-3 µA cm^{-2} for $Sb_2Se_3/CdS/TiO_2$). The spikes in the light chopped LSV demonstrated that the photoelectrons are not being utilised at a fast-enough rate by the catalyst, instead recombination is dominating.[23] The low photocurrent of the $Sb_2Se_3/CdS/TiO_2/$**NiP** electrode was attributed to the low loading of **NiP** compared with previous devices.[20,21] Table 7 contains the **NiP** loading on previously reported photocathodes.
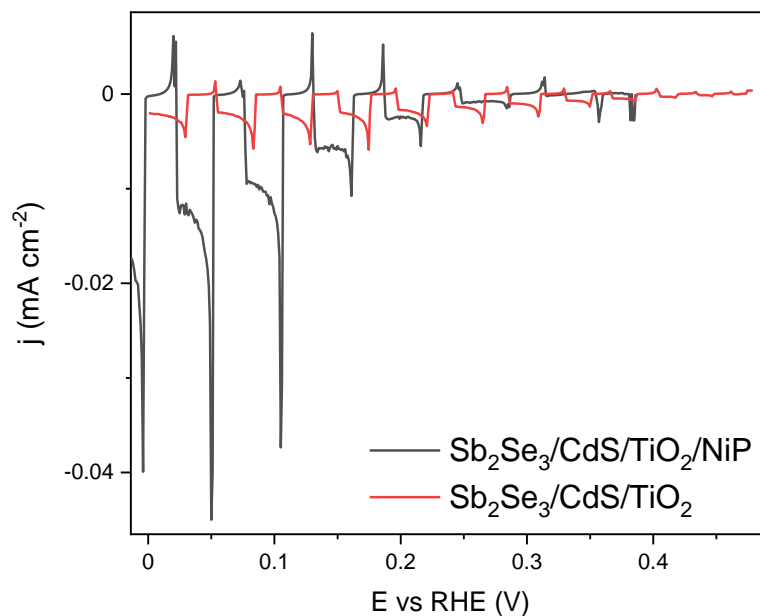

Figure 51 *Chopped light LSV of $Sb_2Se_3/CdS/TiO_2$ and $Sb_2Se_3/CdS/TiO_2/NiP$ in 0.1 M Na_2SO_4 pH 3 under N_2 at 10 mV s^{-1} at 100 mW cm^{-2} and $\lambda > 340nm$.*

Table 7. *Hybrid photocathodes for H_2 production using **NiP** as molecular catalyst.*

Photocathode	[NiP] nmol cm^{-2}	−j (mA cm^{-2}) @ 0 V *vs* RHE	Stability (%) t (h)	Electrolyte	Light source	Ref.
p-Si/TiO$_2$/**NiP**	38.3±4.2	0.35	28% 24	0.1 M Acetic Acid pH 4.5	AM 1.5G, 100 mW cm^{-2} λ> 400 nm	21
Au/LTCA/TiO$_2$/**NiP** LTCA: La$_5$Ti$_2$Cu$_{0.9}$Ag$_{0.1}$S$_5$O$_7$	33.7±2.4	0.5	8% 6	0.1 M Na$_2$SO$_4$ pH 3	AM 1.5G, 100 mW cm^{-2}	20
*FTO/TiO$_2$/**NiP**	14.6±2	0.2	25% 8	0.1 M Na$_2$SO$_4$ pH 3	*	22

*This study did not used a light absorber, instead a potential of -0.25 V *vs* RHE was applied.

Table 7 also compares the stability of the HER hybrid photocathodes, which was defined as the photocurrent measured at the beginning of the controlled potential photoelectrode CPP (J_0 @ $t = 0$) against the photocurrent measured at certain time (J @ t (h)) at 0 V *vs* RHE, according to equation 2.

A common approach to achieve higher catalyst loadings on a photoelectrode is to increase the available surface area for catalyst binding through a mesoporous TiO$_2$ scaffold (labelled TiO$_2$-*meso* from now on). Here, the mesoporous TiO$_2$ experimental protocol was tailored to meet the Sb$_2$Se$_3$/CdS interface thermal stability.

3.2 Mesoporous TiO$_2$

3.2.1 Developing TiO$_2$-*meso* on FTO

Typically, following the TiO$_2$ nanoparticle-organic binder paste deposition, a thermal annealing is carried out in air (~450 °C) to remove the binder and sinter the TiO$_2$ nanoparticles forming conductive pathways.[23] Sb$_2$Se$_3$ is unstable at these temperatures in air,[3] therefore the UV curing approach to include a TiO$_2$-*meso* onto CuO$_2$/AZO/TiO$_2$ photocathodes, successfully developed by the Grätzel group was modified here.[24]

3.2.2.1 UV-curing

To simplify the process, the mesoporous TiO$_2$ films were first optimised on FTO without the underlying Sb$_2$Se$_3$/CdS/TiO$_2$-*sputtered* structure, and labelled as TiO$_2$-*meso*, note that FTO was not included in the naming structure for clarity. Following the slot-coating of an anatase TiO$_2$ paste (Greatcell Solar® 18NR-T Titania Paste *av*. particle size 20 nm diameter) with scotch tape as template on FTO to control the thicknesses of the TiO$_2$-*meso*, the sample was UV cured using a 365 nm LED (LZ4-04UV00/ LED Engin, see section 6.1.2.3 for fully described experimental details). Figure 52a shows the picture of a sample with an UV-cured region (1), and region (2) which was not exposed to the LED, and a clear difference in colour was observed after 68 h.
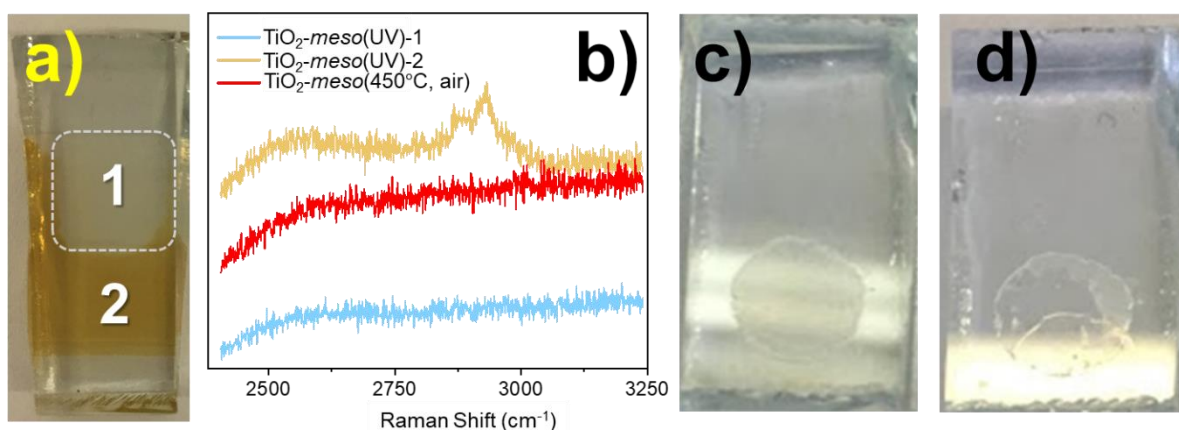

Figure 52 *(a) TiO$_2$-meso(UV) film. Region (1) was UV-cured for 68 hrs. Region (2) was not UV cured. (b) Raman spectra of region 1 (blue trace) and 2 (yellow trace) from panel (a), and TiO$_2$-meso(450°C, air shown as red trace) is also included as a control. TiO$_2$-meso(UV) (c) before and (d) after being immersed in 0.1 M Na$_2$SO$_4$ pH 3.*

To compare physico-chemical properties of the UV cured TiO$_2$-*meso* films *vs* those prepared by the conventional thermal method, the TiO$_2$ paste was slot-coated on clean FTO in the same manner previously described, then air annealed at 450 °C for 1 h instead of the UV-curing. The thickness of the film was *ca.* 5 μm measured by profilometry. The resulting samples were labelled as TiO$_2$-*meso*(450°C, air), and used as a control/benchmark due to their stability and electrochemical properties for a molecular catalyst scaffold.[23]

Commercial TiO$_2$ paste contains α-terpineol as binder, and its C-H stretching modes can be readily identified by Raman Spectroscopy. Without the UV-curing (yellow area, and Raman spectra labelled as TiO$_2$-meso(UV)-2 in Figure 52a), the sample exhibits the peaks at 2870 and 2910 cm^{-1} related to the binder, meanwhile the transparent zone (TiO$_2$-*meso*(UV)-1) lacks of the α-terpineol Raman features,[25] similar to the control sample TiO$_2$-*meso*(450 °C, air) shown in Figure 52b.

Even though the binder was successfully removed after the UV-curing, the TiO$_2$-*meso* adhesion on FTO was poor. The TiO$_2$-*meso*(UV) films delaminated following the immersion in 0.1 M Na$_2$SO$_4$ pH 3 (after *ca.* 20 min), preventing any further electrochemical study (Figure 52c and Figure 52d). Therefore, different treatments and deposition approaches were explored to address the poor mechanical stability of TiO$_2$-*meso*(UV) films, and to also assess if the electrochemical properties could be enhanced.

3.2.2.2 TiCl$_4$ treatment

Initially, a TiCl$_4$ treatment was carried out to improve the nanoparticle interconnectivity where smaller TiO$_2$ particles are formed after the Ti precursor hydrolysis, shown as yellow circles in Figure 53a. Following 68 h of UV-curing, the samples were soaked in 40 mM TiCl$_4$ at 70 °C for 20 min however, the films still delaminated during treatment. Then the TiO$_2$ paste amount was reduced by using a glass rod for the doctor-blading without the scotch tape as template, while the UV curing time was kept constant (68 h). These films were labelled as TiO$_2$-*meso*(UV, TiCl$_4$) and the cyclic voltammetry in 0.1 M Na$_2$SO$_4$ pH 3 before and after the TiCl$_4$ is shown in Figure 53b. Note that even before the TiCl$_4$ treatment, a thinner TiO$_2$-*meso* (<2 μm determined by profilometry) did not delaminate after the electrochemistry analysis, suggesting that the mechanical stability of TiO$_2$-*meso* improved either from the reduced thicknesses and/or the TiCl$_4$ treatment afterwards. It is important to point out that *ca.* 5 μm TiO$_2$-*meso* thick is required to achieve higher **NiP** loadings and consequently a more active PEC device.[21] In the next section 3.3.2, the results of TiO$_2$-*meso*(UV, TiCl$_4$) films when assessed as scaffold

for catalyst immobilization will be presented, however the **NiP** loading and electrochemical activity was significantly lower than previous reports summarised in Table 7.
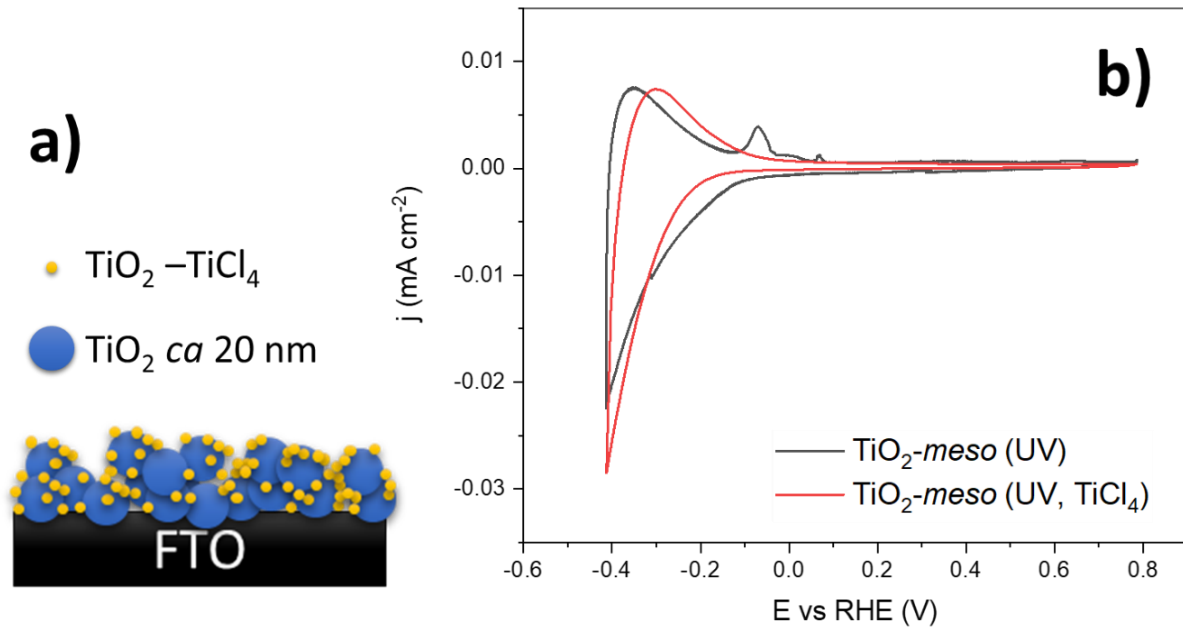

Figure 53 *(a) Scheme of FTO-TiO$_2$-meso(UV, TiCl$_4$) not drown at scale. (b) Cyclic voltammetry of TiO$_2$-meso(UV) before and after the TiCl$_4$ treatment (red trace) at 20 mV s^{-1} in 0.1 M Na$_2$SO$_4$ pH 3, under N$_2$.*

Consecutive TiO$_2$-*meso* (<2 μm) layers followed by the TiCl$_4$ treatment were also considered, however even if the film thickness was successfully increased, a decrease in the surface area was hypothesized since the smaller particles formed during the TiCl$_4$ treatment could block the pores. Furthermore, it was also found that the TiCl$_4$ treatment compromised the PEC activity of the Sb$_2$Se$_3$-based photocathodes (Sb$_2$Se$_3$/CdS/TiO$_2$-S(100 nm)/TiO$_2$-*meso*/Pt) due to lower photoelectron generation after the TiCl$_4$ treatment, as will be discussed below in section 3.3.3.

3.2.2.3 N$_2$ annealing

Finally, it was found that N$_2$ annealing at 350 °C for 60 min aided TiO$_2$ interconnectivity and substrate adhesion. The samples were made by slot-coating titania paste using scotch tape as template, and labelled as TiO$_2$-*meso*(UV, N$_2$). Following the 68 h UV curing, the samples underwent an annealing process under constant N$_2$ flow. Figure 54 compares the (a) cyclic voltammetry and (b-d) Electrochemical Impedance Spectroscopy (EIS) spectra of TiO$_2$-*meso* after N$_2$ annealing (TiO$_2$-*meso*(UV, N$_2$)) *vs* the control sample TiO$_2$-*meso*(450°C, air) in 0.1 M Na$_2$SO$_4$ pH 3 under N$_2$. The N$_2$ annealing indeed aided the TiO$_2$ particle adhesion, the films did not delaminate after the electrochemical analysis. The current density of TiO$_2$-*meso*(UV, N$_2$) shown in Figure 54 was significantly increased compared with TiO$_2$-*meso* (UV, TiCl$_4$) of Figure 53, being −1 and −0.027 mA cm^{-2}, respectively at −0.4 V *vs* RHE.

The electrochemical properties of the different ways of making TiO$_2$-*meso* films were further investigated by EIS (Figure 54c-d). Note that the potentials were selected at three different regions: at 0 V *vs* RHE where the capacitive current dominates, −0.42 V *vs* RHE where the HER takes place, and at potential between these two processes (−0.25 V *vs* RHE). Figure 54b only compares the EIS spectra at 0 V *vs* RHE and from this figure, it is evident that the TiO$_2$-*meso*(UV, N$_2$) and TiO$_2$-*meso*(450°C, air)) samples were different. The equivalent circuit shown in Figure 54e was used to determine the resistance of TiO$_2$-*meso* films and magnitude of all the electrical components are indicated in Table 8. A $\mathbf{R_S} + \mathbf{R_{TiO_2}}/\mathbf{C_{TiO_2}} + \mathbf{R_{CT}}/\mathbf{CPE_{CT}}$ circuit was selected since the applied potential did not modify the $\mathbf{R_{TiO_2}}/\mathbf{C_{TiO_2}}$ semicircle in the Nyquist plot, meanwhile $\mathbf{R_{CT}}/\mathbf{CPE_{CT}}$ component was affected by the potential indicative of charge transfer. Note that the error in the fitting of the second RC element was higher, however the α of the CFE$_{CT}$ decreases from 1 to lower values (*ca.* 0.5) in both films suggesting it passed from almost an ideal capacitor to a Warburg element, which could be related to H$^+$ diffusion in the TiO$_2$-*meso* during H$_2$ production at more negative potentials. The frequency range for the EIS analysis was from 1 MHz to 0.1 Hz and lower frequencies could provide more information to analyse in depth the $\mathbf{R_{CT}}/\mathbf{CPE_{CT}}$ component.
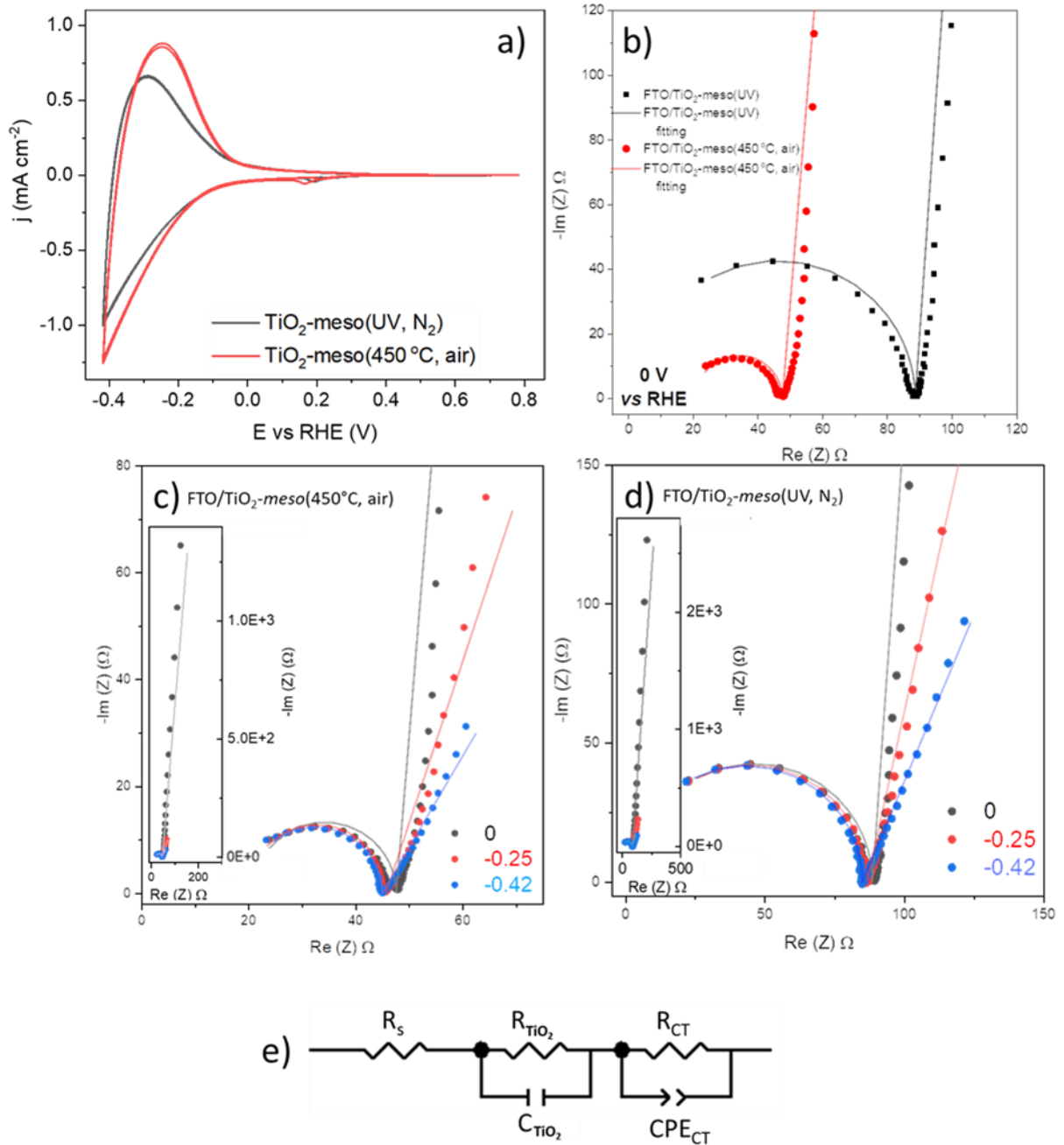
Figure 54 *Comparison of the electrochemical properties of TiO$_2$-meso: (a) Cyclic voltammetry at 100 mV s^{-1} and (b) EIS spectra at 0 V vs RHE of the films made by UV curing followed by N$_2$ annealing at 350 °C (TiO$_2$-meso (UV, N$_2$), black trace) and the control sample annealed at 450 °C in air (TiO$_2$-meso(450°C, air) red trace). (c) and (d) present the EIS spectra collected at different potentials: 0, -0.25 and -0.42 V vs RHE of TiO$_2$-meso(450°C, air) and TiO$_2$-meso (UV, N$_2$), respectively. For the EIS analysis, the experimental data is represented with dots, and the equivalent circuit shown panel (e) was used for modelling and shown as continuous lines. Electrolyte: 0.1M Na$_2$SO$_4$ pH 3, under N$_2$.*

Finally, the EIS analysis provides information regarding to the resistance of the TiO₂-*meso* under operating conditions, and it was found higher for the film made by UV curing than by the traditional air annealing process, 84.34 ± 0.63 and 26.38 ± 0.45 Ω respectively.

Table 8 *Parameters of the electrical components in the equivalent circuit shown in Figure 54e used for modelling the EIS spectra of TiO₂-meso in 0.1M Na₂SO₄ pH 3, under N₂.*

	TiO₂-*meso* (450°C, air)			**TiO₂-*meso* (UV, N₂)**		
E (V) RHE	0	−0.2	−0.4	0	−0.2	−0.4
−j (mA cm⁻²)	0.04	0.44	1.25	0.04	0.37	1.22
R_S (Ω)	20.89	19.90	19.98	3.44	2.48	1.30
R_{TiO_2} (Ω)	26.70	25.75	26.70	85.19	84.17	83.67
C_{TiO_2} (nF)	6.18	5.84	17.46	1.80	1.78	1.76
R_{CT} (Ω)	5.95×10^{19}	2.22×10^{27}	3.69×10^{27}	8.49×10^{10}	2.03×10^{29}	1.51×10^{41}
CPE_{CT} (F.s$^{\alpha-1}$)	1.20×10^{-3}	0.02	0.04	6.07×10^{-4}	6.33×10^{-3}	0.01
α	0.94	0.80	0.66	0.96	0.86	0.75

Note that there is trade-off between TiO₂-*meso* particle interconnectivity and the stability of the Sb₂Se₃/CdS interface, however the PEC activity after the N₂ annealing at 350 °C was confirmed, and the results will be shown in Section 3.3.3.

To keep the process of making TiO₂-*meso* films simple, the N₂ annealing without prior UV-curing was explored as alternative. The samples were labelled as TiO₂-*meso*(N₂, X°C), where X indicate the annealing temperatures at 234, 350 and 450 °C in N₂. In Figure 55a, the pictures of those samples are shown, while panel (b) presents the UV-Vis spectra. The N₂ annealed samples at 234, 350 °C went black probably due to the α-terpineol incomplete combustion (at 425 °C).[26] Note that not only the colour was not appropriate for the TiO₂ scaffold, also the mechanical properties were compromised since the TiO₂-*meso*(N₂, 234 and 350°C) delaminated during the overnight soaking in methanol required for the **NiP** immobilization. The film adhesion and

transparency were improved only after increasing the temperature upon 450 °C in the N_2. However, at this temperature the stability of the light absorber is compromised.[27]
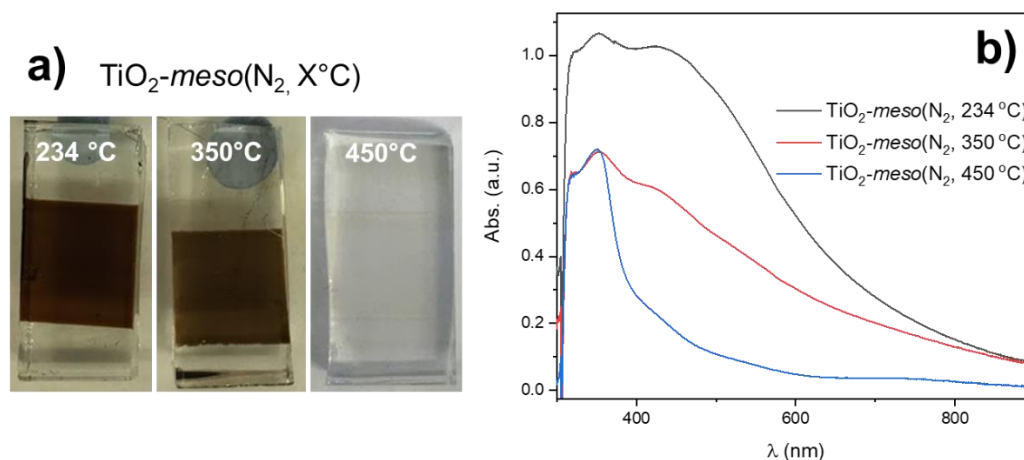

Figure 55 *(a) TiO₂-meso after N₂ annealing at different temperatures 234, 350 and 450 °C for 1 h, (b) UV-Vis spectra of those samples, without prior UV curing.*

It was then concluded that both UV curing and N_2 annealing were required to produce *ca.* 5 μm thick TiO₂-*meso* scaffold with similar electrochemical properties to the air annealed films. The UV-curing was essential for the binder combustion through a photocatalytic reaction for 68 h, while the N_2 annealing enhanced the particle interconnectivity thus the TiO₂-*meso* adhesion to the substrate.

3.3.2 NiP immobilization on FTO/TiO₂

Once the experimental protocol for stable TiO₂-*meso* films in aqueous electrolytes was successfully developed avoiding temperatures > 350ºC, then the electrochemical activity of those samples when used as a **NiP** scaffold was benchmarked *vs* the control TiO₂-*meso*(450ºC, air).

NiP was immobilised on UV-cured TiO₂-*meso* films and the control TiO₂-*meso*(450°C, air) using the experimental protocol previously described (overnight soaking in 0.5 mM **NiP** in dry methanol), resulting in the reddish films shown in the insert of Figure 56. The CVs at 100 mV s⁻¹ before and after the **NiP** immobilization on TiO₂-*meso*(UV, N₂-350 °C) in 0.1 M Na₂SO₄ pH 3 are presented in Figure 56. The bare TiO₂-*meso* scaffold displays the "trumpet shape" typically associated to the filling and

emptying of the TiO$_2$ CB. After the **NiP** immobilization, the oxidation current significantly diminishes indicating effective electron consumption by the molecular catalyst to produce H$_2$. The cathodic to anodic charge ratio was 16, in line with the electron consumption rate previously reported on air annealed TiO$_2$-*meso* films at the same scan rate.[22]

By spectroelectrochemical measurements, it was previously found that **NiP** catalyst can consume electrons from the TiO$_2$-*meso* films at −0.43 V *vs* RHE by bleaching the typical Ti^{3+} states (absorption at 800 nm) produced when the electrons are not extracted effectively. However, it only requires modest overpotentials −0.25 V *vs* RHE for H$_2$ production.[22] Therefore, the CPP was carried out at this potential and the results are presented in Figure 57. The electrochemical activity of TiO$_2$-*meso*(UV, 350°C N$_2$)/**NiP** and TiO$_2$-*meso*(450°C, air)/**NiP** was similar with slightly lower current for the sample made by UV curing, presumably due to the higher film resistance (87.2 Ω for the UV cured and 35 Ω for the air annealed sample), considering the comparable catalyst loading shown in Table 9. Figure 57 also highlighted the **NiP** catalytic activity since a negligible current of 1.5 μA cm^{-2} was recorded at -0.25 V *vs* RHE without the catalyst (TiO$_2$-*meso* (450°C, air)).
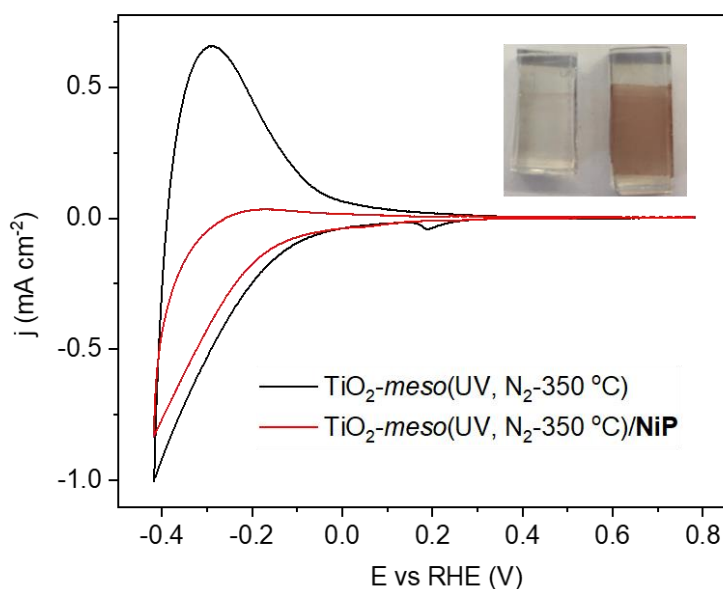

Figure 56 *Cyclic voltammetry before (black trace) and after **NiP** immobilization (red trace) on TiO$_2$-meso(UV, N$_2$-350 °C), under Ar.*

The **NiP** activity was also explored on a N$_2$ annealed film at lower temperature and the results shown in Figure 57. TiO$_2$-*meso*(UV N$_2$-250°C)/**NiP** exhibited slightly lower dark current compared with the sample annealed at 350 °C, being 130 and 190 µA cm^{-2}, respectively. However, the film delaminated after the CA test, likely because 250 °C was not high enough to sinter the TiO$_2$ nanoparticles in the mesoporous layer.

Table 9 NiP molecular catalyst loading on FTO/TiO$_2$-*meso*

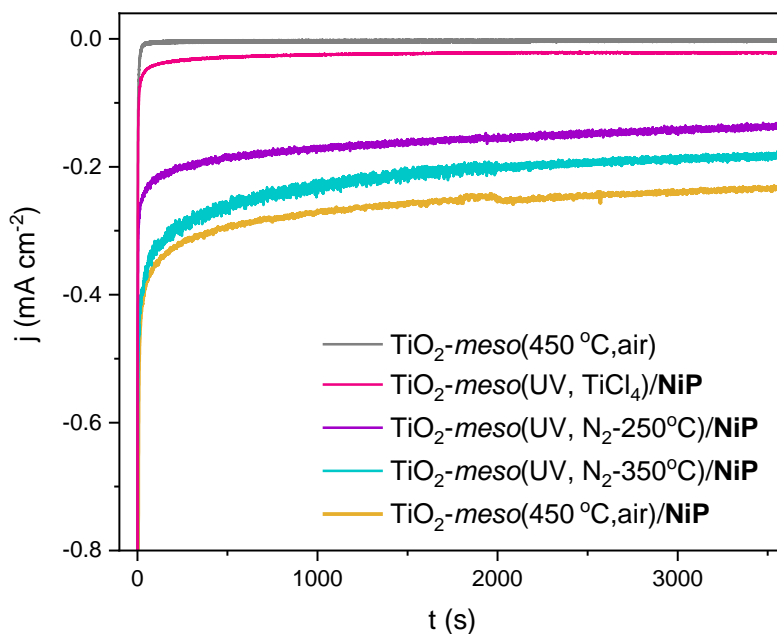| Electrode	NiP [nmol cm^{-2}]
TiO$_2$-*meso* (UV, 350°C N$_2$)	37.36 ± 9.03
TiO$_2$-*meso* (450°C, air)	39.04 ± 8.36
TiO$_2$-*meso* (UV, TiCl$_4$)	23.40 ± 1.67

Figure 57 *Chronoamperometry test at -0.25 V vs RHE of TiO$_2$-meso/NiP with the TiO$_2$-meso made by air annealing (TiO$_2$-meso(450°C, air)/NiP), or UV cured followed by either N$_2$ annealing at 250 and 350 °C (TiO$_2$-meso(UV, 250°C-N$_2$) and TiO$_2$-meso(UV, 350°C-N$_2$), respectively) or TiCl$_4$ treatment (TiO$_2$-meso(UV, TiCl$_4$)/NiP) in 0.1 M Na$_2$SO$_4$ pH 3, under Ar.*

It was demonstrated previously that thinner TiO_2-*meso* films (> 2 μm) followed by a $TiCl_4$ treatment led to stable mesoporous TiO_2 scaffolds. The **NiP** catalytic activity anchored to these samples was also studied and shown in Figure 57. The sample labelled as TiO_2-*meso*(UV, $TiCl_4$)/**NiP** displayed the lowest current density of 21.3 μA cm^{-2} at −0.25 V *vs* RHE after **NiP** immobilisation, likely due to the low catalyst content 23.40 ± 1.67 nmol cm^{-2}, compared to the UV cured TiO_2-*meso* films that underwent N_2 annealing (Table 9). Consequently, the UV cured-$TiCl_4$ protocol was not suitable for achieving a high surface area scaffold for **NiP** catalysts binding.

3.3.3. PEC activity of Sb₂Se₃/CdS interface after adding TiO₂-*meso*

In the previous section, it was found that a N_2 annealing treatment at 350 °C was required to develop a suitable TiO_2-*meso* scaffold for **NiP** immobilization. However, it has been reported previously that the interdiffusion at the Sb_2Se_3/CdS interface hinders light absorption in solar cells following thermal annealing.[1,27,28]

To assess the PEC activity of Sb_2Se_3/CdS interface after the N_2 annealing, Pt was used as benchmark catalyst for H_2 production (note that N_2 annealing was carried out before Pt photoelectrodeposition, the experimental protocol is fully described in section 6.2.5). Figure 58 shows the light chopped LSV of Sb_2Se_3/CdS/TiO_2(S-100nm)/Pt samples annealed at 250 and 350 °C under N_2 and the control without the thermal treatment at 10 mV s^{-1} in 0.1 M H_2SO_4, 100 mW cm^{-2} and $\lambda > 340$ nm. It was found that the photocurrent increased following the N_2 annealing. However, the device annealed at 350 °C exhibited lower photocurrent (−5.7 mA cm^{-2}) in comparison to 250 °C (−11.43 mA cm^{-2}) at 0 V *vs* RHE. The decrease in photocurrent could be related to interdiffusion at the Sb_2Se_3/CdS interface observed by EDX cross sectional mapping and STEM bright-field images, which in extreme cases created the interfacial voids and lower the current density when a similar architecture but in a superstrate configuration (FTO/ZnO/CdS/Sb_2Se_3/Au) was studied.[27] Another possible issue related to the high temperature annealing of the Sb_2Se_3/CdS interface is the formation of CdSe at the interface, ($E_g = 1.74$

eV), where 712 eV photons no longer contribute to the photocurrent and consequently the photocurrent decreased.[28]

Even though the highest PEC activity was observed at 250 °C, it was shown previously that this temperature was not high enough to sinter the TiO_2 nanoparticles in the mesoporous layer, since TiO_2-*meso*(UV N₂-250°C)/**NiP** films delaminated after the CA test carried out at −0.25 V *vs* RHE in 0.1 M Na₂SO₄ pH 3 for 1 h (see Figure 57). Therefore 350 ºC was chosen as the sintering temperature of TiO_2-*meso* even with the possible interdiffusion at the Sb_2Se_3/CdS interface.
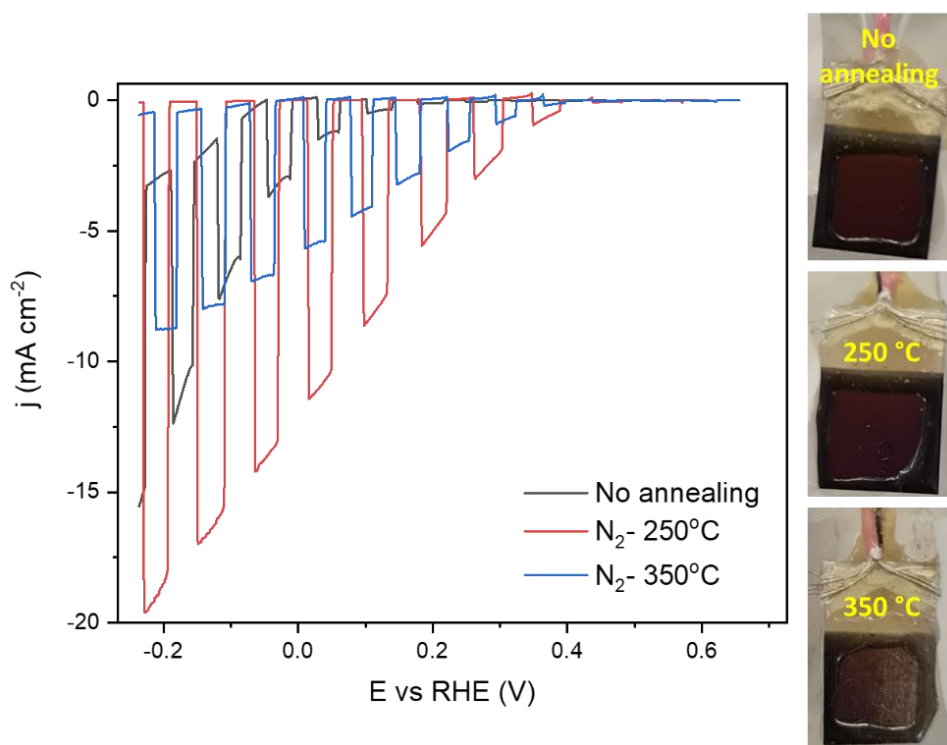

Figure 58 *Light chopped LSV at 10 mV s⁻¹ of Sb₂Se₃/CdS/TiO₂(S-100nm)/Pt with N₂ annealing at 250 and 350 °C for 1 h and a control without thermal treatment in 0.1 M H₂SO₄ under N₂ at 100 mW cm⁻² and λ > 340 nm.*

The increase in photocurrent recorded after the N₂ annealing and using Pt as HER catalyst observed in Figure 58 was likely attributed to the improvement in crystallinity of the RF magnetron sputtered TiO_2 layer shown in Figure 59. By Raman analysis, the TiO_2 peaks associated to the anatase phase were identified at 144, 195, 393, 517 and 638 cm⁻¹ on the sputtered TiO_2 on FTO and the complete device

Sb$_2$Se$_3$/CdS/TiO$_2$(S-100nm), shown in panel a and b respectively.[19,29] Another possible contribution of the enhanced PEC activity could be related to the promotion of a void free Sb$_2$Se$_3$/CdS interface after a mild annealing treatment at 280 °C, reported previously by Liang and collaborators.[30]
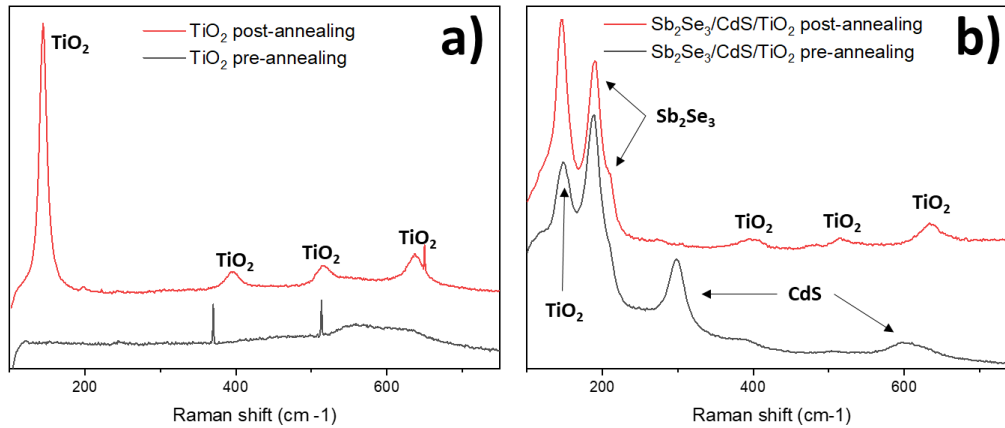

Figure 59 *Raman spectra pre (black trace) and post (red trace) N$_2$ annealing at 350 °C of (a) sputtered TiO$_2$ on FTO and (b) Sb$_2$Se$_3$/CdS/TiO$_2$(S-100nm).*

It was found that Sb$_2$Se$_3$/CdS/TiO$_2$(S-20nm) exhibited the highest PEC activity when Pt was used as catalyst, as shown in section 2.2.2.2 in Chapter 2. However, when this architecture underwent all the TiO$_2$-*meso* experimental protocol (UV curing followed by N$_2$ annealing at 350 °C), it was found out that the photocurrent significantly decreased from *ca.* −16 to −8 mA cm^{-2} at 0 V *vs* RHE after the TiO$_2$-*meso* addition in Sb$_2$Se$_3$/CdS/TiO$_2$(S-20nm)/TiO$_2$-*meso*/Pt, as shown on Figure 60a. The loss of activity was attributed to the 20 nm thick sputtered TiO$_2$ layer which probably did not act as an UV filter to protect the CdS layer underneath during the 68 h UV curing process required to remove the binder. A thicker sputtered TiO$_2$ layer was then explored (100 nm) and the chopped light LSV is shown in Figure 60b. Sb$_2$Se$_3$/CdS/TiO$_2$(S-100nm)/Pt exhibited lower photocurrent (*ca.* −8.3 mA cm^{-2} at 0 V *vs* RHE) compared with Sb$_2$Se$_3$/CdS/TiO$_2$(S-20nm)/Pt, likely because the increased resistance generated in a thicker sputtered TiO$_2$ layer. However, after the TiO$_2$-*meso* deposition (sample labelled as Sb$_2$Se$_3$/CdS/TiO$_2$(S-100nm)/TiO$_2$-*meso*/Pt), the photocurrent increased to −13 mA cm^{-2} at 0 V *vs* RHE. Therefore, from now on all the devices presented include a 100 nm sputtered TiO$_2$ layer.
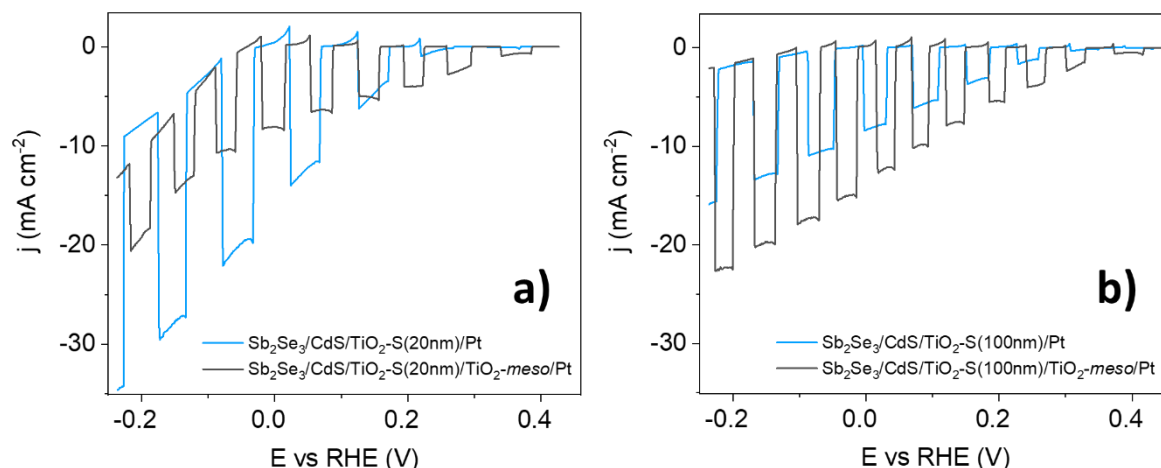
Figure 60 *Light chopped LSV of (a) Sb$_2$Se$_3$/CdS/TiO$_2$-S(20 nm)/TiO$_2$-meso/Pt and (b) Sb$_2$Se$_3$/CdS/TiO$_2$-S(100 nm)/Pt with and without TiO$_2$-meso in 0.1 M H$_2$SO$_4$ under N$_2$ at 100 mW cm^{-2} and λ > 340 nm.*

In an attempt to further improve the PEC activity of Sb$_2$Se$_3$/CdS/TiO$_2$-S(100 nm)/TiO$_2$-*meso* devices (where the TiO$_2$-*meso* was deposited by the UV cured-N$_2$ annealing at 350 °C process), a final TiCl$_4$ treatment was carried out in the same way than previously described (40 mM TiCl$_4$ at 70 °C for 20 min). However, after the sample was platinized (Sb$_2$Se$_3$/CdS/TiO$_2$(S-100nm)/TiO$_2$-*meso*(TiCl$_4$)/Pt), a significant lost in photoelectron generation was observed during the chopped light LSV in 0.1 M H$_2$SO$_4$, as shown in Figure 61. Indicating that a final TiCl$_4$ hindered the light harvesting, which could be associated to the failure of the TiO$_2$(S-100nm) acting as a protective layer during the TiCl$_4$ treatment at 70 °C, suggesting that TiO$_2$ is not fully acting as a protective layer even for 100 nm thick.

In this section it was demonstrated that the experimental protocol developed for adding a TiO$_2$-*meso* (UV-cured followed by N$_2$ annealing at 350 °C) onto Sb$_2$Se$_3$/CdS/TiO$_2$(S-100nm) does not affect the light harvesting capabilities of the device, in fact the PEC activity was enhanced after the N$_2$ annealing and no further TiCl$_4$ was required when Pt was used as catalyst. This structure is labelled as Sb$_2$Se$_3$/CdS/TiO$_2$(S-100nm)/TiO$_2$-*meso* from now on, where the experimental conditions for the TiO$_2$-*meso* are not included for clarity.
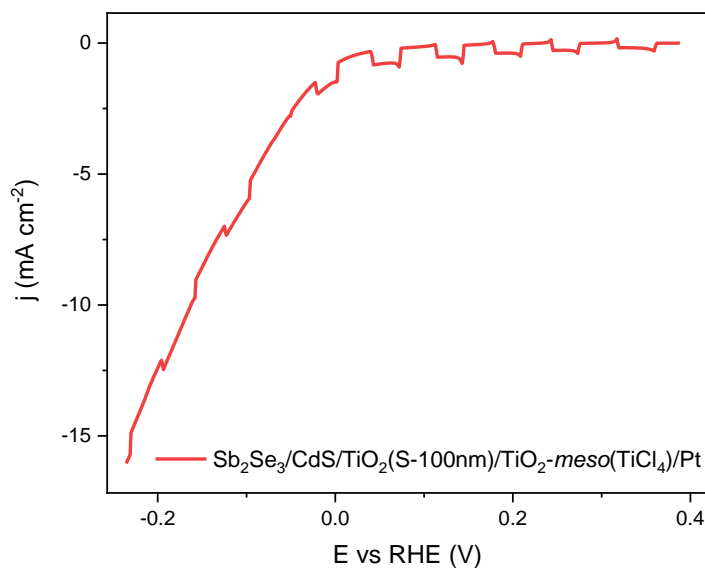
Figure 61 *Light chopped LSV at 10 mV s^{-1} of Sb$_2$Se$_3$/CdS/TiO$_2$(S-100nm)/TiO$_2$-meso(TiCl$_4$)/Pt in 0.1 M H$_2$SO$_4$ under N$_2$ at 100 mW cm^{-2} and λ > 340 nm.*

3.4 Hybrid photocathode for H$_2$ production using Sb$_2$Se$_3$/CdS/TiO$_2$-*meso*/NiP

Optimisation of the alternative synthesis parameters for the TiO$_2$-*meso* on FTO led to a similar electrocatalytic activity of UV-cured TiO$_2$-*meso*/**NiP** compared to previous literature on air-annealed samples.[22] These new milder conditions also demonstrated to have no detrimental light harvesting effects in the PEC activity of Sb$_2$Se$_3$ based photocathodes, allowing the complete hybrid photocathode to finally be assembled. Figure 62 shows the top view SEM images before and after adding TiO$_2$-*meso* in panel (a) and (b) respectively, while panel (c) presents the cross-sectional SEM image of Sb$_2$Se$_3$/CdS/TiO$_2$(S-100nm)/TiO$_2$-*meso*.
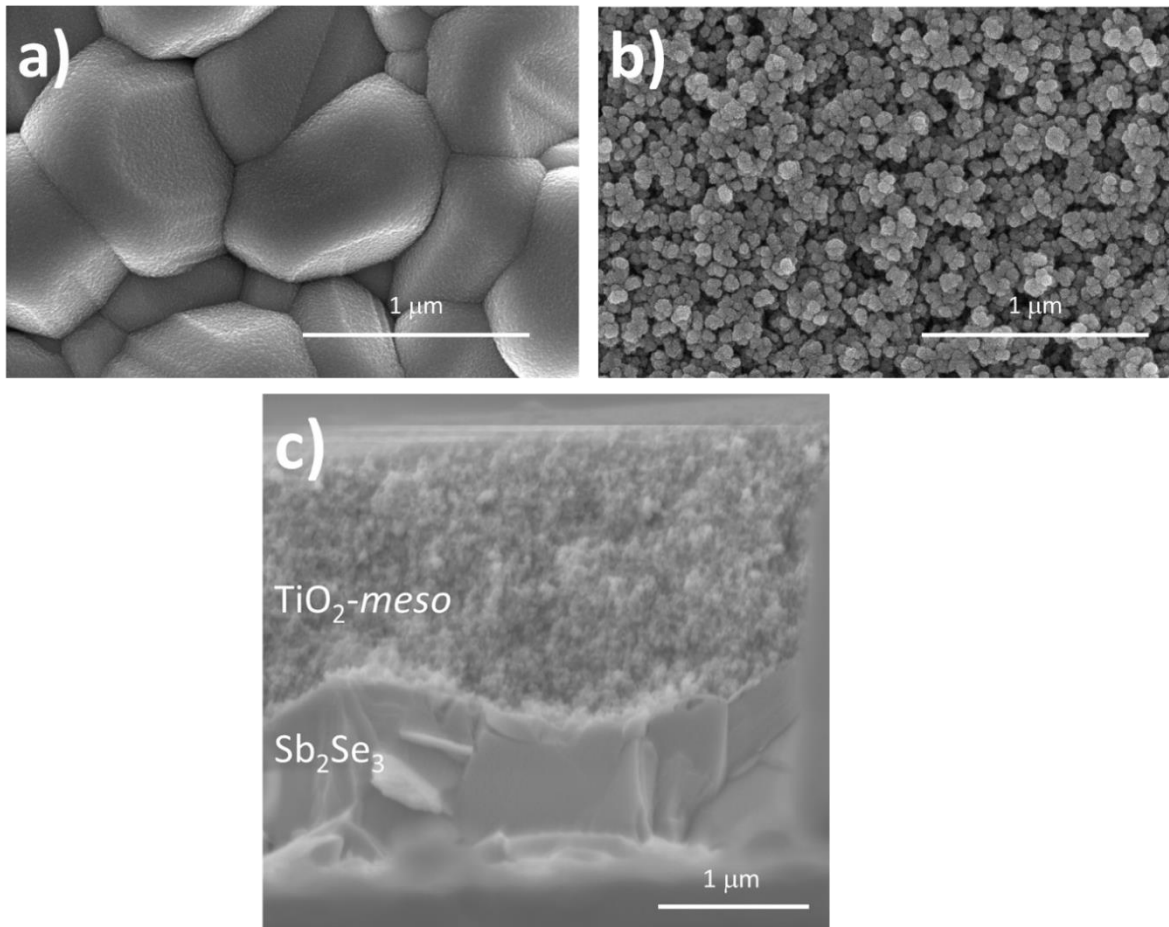
Figure 62 *Top view SEM images of (a) Sb₂Se₃/CdS/TiO₂(S-100nm) and (b) Sb₂Se₃/CdS/TiO₂(S-100nm)/TiO₂-meso, the cross-sectional SEM image of this sample is shown in panel (c).*

The energy-dispersive X-ray spectroscopy (EDX) analysis was carried out in a cross-sectional image of Sb₂Se₃/CdS/TiO₂(S-100nm)/TiO₂-*meso*, and the results shown in Figure 63, where Ti, O, Sn, Se, Sb, Si, Au, Cd, S were identified in the elemental analysis. Note that for the Au, Cd, S seemed to be dispersed across to the structure and it could be indicative of interdiffusion of the CdS on the Sb₂Se₃ giving rise to Sb₂S₃ and CdSe.[28]
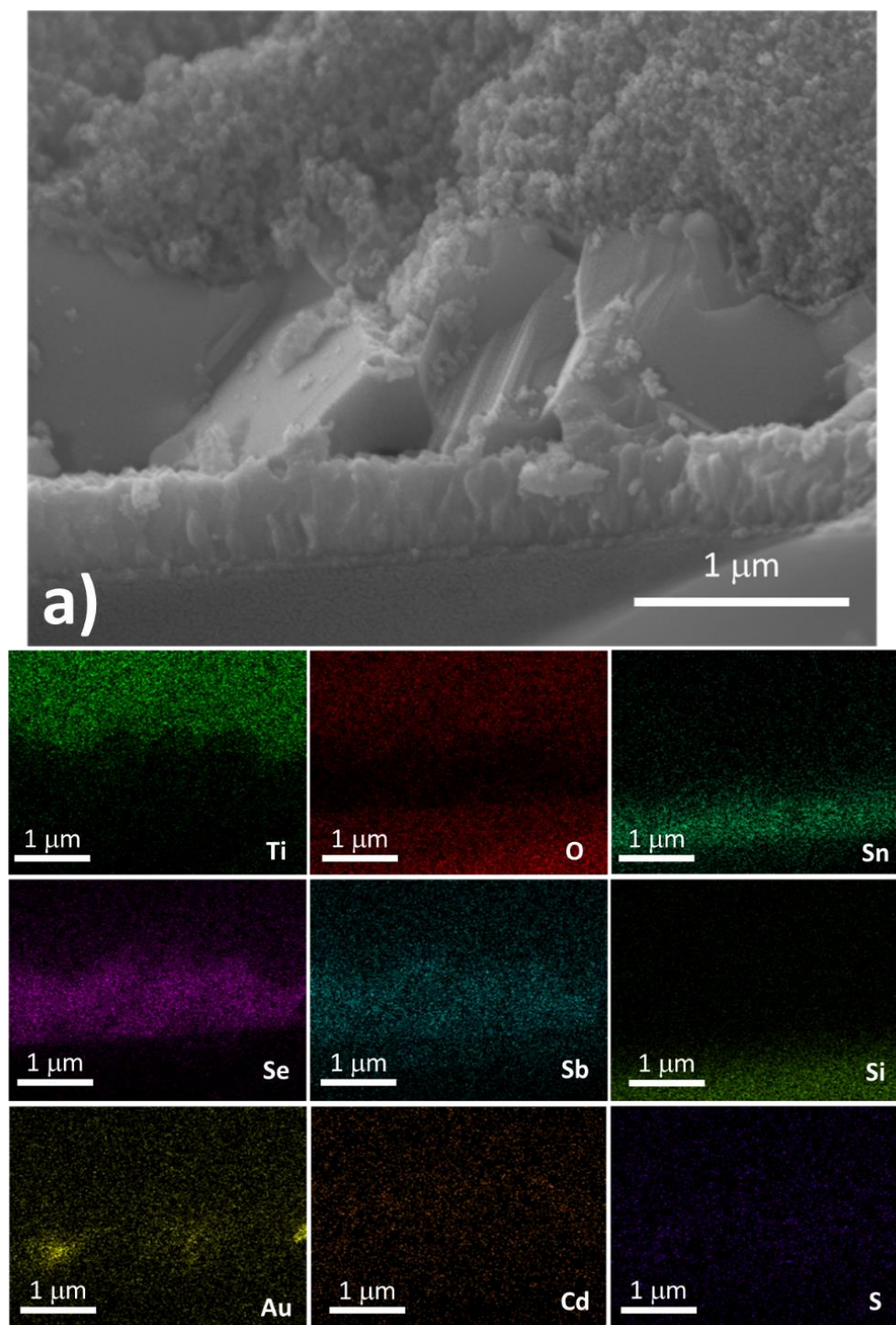
Figure 63 *(a) Cross-sectional SEM image of Sb₂Se₃/CdS/TiO₂(S-100nm)/TiO₂-meso and EDX maps of Ti, O, Sn, Se, Sb, Si, Au, Cd, S.*

The **NiP** immobilization on the Sb_2Se_3/CdS/TiO_2(S-100nm)/TiO_2-*meso* was then carried out using the same experimental protocol (soaking the films overnight in 0.5 mM of **NiP** in dry methanol, rinsed with dry methanol and vacuum dried at 60 °C). Figure 64 shows the picture of all the experimental steps followed to build the Sb_2Se_3/CdS/TiO_2(S-100nm)/TiO_2-*meso*/**NiP** hybrid photocathode.
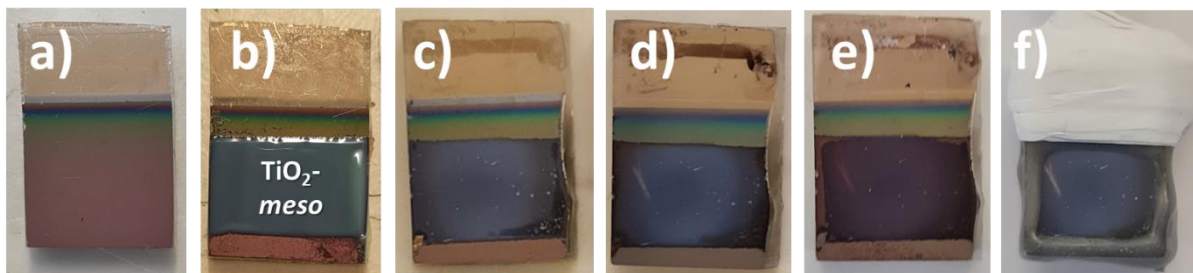

Figure 64 Picture of a Sb_2Se_3/CdS/TiO_2(S-100nm)/TiO_2-meso/NiP sample after each experimental step: (a) bare Sb_2Se_3/CdS/TiO_2(S-100nm), (b) doctor-bladed TiO_2-meso before and (c) after 68 h UV curing, (d) after N_2 annealing at 350 °C, (e) after NiP immobilization, and (f) after NiP stripping to determine the catalyst loading.

The final Sb_2Se_3/CdS/TiO_2(S-100nm)/TiO_2-*meso*/**NiP** photocathode achieved an increased **NiP** loading of 45.76 ± 0.81 nmol cm^{-2}, 6.5 times higher than the catalyst loading on the planar device (7.08 ± 0.43 nmol cm^{-2}). After the TiO_2-*meso* addition, the catalyst content was then consistent with the **NiP** loading reported previously shown in Table 7.[21]

The **NiP** dispersion onto the Sb_2Se_3/CdS/TiO_2(S-100nm)/TiO_2-*meso* surface was studied by EDX analysis, and found that the molecular catalyst followed by the Ni and P in the elemental analysis indicated that **NiP** was evenly distributed on the photocathode surface as shown in Figure 65.
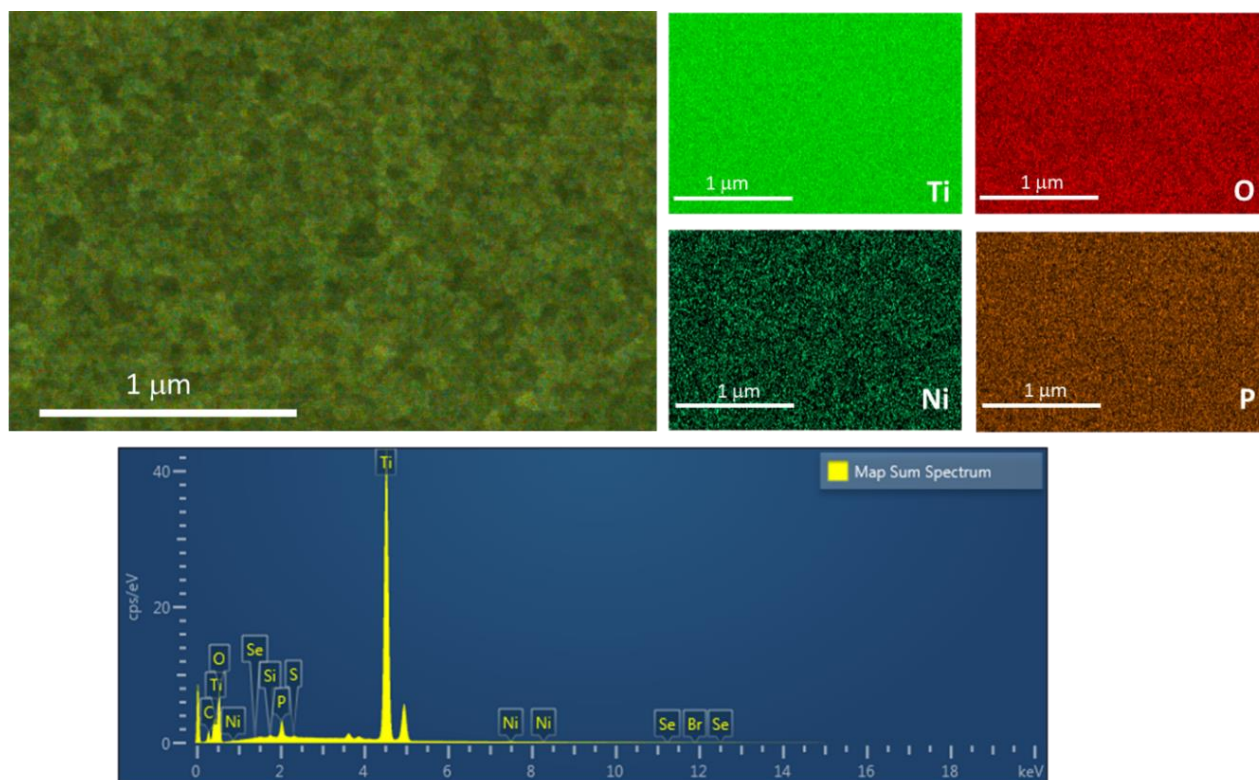
Figure 65 *Top view EDX analysis of the **NiP** dispersion onto Sb₂Se₃/CdS/TiO₂(S-100nm)/TiO₂-meso, Ni and P indicative of **NiP** are represented in green and brown respectively.*
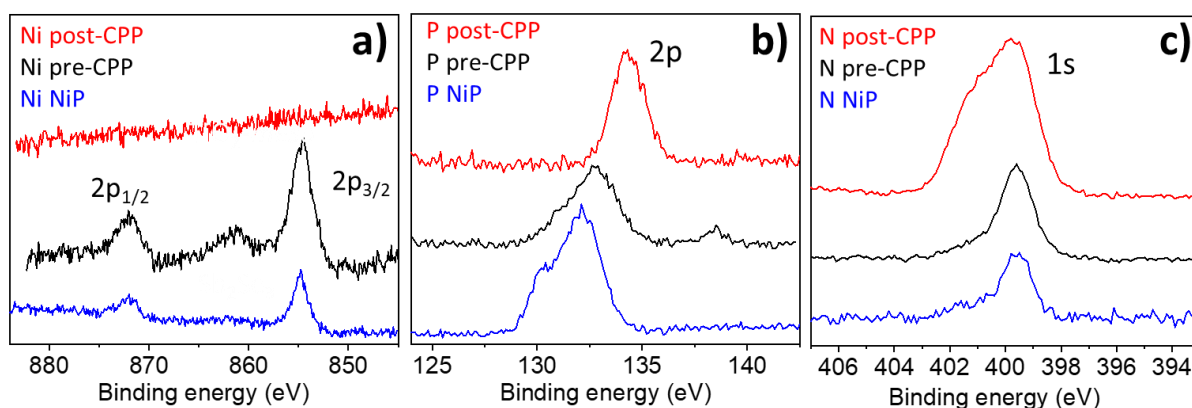
Figure 66 *XPS spectra of **NiP** molecular catalyst (blue trace), after immobilized on Sb₂Se₃/CdS/TiO₂(S-100nm)/TiO₂-meso, labelled as pre-CPP (black trace), and after 5 h of CPP test at 0 V vs RHE (post-CPP, red trace) with light intensity of 100 mW cm⁻² and λ > 340 nm in 0.1M Na₂SO₄ at pH 3. (b, c, d) XPS spectra showing Ni 2p, P 2p and N 1s regions respectively.*

Furthermore, the **NiP** integrity after immobilisation on the top of Sb$_2$Se$_3$/CdS/TiO$_2$(S-100nm)/TiO$_2$-*meso* was verified by X-ray photoelectron spectroscopy (XPS), and the spectra are shown in Figure 66 (black trace, labelled as pre-CPP). The energies of the Ni 2p (Figure 66a, ½ at 872.1 eV and ¾ at 854.6), P 2p (Figure 66b, 132.6 eV) and N 1s (Figure 66c, 399.6 eV) peaks are in good agreement with the **NiP** catalyst prior to immobilisation (blue trace). Table 10 compares the actual XPS peak position founded in this study with the literature.[20–22]

Table 10 *XPS peak position of **NiP** catalyst pre and post CPP test for 5 h at 0 V vs RHE in 0.1M Na$_2$SO$_4$ pH 3 at 100 mW cm^{-2} and λ > 340 nm.*

Hybrid photoelectrode	CPP Test	N (1s)	P (2p)	Ni (2p 1/2)	Ni (2p 3/2)	Ref.
p-Si/TiO$_2$/**NiP**	pre	399.6	132.5	872	854.8	[21]
	post	400.2	132		854.8	
FTO/TiO$_2$/**NiP**	pre	396.4	129.4	868.9	851.5	[22]
	post	396.2	129	869.1	851.5	
Au/La$_5$Ti$_2$Cu$_{0.9}$Ag$_{0.1}$S$_5$O$_7$/TiO$_2$/**NiP**	pre	398.67	132.5	860.4	855	[20]
	post	400.2	132.5	na	na	
Sb$_2$Se$_3$/CdS/TiO$_2$(S-100nm)/TiO$_2$-*meso*/**NiP**	pre	399.6	132.6	872.1	854.6	This work
	post	399.8	134.3	na	na	
NiP		399.5	133.1	872	854.8	

The chopped light LSV of the complete photocathode (Sb$_2$Se$_3$/CdS/TiO$_2$(S-100nm)/TiO$_2$-*meso*/**NiP**) achieves a photocurrent of −1.3 mA cm^{-2} at 0 V *vs* RHE with an onset potential of *ca.* +0.37 V *vs* RHE, shown in Figure 67. The photocurrent generated at the Sb$_2$Se$_3$-**NiP** based structures is amongst the highest reported for a **NiP** decorated photocathode (see Table 7). **NiP** has been previously studied on Si/TiO$_2$-*meso* photocathode to achieve a photocurrent of −0.3 mA cm^{-2} at 0 V *vs* RHE,[21] and−0.6 mA cm^{-2} at 0 V *vs* RHE for a La$_5$Ti$_2$Cu$_{0.9}$Ag$_{0.1}$S$_5$O$_7$/TiO$_2$ device. [20] In Figure 67, the control experiment without the catalyst (Sb$_2$Se$_3$/CdS/TiO$_2$-*meso*) demonstrates the importance of the **NiP**, as a photocurrent of only −0.12 mA cm^{-2} at 0 V *vs* RHE was recorded.
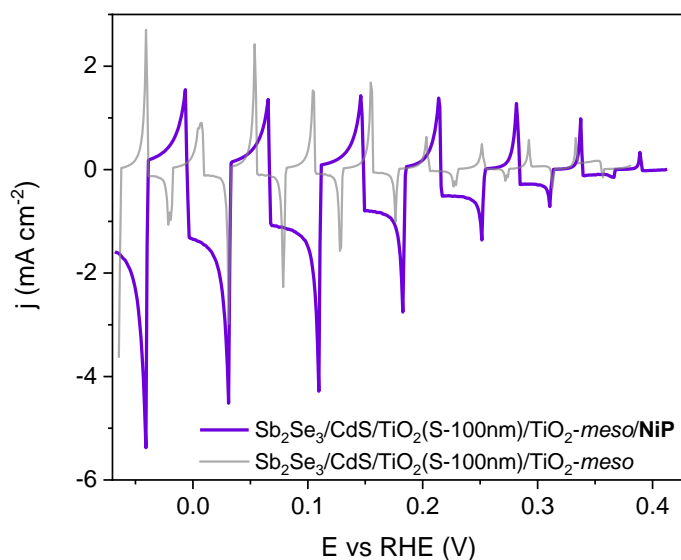
Figure 67 *Light chopped LSV at 10 mV s⁻¹ of Sb₂Se₃/CdS/TiO₂(S-100nm)/TiO₂-meso with **NiP** and without catalyst in 0.1 M Na₂SO₄ pH 3 under Ar at 100 mW cm⁻² and λ > 340 nm.*

To quantify how different energy photons contribute to the total photocurrent assumed for H₂ production, the Incident Photon to Current Efficiency (IPCE) analysis was carried out at 0 V *vs* RHE in 1 M Na₂SO₄ pH 3, the response of **NiP** was compared *vs* Pt as an HER ideal catalyst, and the results are shown in Figure 68. Sb₂Se₃/CdS/TiO₂(S-100nm)/TiO₂-*meso*/**NiP** is able to collect photons at wavelengths up to 900 nm, in-line with its band gap, note that the absorption coefficient of Sb₂Se₃ is also indicated,.[6,7] However, the IPCE response show that the activity is significantly decreased at λ < 500 nm. This wavelength corresponds to the onset of the CdS light absorption suggesting that photon absorption in this layer is not leading to useful photoelectron generation and that parasitic photon absorption occurs.[7,30]

The parasitic CdS absorption *ca.* 500 nm on Sb₂Se₃-based photocathodes has been reported previously,[7,30] and pointed out that a careful tailoring of the CdS thicknesses is necessary to improve the fill factor and onset potential without diminishing the photocurrent. Yang et at.[7] noticed that the photocurrent dropped from −24 to −19 mA cm⁻² at 0 *vs* RHE after including a CdS layer in a Sb₂Se₃-based photocathode and Pt as catalyst (Sb₂Se₃/CdS/TiO₂/Pt). Note that this photocathode is particularly

similar to ours because the Sb₂Se₃ was made by a two-step CSS,[7] and significant higher IPCE values were recorded up to 70% at wavelengths around 500-700 nm. The discrepancy in PEC performance with our device in terms of photocurrent and IPCE values was attributed to the different *p-n* junction at the Sb₂Se₃ interface (either by the ALD TiO₂ or the CdS made by chemical bath deposition), which determines the photoelectron extraction, as was fully discussed in section 2.2.2.
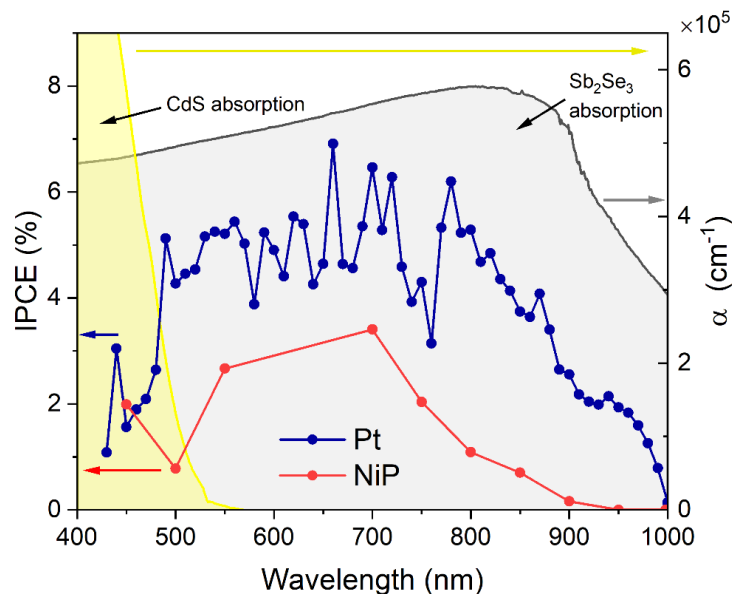
Figure 68 *IPCE of Sb₂Se₃/CdS/TiO₂(S-100nm)/TiO₂-meso with **NiP** (red trace) and Pt (blue trace) as HER catalyst at 0 V vs RHE in 0.1M Na₂SO₄ pH 3 under Ar. Overlaid is the absorption spectra of the CdS and Sb₂Se₃.*

Now focussing only on the Sb₂Se₃/CdS/TiO₂(S-100nm)/TiO₂-*meso* devices studied here, Pt addition provided more efficient electron consumption, the IPCE values were almost twice that of the **NiP**-based photocathode (although with the same trend), indicating that the Sb₂Se₃ based architecture is able to generate a higher photoelectron flux and the catalytic rate of **NiP** is too low to keep up. Consequently, the charges are not used efficiently and recombine, in line with the large spikes observed during the chopped light LSV shown in Figure 67, which disappeared when Pt is used as HER catalyst (See below, Figure 70). This effect will be further discussed in section 3.5

To assess the stability of the Sb₂Se₃/CdS/TiO₂(S-100nm)/TiO₂-*meso* /**NiP** device a controlled potential photoelectrolysis (CPP) was carried out at 0 V *vs* RHE, and the results shown in Figure 69. By gas

chromatography, the H_2 faradaic efficiency after 1 h was $77.5 \pm 9.1\%$, giving a TON_{NiP} of 12.8 ± 2.8. However, the photocurrent decreased significantly in the first hour and by 5 hours, it was only -15 μA cm^{-2}. In past studies, **NiP** decorated photocathodes exhibited longer stability than the achieved on Sb_2Se_3-based photocathodes (see Table 7).[20,21] Therefore the deactivation mechanism was investigated in the next section.
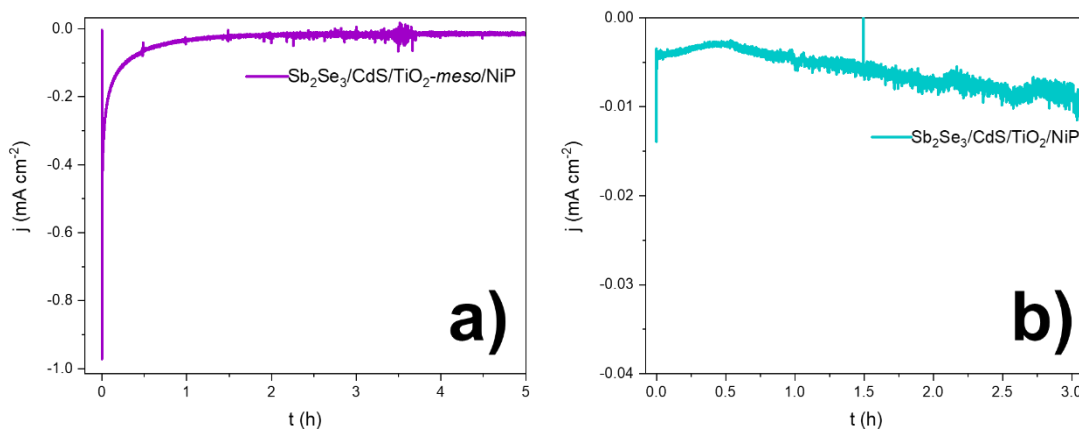

Figure 69 *Controlled Potential Photoelectrolysis (CPP) at 0 V vs RHE of Sb_2Se_3/CdS/TiO_2(S-100nm)/(TiO_2-meso /)**NiP** with (a) and without (b) the TiO_2-meso layer in 0.1M Na_2SO_4 pH 3 under Ar at 100 mW cm^{-2} and $\lambda > 340nm$.*

3.4.1 Deactivation mechanism of the hybrid photocathode

To start at TiO_2-*meso*/**NiP** interface, the loss of photoactivity of **NiP** decorated photoelectrodes has previously been attributed to the hydrolysis of the phosphonic anchoring group from the TiO_2.[20,21] However, from the XPS analysis of the Sb_2Se_3/CdS/TiO_2(S-100nm)/TiO_2-*meso*/**NiP** post-CPP, it was clear that both the N 1s and P 2p signals from the phosphonic anchoring group were still present, although significantly shifted. A broadening of the N 1s band has previously been assigned to protonation of the amine in the acidic electrolyte[20] and the shifting of the P band (P (2p) at 134.3 eV) is due to the loss of the metal centre,[31] leading to the possible formation of the following compounds: phosphoryl nitride (PON, P (2p) at 134.5 eV),[32] diamidophosphoric acid ((NH_2)$_2$PO(OH), P (2p) at 134.4 eV)[33], and/or ammonium dihydrogen phosphate ((NH_4)H_2PO_4, P (2p) at 134.4 eV).[34] The XPS

results of the hybrid photocathode post-CPP also demonstrated the complete loss of the Ni^{2+} bands (red trace in Figure 66). Therefore, the XPS analysis suggested that the phosphonate linkage was retained in-line with the stability of the phosphonate linkage at pH < 7,[35] but the Ni was no longer coordinated to the ligand.

It is interesting to compare the photoelectrochemical stability of the Sb$_2$Se$_3$/CdS/TiO$_2$(S-100nm)/TiO$_2$-*meso*/**NiP** device to the dark electrochemical stability of the TiO$_2$-*meso*/**NiP** interface (without Sb$_2$Se$_3$/CdS underneath) during CPP at −0.25 V *vs* RHE, shown in Figure 57. During the dark electrochemical test, after the initial current drop at the first 600 s, the electrode maintained a stable current of −0.24 mA cm^{-2} for 1h. This indicated the TiO$_2$-*meso*/**NiP** interface was stable at this potential and capable of operating at low current density. However, the current spikes observed with Sb$_2$Se$_3$/CdS/TiO$_2$(S-100nm)/TiO$_2$-*meso*/**NiP** when the light is turned on/off in Figure 67 are typical features of electron accumulation in the TiO$_2$, suggesting that the **NiP** catalyst was unable to turnover at the rate of photoelectron generation under 100 mW cm^{-2} illumination. The possible **NiP** photodecomposition was ruled out since Leung, J *et at.* reported that p-Si/TiO$_2$/**NiP** photocathode was still active after 24 h of constant front illumination at 100 mW cm^{-2}, AM 1.5G, λ> 400 nm (Table 7).[21]

Then, the hypothesis that the **NiP** catalyst became destabilised by photoelectron accumulation in the TiO$_2$ structure was assessed by considering the known catalytic activity of **NiP**. Based on the concentration of immobilised **NiP** (45.76 ± 0.81 nmol cm^{-2}), and the highest reported turnover frequency of **NiP** (460 ± 5 h^{-1}),[18] the **NiP** on the surface could support a photocurrent of −1.15 mA cm^{-2}. This magnitude of photocurrent was achieved briefly in the chopped light LSV (−1.3 mA cm^{-2} at 0 V *vs* RHE Figure 67), however the photocurrent decreases rapidly as the **NiP** degrades during the CPP, suggesting that the **NiP** operated briefly at its maximum turnover frequency, in-line with their being an excess of photoelectrons.

To further assess the photoelectron generation rate of Sb$_2$Se$_3$/CdS/TiO$_2$(S-100nm)/TiO$_2$-*meso*, Pt was used as a benchmark catalyst (Pt photoelectrodeposition synthetic details are provided in 6.2.5). The Sb$_2$Se$_3$/CdS/TiO$_2$(S-100nm)/TiO$_2$-*meso*/Pt electrode achieved a stable photocurrent of −3 mA cm^{-2} at 0

V *vs* RHE for 5 hours, as shown in Figure 70. This figure clearly demonstrates that the rate of photoelectron generation at the Sb$_2$Se$_3$/CdS interface greatly exceeds the maximum current density that **NiP** can sustain.
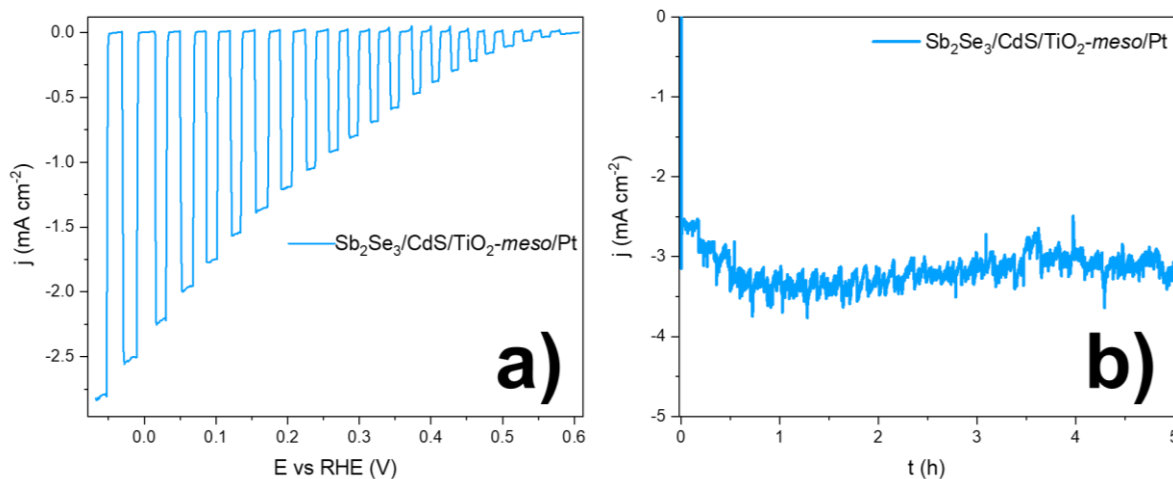

Figure 70 *(a) Light chopped LSV of Sb$_2$Se$_3$/CdS/TiO$_2$-meso/Pt at 10mV s^{-1}, and (b) CPP at 0 V vs RHE in 0.1 M Na$_2$SO$_4$ pH 3 under Ar at 100 mW cm^{-2} and λ > 340 nm.*

We hypothesised that the **NiP** deactivation due to the photoelectron excess generated at the Sb$_2$Se$_3$/CdS interface could be related to the following mechanisms. First, consider the catalytic mechanism of **NiP** for H$_2$ production shown in Figure 71, where the pendant amines supply protons to the Ni centre.[17] After the **NiP** immobilization, there is a trade-off between the improved the electron transfer from the light absorber towards the catalyst and the pendant amines limited mobility, which could hinder the performance of the molecular catalyst if the proton relay is not delivered at fast-enough rate. Then, a second reduction from Ni^I to Ni^0 is likely to occur deactivating the catalyst.

Note that **NiP** is an O$_2$ sensitive molecular catalyst,[36] and quick deactivation of DuBois-type catalyst has been reported previously after the covalent immobilization on a conductive polymer matrix. Due to the improved electron transfer, the catalyst operated at its higher turnover frequencies leaving it at its most sensitive form for oxygen deactivation (Ni^{2+}).[37] The electrochemical cell used to carry out these experiments is shown in Figure 108 with a Nafion 117 membrane to separate the anode (where the

oxygen was likely generated) from the cathode, however crossover oxygen transport could be another

deactivation pathway.
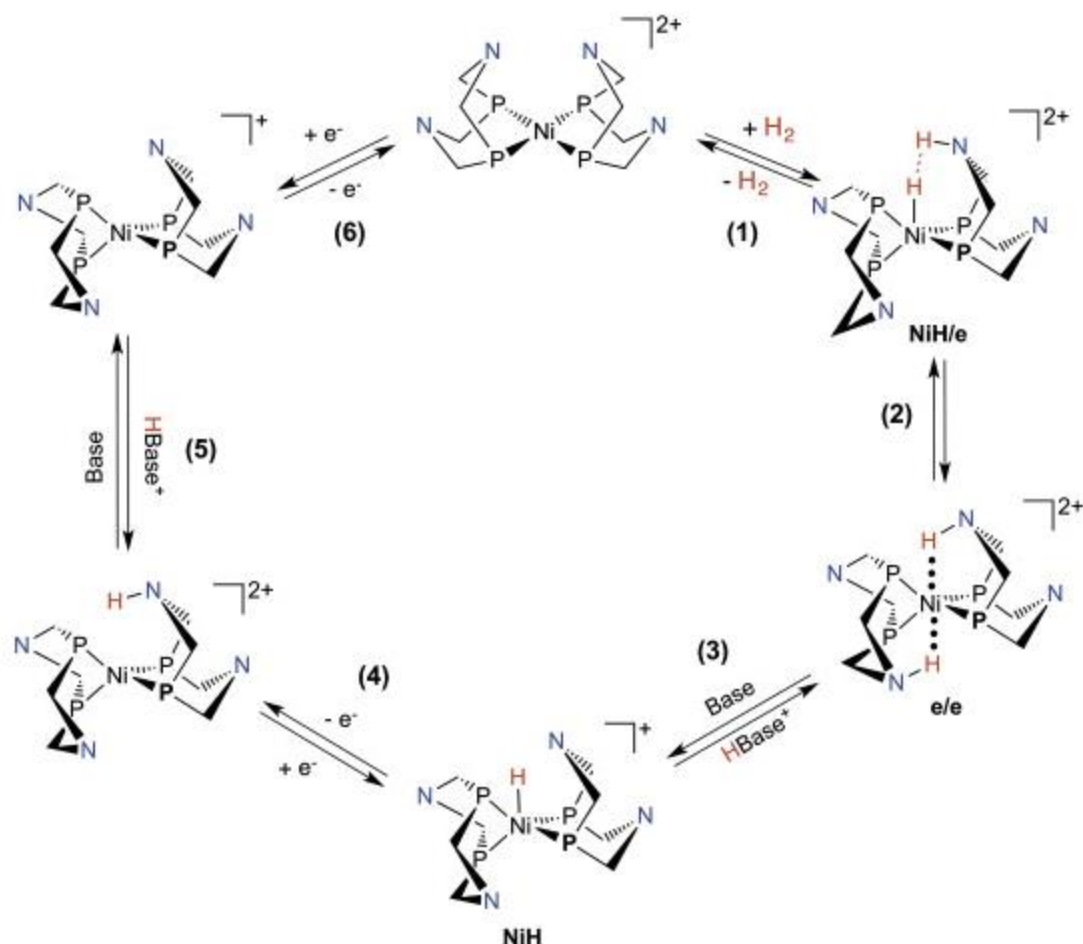
***Figure 71 NiP** reaction mechanism for H₂ production (anti-clockwise).[17] Only the **NiP** core ([Ni(P₂^{R'}N₂^{R''})₂]²⁺) is shown and the R and R' substituents were omitted for clarity. (P₂^{R'}N₂^{R''} = bis(1,5-R'-diphospha-3,7-R''-diazacyclooctane).*

After the CPP, the XPS analysis did not shown any Ni on the surface of photocathode neither

electroreduced, nor oxidized spices, suggesting that the Ni centre leached to the electrolyte. However,

ICP post-CPP analysis was not carried out after the test to further confirm this hypothesis.

To explore if limiting the photoelectron generation on the Sb_2Se_3 would be beneficial,

photoelectrochemical experiments at 20 mW cm⁻² were carried out by lowering the light intensity using

neutral density filters. Notably, for the chopped light LSV (Figure 72a) only a small decrease in photocurrent was observed from −1.30 to −0.81 mA cm^{-2} at 0 V *vs* RHE. This is a *ca.* 38% photocurrent decrease compared to the change in light intensity (80% decrease). Furthermore, the spikes related to photoelectron accumulation on the TiO$_2$ decreased at 20 mW cm^{-2}, but did not disappear completely.

For the CPP test at 0 V *vs* RHE (Figure 72b), 20% of photocurrent was retained after 1800 s compared with the 11% at 100 mW cm^{-2}, suggesting that the lower light intensity increased the device stability in-line with the proposed degradation mechanism of the **NiP** catalyst being over-reduction, and even lower light intensity (*e.g.* 5 mW cm^{-2}) could improve the stability of the hybrid Sb$_2$Se$_3$/CdS/TiO$_2$(S-100nm)/TiO$_2$-*meso*/**NiP** photocathode.
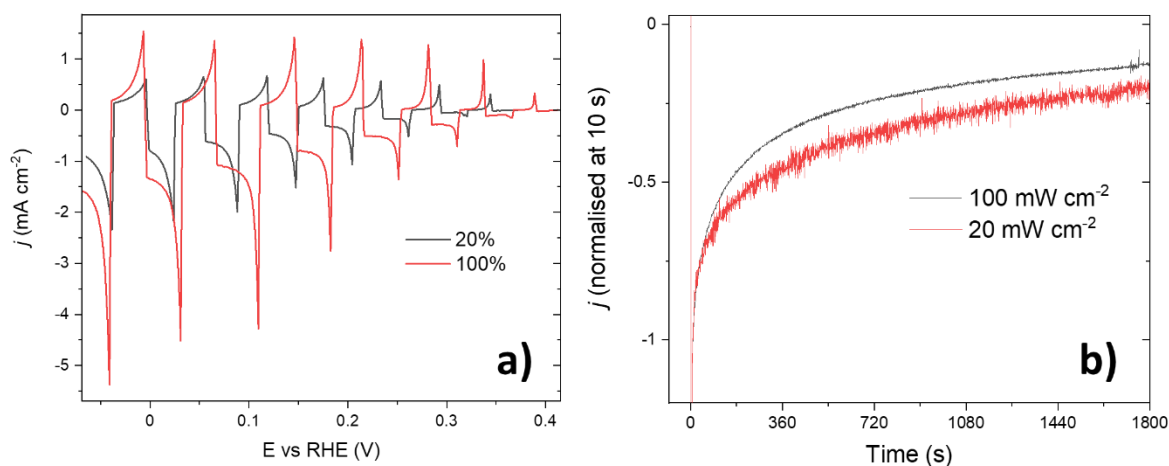
Figure 72 *(a) Chopped light LSV of Sb$_2$Se$_3$/CdS/TiO$_2$(S-100nm)/TiO$_2$-meso/**NiP** at 10 mV s^{-1}, and (b) normalised at 10 s CPP at 0 V vs RHE at 20 mW cm^{-2} and 100 mW cm^{-2} in 0.1 M Na$_2$SO$_4$ pH 3 under Ar, and λ > 340 nm.*

Another possible deactivation mechanism could be related to TiO$_2$ dissolution due to photoelectron accumulation, reaction indicated in equation 4. Past studies using precious metal HER catalysts like Pt on planar TiO$_2$ coated Sb$_2$Se$_3$ photocathodes noted changes in morphology post-CPP. [6,8,19] To verify if this degradation pathway is also occurring alongside **NiP** loss, SEM analysis of photocathodes tested at 100 mW cm^{-2} was carried out. The SEM images pre (Figure 73a-b) and post-CPP (Figure 73a'-b') for the planar (Sb$_2$Se$_3$/CdS/TiO$_2$(S-100nm)/**NiP**, panel a, a') and high surface area photoelectrode

(Sb$_2$Se$_3$/CdS/TiO$_2$(S-100nm)/TiO$_2$-*meso*/**NiP**, panel b, b') did not show significant change in the morphology after CPP, despite the demonstration of electron accumulation in the device.

$$TiO_2 + H_3O^+ + e^- \rightarrow Ti(OH)_3 \qquad \text{Eq. (4)}$$
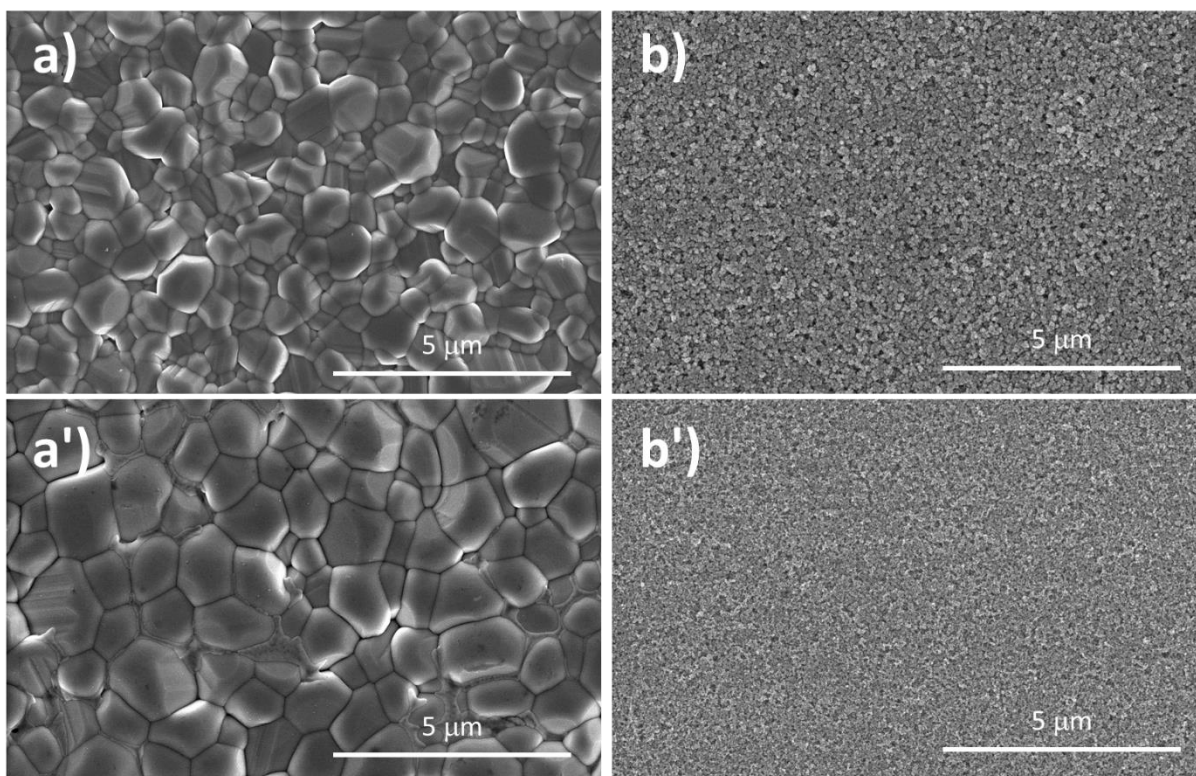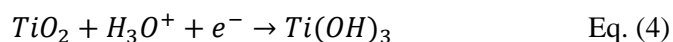
Figure 73 *Top view SEM images of (a, a') Sb$_2$Se$_3$/CdS/TiO$_2$(S-100nm)/**NiP** and (b, b') Sb$_2$Se$_3$/CdS/TiO$_2$(S-100nm)/TiO$_2$-meso/**NiP** pre (a, b) and post-CPP (a', b') for 5 h at 0 V vs RHE in 0.1M Na$_2$SO$_4$ pH 3 at 100 mW cm^{-2} and λ > 340 nm.*

On Sb$_2$Se$_3$ based photocathodes where the TiO$_2$ capping layer is typically 20 – 40 nm thick, the TiO$_2$ dissolution led to the formation of Sb$_2$O$_3$ when the electrolyte reached the light absorber.[7,8] Sb$_2$O$_3$ has a characteristic Raman shift at 254 cm^{-1}, therefore Raman analysis was carried out pre and post-CPP at 0 V *vs* RHE for 5 h at 100 mW cm^{-2}, shown in panel a and b, respectively in Figure 74, on the planar (Sb$_2$Se$_3$/CdS/TiO$_2$(S-100nm)/**NiP**, black trace) and high surface area photocathode (Sb$_2$Se$_3$/CdS/TiO$_2$(S-100nm)/TiO$_2$-*meso*/**NiP**, red trace). However, only the peaks related to Sb$_2$Se$_3$ and TiO$_2$ (anatase phase) were identified and indicated in the Figure 74. No Sb$_2$O$_3$ contribution was

observed in the planar device after the CPP (Sb$_2$Se$_3$/CdS/TiO$_2$(S-100nm)/**NiP**), however due to the *ca.* 5 µm thick TiO$_2$-*meso* layer at the top of Sb$_2$Se$_3$/CdS/TiO$_2$(S-100nm)/TiO$_2$-*meso*/**NiP**, the Raman shifts of other compounds could be masked as it was observed for the Sb$_2$Se$_3$ at 189 cm^{-1}, where its peak intensity was relatively small compared to the TiO$_2$ main feature.
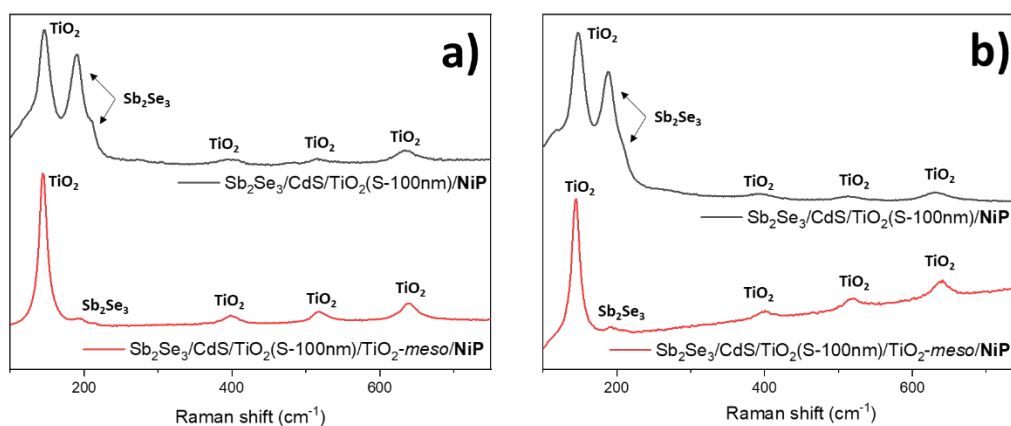

Figure 74 *Raman spectra pre (a) and post-CPP (b) at 0 V vs RHE for 5 h at 100 mW cm^{-2} and λ > 340 nm on Sb$_2$Se$_3$/CdS/TiO$_2$(S-100nm)/**NiP** (black trace), Sb$_2$Se$_3$/CdS/TiO$_2$(S-100nm)/TiO$_2$-meso/**NiP** (red trace).*

Finally, experiments to test if the PEC activity could be recovered by adding a catalyst back (Pt) onto a used Sb$_2$Se$_3$/CdS/TiO$_2$(S-100nm)/TiO$_2$-*meso*/**NiP** structure were carried out. The Sb$_2$Se$_3$/CdS/TiO$_2$(S-100nm)/TiO$_2$-*meso*/**NiP** underwent chopped light LSV followed by a CPP at 0 V *vs* RHE for 1h. Any remaining **NiP** was removed by NaOH stripping, then a Pt catalyst was photoelectrodeposited, and the device was photoelectrochemically tested. The chopped light LSV is shown in Figure 75, significantly higher dark currents (< -5 mA cm^{-2} at 0 V *vs* RHE) and decreased photocurrents were measured compared to a pristine platinized photoelectrode (Figure 70), indicating partial failure of the sputtered TiO$_2$ layer due to photoelectron accumulation. Although characterisation of the Sb$_2$Se$_3$/CdS/TiO$_2$(S-100nm)/TiO$_2$-*meso*/**NiP** photoelectrode post-CPP showed no evidence of the failure of the sputtered TiO$_2$ layer, these activity tests do indicate that it is no-longer protecting the underlying absorber. Overall this study reinforces the importance of preventing photoelectron

accumulation in the Sb₂Se₃/CdS/TiO₂(S-100nm)/TiO₂-*meso*/**NiP** photocathode otherwise deactivation

occurs through both **NiP** loss and as a result of the failure of the TiO₂ protective layer.
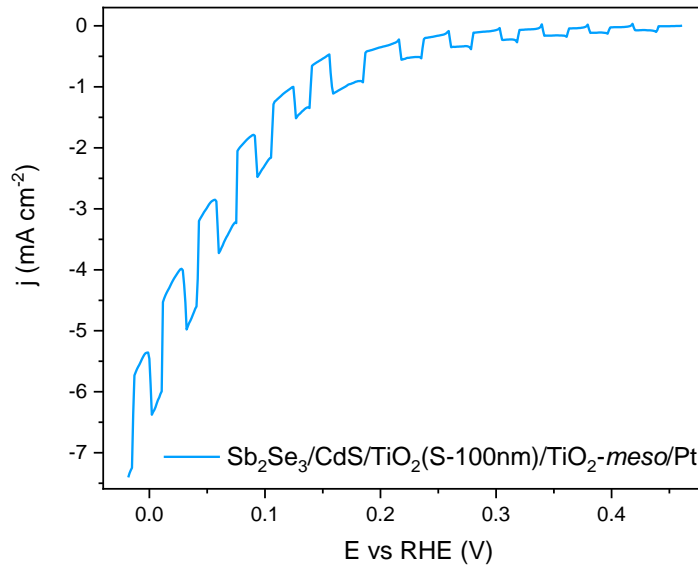
Figure 75 *Light chopped LSV of Sb₂Se₃/CdS/TiO₂(S-100nm)/TiO₂-meso/Pt at 10 mV s⁻¹ in 0.1 M Na₂SO₄ pH 3 under N₂, at 100 mW cm⁻² and λ > 340 nm. Note that Sb₂Se₃/CdS/TiO₂-meso was used first with **NiP** catalyst and swap by Pt after.*

3.5 Transient Photocurrent on Sb₂Se₃/CdS/TiO₂(-*meso*) structures

In the previous section, the catalyst effect on the photocurrent at the thermodynamic potential for H₂

production (0 V *vs* RHE) was described and significant difference was observed by using Pt or **NiP**

catalyst. However, it was also found that the TiO₂(-*meso*)/Pt interface shifted significantly the onset

overpotential (E_{onset}) towards more positive values, as shown in Figure 76. This figure also includes

the chopped light LSV at 10 mV s⁻¹ of the films without any catalyst at 100 mW cm⁻² and λ > 340 nm.

Furthermore, the positive shift of E_{onset} after TiO₂(-*meso*)/Pt was observed at different pHs: 1, 3, 5, 7

and 9. The results of the chopped light LSV were summarised in Figure 77, the potential where −0.5

mA cm⁻² was achieved is presented in panel a, and panel b shows the photocurrent measured at 0 V *vs*

RHE. Note that for the study at different pHs, only Pt was considered since the stability of the phosphonic anchoring groups in **NiP** is compromised in alkaline electrolytes,[35] and the highest catalytic activity is only observed at pH 3.[20,22]
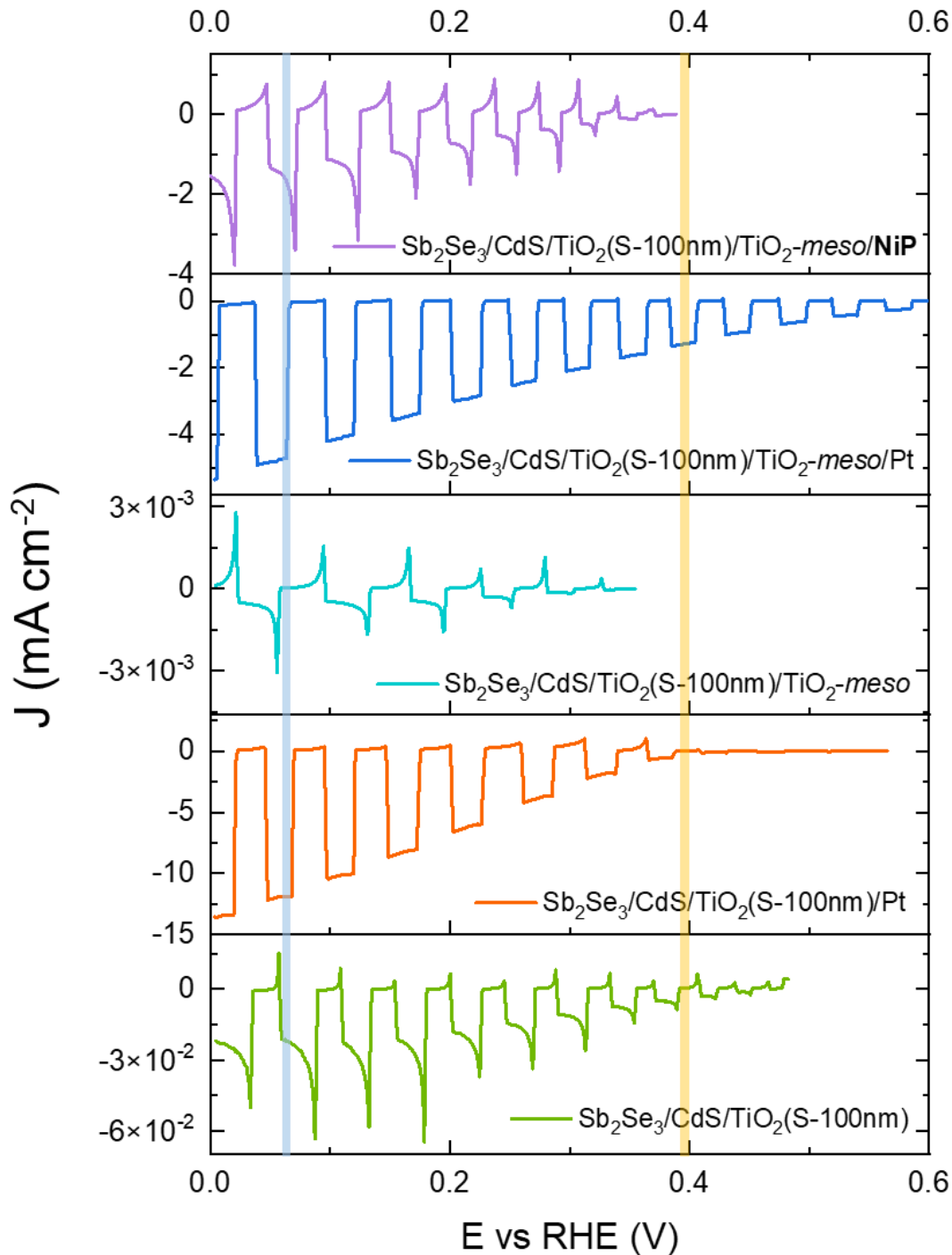
Figure 76 *Chopped light LSV at 10 mV s⁻¹ of Sb₂Se₃/CdS/TiO₂(S-100nm)/(TiO₂-meso) with **NiP** and Pt as catalyst and the bare structure at 10 mV s⁻¹ under Ar, 100 mW cm⁻² and λ > 340 nm. The yellow and blue line at 0.4 V and 0.06 V vs RHE indicate the potentials where the transient photocurrent analysis was carried out.*

For Sb$_2$Se$_3$-based photocathodes, shifts in E_{onset} have previously been seen and related to the improved charge extraction at the Sb$_2$Se$_3$/CdS interface after annealing at 280 °C for 5 min in an inert atmosphere (Ar).[30,38] The mild heat treatment induced a void free interface and promoted a slight Cd^{2+} interdiffusion in the Sb$_2$Se$_3$ lattice. By replacing Sb^{3+}, a more *p*-type Sb$_2$Se$_3$ was favoured and the electric field increased. It is important to point out that all the samples used for the pH study (Figure 76 and Figure 77) underwent the same N$_2$ annealing at 350 °C for 1 h before the Pt electrodeposition, even the planar structure Sb$_2$Se$_3$/CdS/TiO$_2$(S-100nm). Therefore, similar Sb$_2$Se$_3$/CdS interface is expected in this set of samples and the shift in the E_{onset} is unlikely to be related to changes at this interface.
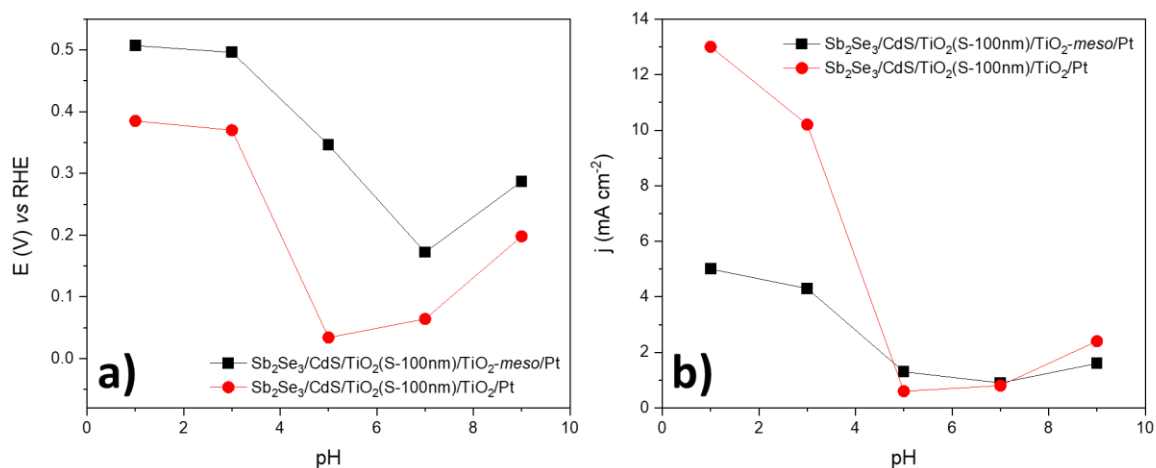
Figure 77 *(a) Potential where −0.5 mA cm^{-2} was recorded, and (b) photocurrent at 0 V vs RHE measured from the chopped light LSV of Sb$_2$Se$_3$/CdS/TiO$_2$(S-100nm)/(TiO$_2$-meso)/Pt at 10 mV s^{-1}, 100 mW cm^{-2} and λ > 340 nm.*

There are relatively few photophysics studies of Sb$_2$Se$_3$ photocathodes. In 2018, Yang W *et al.* published a detailed time-resolved study for photocarriers generated on FTO/Au/Sb$_2$Se$_3$/TiO$_2$/RuO$_x$ using ultrafast terahertz spectroscopy, time-resolved photoluminescence (TRPL) and intensity-modulated photocurrent−photovoltage spectroscopy (IMPS/IMVS).[10] The life times of the different process at 0 V *vs* RHE are summarised in Figure 78. TRPL analysis identified possible hole-electron recombination in the nanosecond scale at the Au/Sb$_2$Se$_3$ interface, and suggested that adding an electron blocking layer at this interface could alleviate recombination. At the millisecond scale, the charge transfer and recombination process were identified and pointed out that the charge transfer remained

constant under applied bias for potentials more negative than 0.3 V *vs* RHE, while the recombination rate decreased. Therefore, the authors attributed the negative E_{onset} to the slow charge transfer for H_2 production.[10]

Note that for this particular study (FTO/Sb_2Se_3/TiO_2/RuO_x),[10] the HER catalyst was RuO_x (with porous structure typical of photoelectrodeposition),[39] which had a dual role in the device. First, RuO_x increased the charge transfer rate at potentials below 0.3 V *vs* RHE when compared without catalyst. Second, it reduced surface recombination, acting as a "reservoir" that prevents electrons to diffuse back to the Sb_2Se_3 after separated at Sb_2Se_3/TiO_2 interface. This effect has also been observed for Pt as HER catalyst on a *p-n*Si/*n*-GaN photocathode, when studied by IMPS.[40]
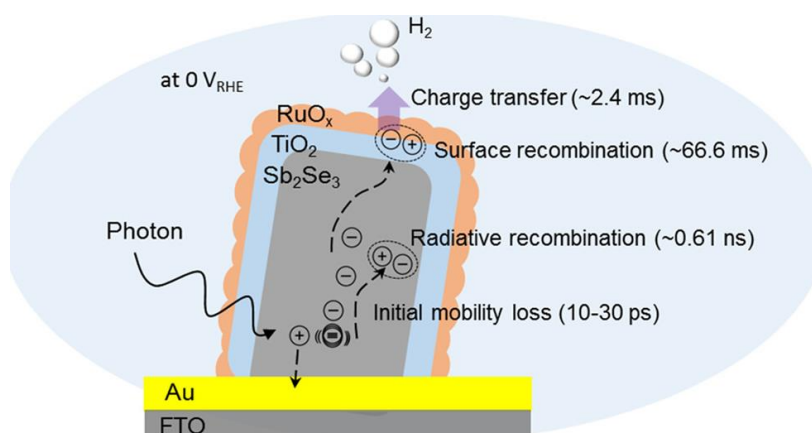
Figure 78 *Time constants for photocarriers generated at FTO/Sb₂Se₃/TiO₂/RuOₓ using different time-resolved spectroscopies at 0 V vs RHE. Scheme reproduced from [10]*

Yang and collaborators also suggested that surface passivation on FTO/Au/Sb_2Se_3/TiO_2/RuO_x was unnecessary, and pointed out that the tailoring at the Sb_2Se_3/TiO_2 interface could further improve the onset potential.[10] Afterwards confirmed by Liang,[38] when the In^{3+} cation dopant on the CdS shifted the onset potential up to 0.54 V *vs* RHE.

This study by Yang *et. al.* represents the state-of-the-art of our current understanding of processes occurring at different time scales at Sb_2S_3-based photocathodes.[10] However, it does not explain the

change in the E_{onset} observed in Figure 76 and Figure 77 when Pt catalyst was used with and without the TiO$_2$-*meso* layer. Therefore, to further assess charge transport at the Sb$_2$Se$_3$/CdS/TiO$_2$(S-100nm)/(TiO$_2$-*meso*)/(Pt) structure, a transient photocurrent (TPC) study was carried out to determine the possible contribution of back hole-electron recombination at the TiO$_2$(-*meso*)/Pt interface in 0.1 M H$_2$SO$_4$.

The experimental set up of TPC study is fully described in section 6.3.9. Briefly, the current passing from the WE to the CE was determined by a known resistor and the voltage drop measured at oscilloscope after a laser excitation at 532 nm, 6ns. Note that this laser wavelength was chosen to avoid absorption at the CdS (λ < 510 nm) or TiO$_2$ (λ < 387 nm). Furthermore, to study the charge extraction/recombination processes in Sb$_2$Se$_3$/CdS/TiO$_2$(S-100nm)/TiO$_2$-*meso* structure under continuous illumination, a monochromatic bias light 532 nm CW (constant wave at 0.8 mW cm^{-2}) was applied in addition to the laser pulse.

TPC measurements were collected at 0.4 and 0.06 V *vs* RHE. These potentials were selected in the region where the spikes were evident after the light was turned on and off in the LSV, which are indicative of recombination (0.4 V *vs* RHE, yellow line in Figure 76), and at 0.06 V *vs* RHE (blue line in Figure 76) where the current spikes disappeared suggesting effective photocharge consumption. The TPC decays were collected for devices with no catalyst and with Pt, shown in Figure 79 and Figure 81, respectively. The fastest reliable time response considered was ~100 μs, since there was no rise in current later than this because the charge has already reached FTO. Also note that the devices with the TiO$_2$ mesoporous layer included the TiO$_2$(S-100nm).

Figure 79 shows the TPC kinetic traces without catalyst for the planar Sb$_2$Se$_3$/TiO$_2$(S-100nm) device (presented in panel a, a'), and the high surface device Sb$_2$Se$_3$/TiO$_2$(S-100nm)/TiO$_2$-*meso* (shown in panel b, b'). For all the traces, there is a rise in the reductive current flow at time scales < 1 ms due to the electron transport through the photocathode to the electrolyte. However, in some cases the current flow changes direction at the millisecond scale, this process was attributed to the electrons being extracted back towards the external circuit (back-hole transfer) which is indicative of recombination. This change in direction of the current flow was exacerbated at 532 nm CW bias due to build up charges

in the device, as shown Figure 79a'. The same trend was seen for Sb$_2$Se$_3$/TiO$_2$(S-100nm)/TiO$_2$-*meso* as shown in Figure 79 b and b'.
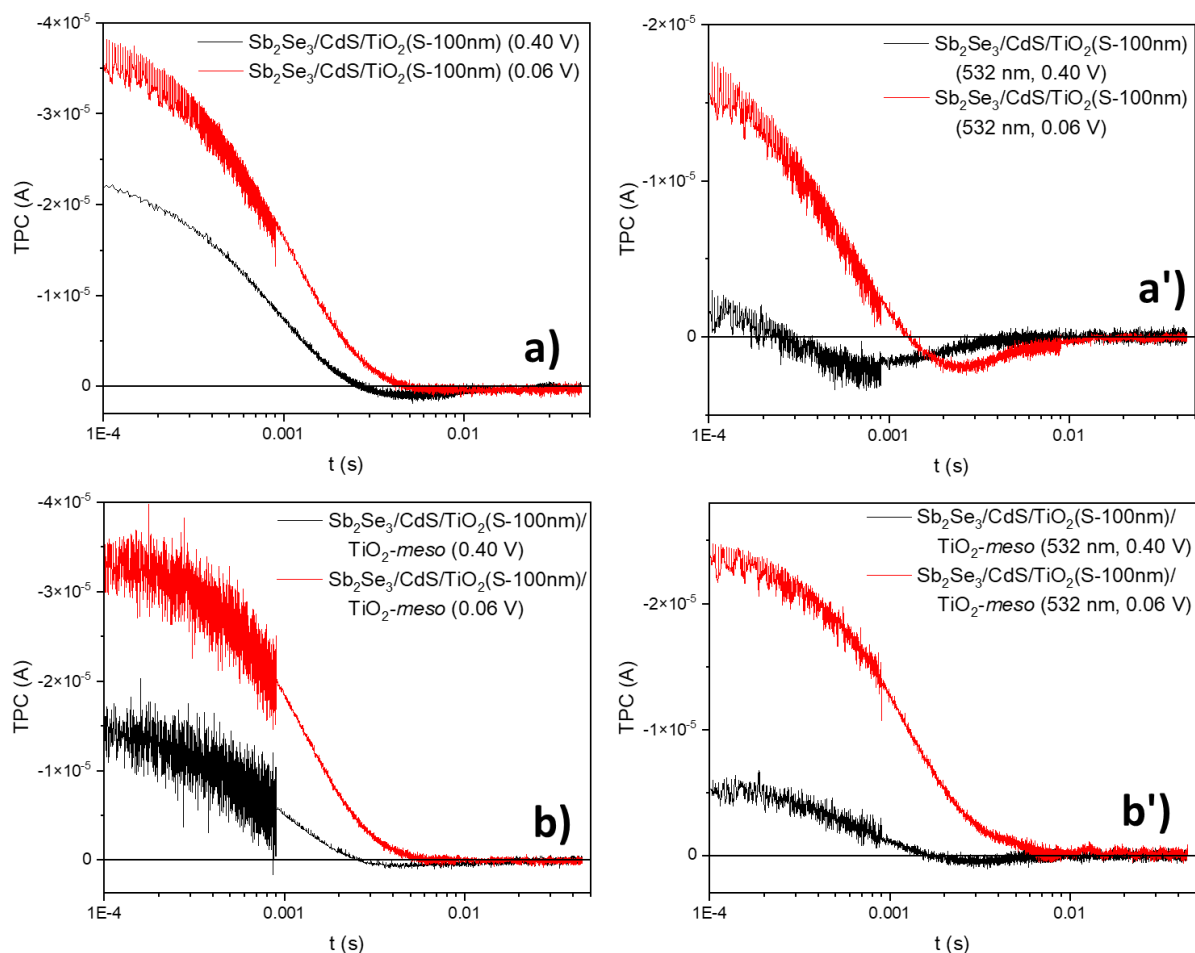
Figure 79 *TPC decays of Sb$_2$Se$_3$/TiO$_2$(S-100nm) devices (a, a'), and Sb$_2$Se$_3$/TiO$_2$(S-100nm)/TiO$_2$-meso (b, b') held at 0.4 (black line) and 0.06 (red line) V vs RHE following laser pulse at 532 nm, 6 ns in 0.1 M H$_2$SO$_4$ under N$_2$. The TPC decays with a 532 nm CW bias light applied are indicated as a' and b'.*

The TPC decays were fitted to a double or triple exponential decay functions, and the results are shown as appendix at the end of this chapter. However, a better understanding of TPC decays is provided by integrating the total charge, and the results are shown in Figure 80. The charge is expected to increase continuously along time following laser extinction, since it represents the electrons that are transferred though the photocathode towards the electrolyte. However, for the devices without catalyst

(Sb₂Se₃/CdS/TiO₂(S-100nm) and Sb₂Se₃/CdS/TiO₂(S-100nm)/TiO₂-*meso*), the total charge injected reached a maximum and then decreased due to recombination, as a result of electrons flowing backwards into the photocathode even when a more negative potential was applied (0.06 V *vs* RHE). For Sb₂Se₃/CdS/TiO₂(S-100nm) at 0.4 V *vs* RHE under 532 CW light, the initial electron flow into the photocathode was not measured and hypothesized that under these conditions, it occurred at faster timescales than the time resolution of our experimental setup (Figure 80a).

Figure 80 *Charge passed on non-platinized photocathodes: (a, a') Sb₂Se₃/TiO₂(S-100nm) and (b, b') Sb₂Se₃/TiO₂(S-100nm)/TiO₂-meso held at 0.4 (black line) and 0.06 (red line) V vs RHE following laser pulse at 532 nm, 6 ns, and with bias light 532 nm CW applied (a' and b'), in 0.1 M H₂SO₄ under N₂.*

The time scale associated to the maximum charge ($\tau_{Q_{max}}$) is presented in Table 11. As a general trend it is observed that (i) applying a more negative potential *i.e.* 0.064 V *vs* RHE slows down the

recombination process as h$^+$ extraction occurs efficiently and back-hole injection is suppressed, (ii) the 532 nm CW bias light promoted faster recombination due to increased photocharge generation leaving to a higher steady state concentration of e$^-$/h$^+$, and (iii) the total charge increased when applying more negative potentials. The Sb$_2$Se$_3$/TiO$_2$(S-100nm)/TiO$_2$-*meso* exhibited similar behaviour, and from these results is clear that the Sb$_2$Se$_3$-based photocathodes required a catalyst for photoelectron extraction and thus to decrease recombination rates.

Table 11 *Time constant of the maximum in charge passed on Sb$_2$Se$_3$ based photocathodes*

Photocathode	Constant wave (CW)	$\tau_{Q_{max}}$ (ms)	
		0.4 V *vs* RHE	0.064 V *vs* RHE
Sb$_2$Se$_3$/TiO$_2$(S-100nm)	---	2.6	4.7
	532	0.3	1.3
Sb$_2$Se$_3$/TiO$_2$(S-100nm)/TiO$_2$-*meso*	---	2.4	11
	532	1.6	6.7
Sb$_2$Se$_3$/TiO$_2$(S-100nm)/Pt	---	2.2	---
	532	0.6	---
Sb$_2$Se$_3$/TiO$_2$(S-100nm)/TiO$_2$-*meso*/Pt	---	---	---
	532	2.9	---

The TPC decays for the platinized Sb$_2$Se$_3$-based photocathodes are shown in Figure 81. When Pt was used as HER catalyst, the back-hole transfer was only observed on the planar photocathode (Sb$_2$Se$_3$/TiO$_2$(S-100nm)/Pt, Figure 81a) at 0.4 V *vs* RHE, which was also shifted by 532 nm CW bias towards smaller times scales from 3.5 to 1 ms indicating accelerated recombination due to higher photocarriers concentration (Figure 81a').
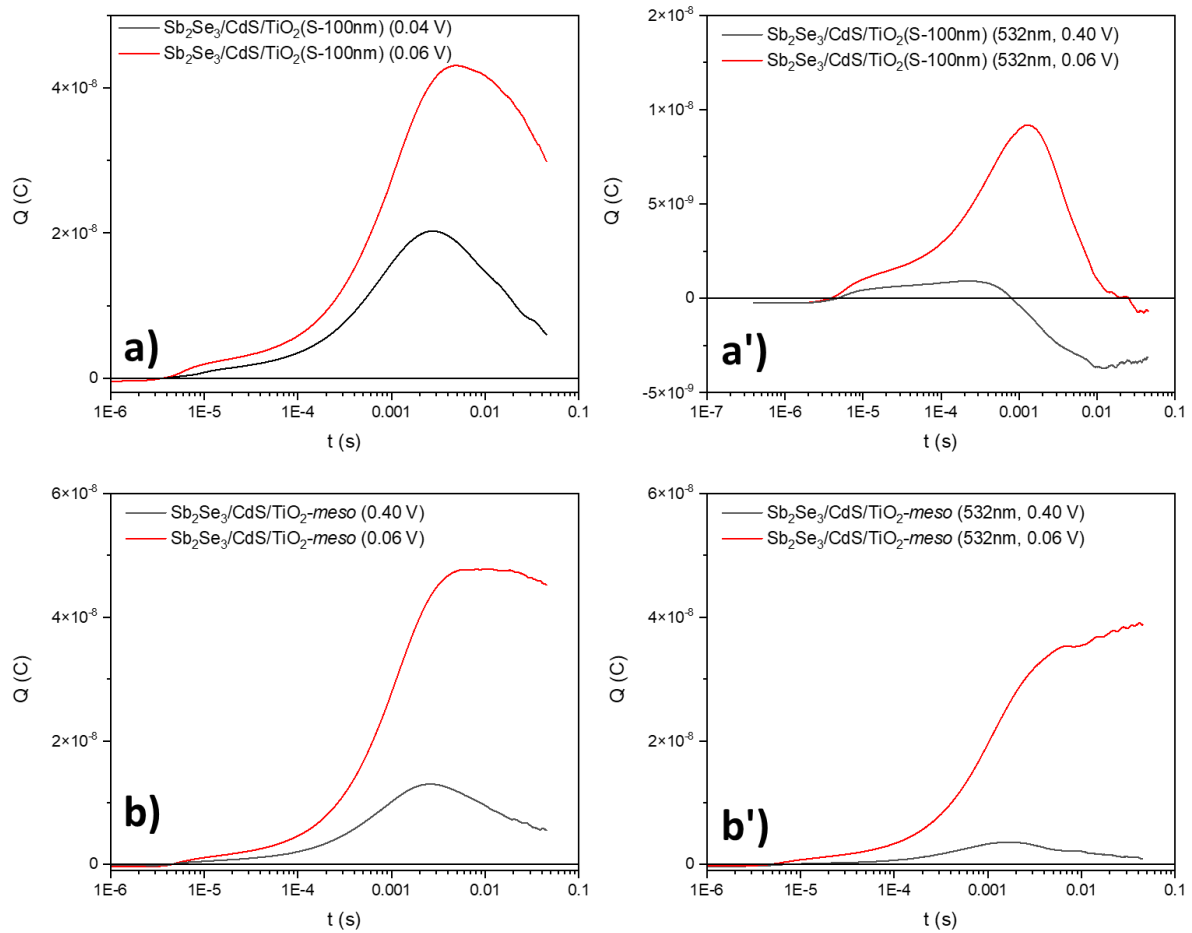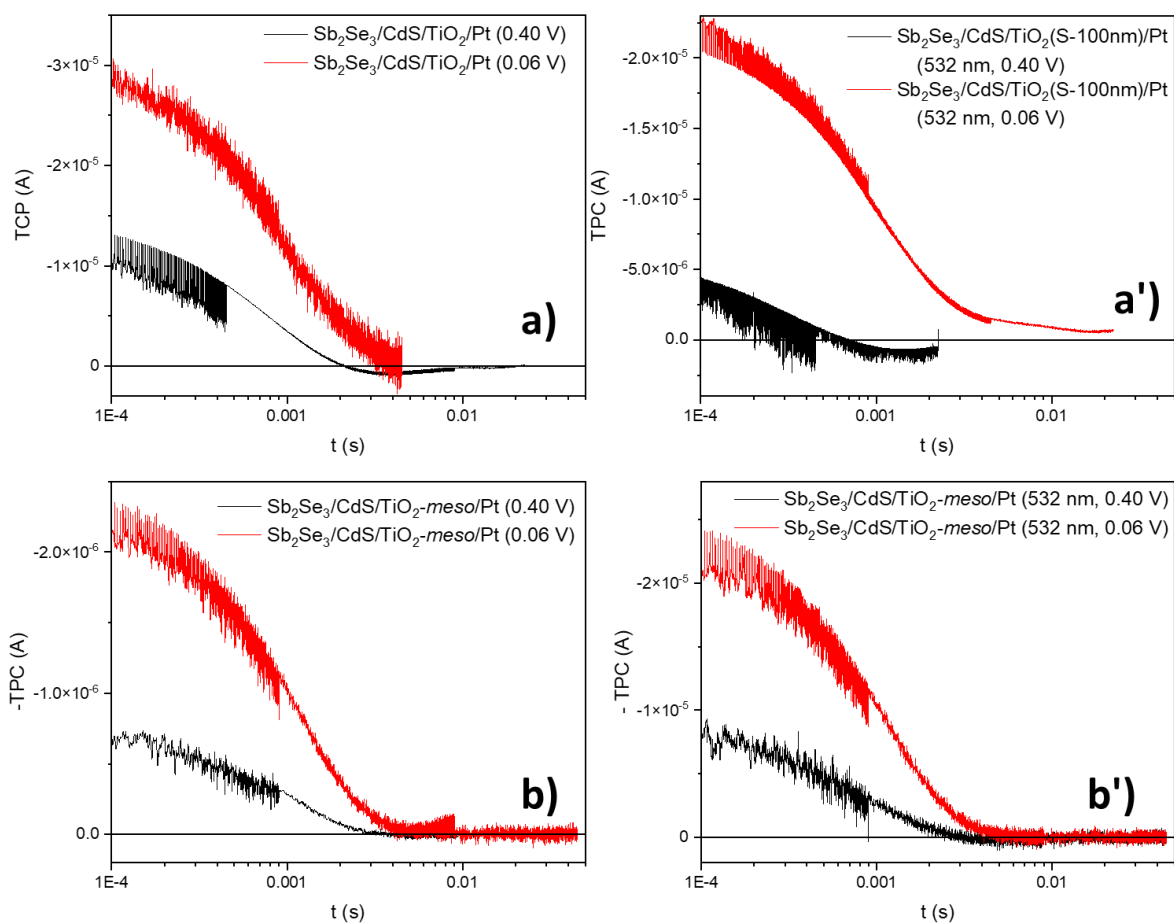
Figure 81 *TPC decays on platinized photocathodes: (a, a') Sb₂Se₃/TiO₂(S-100nm)/Pt and (b, b') Sb₂Se₃/TiO₂(S-100nm)/TiO₂-meso/Pt held at 0.4 (black line) and 0.06 (red line) V vs RHE following laser pulse (532 nm, 6 ns), and with a 532 nm CW bias light indicated as a' and b', in 0.1 M H₂SO₄ under N₂.*

The total charge of the platinized photocathodes is shown in Figure 82. For a planar device (Sb_2Se_3/TiO_2(S-100nm)/Pt, Figure 82a, a'), recombination was minimised only at more negative applied potential 0.06 V *vs* RHE. After the addition of the TiO_2-*meso*, the total passed charge increased and kept constant even at 0.4V *vs* RHE, suggesting efficient photoelectron extraction and low recombination levels (Sb_2Se_3/TiO_2(S-100nm)/TiO_2-*meso*/Pt, Figure 82b). This indicates that the most positive onset potential (*ca.* 0.5 V *vs* RHE) recorded for this architecture was the result of decreased recombination at 0.4V *vs* RHE, presumably due to the TiO_2-*meso* acting as a "electron reservoir". The Sb_2Se_3/TiO_2(S-100nm)/TiO_2-*meso* underwent a N_2 annealing at 350 °C which could induce Ti^{3+} states which are known as deep trap states[41] improving the electron storage at the TiO_2-*meso*.
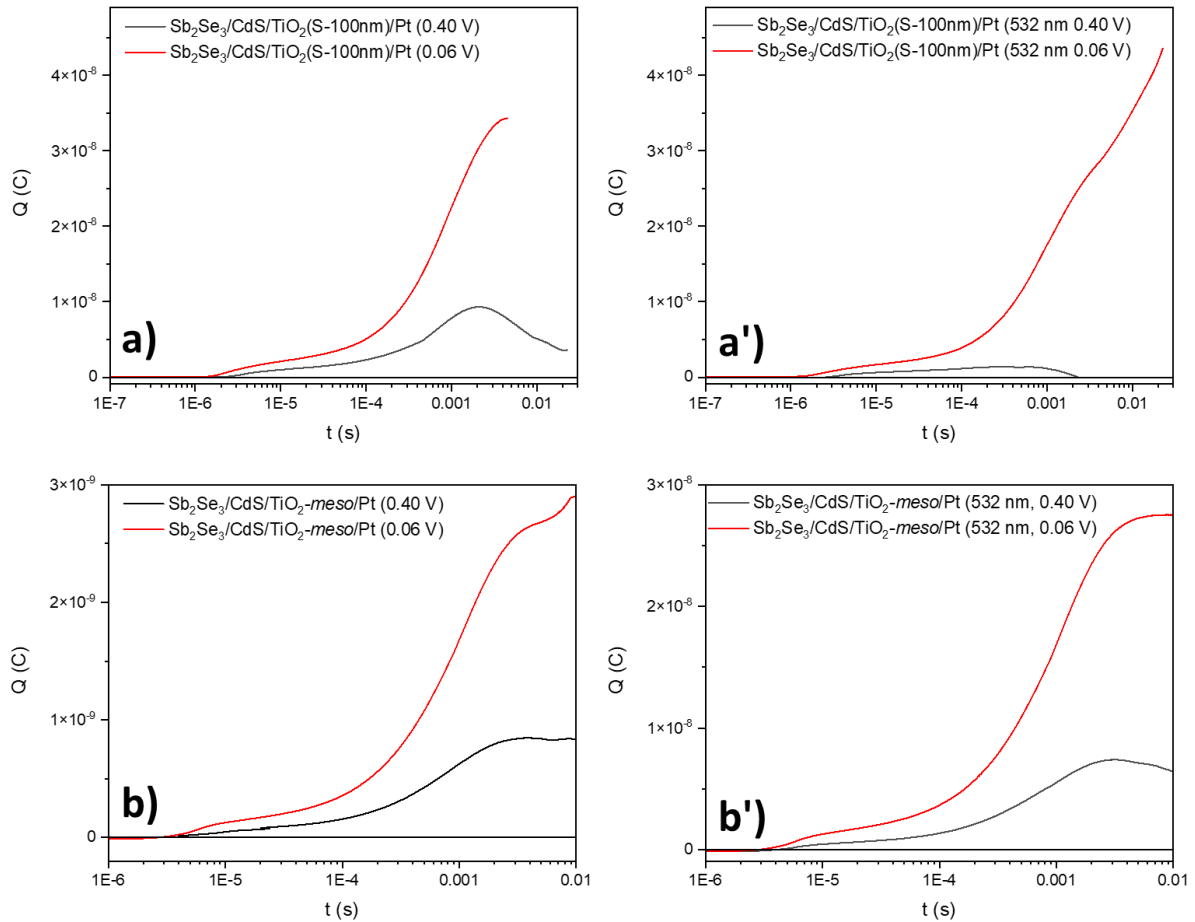
Figure 82 *Charge passed on platinized photocathodes: (a, a') Sb$_2$Se$_3$/TiO$_2$(S-100nm)/Pt and (b, b')*
Sb$_2$Se$_3$/TiO$_2$(S-100nm)/TiO$_2$-meso/Pt held at 0.4 (black line) and 0.06 (red line) V vs RHE following laser pulse
532 nm, 6 ns, and with a bias light 532 nm CW applied (a' and b'), in 0.1 M H$_2$SO$_4$ under N$_2$.

Interestingly, under 532 nm CW illumination the TiO$_2$-*meso*/Pt "buffer interface" seemed not to be

enough for keep up with the photoelectron generation to avoid the slow recombination at *ca.* 3 ms

(Sb$_2$Se$_3$/TiO$_2$(S-100nm)/TiO$_2$-*meso*/Pt, Figure 82b'). This slow recombination process is described by

the yellow arrows Figure 83 representing the electrons reinjected back into the photocathode,

where the green path indicates the favourable photocharge transfer for making H$_2$.
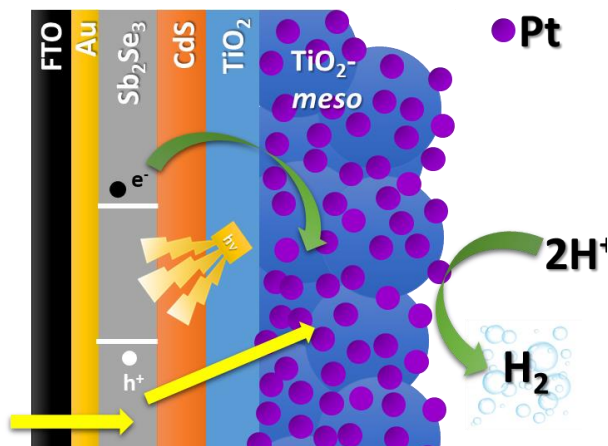
***Figure 83** Scheme of the millisecond hole recombination on Sb$_2$Se$_3$/TiO$_2$(S-100nm)/TiO$_2$-meso/Pt identified by TPC decays, where the green arrows representing the favourable photocharge transfer for H$_2$ production, and the yellow arrows are indicative of the slow recombination process.*

Au was incorporated to Sb$_2$Se$_3$/TiO$_2$(S-100nm)/TiO$_2$-*meso*/Pt as a hole transport layer (HTL), which should prevent recombination at the Au/Sb$_2$Se$_3$ *via* hole injection to the FTO. To further investigate this interface, a most exhaustive EDX analysis was carried out and the elemental analysis of the cross-sectional EDX is presented in Figure 84. Round Au agglomerates were identified in some regions (shown in purple) demonstrating partial failure of the HTL leading to the millisecond recombination process by the back-hole injection into the device. Note that the cross-sectional EDX analysis was carried out only after the TiO$_2$-*meso* layer was incorporated onto the complete device, therefore it was not possible to identify if the morphology of the Au layer changed during the N$_2$ annealing at 350 °C or from the CSS Sb$_2$Se$_3$ deposition at the same temperature.

Even with the partial failure of the Au layer, the TPC study demonstrated that the TiO$_2$-*meso*/Pt interface improved the onset potential of the Sb$_2$Se$_3$-based photocathodes by acting as a "buffer layer" that prevented recombination at the millisecond scale. This slow back hole-electron recombination was the cause of the large overpotential required to drive the HER on the planar structure (Sb$_2$Se$_3$/TiO$_2$(S-100nm)/Pt).
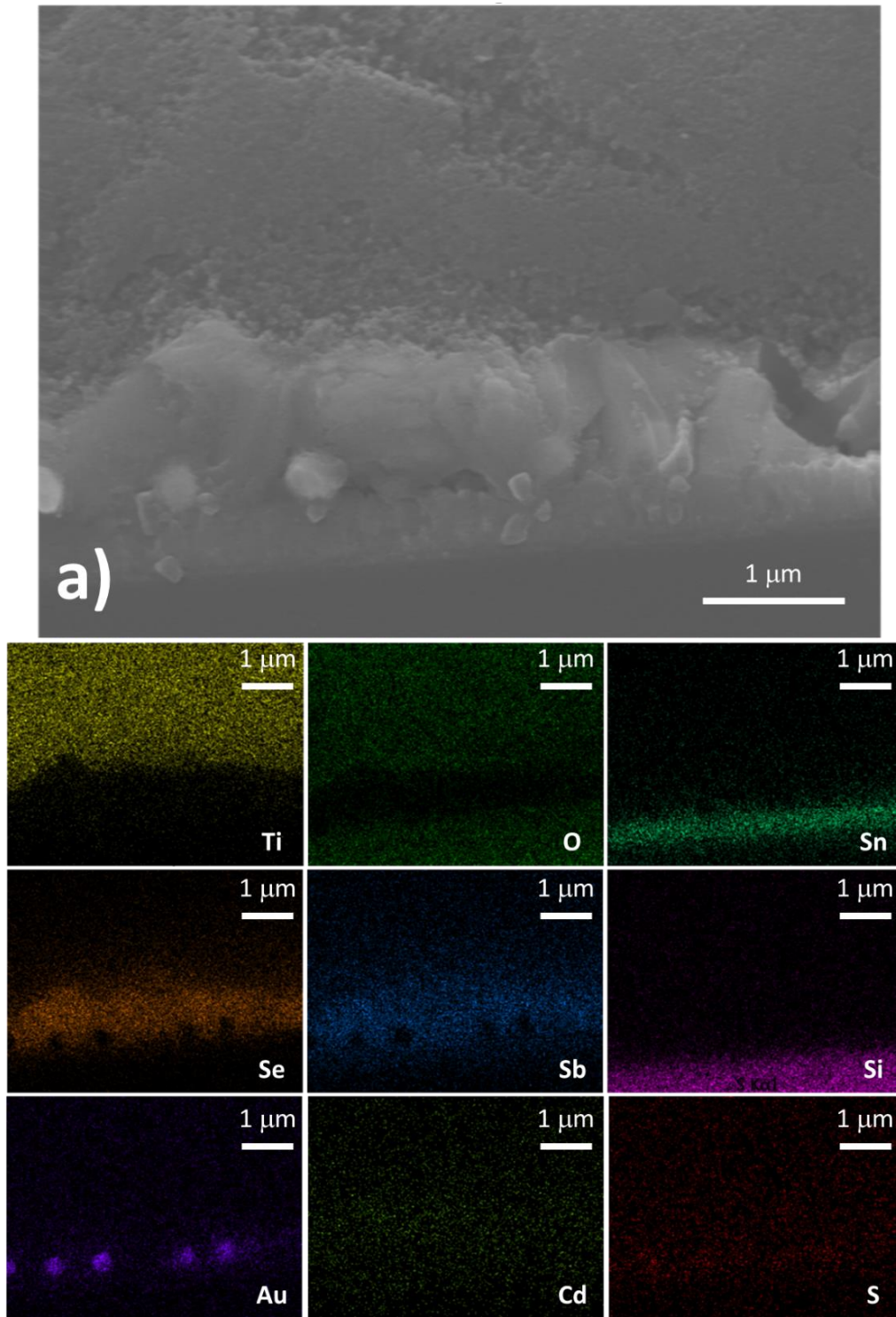
Figure 84. *(a) Cross-sectional SEM image of Sb$_2$Se$_3$/CdS/TiO$_2$(S-100nm)/TiO$_2$-meso and EDX maps of Ti, O, Sn, Se, Sb, Si, Au, Cd, S.*

Finally, the TPC analysis was also carried out on Sb₂Se₃/TiO₂(S-100nm)/TiO₂-*meso*/**NiP** in 0.1 M H₂SO₄ pH 3 (Figure 85). Notably, the **NiP** catalyst can efficiently extract the photoelectrons since no current flowing in the opposite direction related to the millisecond recombination process caused by the back-hole transfer was recorded when the potential was held at 0.4 V *vs* RHE. Even under 532 nm CW bias illumination, this recombination process was not observed. This result is in good agreement with the low light intensity test shown in section 3.4.1 confirming that the **NiP** can only cope with low photoelectron flux.
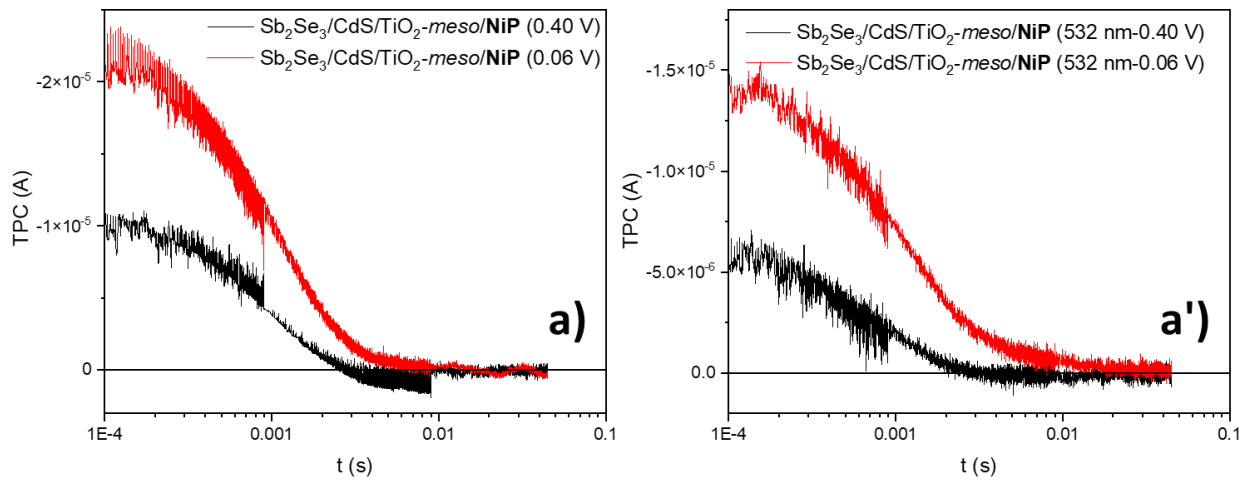
Figure 85 *TPC decays on Sb₂Se₃/TiO₂(S-100nm)/TiO₂-meso/**NiP** held at 0.4 (black line) and 0.06 (red line) V vs RHE following laser pulse (532 nm, 6 ns), and (a') with a 532 nm CW bias light, in 0.1 M Na₂SO₄ pH 3 under Ar.*

Appendix

Bi- and tri- exponential functions used to fit the TPC decays shown in Figure 79, Figure 81 and Figure 85.

$$y = A_1 * \exp\left(\frac{-x}{t_1}\right) + A_2 * \exp\left(\frac{-x}{t_2}\right) + y_0$$

$$y = A_1 * \exp\left(\frac{-x}{t_1}\right) + A_2 * \exp\left(\frac{-x}{t_2}\right) + A_3 * \exp\left(\frac{-x}{t_3}\right) y_0$$

Table 12 Fitted parameters using bi- and tri- exponential function of TPC decays shown in Figure 79, Figure 81, Figure 85.

Sample No.	532nm CW	0.4 V *vs* RHE						0.06 V *vs* RHE					
		A₁	T₁	A₂	T₂	A₃	T₃	A₁	T₁	A₂	T₂	A₃	T₃
1. TiO₂-*meso*/**NiP**	---	2.428E-4 ± 1.113E-5	4.881E-6 ± 8.579E-8	1.247E-5 ± 3.070E-8	0.001 ± 6.840E-6			3.251E-4 ± 6.144E-6	6.563E-6 ± 5.521E-8	2.348E-5 ± 3.479E-8	0.001 ± 3.857E-6		
	X	1.528E-4 ± 4.783E-6	5.381E-6 ± 7.168E-8	6.860E-6 ± 2.486E-8	6.834E-4 ± 4.628E-6			1.2727E-4 ± 1.394E-6	9.080E-6 ± 5.957E-8	1.488E-5 ± 2.091E-8	0.001 ± 4.414E-6		
2. TiO₂-*meso*/Pt	---	7.030E-6 ± 3.248E-7	6.820E-6 ± 1.598E-7	7.829E-7 ± 3.084E-9	9.121E-4 ± 8.154E-6	---	---	1.506E-5 ± 3.775E-7	7.305E-6 ± 9.041E-8	2.353E-6 ± 3.144E-9	0.001 ± 3.402E-6		
	X	8.094E-5 ± 4.403E-6	6.796E-6 ± 1.589E-7	9.280E-6 ± 2.638E-8	7.497E-4 ± 4.129E-6	----	----	1.480E-4 ± 3.260E-6	7.860E-6 ± 9.014E-8	2.387E-5 ± 3.316E-8	0.001 ± 3.494E-6		
3 TiO₂-*meso*	---	4.623E-5 ± 3.402E-6	9.835E-6 ± 4.597E-7	8.742E-6 ± --	8.529E-4 ± 0.201	8.200E-6 ± --	8.5293E-4 ± 0.215	2.449E-4 ± 1.101E-5	6.456E-6 ± 1.334E-7	3.792E-5 ± 6.222E-8	0.001 ± 6.052E-6		
	X	-1.373E-4 ± 0.011	0.001 ± 0.002	6.174E-5 ± 3.758E-6	5.917E-6 ± 1.565E-7	1.435E-4 ± 0.011	0.001 ± 0.001	2.229E-4 ± 3.802E-6	7.014E-6 ± 5.850E-8	2.612E-5 ± 2.714E-8	0.001 ± 3.858E-6		
4 TiO₂/Pt	---	9.683E-5 ± 4.221E-6	6.919E-6 ± 1.741E-7	1.005E-5 ± 8.848E-8	9.335E-4 ± 1.484E-5	7.477E-6 ± 1.854E-7	8.297E-5 ± 3.401E-6	1.238E-4 ± 1.038E-6	8.787E-6 ± 4.502E-8	3.141E-5 ± 5.462E-8	0.001 ± 5.181E-6		
	X	5.403E-5 ± 3.498E-6	7.578E-6 ± 2.672E-7	7.048E-6 ± 2.727E-7	1.288E-4 ± 7.406E-6	1.029E-6 ± 3.049E-7	5.864E-4 ± 1.952E-4	1.119E-4 ± 1.319E-6	8.069E-6 ± 5.458E-8	2.258E-5 ± 3.054E-8	0.001 ± 4.291E-6		
5 TiO₂	---	2.718E-5 ± 3.830E-8	9.054E-4 ± 2.568E-6	4.669E-4 ± 1.002E-5	5.452E-6 ± 4.686E-8	-1.691E-6 ± 3.039E-8	0.008 ± 2.474E-4	4.208E-4 ± 7.008E-6	6.097E-6 ± 4.484E-8	3.972E-5 ± 3.760E-8	0.001 ± 2.359E-6		
	X	-6.863E-6 ± 4.462E-7	0.001 ± 3.705E-5	1.277E-4 ± 4.330E-6	5.984E-6 ± 9.135E-8	1.085E-5 ± 4.242E-7	3.433E-4 ± 1.003E-5	1.121E-5 ± 0.32928	4.517E-4 ± 0.108	9.957E-6 ± 0.3298	4.517E-4 ± 0.122	1.763E-4 ± 7.547E-6	6.776E-6 ± 1.245E-7

1. Sb_2Se_3/CdS/TiO_2(S-100nm)/TiO_2-*meso*/**NiP**, **2** Sb_2Se_3/CdS/TiO_2(S-100nm)/TiO_2-*meso*/Pt, **3**. Sb_2Se_3/CdS/TiO_2(S-100nm)/TiO_2-*meso*,

4. Sb_2Se_3/CdS/ TiO_2(S-100nm)/Pt, **5** Sb_2Se_3/CdS/TiO_2(S-100nm)

3.6 Conclusions

Emergent chalcogenides semiconductors such as Sb$_2$Se$_3$ are promising photocathodes for their ability to achieve a high rate of photoelectron generation but they suffer from thermal instability. Furthermore, Sb$_2$Se$_3$ interfaces need to be protected by metal oxide capping layers where corrosion could occur due to photoelectron accumulation. However, research has mainly focused on the use of precious metal HER catalysts to prevent electron accumulation.

In this chapter, an alternative approach using a Sb$_2$Se$_3$/CdS/TiO$_2$(S100-nm)/TiO$_2$-*meso* photocathode to prevent photoelectron accumulation was studied. The high surface area TiO$_2$ scaffold was achieved by 68 h UV curing followed by N$_2$ annealing and demonstrated not to hinder Sb$_2$Se$_3$/CdS PEC activity. The high surface area photocathode enabled the loading increase of the earth abundant molecular catalyst **NiP** from 7.08 ± 0.43 nmol cm^{-2} to 45.76 ± 0.81 nmol cm^{-2}. Consequently, an 81-fold increment in the photocurrent was accomplished when compared to a similar device without the mesoporous TiO$_2$ (from -16 µA cm^{-2} up to -1.3 mA cm^{-2} at 0 V *vs* RHE). However, stability and activity under 100 mW cm^{-2} was still limited by the **NiP** turnover frequencies.

The hybrid photocathode Sb$_2$Se$_3$/CdS/TiO$_2$(S100-nm)/TiO$_2$-*meso*/**NiP** deactivated, presumably by the loss of the Ni centre since the XPS analysis post controlled potential photoelectrolysis (post-CPP) indicated that P, N, O related to the phosphonic ligand were retained although significantly shifted. Then, **NiP** deactivation triggered photoelectron accumulation causing the partial failure of the sputtered-TiO$_2$ layer. Although post-CPP characterization did not show changes in the morphology on the TiO$_2$ or Raman peaks associated to the Sb$_2$O$_3$ formed when the electrolyte reached the Sb$_2$Se$_3$. The failure of the sputtered TiO$_2$ was corroborated by the fact that the PEC activity of Sb$_2$Se$_3$/CdS/TiO$_2$(S100-nm)/TiO$_2$-*meso* structure was almost lost after using **NiP** catalyst in a CPP for 1 h, when the molecular catalyst was swapped by Pt for the same device architecture, compared with a pristine Sb$_2$Se$_3$/CdS/TiO$_2$(S100-nm)/TiO$_2$-*meso*/Pt photoelectrode exhibited a stable photocurrent of -2.5 mA cm^{-2} for 5 h with and E_{onset} of 0.5 V *vs* RHE.

The charge transfer in these devices was studied by transient photocurrent analysis and found that after light excitation, long lived photoelectrons are generated in Sb$_2$Se$_3$ which recombine in the millisecond scale within the planar devices (Sb$_2$Se$_3$/CdS/TiO$_2$(S100-nm)). The TiO$_2$-*meso*/Pt structures minimise the slow recombination process acting as an electron sink that enables a positive E_{onset} giving sufficient time for HER at Pt to occur. This slow recombination process dominated at low applied overpotentials where charge recombination is faster than H$_2$ catalysis (0.4 V *vs* RHE). Notably **NiP** was able to avoid recombination at low applied overpotentials however it can only cope with a limited photoelectron flux.

Further improvements in hybrid photocathode architectures for H$_2$ evolution require a molecular catalyst with higher turnover frequencies otherwise photoelectron accumulation may deactivate the device as observed for the Sb$_2$Se$_3$-based photocathodes. However, in order to develop the complete photoelectrochemical cell as the approach shown in Figure 1a an efficient photoanode, in terms of light absorption and high catalytic activity for oxygen evolution reaction is required to keep up with the photocurrent generated at the photocathode.

3.7 References

1   H. Shiel, O. S. Hutter, L. J. Phillips, J. E. N. Swallow, L. A. H. Jones, T. J. Featherstone, M. J. Smiles, P. K. Thakur, T. L. Lee, V. R. Dhanak, J. D. Major and T. D. Veal, *ACS Appl. Energy Mater.*, 2020, **3**, 11617–11626.

2   O. S. Hutter, L. J. Phillips, K. Durose and J. D. Major, *Sol. Energy Mater. Sol. Cells*, 2018, **188**, 177–181.

3   A. Mavlonov, T. Razykov, F. Raziq, J. Gan, J. Chantana, Y. Kawano, T. Nishimura, H. Wei, A. Zakutayev, T. Minemoto, X. Zu, S. Li and L. Qiao, *Sol. Energy*, 2020, **201**, 227–246.

4   S. Chen, T. Liu, Z. Zheng, M. Ishaq, G. Liang, P. Fan, T. Chen and J. Tang, *J. Energy Chem.*, 2022, **67**, 508–523.

5   B. A. Pinaud, J. D. Benck, L. C. Seitz, A. J. Forman, Z. Chen, T. G. Deutsch, B. D. James, K. N. Baum, G. N. Baum, S. Ardo, H. Wang, E. Miller and T. F. Jaramillo, *Energy Environ. Sci.*, 2013, **6**, 1983.

6   W. Yang, J. Park, H.-C. C. Kwon, O. S. Hutter, L. J. Phillips, J. Tan, H. Lee, J. Lee, S. D. Tilley, J. D. Major and J. Moon, *Energy Environ. Sci.*, 2020, **13**, 4362–4370.

7   W. Yang, J. H. Kim, O. S. Hutter, L. J. Phillips, J. Tan, J. Park, H. Lee, J. D. Major, J. S. Lee and J. Moon, *Nat. Commun.*, 2020, **11**, 1–10.

8   J. Tan, W. Yang, Y. Oh, H. Lee, J. Park, R. Boppella, J. Kim and J. Moon, *Adv. Energy Mater.*, 2019, **9**, 1900179, 1–12.

9   J. Park, W. Yang, J. Tan, H. Lee, J. W. Yun, S. G. Shim, Y. S. Park and J. Moon, *ACS Energy Lett.*, 2020, **5**, 136–145.

10   W. Yang, S. Lee, H.-C. Kwon, J. Tan, H. Lee, J. Park, Y. Oh, H. Choi and J. Moon, *ACS Nano*, 2018, **12**, 11, 11088–11097.

11   R. R. Prabhakar, W. Septina, S. Siol, T. Moehl, R. Wick-Joliat and S. D. Tilley, *J. Mater. Chem. A,* 2017, **5**, 23139–23145.

12   F. Niu, D. Wang, F. Li, Y. Liu, S. Shen and T. J. Meyer, *Adv. Energy Mater.*, 2019, **10**, 1900399, 1–24.

13   W. Jiang, X. Yang, F. Li, Q. Zhang, S. Li, H. Tong, Y. Jiang and L. Xia, *Chem. Commun.*, 2019, 55, 1414.

14   L. Gong, H. Yin, C. Nie, X. Sun, X. Wang and M. Wang, *ACS Appl. Mater. Interfaces*, 2019, **11**, 34010−34019.

15   K. L. Materna, R. H. Crabtree and G. W. Brudvig, *Chem. Soc. Rev.*, 2017, **46**, 6099–6110.

16   M. L. Helm, M. P. Stewart, R. M. Bullock, M. R. DuBois and D. L. DuBois, *Science*, 2011, **333**, 863–866.

17   W. J. Shaw, M. L. Helm and D. L. DuBois, *Biochim. Biophys. Acta Bioenerg.*, 2013, **1827**, 1123–1139.

18   M. A. Gross, A. Reynal, J. R. Durrant and E. Reisner, *J. Am. Chem. Soc.*, 2014, **136**, 356–366.

19   A. Paracchino, V. Laporte, K. Sivula, M. Grätzel and E. Thimsen, *Nat. Mater.*, 2011, **10**, 456–461.

20   T. E. Rosser, T. Hisatomi, S. Sun, D. Antón-García, T. Minegishi, E. Reisner and K. Domen, *Chem. Eur. J.*, 2018, **24**, 18393–18397.

21   J. J. Leung, J. Warnan, D. H. Nam, J. Z. Zhang, J. Willkomm and E. Reisner, *Chem. Sci.*, 2017, **8**, 5172–5180.

22   T. E. Rosser, M. A. Gross, Y. H. Lai, E. Reisner, B. C. M. Martindale, G. A. M. Hutton, C. A. Caputo, E. Reisner, M. A. Gross, A. Reynal, J. R. Durrant, E. Reisner, J. J. Leung, J. Warnan, D. H. Nam, J. Z. Zhang, J. Willkomm and E. Reisner, *Chem. Sci.*, 2016, **7**, 4024–4035.

23   T. Berger, D. Monllor-Satoca, M. Jankulo*v*ska, T. Lana-Villarreal and R. Gomez, *ChemPhysChem*, 2012, **13**, 2824–2875.

24   M. Schreier, J. Luo, P. Gao, T. Moehl, M. T. Mayer and M. Grätzel, *J. Am. Chem. Soc.*, 2016, **138**, 1938–1946.

25   D. R. Lide and G. W. A. Milne, Handbook of Data on Organic Compounds, CRC Press, Florida, 3rd edn., 1993.

26   N. Negishi, K. Takeuchi, *Thin Solid Films*, 2001, **392**(2), 249–253.

27   R. E. Williams, Q. M. Ramasse, K. P. McKenna, L. J. Phillips, P. J. Yates, O. S. Hutter, K. Durose, J. D. Major and B. G. Mendis, *ACS Appl. Mater. Interfaces*, 2020, **12**, 21730–21738.

28   L. J. Phillips, C. N. Savory, O. S. Hutter, P. J. Yates, H. Shiel, S. Mariotti, L. Bowen, M. Birkett, K. Durose, D. O. Scanlon and J. D. Major, *IEEE J. Photovolt.*, 2019, **9**, 544–551.

29   A. Paracchino, N. Mathews, T. Hisatomi, M. Stefik, S. D. Tilley and M. Grätzel, *Energy Environ. Sci.*, 2012, **5**, 8673–8681.

30   G. Liang, T. Liu, M. Ishaq, Z. Chen, R. Tang, Z. Zheng, Z. Su, P. Fan, X. Zhang and S. Chen, *J. Chem. Eng.*, 2022, **431**, 133359.

31   NIST X-ray Photoelectron Spectroscopy (XPS) Database, Version 3.5, https://srdata.nist.gov/xps/, (accessed 26 July 2022).

32   R. Franke, T. Chassé, P. Streubel and A. Meisel, *J. Electron. Spectros. Relat. Phenomena*, 1991, **56**, 381–388.

33   M. Pelavin, D. Hendrickson, J. Hollander, W. Jolly, D. N. Hendrickson, J. M. Hollander and W. L. Jolly, *J. Phys. Chem.*, **74**, 5, 1116–1121.

34   L. S. Dake, D. R. Baer and D. M. Friedrich, *J. Vac. Sci. Technol.*, 1989, **7**, 1634–1638.

35   K. L. Materna, R. H. Crabtree and G. W. Brudvig, *Chem. Soc. Rev.*, 2017, **46**, 6099–6110.

36   D. W. Wakerley, M. A. Gross and E. Reisner, *Chem. Commun.*, 2014, **50**, 15995–15998.

37   A. Ruff, S. Janke, J. Szczesny, S. Alsaoub, I. Ruff, W. Lubitz and W. Schuhmann, *ACS Appl. Energy Mater.*, 2019, **2**, 2921–2929.

38   S. Chen, T. Liu, M. Chen, M. Ishaq, R. Tang, Z. Zheng, Z. Su, X. Li, X. Qiao, P. Fan and G. Liang, *Nano Energy*, 2022, **99**, 107417.

39   S. D. Tilley, M. Schreier, J. Azevedo, M. Stefik and M. Gratzel, *Adv. Funct. Mater.*, 2014, **24**, 303–311.

40   J. E. Thorne, Y. Zhao, D. He, S. Fan, S. Vanka, Z. Mi and D. Wang, *Phys. Chem. Chem. Phys*, 2017, **19**, 29653.

41   N. Beermann, G. Boschloo and A. Hagfeldt, *J. Photochem. Photobiol. A*, 2002, **152**, 213–218.

Chapter 4

Integrating a photocathode for CO_2 Reduction

Scope of the chapter

In this chapter, a Sb_2Se_3 based device for light absorption was coupled with Ni-based molecular catalysts for building a precious metal-free hybrid photocathode. Two different approaches were studied, first the homogeneous inclusion of Ni cyclam in solution (**Ni(cyc)$^{2+}$**), and second the covalent binding of a Ni cyclam modified with a phosphonic acid as anchoring group, **Ni(cycP)**. Both approaches had poor photoelectrochemical activity towards CO production, and low photocurrent: *ca.* 5 µA cm^{-2} at -0.41 V *vs* RHE for **Ni(cyc)$^{2+}$** in solution, and *ca.* 20 µA cm^{-2} at -0.39 V *vs* RHE for Sb_2Se_3/TiO_2(S-20 nm)/**Ni(cycP)**. Large spikes were evident in the LSV indicating that photoelectrons were not extracted efficiently by the catalyst. To increase **Ni(cycP)** loading, and therefore the photoelectron extraction, a TiO_2 mesoporous layer was incorporated. The TiO_2-*meso*/**Ni(cycP)** interface was first studied without the Sb_2Se_3 light absorber. Since the **Ni(cycP)** has a strong coordination between the anchoring group and the Ni centre, different attempts to decrease their intramolecular interaction were carried out by changing the solvent, the immobilization length, and by adding Ag on the TiO_2-*meso* to provide a different surface for the molecular catalyst binding. By ICP, it was found that **Ni(cycP)** content remained ~14 nmol cm^{-2} for most of the attempts, which was with significantly lower loading compared with other phosphonated molecular catalyst anchored on TiO_2-*meso* scaffolds (40-80 nmol cm^{-2})[1,2].

Elemental analysis post electrolysis revealed P and Ni on the electrode surface, however the low CO selectivity (CO:H$_2$ 4.2:95.8) suggested the **Ni(cycP)** was not a suitable catalyst for a hybrid CO$_2$ photocathode.

Co based molecular catalysts were also explored, however the complete hybrid photocathode was not assembled due to the low stability of the carboxylic acid anchoring group in **CoPP** and the low catalytic activity of **CoPc** when immobilised on CNT by π-π stacking, recently reported.[3]

The Sb$_2$Se$_3$ based photocathodes studied in this chapter were made in collaboration with Dr Jon Major's group (Dr Thomas Shalvey and Dr Oliver Hutter) and the **Ni(cycP)** molecular catalyst was kindly provided by Dr Gaia Neri from the Stephenson Institute for Renewable Energy at University of Liverpool.

4.1 Ni cyclam molecular catalyst

Ni cyclams have demonstrated high catalytic activity for CO production in aqueous electrolytes.[4] In this section, **Ni(cyc)$^{2+}$**, **cyc** = 1,4,8,11-tetraazacyclotetradecane and the modified catalyst with phosphonic pendant arm, **Ni(cycP)**, **cycP** = [(1,4,8,11-tetraazacyclotetradecan-1-yl)methyl] phosphonic acid were used alongside Sb₂Se₃ as light absorber to build hybrid CO₂R photocathodes. Their molecular structure is shown in Figure 86.
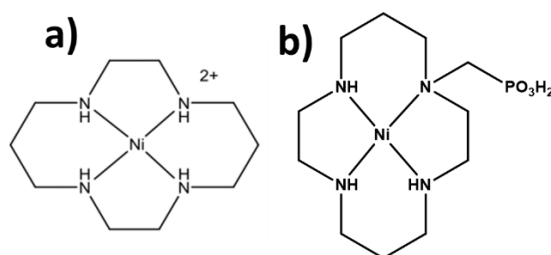

Figure 86 *Molecular structure of Ni(cyc)$^{2+}$ and **Ni(cycP)** catalysts.*

Ni cyclam is an active catalyst for CO₂RR in aqueous electrolyte and presents high selectivity towards CO especially at mild acidic conditions.[5,6] The highest catalytic activity was observed on a Hanging Mercury Drop Electrode (HMDE) since the key intermediate [(L)Ni(CO)]$^+$ was destabilised by lowering the Ni^I-CO interaction at the strongly adsorbed catalyst on Hg.[4,7] Otherwise, the CO binding on Ni^I is too strong that promotes the catalyst deactivation.[8] The proposed **Ni(cyc)$^{2+}$** reaction mechanism is shown in Figure 87.

It has been reported that **Ni(cyc)$^{2+}$** can also reduce CO₂ using other conductive substrates like Glassy Carbon (GC), acting as homogeneous catalyst.[4,9] Therefore, the first hybrid photocathode was based on **Ni(cyc)$^{2+}$** in solution and Sb₂Se₃/TiO₂-S(20 nm) as light absorber.

Regarding to the electrolyte, acetonitrile (MeCN) was chosen as solvent considering the solubility of CO₂ is higher in MeCN (280 mM) than in water (33 mM)[10]. CO₂R at **Ni(cyc)$^{2+}$** is a proton dependant electron transfer reaction,[6] therefore H₂O was used here as the proton source required to drive catalysts. The water concentration (5% H₂O, 6 M) was chosen based on two criteria: (i) to ensure the TiO₂ CBM was negative enough to drive CO₂R (at -1.14 V *vs* NHE in 0.1 M TBAPF₆, 5% H₂O, MeCN).[11] And (ii)

considering the water content for the optimal **Ni(cyc)$^{2+}$** catalytic activity in MeCN (3-8 M H$_2$O).[12] Figure 88 shows the CV of 1 mM **Ni(cyc)$^{2+}$**, 5% H$_2$O, 0.1 M TBAPF$_6$ in MeCN under N$_2$ and CO$_2$ using GC as WE. Under N$_2$, the Ni$^{I/II}$ redox couple is evident at -1.27 V *vs* NHE, which vanished in a CO$_2$-sataurated electrolyte as well as the increase in current in line with previous reports.[9]
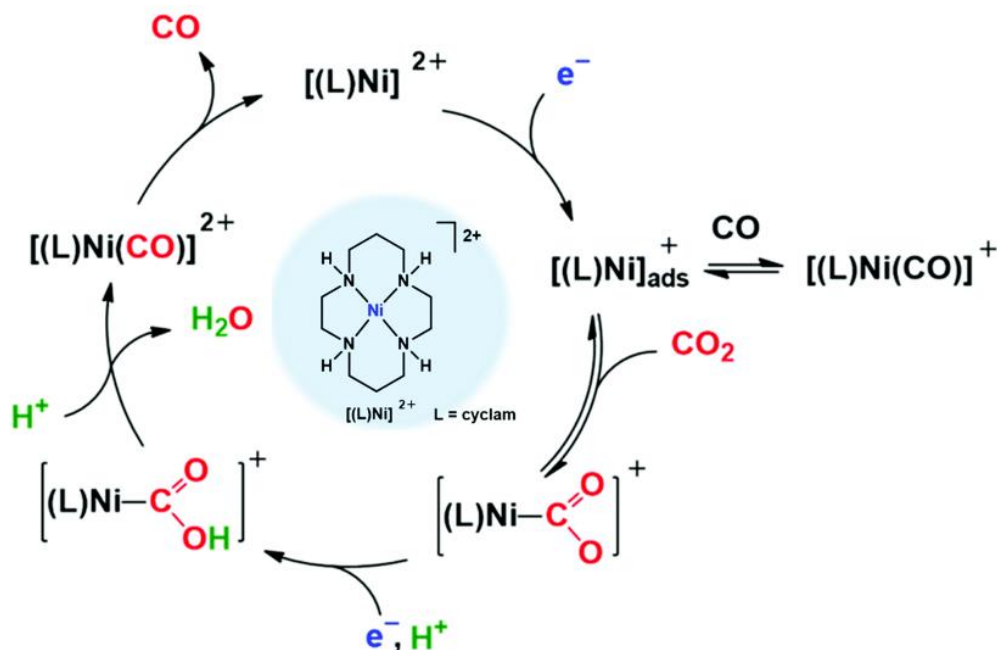

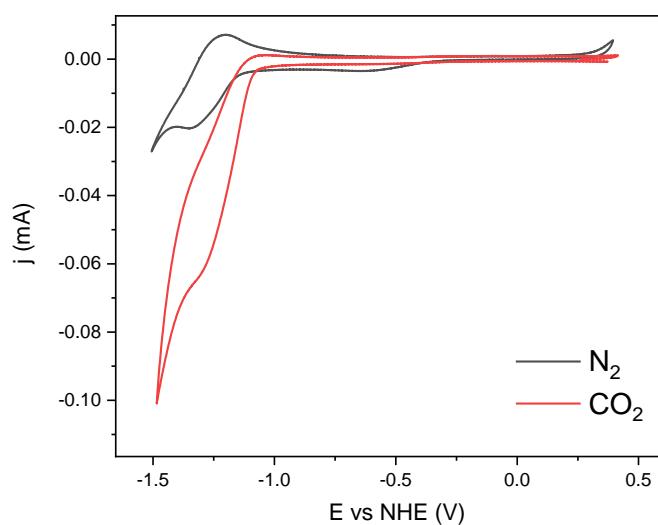**Figure 87** *Ni(cyc)$^{2+}$ reaction mechanism, reproduced from^{4,7}*

Figure 88 *CV of 1 mM Ni(cyc)$^{2+}$ in 0.1 M TBAPF$_6$, 5% H$_2$O, MeCN at 100 mV s^{-1} under N$_2$ and CO$_2$.*

4.1.1 Sb₂Se₃ photoelectrodes with benchmark metal catalysts

It is important to point out that the Sb_2Se_3-based photocathodes studied in this section did not include the CdS buffer layer, which exhibited the best PEC performance in Chapter 2 since these experiments were carried out before the photocathode optimisation. However, the Sb_2Se_3/TiO_2-S(20nm)/Pt architecture used here exhibited -6 mA cm^{-2} at 0 V *vs* RHE in 0.1 M H_2SO_4, and control devices with Au and Pt were made to benchmark the photoelectron generation available for CO_2R or H_2, respectively in 0.1 M TBAPF$_6$, 5% H_2O, MeCN under N_2 and CO_2. Pt was electrodeposited at -30 µA cm^{-2} for 15 min in 0.1 M Na_2SO_4 and ~1.5 nm Au was thermally evaporated on Sb_2Se_3/TiO_2-S(20 nm), all the experimental details are provided in section 6.2.5. Figure 89 shows the LSV at 10 mV s^{-1} of (a) Sb_2Se_3/TiO_2(S-20 nm)/Pt and (b) Sb_2Se_3/TiO_2(S-20 nm)/Au in 0.1 M TBAPF$_6$, 5% H_2O, MeCN under N_2 and CO_2. When Pt is used as electron extractor (Figure 89a), a photocurrent of 50 µA cm^{-2} is observed at -1.0 V *vs* RHE, and the dark current significantly increases after this potential. In contrast, when Au is used as catalyst in a CO_2-saturated electrolyte, an increase in photocurrent is observed at more positive potentials compared with the photocurrent measured under N_2 at ~-0.4 V *vs* NHE. However, large spikes are evident for both metal catalysts indicating inefficient charge extraction.[13] Note that the Au loading was not optimised, and significant difference in photocurrent and CO:H_2 selectivity were reported from 2 up to 20 nm Au thicknesses when used as a catalyst on *p*-Si/TiO_2 in aqueous electrolyte 0.1 M HKCO$_3$.[14]
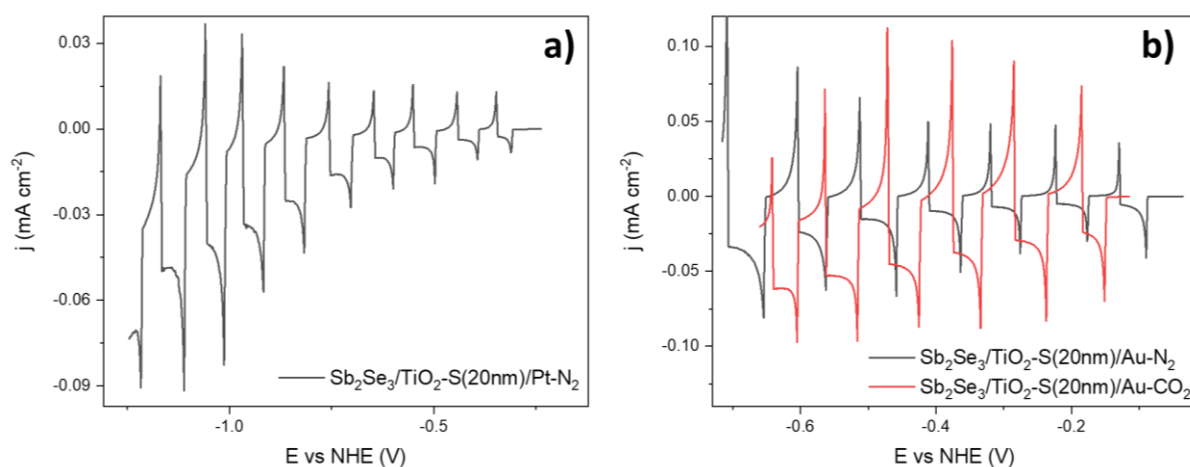

Figure 89 *Chopped Light LSV at 10 mV s⁻¹ of (a) Sb₂Se₃/TiO₂(S-20 nm)/Pt and (b) Sb₂Se₃/TiO₂(S-20 nm)/Au in 0.1 M TBAPF₆, 5% H₂O, MeCN under N₂ and CO₂.*

Although an increase in Au loading could improve the photoelectron extraction, Figure 89 provides a noble metal catalyst benchmark performance for the Sb$_2$Se$_3$/TiO$_2$(S-20nm) architecture in a non-aqueous electrolyte with 5% water.

4.1.2 Ni(cyc)$^{2+}$ homogeneous approach for CO$_2$R hybrid photocathodes

Once the **Ni(cyc)$^{2+}$** catalytic activity was assessed (Figure 88), and the PEC activity of Sb$_2$Se$_3$ photocathodes was evaluated using Au and Pt as benchmark catalysts (Figure 89). The first CO$_2$R hybrid photocathode was assembled using Sb$_2$Se$_3$/TiO$_2$(S-20 nm), where the TiO$_2$ capping layer was made by sputtering, and previously annealed (200 °C) to improve the TiO$_2$ crystallinity, all the experimental details are provided in section 6.1.2.2. Figure 90a shows the chopped light LSV at 10 mV s^{-1} in 1 mM **Ni(cyc)$^{2+}$**, 0.1 M TBAPF$_6$, 5% H$_2$O, MeCN, and only a small increase in photocurrent under CO$_2$-saturated electrolyte was observed when compared with N$_2$. Additionally, large spikes in the LSV demonstrate catalysis was not fast enough to keep up with the photoelectrons generated.[13] The LSV were recorded consecutively, first under N$_2$ and followed by CO$_2$-saturated electrolyte, the increase in dark current under CO$_2$ was likely associated to the degradation of the semiconductor at potentials more negative than −0.8 V *vs* NHE. The CA test (shown in Figure 90b) was carried out for 2 h with a pristine sample at −0.41 V *vs* RHE which corresponds to the highest photocurrent under CO$_2$ in Figure 90a, the photocurrent was *ca.* −5 μA cm^{-2} for 2 h with selectivity CO:H$_2$ of 59.4:40.6.

Due to the large spikes in the chopped light LSV and low photocurrent density in the CA test compared with the state-of-the-art hybrid devices for CO$_2$R presented in Chapter 1, the covalent immobilization of the molecular catalyst on TiO$_2$ was then explored, since it could potentially improve the charge transfer at this interface.[15]
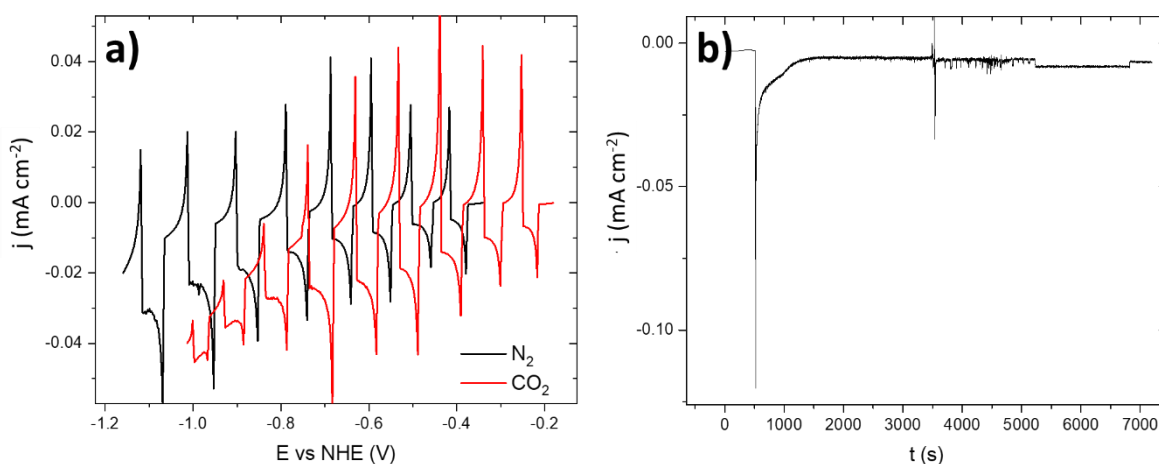
Figure 90 *(a) Chopped Light LSV of Sb₂Se₃/TiO₂(S-20 nm) at 10 mV s⁻¹ under N₂ and CO₂, and (b) CPP test at -0.41 V vs RHE for 2 h in 1 mM Ni(cyc)²⁺, 0.1 M TBAPF₆, 5% H₂O, MeCN saturated with CO₂, 60 mW cm⁻², 340≤ λ ≤900 nm.*

4.1.3 Ni(cycP) covalently linked on TiO₂ for CO₂R

4.1.3.1 Previous studies using Ni(cyc)²⁺ derivatives

Ni(cyc)²⁺ has been successfully modified with anchoring groups like carboxylic (**Ni(cycC)**)[16] and phosphonic acid groups (**Ni(cycP)**)[17] for the covalent linking on metal oxides.[6] When -COOH anchoring group was incorporated to the **Ni(cyc)²⁺**, the catalytic activity of the parent compound was retained in solution, and high CO selectivity was achieved even at low pH's.[16,18] However, previous studies developed in the group demonstrated that the strength of the covalent linking through the carboxylic acid of **Ni(cycC)** on TiO₂ was not enough to be used in an CO₂R hybrid photocathode, since the molecular catalyst washed off during the consecutive scans in the CV analysis.[6]

Phosphonic acid groups exhibit higher stability compared to carboxylic anchors. However, there is a stability trade-off for electron injection rate at the metal oxide/molecular catalyst interface, being slower at phosphonic acid anchors.[19] However, by TAS analysis was demonstrated that the immobilization of the **Ni(cycP)** on TiO₂-*meso* films through phosphonic anchor groups improved the electron transfer rate. Following the typical absorption of electron accumulation on the TiO₂ CB at 900 nm, a time decay of $\tau_1=10.00 \pm 0.24$ s was recorded when the **Ni(cyc)²⁺** was in solution. In contrast, a faster decay was

observed after **Ni(cycP)** immobilization: $\tau_1 = 2.07 \times 10^{-4} \pm 2.1 \times 10^{-5}$ s and $\tau_2 = 5.6 \times 10^{-3} \pm 4 \times 10^{-4}$ s in MeCN, using 0.1 TEOA (triethanolamine) as hole scavenger.[6] Additionally, effective CO catalysis was demonstrated when **Ni(cycP)** was used alongside a Ru dye for light harvesting (**RuP** = Ru^{II}(2,2'-bipyridine)$_2$(2,2'-bipyridine-4,4'-diylbis(phosphonic acid)), when both were immobilised on ZrO_2 nanoparticles. A CO production of 322 μmol h^{-1} g^{-1}$_{(RuP+ \textbf{Ni(cycP)})}$ was measured after 7 h of constant light irradiation at 40 mW cm^{-2}, and $375 \leq \lambda \leq 795$ nm.[17] In the next section, the **RuP** dye was replaced by the Sb_2Se_3 based photocathode for light collection and **Ni(cycP)** as CO_2R catalyst.

4.1.3.2 Ni(cycP) on planar TiO₂

The interface TiO_2(S-100 nm)/**Ni(cycP)** was first investigated without the light absorber underneath. Note that for the control experiment the TiO_2 thickness was increased from 20 to 100 nm, considering that pinhole-free ALD TiO_2 films require over 40 nm thickness.[20] The immobilization was carried out by soaking a TiO_2(S-100 nm) films in 10 mM **Ni(cycP)** ethanolic solution for 48 h, all the experimental details are provided in the section 6.2.2. The TiO_2(S-100 nm) SEM image without Sb_2Se_3 underneath is shown in Figure 91 panel (a), and panel (b) presents the CV of TiO_2(S-100 nm)/**Ni(cycP)** at 100 mV s^{-1} in 0.1 M TBAPF$_6$, 5% H_2O, in MeCN under N_2 and CO_2, and a control film with no catalyst (TiO_2(S-100 nm), indicated as dotted lines). An increase in the current under a CO_2-saturated electrolyte was observed, interestingly the same trend was noticed for the film with no catalyst, although with a smaller increase in the current. This behaviour has been previously associated with the catalytic activity of the Ti^{3+} states towards CO_2R for methanol production at potentials more negative than -1.58 V *vs* Fc$^+$/Fc (-0.95 V *vs* NHE).[21] Note that no redox features associated to the Ni$^{II/I}$ couple were identified on TiO_2(S-100 nm)/**Ni(cycP)** at -1.53 V *vs* Fc$^+$/Fc (-0.9 V *vs* NHE), contrary to **Ni(cycP)** covalently anchored to the ZrO_2.[17]
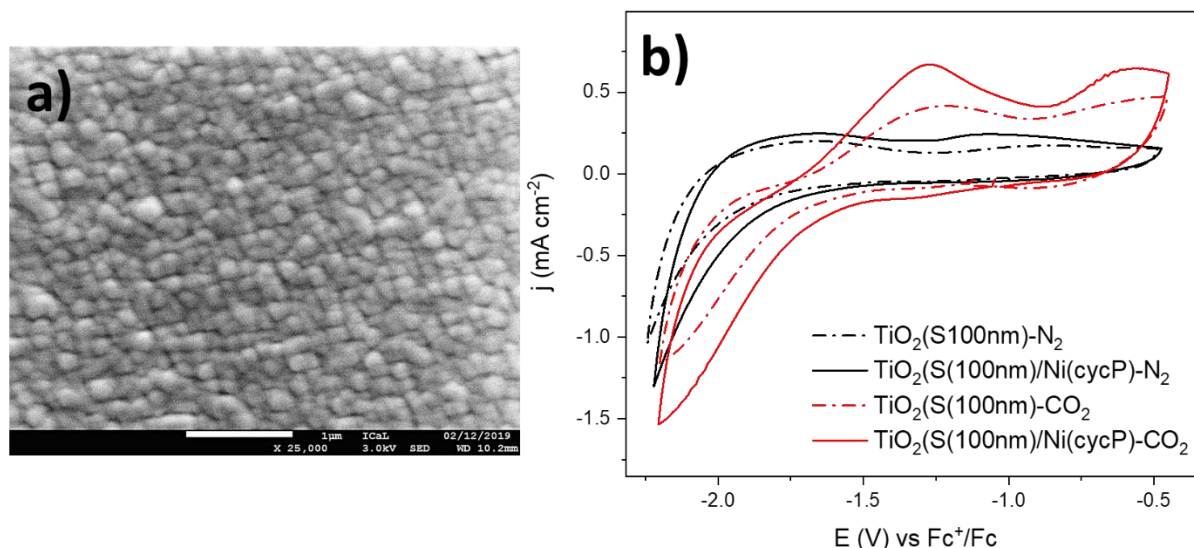
Figure 91. *(a) SEM image of TiO$_2$(S-100 nm) without Sb$_2$Se$_3$ underneath, and (b) CV of TiO$_2$(S-100 nm)/**Ni(cycP)** at 100 mV s^{-1} in 0.1 M TBAPF$_6$, 5% H$_2$O, in MeCN under N$_2$ and CO$_2$, and the control film with no catalyst TiO$_2$(S-100 nm), indicated as dotted lines.*

Longer soaking times were also carried out up to 7 days, as well as prior TiO$_2$(S-100 nm) cleaning by UV light before the **Ni(cycP)** immobilization, however no redox features associated with the Ni$^{II/I}$ couple were observed.

The immobilization of **Ni(cycP)** on Sb$_2$Se$_3$/TiO$_2$(S-20 nm) was carried out following the same experimental protocol described above (section 6.2.2). Figure 92a shows the chopped light LSV of Sb$_2$Se$_3$/TiO$_2$(S-20 nm)/**Ni(cycP)** at 10 mV s^{-1} in 0.1 M TBAPF$_6$, 5% H$_2$O, in MeCN, under N$_2$ and CO$_2$. Only a small increase in photocurrent was observed in a CO$_2$-saturated electrolyte at -1.0 V *vs* Fc$^+$/Fc. The CPP was carried out at -1 V *vs* Fc$^+$/Fc (Figure 92b) since an increase in photocurrent was observed at this potential without the significant dark current increment. The photocurrent was *ca.* 20 μA cm^{-2} during the first hour and increased over the time, which could be associated with photocorrosion of Sb$_2$Se$_3$ due to the failure of the TiO$_2$ protection layer. After 2 h of continuous CPP test, the selectivity was 2:1 for H$_2$ and CO respectively. However, as a tracer was not used the total Faradic Efficiency was only *ca.* 9% which was associated with a non-gas tight electrochemical cell (a flat glass cell was used instead of the customised gas tight H cell, the experimental details are fully described section 6.3.7).

The fact that CO was measured indeed demonstrated some catalytic activity of **Ni(cycP)** after the covalent immobilization although not accurately.
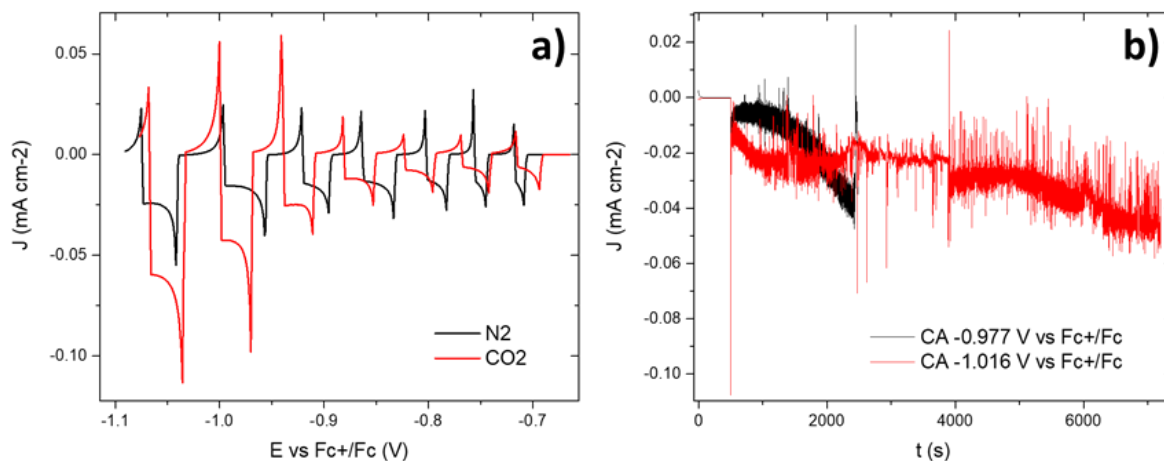

Figure 92 *(a) Chopped Light LSV of Sb₂Se₃/TiO₂(S-20 nm)/**Ni(cycP)** at 10 mV s⁻¹ under N₂ and CO₂, and (b) CPP test at -1.02 V vs Fc⁺/Fc for 2 h in 0.1 M TBAPF₆, 5% H₂O, CO₂-saturated MeCN, using 60 mW cm⁻², 340≤ λ ≤900 nm*

To determine the **Ni(cycP)** loading on Sb₂Se₃/TiO₂(S-20 nm), the UV vis spectrum of 10 mM **Ni(cycP)** ethanolic solution was recorded before and after the catalyst immobilization. However, no significant difference was measured due to the low **Ni(cycP)** extinction coefficient (indicated in Table 13).[6] As an alternative quantification method, the **Ni(cycP)** was stripped off by soaking the film in 1 M NaOH for 72 h. By ICP was found that the catalyst loading was 6.84 x10 ⁻² nmol cm⁻². Note that even the Ni signal was identified by ICP, this value was very close to the detection limit of the instrument. Although **Ni(cycP)** loading in the planar device needs to be taken with caution, it suggested that the low photocurrent was likely associated to the low catalyst content.

4.1.3.3 Ni(cycP) on TiO₂-mesoporous films

One of the possible reasons of the low **Ni(cycP)** content on TiO₂ is the chemical structure of the catalyst itself (Figure 86b). By ATR-FTIR analysis was previously found that the phosphonic anchor arm has a

strong intramolecular coordination with the Ni centre since the bands at 982 and 970 cm^{-1} associated to the v_{as}(P-O-Ni) and v_s(P-O-Ni) were identified for **Ni(cycP)** crystals and when the molecular catalyst was dissolved in water.[6] This strong binding to the Ni centre may make the phosphonic group less available to bind to the TiO₂ support, resulting in lower overall catalyst loading. In ethanol, **Ni(cycP)** forms a purple solution, and the UV vis spectra shown in Figure 93 provides information about how the phosphonic group interacts with metal centre through the Ni d-d transitions. Two maxima are observed at 343 and 544 nm, which are indicative of the octahedral configuration. (Table 13 shows the possible Ni(cyclam) molecular geometries). The UV-Vis spectrum of the parent Ni(cyclam) in aqueous solution presented in Figure 93b[6] shows a maximum at 453 nm typical of the square planar configuration (71%), and at 453 nm for the octahedral configuration (29%).[22] Here, it is important to note that in the square planar configuration of Ni(cyclam), the Ni centre does not exhibit a steric hindrance for either being adsorbed to the HMDE (commonly studied as working electrode, WE),[4,23,24] or binding to CO₂ trough the proton amines.[9,25] Furthermore, this configuration promotes the CO detachment from the [Ni(CO)(cyc)]$^+$ intermediates.[12]
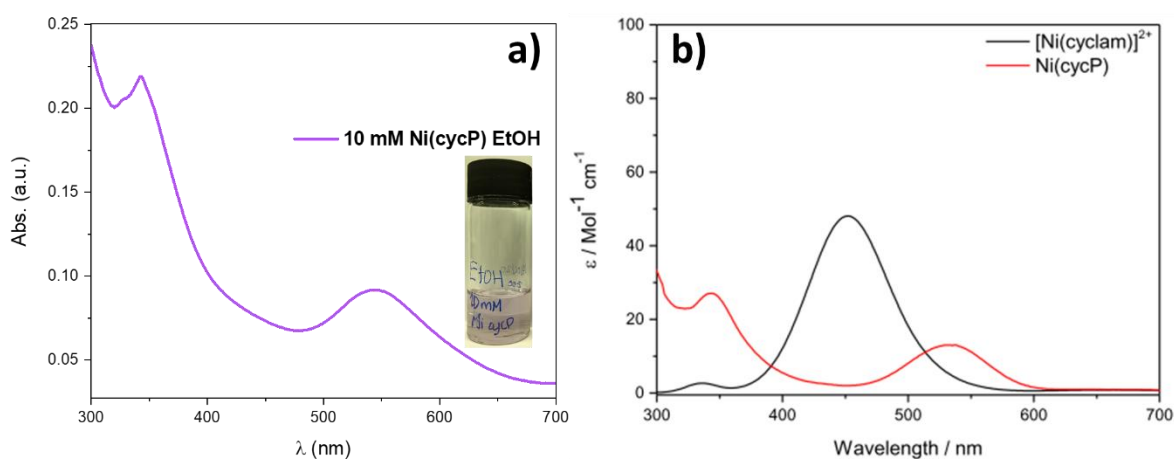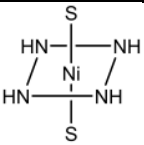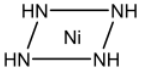

Figure 93 *UV vis spectra of 10 mM **Ni(cycP)** in (a) ethanol and (b) water. Panel (b) was reproduced from*[6]

Table 13 Possible Ni(cyclam) molecular geometries.[6]

Molecular structure	Solvent coordination	UV-Vis absorption peaks
Octahedron	Strong	344 nm ($\varepsilon_{344 \, nm}$ = 24 M^{-1} cm^{-1})[6]
		533 nm ($\varepsilon_{533 \, nm}$ = 12 M^{-1} cm^{-1})[6]
Square planar	Weak	453 nm [6]

In previos ATR-FTIR studies developed in the group, it was found that after lowering the pH of an **Ni(cycP)** aqueous solution, the peak at 1075 cm^{-1} associated to the v_{as}(PO₃) disappeared, meanwhile a new peak at 1162 cm^{-1} indicated the protonation of the phosphonic groups (P-O-H). However, the peaks related to v_{as}(P-O-Ni) and v_s(P-O-Ni) did not disappear completely, instead they were shifted and assigned to oxygen protonation in P-O-Ni indicating that the phosphonic anchoring group in **Ni(cycP)** remained intermolecularly coordinated to the Ni center.[6]

Before the catalyst immobilization on TiO₂-*meso*, different solvents and soaking times were explored in an attempt to change the molecular geometry of **Ni(cycP)** from octahedral to square planar (by lowering the interaction strength between the anchoring group and the Ni centre), in this way the pendant phosphonic acid group would be readily available to be anchored to the TiO₂. The change in **Ni(cycP)** molecular structure was followed by UV-vis spectroscopy. Figure 94a shows the picture (after 21 days) of 10 mM of **Ni(cycP)** in different solvents (H₂O, MeOH, EtOH), and Figure 94b-d present their UV-vis spectra at different aging times. When **Ni(cycP)** was dissolved in water, the colour of the solution did not change, contrary a clear change in colour was noticed after 21 days in MeOH. This behaviour was also observed only after 90 days when ethanol was used as a solvent. Even though a clear change in colour was observed for longer soaking times in MeOH and EtOH, the peak at 533 nm did not disappear completely, whereas the peak at 344 nm was shifted towards longer wavelengths (374 nm) without reaching 453 nm associated to the square planar configuration. Only after 90 days in EtOH,

a small peak was observed at 433 nm. This either suggested that the protonation process of the phosphonic acid group was a slow process and/or the **Ni(cycP)** remained in equilibrium between the octahedral and square planar geometries. Figure 94 suggested that the **Ni(cycP)** molecular geometry did not change significantly from octahedral to square planar by using different solvents or aging times, since no absorption peak was observed at 453 nm, indicative of the square planar configuration.
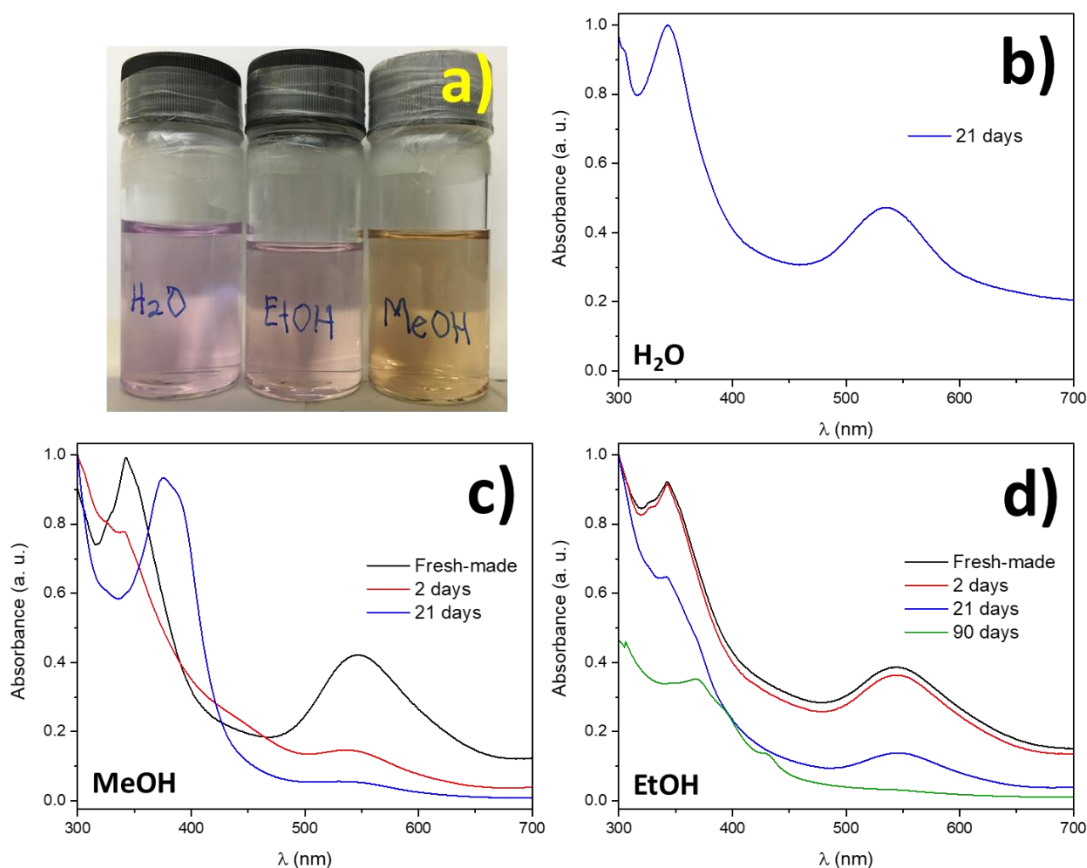
Figure 94 *(a) Picture of 10 mM of **Ni(cycP)** after 21 days in different solvents: (a) H₂O, (b) MeOH and (c) EtOH and UV-vis spectra at different aging times.*

The fact that the **Ni(cycP)** was successfully immobilised on ZrO_2, previously demonstrated by **(i)** ATR-FTIR where the peak associated to the Ni-O-P at 963 cm^{-1} disappeared, and at 1152 cm^{-1} a new peak related to the P-O-H appeared after the catalyst immobilization,[6] and **(ii)** the CV exhibited the redox features of the Ni$^{I/II}$ couple at -0.8 V *vs* NHE in MeCN:H₂O 9:1, 0.1 M TBAPF₆ under N₂ and CO₂,[17] proved that the phosphonic acid group can be covalently anchored to a metal surface. However, it also

suggested that **Ni(cycP)** immobilization on metal oxides is strongly dependent on the nature of the metal oxides and properties such as the acid/basic character could promote/inhibit the catalyst immobilization.

The next approach was adding Ag onto TiO_2-*meso* to provide different anchoring centres for the **Ni(cycP)**. It was previolsy demonstrated that the phosphonated Ru-Ru absorber-catalyst structure immobilised on TaON[26] and C_3N_4[27] significantly improved the photocatalytic activity after the addition of Ag nanoparticles. The catalytic role of Ag was ruled out as no CO_2 reduction was seen in the absence of the Ru-Re supramolecular structure. Instead TAS analysis indicated that the Ag nanoparticles were able to collect shallow trapped photoelectrons generated by the C_3N_4, pooling electrons at the carbon nitride/Ru-Re interface and facilitating charge transfer.[27] It is therefore feasible that addition of metal nanoparticles to the semiconductor-catalyst interface of hybrid photoelectrodes may also be beneficial.

Figure 95a shows a scheme of the Ag decorated TiO_2-*meso* structure for **Ni(cycP)** anchoring. Ag was electrodeposited on TiO_2-*meso* by applying a constant current of -30 µA cm⁻² for 10 min (Charge: 0.018 C) in 1 mM $AgNO_3$, 0.1 M KNO_3, under N_2. All the experimental details are included in section 6.2.6. After the Ag deposition no change in film colour, nor agglomerates were observed in the SEM image (Figure 95b), only the typical TiO_2-*meso* morphology.

After Ag electrodeposition, the molecular catalyst was immobilised by soaking the film in a fresh-made 0.1 mM **Ni(cycP)** ethanolic solution for 48 h. Figure 96 shows the CV of (a) the bare TiO_2-*meso*, (b) TiO_2-*meso*/Ag, and (c) TiO_2-*meso*/Ag/**Ni(cycP)** at 100 mV s⁻¹ in 0.1 M TBAPF₆, 5% H_2O, in MeCN under N_2 (black trace) and CO_2 (red trace). The current increased significantly under CO_2-saturated electrolyte even without catalyst addition (or Ag) consistent with Figure 91b. The comparison of the current density at -1 V *vs* NHE, which could be related to the **Ni(cycP)** catalytic effect, is presented in Table 14, being the highest on TiO_2-*meso*/Ag/**Ni(cycP)** electrode. Furthermore, no clear redox features associated to the Ni$^{I/II}$ couple were observed at -0.9 V *vs* NHE.[6]
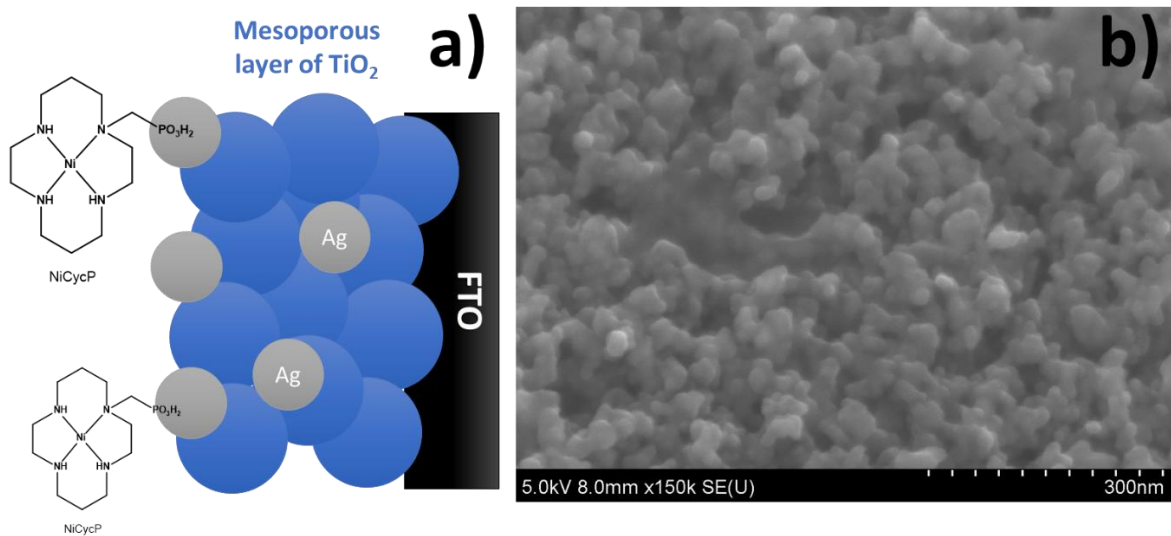
Figure 95 *(a) Scheme of Ag decorated TiO_2-meso structure (not drawn at scale). (b) SEM image of TiO_2-meso after Ag electrodeposition.*

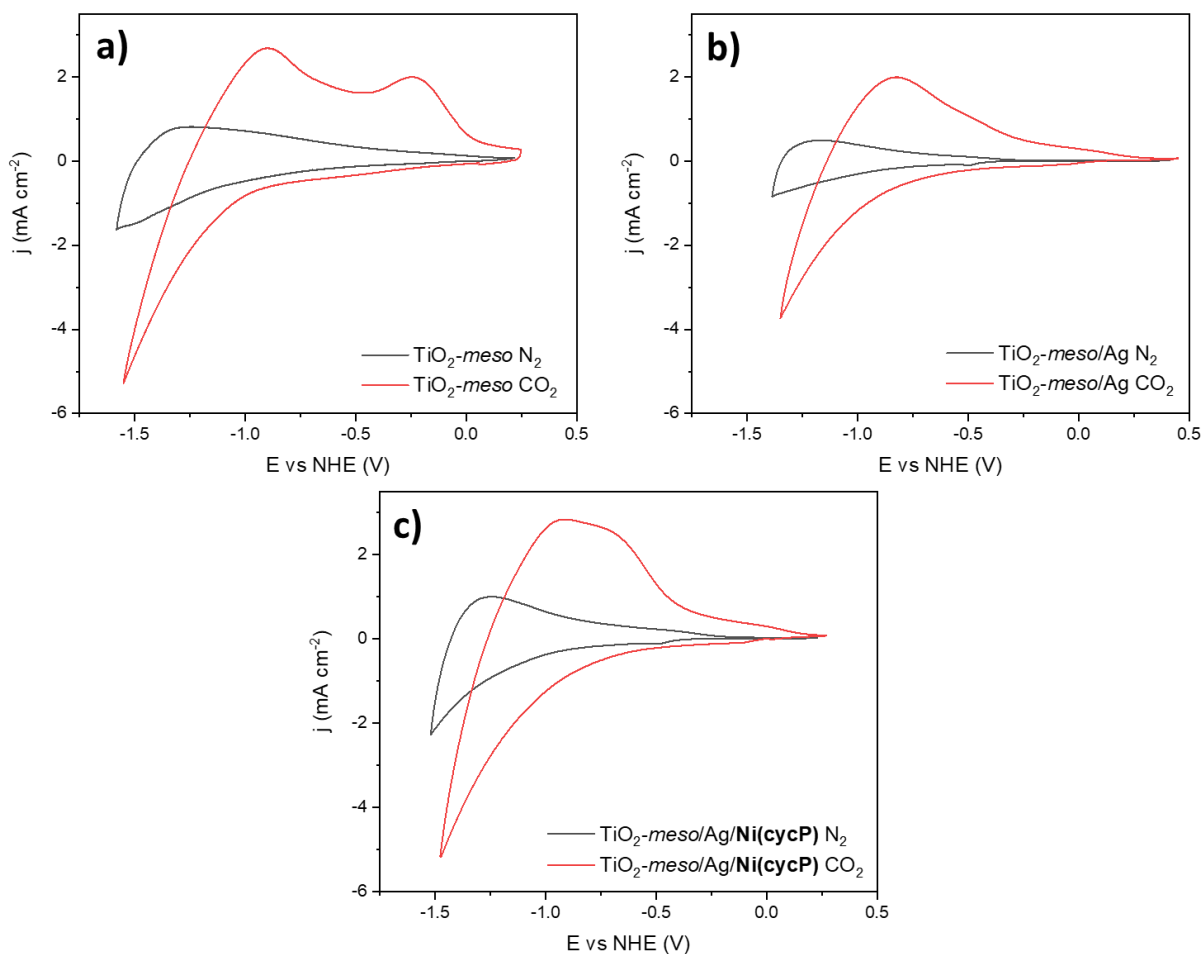***Figure 96*** *CV of (a) the bare TiO_2-meso, (b) TiO_2-meso/Ag, and (c) TiO_2-meso/Ag/**Ni(cycP)** at 100 mV s^{-1} in 0.1 M TBAPF$_6$, 5% H$_2$O, in MeCN under N$_2$ (black trace) and CO$_2$ (red trace).*

Since only a small increase in current was observed in the CV and to further assess the TiO$_2$-*meso*/Ag/**Ni(cycP)** catalytic activity, a CA test was carried out at *ca.* -1.0 V *vs* RHE for 30 min, the charge and faradic efficiency are presented in Table 14. TiO$_2$-*meso*/Ag/**Ni(cycP)** exhibited the highest production of CO compared with the samples without **Ni(cycP)**, however the selectivity CO:H$_2$ was 4:96, indicating that almost all the charge was used to produce H$_2$. Note that for these set of experiments, the Faradaic Efficiencies were far off 100%, which was attributed to a gas leaking electrochemical flat cell, and the lack of methane tracer.

Table 14 Electrochemical tests summary of CV analysis at 100 mV s^{-1} under N$_2$ and CO$_2$ (Figure 96) and CA (ca. −1.0 V vs RHE for 30 min) on the bare TiO$_2$-meso, (b) TiO$_2$-meso/Ag, and (c) TiO$_2$-meso/Ag/Ni(cycP) in CO$_2$ saturated 0.1 M TBAPF$_6$, 5% H$_2$O, in MeCN.

| | | CV | | CA | | | |
| | | $-j$ (mA cm^{-2}) @ -1.0 V *vs* RHE | E$_{app}$ *vs* RHE | Charge | % FE | | % Total |
Electrode	**Gas**			**C**	**H$_2$**	**CO**	
TiO$_2$-*meso*	N$_2$	-0.48	-1.32	0.030	57.38	0.39	57.78
	CO$_2$	-0.82	-1.04	0.333	38.98	0.00	38.98
TiO$_2$-*meso*/Ag	N$_2$	-0.31	-1.06	0.025	26.87	0.25	27.12
	CO$_2$	-1.18	-0.98	0.373	46.71	0.13	46.84
TiO$_2$-*meso*/Ag/**Ni(cycP)**	N$_2$	-0.37	-1.01	0.038	30.74	0.00	30.74
	CO$_2$	-1.24	-1.01	0.114	41.70	1.83	43.53

To confirm that the **Ni(cycP)** remained attached on the electrode surface, an EDX mapping (Figure 97) and elemental analysis were carried out after the CA test. Ni and P indicated the presence of the **Ni(cycP)** post electrolysis. The elemental composition of three different samples is presented in Table 15, where Ti was the main constituent and Sn was assigned to the FTO. From the EDX mapping is also evident that Ag was well-dispersed on the TiO$_2$-*meso*, since no agglomerates were observed.
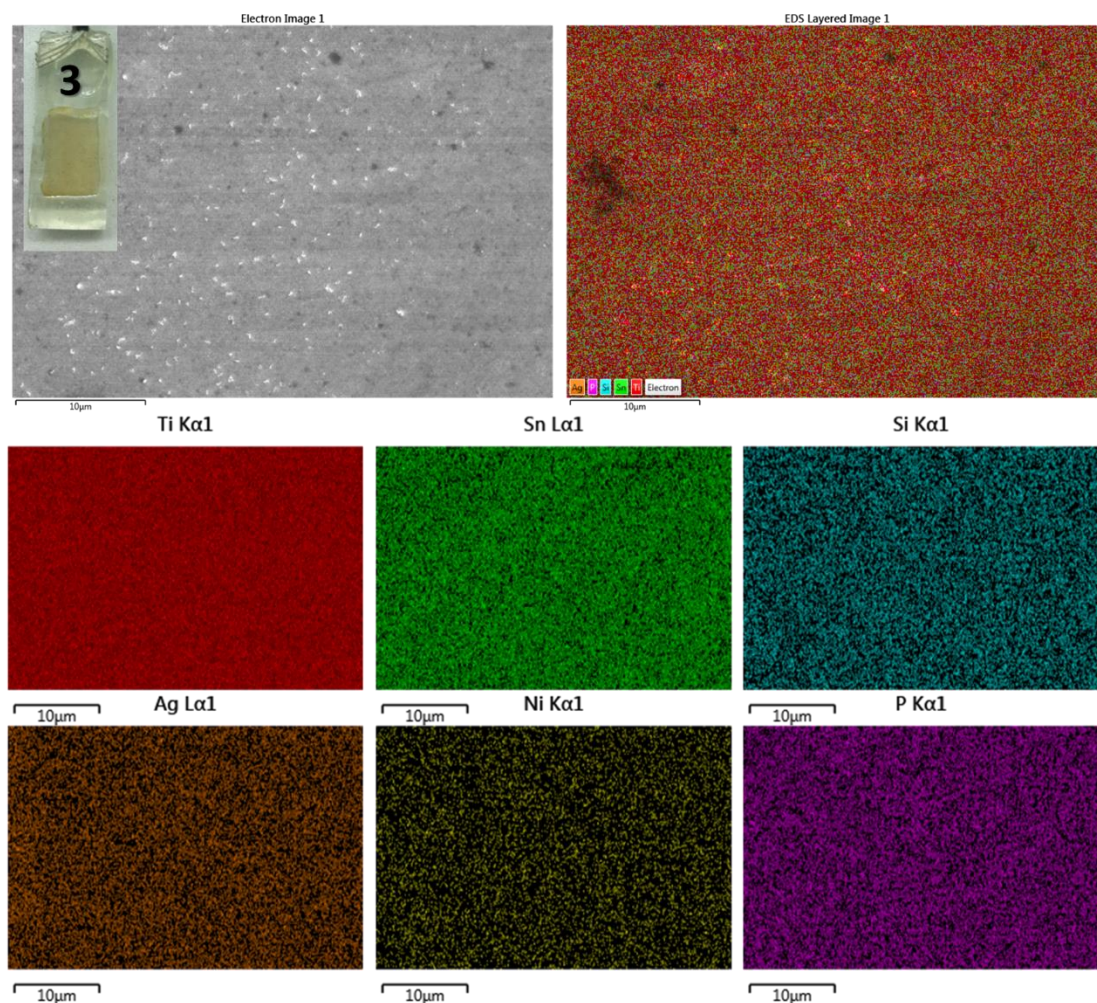
*Figure 97 EDX mapping of TiO$_2$-meso/Ag/**Ni(cycP)** after the CA test at −1.0 V vs RHE for 30 min in a CO$_2$-saturated 0.1 M TBAPF$_6$, 5% H$_2$O, in MeCN.*

*Table 15 Elemental analysis of TiO$_2$-meso/Ag/**Ni(cycP)** after the CA test at ca. −1.0 V vs RHE for 30 min in a CO$_2$-saturated 0.1 M TBAPF$_6$, 5% H$_2$O, in MeCN.*

Element	Atomic %
Ti	94.560 ± 0.433
Sn	3.070 ± 0.139
P	1.257 ± 0.012
Ni	0.413 ± 0.012
Ag	0.367 ± 0.006

In an attempt to further increase the molecular catalyst loading on TiO_2-*meso*/Ag, 21-day-old solution (10 mM **Ni(cycP)** in H_2O, EtOH and MeOH) were used instead of a fresh made solution, since the **Ni(cycP)** aging time in different solvents slightly modify the catalyst geometry, which could promote the covalent binding on TiO_2-*meso* as shown in Figure 94. The immobilization time was kept constant for 48 h. Figure 98 shows the CV of TiO_2-*meso*/Ag/**Ni(cycP)** at 100 mV s^{-1} in 0.1 M $TBAPF_6$, 5% H_2O, in MeCN under N_2 (black trace) and CO_2 (red trace). The redox features associated to the $Ni^{I/II}$ redox couple were not identified and no clear increase in current density was observed regardless of the solvent used for the immobilisation. Table 16 shows the current density at -1.0 V *vs* RHE and control TiO_2-*meso*/Ag without catalyst, which in fact exhibit the highest current density. ICP analysis was used to determine the catalyst loading, and the stripping off was carried out according to the protocol previously described (1 M NaOH for 48 h). Table 16 also presents the **Ni(cycP)** content on TiO_2-*meso* using 21-day-old solution of 10 mM **Ni(cycP)** in H_2O, ethanol and methanol as solvents for catalyst immobilisation, the highest loading (14 nmol cm^{-2}) was achieved with ethanol. The soaking time for **Ni(cycP)** immobilization was extended from 48 h up to 7 days, however no significant loading increase was observed. The **Ni(cycP)** loading was *ca*. 14 nmol cm^{-2}, regardless the soaking time and solvent used.

Table 16 *Current density at -1.0 V vs RHE from CV's of Figure 98, and **Ni(cycP)** loading when a 21-day-old 10 mM **Ni(cycP)** in H_2O, ethanol and methanol were used for the catalyst immobilisation, and **Ni(cycP)** content determined by ICP analysis after stripping in 0.1 M NaOH.*

Electrochemical technique	Gas	$-j$ (mA cm^{-2}) @ -1.0 V *vs* RHE			
		No Ni(cycP)	H₂O	EtOH	MeOH
Cyclic voltammetry	**N₂**	-1.40	-1.04	-1.30	-1.29
	CO₂	-2.65	-1.84	-2.24	-2.17
		Immobilisation time	**[Ni(cycP)] nmol cm^{-2}**		
ICP analysis		48 h	7.37	14	7.22
		7 days	--	13.5	14.1
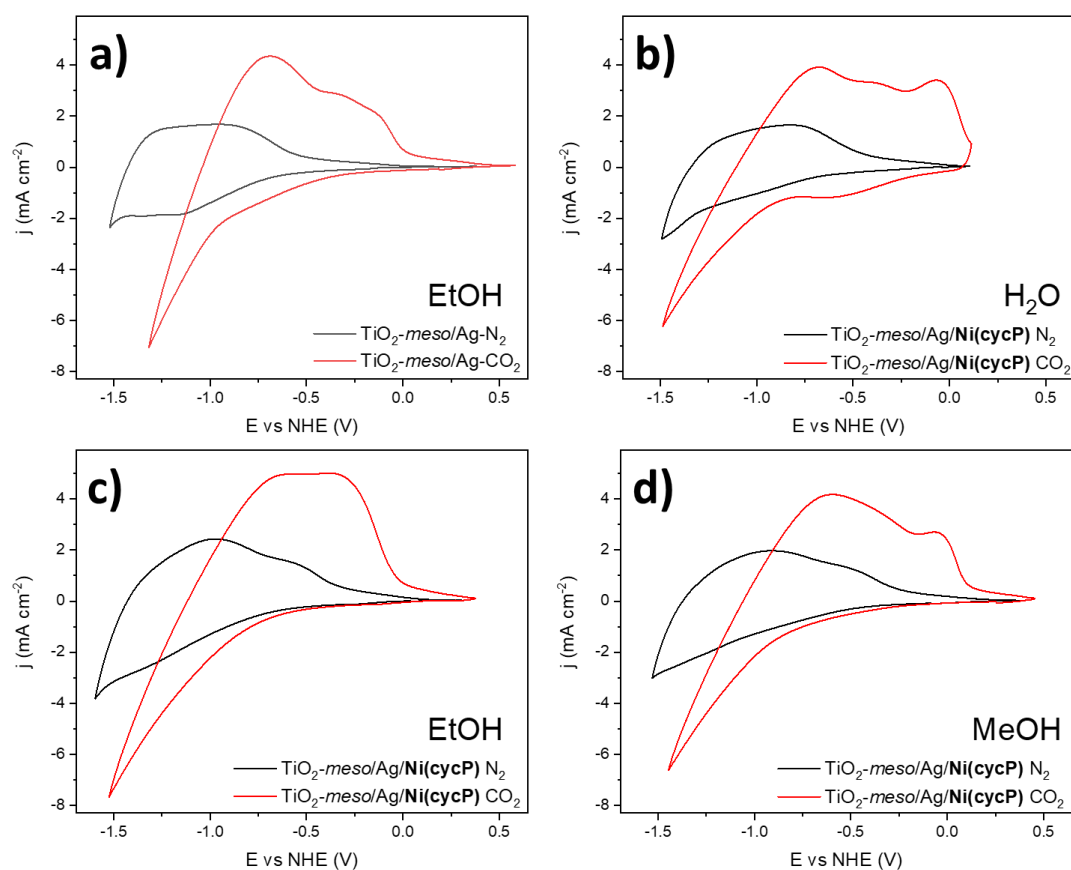
Figure 98 *CV of (a) TiO₂-meso/Ag, (b-d) TiO₂-meso/Ag/**Ni(cycP)** at 100 mV s⁻¹ in 0.1 M TBAPF₆, 5% H₂O, in MeCN under N₂ (black trace) and CO₂ (red trace), soaked in 10 mM **Ni(cycP)** in different solvents: (b) H₂O, (c) ethanol, (d) methanol for 48 h for the catalyst immobilization.*

Although, the TiO₂-*meso* layer allowed an increase of **Ni(cycP)** content compared to the TiO₂ planar device (Sb₂Se₃/TiO₂(S-20 nm)/**Ni(cycP)**)) from 6.84 x10⁻² to 14 nmol cm⁻², it remained low compared with phosphonated Ru (85 nmol cm⁻²)[2] or Co (45.0 ± 7.4)[1] molecular catalyst covalently bonded to TiO₂ mesoporous scaffolds (see Table 17). And considering that the TON$_{Ni(cycP)}$ is 4.8 after 7 h for CO production[17] and 70 for the Re molecular catalyst,[2] it is anticipated that a higher catalyst loading is required to keep up with the photoelectron generation at the Sb₂Se₃. The lower catalytic activity of the **Ni(cycP)** compared with the parent **Ni(cyc)²⁺** on HMDE was previously attributed to the replacement of a proton amine by the phosphonic acid group since the proton amines stabilise the CO₂ binding.[6,28]

The complete CO₂R hybrid photocathode using **Ni(cycP)** as catalyst on TiO₂-*meso*(/Ag) was not further studied since several strategies were adopted to improve its covalent immobilization without success, and given the negative impact of the proton amine substitution by the phosphonic anchor group, a poor PEC performance was anticipated. Instead, Co based molecular catalyst were studied due to their high catalytic activity towards CO production.
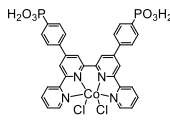
4.2 Co based molecular catalyst
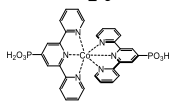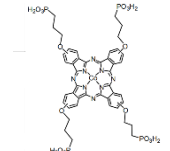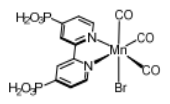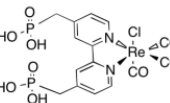
Ni cyclam derivatives did not show promising catalytic features to be included in CO₂R hybrid photocathodes, instead Co based molecular catalyst were explored since they also exhibited high catalytic activity towards CO production.[5] As pointed out in the introduction of this thesis, some molecular catalysts like Co bis(terpyridine) **CotpyP**,[1] Co quarter pyridine **Co-qPyH**,[29] and Co phthalocyanine **CoPcP**[30] have been covalently anchored on TiO₂ by phosphonic acid groups. Table 17 contains the most representative Co based hybrid devices for CO₂R.

In the following section, the covalent binding of Co protoporphyrin IX (**CoPP**) through carboxylic acid anchoring groups is first presented, followed by the Co phthalocyanine (**CoPc**) immobilization on CNT by π-π stacking, considering that one of the most active PEC devices for CO production was accomplished by π-π stacking between the catalyst and CNTs.[31]

4.2.1 CoPP: Co protoporphyrin IX

The molecular structure of the cobalt protoporphyrin IX (**CoPP**) is shown in the insert of Figure 99a. **CoPP** is an active molecular catalyst for CO production,[32,33] which has been covalently grafted on CNTs by hydroxylic groups reaching a current density of -25.1 mA cm^{-2} at 490 mV overpotential for CO production (-0.6 V *vs* RHE) in 0.5 M NaHCO₃.[34]

Table 17 *State-of-the-art of CO_2 hybrid photocathodes using covalent binding between the molecular catalyst and metal oxide.*

Light absorber	Molecular catalyst	Catalyst loading [nmol cm⁻²]	−j (mA cm⁻²)	E (V) vs NHE	CO selectivity	Time h	TON	Electrolyte	Ref.
FTO/Mo/CIGS/CdS/AZO/TiO₂	**Co-qPyH**	3 ± 1	0.81	−0.06	97%	2	8031	0.1 M KHCO₃	29
p-Si/TiO₂-*meso*	**CotpyP**	45.0 ± 7.4	0.08	−0.37	46 CO 12.8 Formate	8	124 CO 33.9 Formate	6:4 MeCN:H₂O 0.1M TBABF₄	1
p-Si/TiO₂-*meso*	**CoPcP**	24 ± 2	0.15	−0.53	66	12	929	0.5 M KHCO₃	30
p-Si/TiO₂-*meso*	**MnP**	48.2	0.13	−0.53	61	12	342	0.5 M KHCO₃	30
CuO₂/Al:ZnO/TiO₂	**ReP**	85	2.5	−1.42	80-95	1.5	70	0.1 M Bu₄NPF MeCN	2

The carboxylic acid groups of **CoPP** were linked to TiO$_2$-*meso* as a starting approach since it was anticipated that high surface area was required to cope with the photoelectron generation at the light absorber, as pointed out in section 4.1.3.3. The immobilization was carried out in 100 μM **CoPP** ethanolic solution overnight (16 h), and all the experimental details are provided in section 6.2.3. Figure 99a shows the UV-vis spectrum of 100 μM **CoPP** ethanolic solution before and after the overnight immobilization. **CoPP** shows distinctive peaks at 418, 530, 564 nm and considering the peak with the highest intensity at 418 nm after the immobilization, the **CoPP** loading on the TiO$_2$ was 127.38 nmol cm^{-2}, higher than the cobaloxime derivative anchored to an ALD TiO$_2$ planar structure by carboxylic acid groups (12.7$\pm$1.2 nmol cm^{-2}).[35] Figure 99b shows the UV-vis spectra of TiO$_2$-*meso*/**CoPP** where the **CoPP** features at 418, 530, 564 nm were evident after the immobilization.
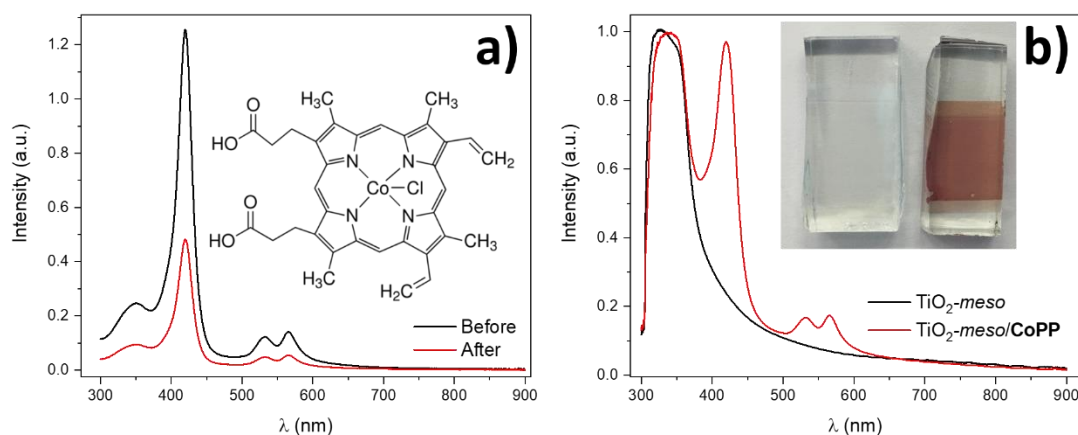
Figure 99 *UV-vis spectra of (a) 100 μM CoPP ethanolic solution before and after overnight immobilization on TiO$_2$-meso, and (b) UV-Vis spectra of TiO$_2$-meso(/CoPP).*

Figure 100a shows the cyclic voltammetry of TiO$_2$-*meso*/**CoPP** in 0.1 M TBAPF$_6$, 1% H$_2$O, in MeCN at 10 mV s^{-1} under N$_2$ and CO$_2$. The current significantly increased in a CO$_2$-saturated electrolyte, however the molecular catalyst desorbed from the TiO$_2$-*meso* scaffold during the scan. Figure 100b shows the absorbance spectra of the TiO$_2$-*meso*/**CoPP** after the CVs under N$_2$ and CO$_2$, the **CoPP** absorption peaks at 418, 530, 564 nm disappeared completely.
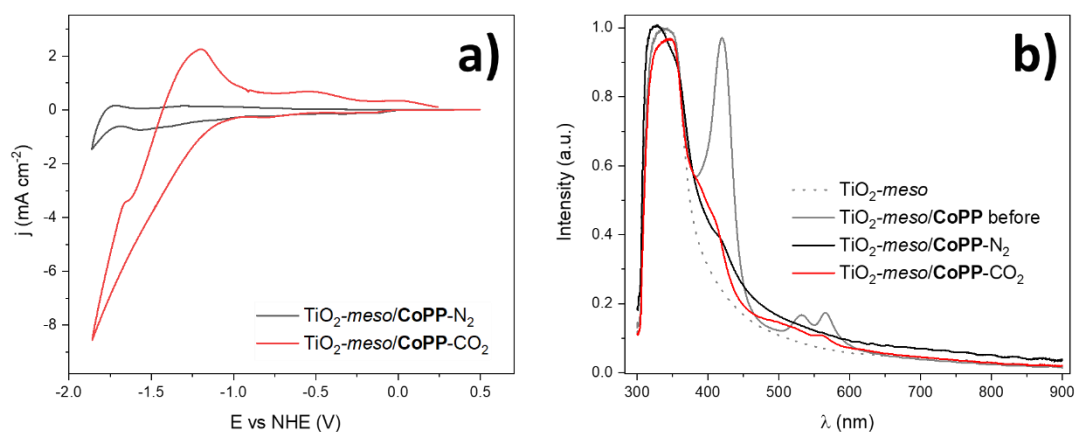
Figure 100 *(a) CV of TiO₂-meso/**CoPP** in 0.1 M TBAPF₆, 1% H₂O, in MeCN at 10 mV s⁻¹ under N₂ and CO₂, and (b) UV-vis spectra of TiO₂-meso/**CoPP**: the pristine sample before the CV (labelled as before, grey trace) and after the scans under N₂ and CO₂.*

It is also worthy to note that two different films were used for the scan under N_2 and CO_2, which demonstrated poor stability of the carboxylic acid as anchoring groups, in line with previous reports.[19,35] Therefore, **CoPP** was not further considered as a suitable molecular catalyst for CO_2R hybrid photocathodes. A possible way to overcome the instability issue of the carboxylic acid anchoring groups is by adding thin layer (∼0.4 nm) of either TiO_2 or Al_2O_3 by ALD.[35] However, a trade-off between improved anchor stability and surface area lowering after the ALD TiO_2 deposition is anticipated. Unfortunately, due to the limited access to the ALD-TiO_2, this approach could not be explored in detail. Instead, in the next section cobalt phthalocyanine (**CoPc**) was studied as alternative catalyst for hybrid photocathodes for CO_2R.

4.2.2 CoPc: Cobalt phthalocyanine

Cobalt phthalocyanine ranks amongst the most active catalyst for CO_2R (**CoPc**, molecular structure shown in the insert of Figure 101), with current densities reaching up to −150 mA cm⁻² in a zero-gap cell, and more than 95% selectivity towards CO. It represents the state-of-the-art molecular catalyst

performance for large scale applications.[36] **CoPc** has also been recently modified with phosphonic acid anchoring groups to be covalently linked to TiO_2-*meso* and *p*-Si as light absorber, it reached a photocurrent of 150 μA cm⁻² at -0.53 V *vs* SHE with $66 \pm 3\%$ CO selectivity in a CO_2-saturated solution of 0.5 M $KHCO_3$, pH 7.3. However, when **CoPc** was immobilized on CNT *via* π -π stacking and used alongside a perovskite buried junction for light collection, a photocurrent of -15.5 mA cm⁻² at -0.11 V *vs* RHE was recorded in 0.5 $KHCO_3$ with remarkable stability of 25 h.[31] The later approach was then selected to build the hybrid photocathode.

CoPc has low conductivity, thus the catalytic activity is highly dependent on the proper catalyst dispersion and immobilization on conductive substrates *via* π-π stacking, and CNTs are the most used material.[37] In this work, **CoPc** was first immobilized on CNTs according to previous reports.[31,38] after an ink with the active composite (**CoPc@CNT**, 2 mg) was made in 950 μL of ethanol, and 50 μL of 5% Nafion solution, and drop casted on GC (0.071 cm²) previously polished, and all the experimental details are included in section 6.2.4). The **CoPc** loading on CNT was determined by UV-Vis spectroscopy and Figure 101 shows the UV-vis spectra of 81 μM of **CoPc** in THF before (blue trace) and after the immobilization (grey trace). The **CoPc** peaks at 219, 284, 324 and 657 nm disappeared completely after CNT addition, and the **CoPc** loading on CNT was 9.13 nmol cm⁻², in agreement with the report followed for the immobilization process (8.1 nmol cm⁻²).[31]

The CVs of GC/**CoPc@CNT** in 0.5 M $KHCO_3$ under N_2 and CO_2 at 20 mV s⁻¹ are shown in Figure 102a, the current in CO_2-saturated electrolyte is higher than under N_2, and a plateau is achieved at *ca.* -0.6V *vs* RHE, which corresponds to the highest catalytic activity towards CO.[31,37,39,40] At higher scan rate (400 mV s⁻¹), the reversible couple of the $Co^{II/I}$ molecular catalyst at *ca.* 0.06 V *vs* RHE is evident and vanished under CO_2.[39] Considering the charge passed at this redox couple, it was found that the **CoPc** content was 5 nmol cm⁻², in line with the catalyst loading determined by UV-vis (9.13 nmol cm⁻²). The **CoPc** catalytic reaction mechanism towards CO production is shown in Figure 103a.[41]
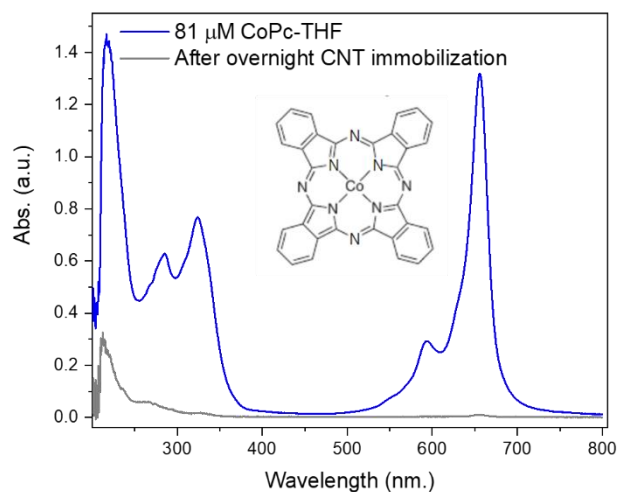
Figure 101 *UV-Vis spectra of 81 μM of **CoPc** before (blue trace) and after (grey trace) the overnight immobilization on CNT.*
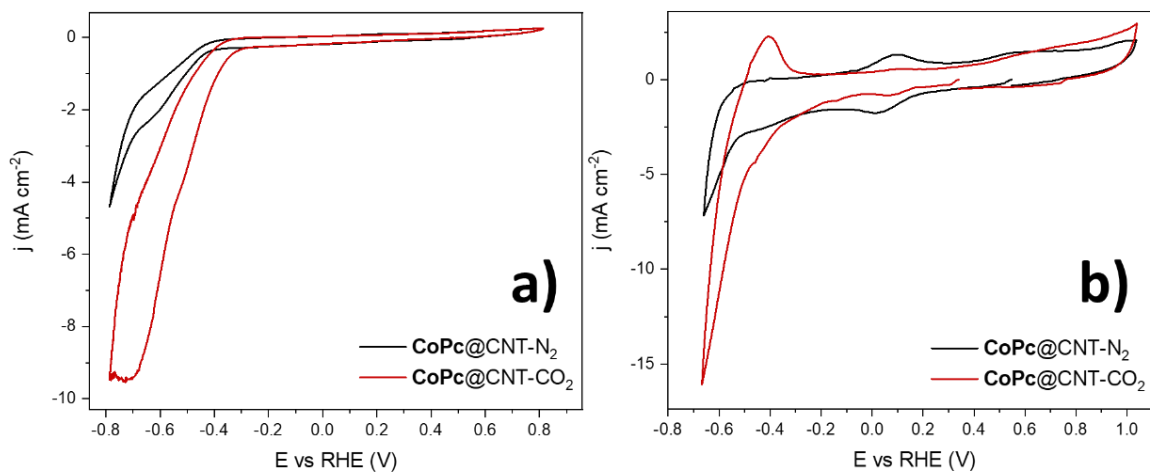
Figure 102 *CV of GC/**CoPc**@CNT under N₂ (black trace) and CO₂ (red trace) at (a) 20 mV s⁻¹ and (b) 400 mV s⁻¹ in 0.5 M KHCO₃.*

170
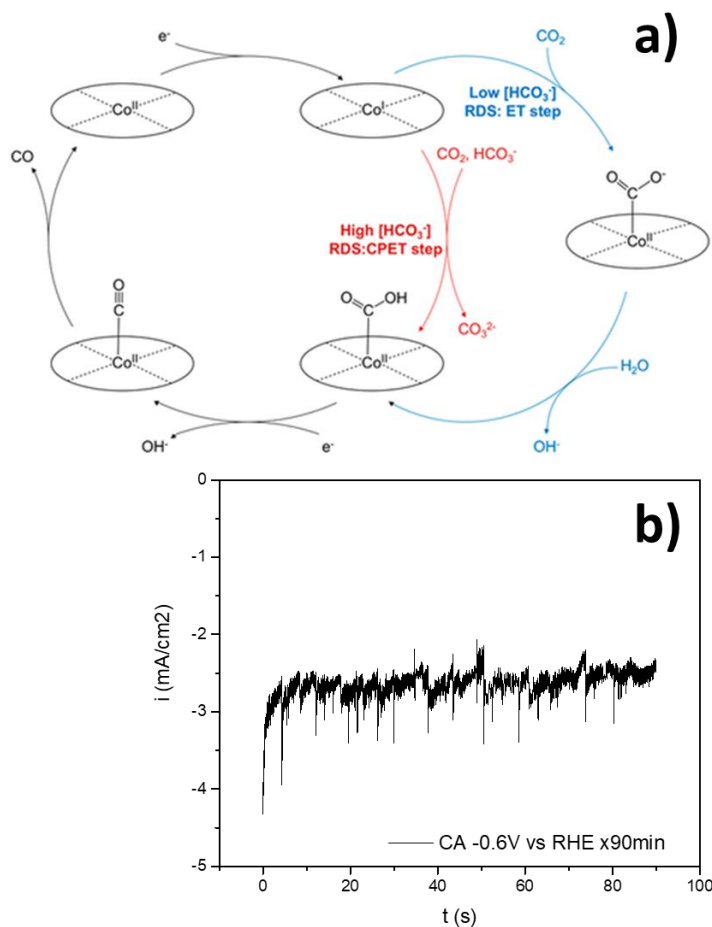
Figure 103 *(a)* ***CoPc*** *reaction mechanism reproduced from,[41] and (b) CA at −0.6 V vs RHE for 90 min in 0.5 M KHCO₃ saturated with CO₂.*

A chronoamperometry test was carried out at −0.6 V *vs* RHE for 90 min (Figure 103b), the current density recorded was close to −3 mA cm⁻², and FE_{CO} 80% was achieved in line with previous reports.[31] Although **CoPc** was successfully immobilized on CNT, the development of the Sb₂Se₃-**CoPc** hybrid photocathode requires further optimization for trading-off between light absorption and catalyst loading since the **CoPc**@CNT active material will restrain Sb₂Se₃ light collection due to front illumination.

At the same time these experiments were carried out, a hybrid photocathode *p-n*Si/TiO₂/Co based molecular catalysts was published [3]. This report used of one of the most efficient and well-developed light absorbers *p-n*Si, an ALD TiO₂ (5nm) as protective layer, and several cobalt molecular catalysts were supported on CNT and tested for CO₂R, including **CoPc**. The bromide-substituted **Co^II(qPy)**

(qPy=4',4''-bis(phenyl)-2,2':6',2'':6'',2'''-quaterpyridine) displayed the highest photocurrent of −1.4 mA cm^{-2} at -0.11 V *vs* RHE under continuous irradiation (100 mW cm^{-2}, AM 1.5 G) for 1 h in an aqueous electrolyte of 0.1 M KHCO$_3$ (pH 6.8), whilst the **CoPc** on the same device only achieved a photocurrent of 300 μA cm^{-2}. Consequently, the Sb$_2$Se$_3$/**CoPc**@CNT hybrid photocathode was not assembled.

This study also highlighted the importance of having areas for light collection at the *p-n*Si and free from the active material (**Co^{II}(qPy)/CNT**). [3] For these devices, a CNT ink was first deposited on the top of *p-n*Si/TiO$_2$ followed by the Co molecular catalyst drop casting, however it is likely that catalyst agglomeration led to the losing of catalytic active sites. Only for the most active Co molecular catalyst, the **Co^{II}(qPy)** was immobilized first on CNT giving rise to **Co^{II}(qPy)@CNT**, then the active composite was drop casted on the top of *p-n*Si/TiO$_2$. A similar photocurrent was achieved −1.5 mA cm^{-2} but with a significant decrease in catalyst loading from 41 to 3.08 nmol cm^{-1}, demonstrating the importance of catalyst dispersion to effectively access the active metal centres.[3]

This chapter also highlighted the importance of having an efficient solar cell to build an efficient hybrid CO$_2$ photocathode. Although some devices were made using a Sb$_2$Se$_3$/TiO$_2$(S-100nm), the true potential of the optimised architecture which included CdS (Sb$_2$Se$_3$/CdS/TiO$_2$-*meso*), could not be assessed, but it is anticipated that a CO$_2$R catalyst with high turnover numbers is required for the photocathode to operate efficiently, such as **Co-qPyH**.

4.3 Conclusion

A complete hybrid photocathode was built based on a Sb_2Se_3 photocathode and Ni cyclams as catalyst for CO_2 reduction in a homogeneous approach (**Ni(cyc)$^{2+}$**), and by the covalent immobilisation through the phosphonic acid groups in **Ni(cycP)**. The planar device Sb_2Se_3/TiO_2(S-20 nm)/**Ni(cycP)** exhibited low PEC activity for CO_2R which was attributed to the low catalyst content. The addition of the TiO_2-*meso* increase the catalyst loading, however the immobilization of **Ni(cycP)** was challenging due to the high intramolecular coordination between the Ni centre and the phosphonic acid pendant arm, therefore different solvents and soaking times, as well as silver addition were explored. Although an increase in **Ni(cycP)** content was achieved from 6.84×10^{-2} up to *ca.* 14 nmol cm^{-2}, the low CO selectivity of TiO_2-*meso*/**Ni(cycP)** suggested the catalyst was not a suitable candidate to be used in a CO_2R hybrid photocathode.

Co based molecular catalyst were also studied in this chapter, however the complete CO_2R hybrid photocathode alongside Sb_2Se_3 as light absorber was not assembled. The **CoPP** high solubility/instability after anchored on TiO_2-*meso* by carboxylic acid groups limited its catalytic activity. Meanwhile, **CoPc** represented an interesting approach when immobilized on CNT, a recent report demonstrated **CoPc**@CNT composites exhibited low catalytic activity compared to **Co^{II}(qPy)**@CNT,[3] therefore the hybrid photocathode was not further explored.

Despite some devices were made using Au as benchmark catalyst to assess the PEC activity towards CO_2R, the true potential of the optimised Sb_2Se_3 based photocathode could not be studied in detail due to time constraints, but it is hypothesized that higher photocurrents than *ca.* 50 μA cm^{-2} at -1.0 V *vs* RHE could be achieved after tailoring the Au thicknesses, and by adding a CdS buffer layer, which significantly improved the photoelectron extraction from the Sb_2Se_3 as pointed out Chapter 2.

4.4 References

1   J. J. Leung, J. Warnan, K. H. Ly, N. Heidary, D. H. Nam, M. F. Kuehnel, E. Reisner, V. Kumaravel, J. Bartlett, S. C. Pillai, J. J. Leung, J. Warnan, K. H. Ly, N. Heidary, D. H. Nam, M. F. Kuehnel and E. Reisner, *Nat. Catal.*, 2019, **2**, 354–365.

2   M. Schreier, J. Luo, P. Gao, T. Moehl, M. T. Mayer and M. Grätzel, *J. Am. Chem. Soc.*, 2016, **138**, 1938–1946.

3   Z. Wen, S. Xu, Y. Zhu, G. Liu, H. Gao, L. Sun and F. Li, *Angew. Chem. Int. Ed.*, 2022, **61**, e2022010, 1–7.

4   F. Franco, C. Rettenmaier, H. S. Jeon and B. R. Cuenya, *Chem. Soc. Rev.*, 2020, **49**, 6884–6946.

5   E. Boutin, L. Merakeb, B. Ma, B. Boudy, M. Wang, J. Bonin, E. Anxolabéhère-Mallart and M. Robert, *Chem. Soc. Rev.*, 2020, **49**, 5772–5809.

6   G. Neri, Thesis, University of Liverpool, 2016

7   J. Song, E. L. Klein, F. Neese and S. Ye, *Inorg. Chem.*, 2014, **53**, 7500–7507.

8   G. B. Balazs and F. C. Anson, *J. Electroanal. Chem.*, 1993, **361**, 149–157.

9   J. D. Froehlich and C. P. Kubiak, *Inorg. Chem.*, 2012, **51**, 3932–3934.

10   B. R. Sullivan, K. Krist and H. E. Guard, *Electrochemical and Electrocatalytic Reactions of Carbon Dioxide*, 1993.

11   B. Enright, G. Redmond and D. Fitzmaurice, *J. Phys. Chem.*, 1994, **98**, 6195–6200.

12   J. D. Froehlich and C. P. Kubiak, *J. Am. Chem. Soc.*, 2015, **137**, 3565–3573.

13   T. Berger, D. Monllor-Satoca, M. Jankulo*v*ska, T. Lana-Villarreal and R. Gomez, *ChemPhysChem*, 2012, **13**, 2824–2875.

14   C. Li, T. Wang, B. Liu, M. Chen, A. Li, J. Gong, G. Zhang, M. Du, H. Wang, S. Frank Liu, J. Gong, S. F. Liu and J. Gong, *Energy Environ. Sci.*, 2019, **12**, 923–928.

15   F. Niu, D. Wang, F. Li, Y. Liu, S. Shen and T. J. Meyer, *Adv. Energy Mater.*, 2019, **1900399**, 1–24.

16   G. Neri, I. M. Aldous, J. J. Walsh, L. J. Hardwick and A. J. Cowan, *Chem. Sci.*, 2016, **7**, 1521–1526.

17   G. Neri, M. Forster, J. J. Walsh, C. M. Robertson, T. J. Whittles, P. Farrás and A. J. Cowan, *Chem. Commun.*, 2016, **52**, 14200–14203.

18   B. Siritanaratkul, M. Forster, F. Greenwell, P. K. Sharma, E. H. Yu and A. J. Cowan, *J. Am. Chem. Soc.*, 2022, **144**, 7551–7556.

19   K. L. Materna, R. H. Crabtree and G. W. Brudvig, *Chem. Soc. Rev.*, 2017, **46**, 6099–6110.

20   T. Moehl, J. Suh, L. Sévery, R. Wick-Joliat and S. D. Tilley, *ACS Appl. Mater. Interfaces*, 2017, **9**, 43614–43622.

21   G. K. Ramesha, J. F. Brennecke and P. v. Kamat, *ACS Catal.*, 2014, **4**, 3249–3254.

22   A. Evers and R. D. Hancock, *Inorganica Chim. Acta*, 1989, **160**, 245–248.

23   J. P. Collin and J. P. Sauvage, *Coord. Chem. Rev.*, 1989, **93**, 245–268.

24   J. Schneider, H. Jia, J. T. Muckerman and E. Fujita, *Chem. Soc. Rev*, 2012, **41**, 2036–2051.

25   K. Bujno, R. Bilewicz, L. Siegfried and T. A. Kaden, *J. Electroanal. Chem.*, 1998, **445**, 47–53.

26   K. Sekizawa, K. Maeda, K. Domen, K. Koike and O. Ishitani, *J. Am. Chem. Soc*, **135**, 12, 4596–4599.

27   R. Kuriki, H. Matsunaga, T. Nakashima, K. Wada, A. Yamakata, O. Ishitani and K. Maeda, *J. Am. Chem. Soc.*, 2016, **138**, 5159–5170.

28   Marc. Beley, J. Paul. Collin, Romain. Ruppert, J. Pierre. Sauvage, J. Paul. Collin, Romain. Ruppert and J. Pierre. Sauvage, *J. Am. Chem. Soc.*, 2002, **108**, 7461–7467.

29   P. B. Pati, R. Wang, E. Boutin, S. Diring, S. Jobic, N. Barreau, F. Odobel and M. Robert, *Nat. Commun.*, 2020, **11**, 1–9.

30   S. Roy, M. Miller, J. Warnan, J. J. Leung, C. D. Sahm and E. Reisner, *ACS Catal.*, 2021, **11**, 1868–1876.

31   H. Zhang, Y. Chen, H. Wang, H. Wang, W. Ma, X. Zong and C. Li, *Adv. Energy Mater.*, 2020, **10**, 2002105, 1–9.

32   J. Shen, R. Kortlever, R. Kas, Y. Y. Birdja, O. Diaz-Morales, Y. Kwon, I. Ledezma-Yanez, K. J. P. Schouten, G. Mul and M. T. M. M. Koper, *Nat. Commun.*, 2015, **6**, 8177.

33   J. E. Pander, A. Fogg and A. B. Bocarsly, *ChemCatChem*, 2016, **8**, 3536–3545.

34   M. Zhu, J. Chen, L. Huang, R. Ye, J. Xu and Y. F. Han, *Angew. Chem. Int. Ed.*, 2019, **58**, 6595–6599.

35   J. Gu, Y. Yan, J. L. Young, K. X. Steirer, N. R. Neale and J. A. Turner, *Nat. Mater.*, 2016, **15**, 456–462.

36   S. Ren, D. Joulié, D. Salvatore, K. Torbensen, M. Wang, M. Robert and C. P. Berlinguette, *Science*, 2019, **365**, 367–369.

37   Y. Wu, Y. Liang and H. Wang, *Acc. Chem. Res.*, 2021, **54**, 3149–3159.

38   C. Sun, Y. Hou, N. Lüdi, H. Hu, M. de Jesús Gálvez-Vázquez, M. Liechti, Y. Kong, M. Liu, R. Erni, A. v. Rudnev and P. Broekmann, *J. Catal.*, 2022, **407**, 198–205.

39   X. Zhang, Z. Wu, X. Zhang, L. Li, Y. Li, H. Xu, X. Li, X. Yu, Z. Zhang, Y. Liang and H. Wang, *Nat. Commun.*, 2017, **8**, 1–8.

40   V. Andrei, B. Reuillard and E. Reisner, *Nat. Mater.*, 2020, **19**, 189–194.

41   M. Zhu, R. Ye, K. Jin, N. Lazouski and K. Manthiram, *ACS Energy Lett.*, 2018, **3**, 1381−1386.

Chapter 5

Conclusion and future work

In this work, hybrid photocathodes for solar fuel production based on inorganic semiconductor as light absorber and molecular catalysts were studied for HER and CO_2R.

To achieve this goal, first a suitable light absorber was required and chapter 2 describes this process. The need for an additional (protective) layer to improve charge separation and increase the stability was immediately identified. Pt as photoelectron extractor was used to benchmark the photocathode architectures. ZnTe and Sb_2Se_3 were explored since they exhibited low band gaps (2.26 and 1.17 eV, respectively) and specifically ZnTe has a very negative conduction band which provides large driving force for CO_2 reduction (-1.48 V *vs* RHE).[1] Metal oxides such as ZrO_2, AZO, Ta_2O_5 were studied however the ZnTe-based photocathodes exhibited low PEC activity, which was mainly attributed to the small grain morphology which favoured recombination and is typical of the thermal evaporation used to deposit the films.

Sb_2Se_3 was used instead since it has recently gained the attention of the PV community and quickly became widely-used in the PEC community. Forming a Sb_2Se_3 *p-n* junction with TiO_2 was first studied, showing that the performance was dependant on the deposition technique (sputtered, thermal ALD or plasma enhance ALD). The final photocathode architecture was achieved with an interlayer of CdS, which provides a better band alignment than the TiO_2 and the final device (Sb_2Se_3/CdS/TiO_2(S-20nm)) gave rise to a photocurrent of -20 mA cm^{-2} at 0 V *vs* RHE. Although it was not the highest photocurrent for H_2 production, it provided a suitable platform to explore different molecular catalyst for either HER and CO_2R.

Once a suitable architecture was accomplished, the Sb$_2$Se$_3$/CdS/TiO$_2$(S-100nm) photocathode was coupled covalently with **NiP** ([Ni(P$_2^{R'}$N$_2^{R''}$)$_2$]$^{2+}$ core (P$_2^{R'}$N$_2^{R''}$ = bis(1,5-R'-diphospha-3,7-R''-diazacyclooctane))) molecular catalyst for HER through phosphonic acid groups in chapter 3. It was found that an increase in catalyst loading was imperative to achieve higher photocurrents. Therefore, a mesoporous TiO$_2$ layer was incorporated onto the device to increase the available surface area for catalyst binding. This layer was accomplished by an UV curing process to remove the binder in a photocatalytic reaction followed by the N$_2$ annealing at 350°C to improve particle interconnectivity. This experimental protocol was designed to not compromise the PEC activity of the light absorber. The Sb$_2$Se$_3$/CdS/TiO$_2$(S-100nm)/TiO$_2$-*meso*/**NiP** achieved the highest photocurrent reported for a **NiP** decorated photocathode at -1.3 mA cm^{-2} at 0 V *vs* RHE. However, the hybrid photocathode deactivates on the scale of 10 min, interestingly the stability was improved when the light intensity was reduced from 100 mW cm^{-2} to 20 mW cm^{-2}. To further investigate the deactivation mechanism, post-electrolysis characterization was carried out, revealing that the Ni centre was lost meanwhile the phosphonic acid anchoring remained, consequently photoelectron accumulation provoked the partial failure of the sputtered TiO$_2$ layer. This was further corroborated by benchmarking the device against Pt, and found out that Sb$_2$Se$_3$/CdS/TiO$_2$(S-100nm)/TiO$_2$-*meso*/Pt was able to produce -3 mA cm^{-2} for 5 h with an onset potential of 0.5 V *vs* RHE. Transient photocurrent analysis identified that the addition of a TiO$_2$-*meso/*Pt reduces recombination at low overpotentials (0.4 V *vs* RHE) at the millisecond scale. This slow recombination is suppressed by a more negative overpotential. Conclusively, for a hybrid photocathode to operate efficiently, the turnover frequency molecular catalyst needs to match with generation the photoelectrons generated at the light absorber at the same rate, otherwise electron accumulation could deactivate the photocathode as identified for the Sb$_2$Se$_3$-**NiP** based photocathode.

Finally, the Sb$_2$Se$_3$ based photocathodes were used with Ni cyclams as molecular catalyst for CO$_2$R, the first approach was the catalyst in solution **Ni(cyc)$^{2+}$**, and after a derivative modified with phosphonic anchoring groups **Ni(cycP)**. Although these results were presented as the last experimental chapter 4, the Sb$_2$Se$_3$ base architecture did not include the CdS buffer layer which exhibited higher photocurrents, however the PEC activity of the structure (Sb$_2$Se$_3$/TiO$_2$) was benchmarked with Pt and Au. When the

Ni cyclam was used in solution, the photocurrent was *ca.* 5 μA cm^{-2} at -0.41 V *vs* RHE for **Ni(cyc)$^{2+}$**, therefore the covalent immobilization of a **Ni(cycP)** with phosphonic pendant arms was explored to improve the charge transfer at the interface, but the necessity of an increased catalyst loading was identified since low photocurrents were recorded (*ca.* -20 μA cm^{-2} at -0.39 V *vs* RHE), similar to **NiP** catalyst. The **Ni(cycP)** catalyst was immobilised first in the mesoporous layer however the content was still low even on the high surface area electrode (∼14 nmol cm^{-2}). This behaviour was attributed to the strong intramolecular interaction between the Ni centre and the phosphonic pendant arm. Several attempts were made to decrease the intra molecular interaction by changing the solvents, solution aging and immobilization time, however the catalyst loading could not be increased. Therefore, the hybrid device was not assembled since it was anticipated that higher catalyst loadings were required to cope with the photoelectron flux generated at the Sb$_2$Se$_3$.

Cobalt-based molecular catalysts were also studied due to their high catalytic activity for CO production from CO$_2$R. First, **CoPP** with carboxylic acid anchoring groups was explored but the covalent bond was not strong enough to retain the molecular catalyst at the TiO$_2$-*meso* during the dark electrochemical study. The stability of this interface could be improved by adding an *ca.* 0.5 nm thick ALD TiO$_2$ or Al$_2$O$_3$ to bury the anchoring group without compromising the catalytic activity. **CoPc** was also studied and first immobilised on CNT, similar loadings and CO selectivity to the literature were reproduced when characterised by dark electrochemistry. Although the complete hybrid photocathode for CO$_2$ reduction was not built in this work, it is hypothesised that the Sb$_2$Se$_3$/**CoPc**@CNT could be a plausible combination for an CO$_2$R hybrid photocathode.

In the recent literature, Wen and collaborators reported that the **CoPc**@CNT electrocatalytic activity was overcome by the bromide-substituted **Co^{II}(qPy)** (qPy=4',4''-bis(phenyl)-2,2':6',2'':6'',2'''-quaterpyridine) immobilised on CNT when both catalyst (among others) were used as CO$_2$R catalyst on the *p-n*Si/TiO$_2$ photocathode. Based on this report[2] and the photocurrents shown in chapter 3 for the planar (−2.11 mA cm^{-2}, Sb$_2$Se$_3$/CdS/TiO$_2$/Pt,) and the mesoporous device (−1.46 mA cm^{-2}, Sb$_2$Se$_3$/CdS/TiO$_2$-*meso*/Pt) at -0.11 *vs* RHE using Pt as catalyst for HER on the optimised light absorbing architecture, a Sb$_2$Se$_3$/**CoPc**@CNT photocathode can be expected to reach similar currents,

since those photocurrents were recorded in 0.1 M Na_2SO_4 at pH 7, similar to the pH of CO_2-saturated $KHCO_3$ electrolyte. For the hybrid Sb_2Se_3/**CoPc**@CNT photocathode, the photoelectron sink will be the CNT matrix instead of the TiO_2-*meso* layer used in chapter 3 for **NiP** catalyst. Furthermore, it is anticipated that a careful tailoring between light absorption and catalyst composite content will be required for Sb_2Se_3/**CoPc**@CNT to effectively operate as hybrid photocathode for CO_2R. However, to truly assess the Sb_2Se_3 capabilities to drive CO_2R towards CO production, a metal benchmark catalyst such as Au or Ag should be first used to optimise the photocathode architecture (Sb_2Se_3/CdS/TiO_2-S(100 nm)) for maximum photoelectron extraction, avoiding the confounding effects of molecular catalysis limitations like stability or low turnover frequencies.

Another interesting approach would be coupling the cobalt complex with planar tetra-dentate ligand 2,2′:6′,2″:6″,2‴-quaterpyridine (**Co-qPyH**) alongside Sb_2Se_3/CdS/TiO_2-*meso* architecture in an CO_2 hybrid photocathode. **Co-qPyH** exhibited high catalytic activity when used on FTO/Mo/CIGS/CdS/AZO/TiO_2/**Co-qPyH** displaying a photocurrent of -0.81 mA cm^{-2} at -0.06 V *vs* RHE, with a remarkable 97% CO selectivity in CO_2-saturated 0.5 M $KHCO_3$.[3] When used as a hybrid CO_2R photocathode, the **Co-qPyH** phosphonic anchoring groups were covalently immobilised on TiO_2 leading to low catalyst content 3 ± 1 nmol cm^{-2}. In a PV-EC approach, where the CIGS based solar cell was used as an external photoelectron supply (*i.e.* not in solution) for the TiO_2-*meso*/**Co-qPyH** dark cathode, the photocurrent was -3.25 mA cm^{-2} at -0.06 V *vs* RHE for a higher catalyst loading of 29 ± 4 nmol cm^{-2}. Interestingly, the TON for the PEC approach was almost twice than the PV-EC approach (8031 and 4060 respectively), demonstrating the advantages of the PEC integrated system.[3] It is hypothesised the TiO_2-*meso* could not be incorporated in this study due to the thermal instability of the CIGS/CdS interface, therefore the PV-EC was adopted.

Having a TiO_2-*meso* layer offers high surface area to increase the catalyst content, however it could also represent a limiting factor in accessing the catalytic centres at the bottom of the mesoporous layer. Furthermore, the stability of the phosphonic acid groups could be compromised during catalysis, since the interfacial pH increases during CO_2R[4] and the phosphonic acid groups are stable at pH < 7.[5]

An important challenge in designing efficient hybrid photocathodes is the matching of photocharge generation and catalysis, processes occuring at two completely time scales. Even if significant improvements are made to achieve more efficient light absorbers, the molecular catalyst with higher turnover frequencies are required to leverage the photoelectron generation. An additional challenge is how to interface these two components even when both operate efficiently on their own, as it has been reported previously for example in p-nSi photocathodes[2,5] or the perovskite solar cells[6] and the **CoPc** on CNT which demonstrate high current densities for large scale applications,[7] nevertheless achievements for wide-reaching applications have not been accomplished yet in the PEC community.

5.1 References

1   L. K. Putri, B. J. Ng, W. J. Ong, S. P. Chai and A. R. Mohamed, *Adv. Energy. Mater.*, 2022, **17**, 2201093.

2   Z. Wen, S. Xu, Y. Zhu, G. Liu, H. Gao, L. Sun and F. Li, *Angew. Chem. Int. Ed.*, 2022, **61**, e2022010, 1–7.

3   P. B. Pati, R. Wang, E. Boutin, S. Diring, S. Jobic, N. Barreau, F. Odobel and M. Robert, *Nat. Commun.*, 2020, **11**, 1–9.

4   A. S. Varela, Curr Opin *Green Sustain. Chem.*, 2020, **26**, 1000371, 1–8.

5   K. L. Materna, R. H. Crabtree and G. W. Brudvig, *Chem. Soc. Rev.*, 2017, **46**, 6099–6110.

6   V. Andrei, B. Reuillard and E. Reisner, *Nat. Mater.*, 2020, **19**, 189–194.

7   S. Ren, D. Joulié, D. Salvatore, K. Torbensen, M. Wang, M. Robert and C. P. Berlinguette, *Science*, 2019, **365**, 367–369.

Chapter 6

Experimental techniques

6.1 Materials and synthesis

The ZnTe and Sb_2Se_3 samples, including the sputtered metal oxide coatings were made in collaboration with Dr Jon Major's group (Dr Thomas Shalvey, Dr Oliver Hutter, and Dr Laurie Philips) from the Stephenson Institute for Renewable Energy at University of Liverpool. The ALD capping layers (thermal Al_2O_3, and thermal and PEALD TiO_2) were made in collaboration with Dr Richard Potter from the School of Engineering at University of Liverpool.

The **NiP** molecular catalyst was kindly provided by Professor Erwin Reisner's group (Dr. Carla Casadevall and Dr. Daniel Antón-García) at the Yusuf Hamied Department of Chemistry at University of Cambridge, while the **Ni(cycP)** molecular catalyst was synthesised by Dr Gaia Neri at the Stephenson Institute for Renewable Energy at University of Liverpool.

6.1.1 ZnTe photocathodes

Before ZnTe deposition, the FTO (TEC 15) slides were cleaned with DI water and ethanol using an electric toothbrush and dried under N_2. ZnTe films were grown by thermal evaporation using a ZnTe target (Alfa-Aesar), and kept at room temperature. A tantalum boat was used as source holder, and the pressure inside the chamber was evacuated down to 4.5×10^{-5} Pa. The ZnTe films were thermally evaporated with a deposition rate of 0.2 nm s^{-1}. The thickness of the film was 150 nm determined by profilometry.

A protective/passivation layer on the top of ZnTe was explored to increase the long-term photoelectrode stability and performance. Al_2O_3 and ZrO_2 dip coatings were carried out according to previous reports.[1,2] The experimental protocol (fully described in Table 18) required anhydrous conditions but after heating the precursor solution (0.15 M) at 60 - 70°C for 20 min, the solution is stable and the dip coating was carried out in air at room temperature. The suggested air sintering temperature for Al_2O_3 and ZrO_2 was above the ZnTe decomposition (437 °C).[3] Therefore, lower temperatures were applied (300 and 200°C) since even a slight heat treatment (HT) could increase the long-term stability of metal oxide coated photocathodes.[4] Several attempts to improve the film quality were made such as varying the dipping time (30 s, 1 min, and 3 min), different solvents (water or propanol). However, the dip coating did not produce uniform films, and the ZnTe films changed from brownish-red to black after the metal oxide coating and the PEC performance was poor.

Spin coating produced more uniform Al_2O_3 and ZrO_2 films, the thickness greatly depends on the spinning and solvent evaporation rate, as well as the density and viscosity of the solution[5]. The metal precursor concentration used is indicated in Table 18.

All the metal precursor solutions were freshly made before the dip or spin coating. Note that rinsing the samples with H_2O promoted the hydrolysis of the metal precursor chemisorbed on the surface of the semiconductor,[2] thus the samples were thoroughly rinsed with DI water after each layer.

Table 18 *Experimental details used for metal oxide deposition on ZnTe*

Metal Oxide	Method	Experimental details
Al$_2$O$_3$	Dip Coating	Al(III) precursor: 0.15 M Aluminium tri-sec-butoxide (Sigma-Aldrich) in dry 2-propanol (Sigma-Aldrich). • Number of layers (1, 2, 3, 5) • HT at 300°, 200 °C for 20 min (T increase: 5°C min^{-1}) were carried out after each Al$_2$O$_3$ layer.
	Spin Coating	Al(III) precursor: 0.15 M Aluminium tri-sec-butoxide (Sigma-Aldrich) in dry 2-propanol (Sigma-Aldrich). Each coating was made using 75 μL of Al (IIII) precursor at 4000 rpm for 34 s. • Number of layers (1, 3, 5 ,10) • A final HT was carried out at 200 °C for 20 min (T increase: 5°C min^{-1})
	ALD	Al(III) precursor: Trimethyl-aluminium (TMA) and water. The coating was carried out at low temperature (120 °C) to avoid accidental modifications of the sample[6]. A 2 nm thick was achieved by 20 cycles of (50 ms TMA Dose)(10 s TMA hold)(10 s purge)(30 ms H$_2$O)(10 s H$_2$O hold)(10 s purge)
	Sputtering	100 W, 5 mTorr, RT at room temperature. The film thickness was controlled with the deposition time. Thicknesses: 1 nm (3 min), 5 nm (15 min), 10 nm (30 min), 15 nm (45 min), 20 nm (60min).
AZO	Sputtering	150 W, 5 mTorr, 200 °C, 20 nm thick (8 min).
ZrO$_2$	Dip Coating	Zr(IV) precursor: 0.15 M Zirconium (IV) propoxide in dry 2-propanol (Sigma-Aldrich) • Number of layers (3, 5, 10) • A final HT was carried out at 200 °C for 20 min (T increase: 5°C min^{-1})
	Spin Coating	Zr (IV) precursor: 0.15 M Zirconium (IV) propoxide (Sigma-Aldrich) in dry 2-propanol (Sigma-Aldrich). The suggested temperature of the Zr(IV) precursor during the Spin Coating was 25°C.[2] However, white spots were formed and only after increasing the temperature to 60 °C, homogeneous coatings were achieved. 75 μL were used for each layer at 4000 rpm for 34 s. • Number of layers (5, 10, 15) • A final HT was carried out at 200 °C for 20 min (T increase: 5°C min^{-1})
Ta$_2$O$_5$	Sputtering	100 W, 3 mTorr, RT, 150 nm thick (60 min)

HT: Heat treatment, **T**: temperature

6.1.2 Sb₂Se₃ photoelectrodes

In this section, the experimental protocol to build Sb_2Se_3 devices is first described followed by the photo-electrochemical analysis to select/discard samples highlighting reproducibility issues faced during the development of the Sb_2Se_3 based photocathodes.

6.1.2.1 Sb₂Se₃

SnO_2:F (FTO) coated glass substrates (TEC15, NSG group) were cleaned in ultrasonic baths of Hellmanex III detergent (2%), DI water and isopropyl alcohol in sequence, before drying with compressed nitrogen. A 70 nm Au layer (99.95%, Advent RM) was then thermally evaporated at a rate of ~1 Å s^{-1}.

The Sb_2Se_3 absorber layer was deposited by close-spaced sublimation (CSS) in a two-step process, with a small grain seed layer initially deposited under vacuum with a substrate temperature of 350°C to improve uniformity.[7,8] This is followed by a higher temperature growth stage whereby the chamber is backfilled with 10 Torr N_2 and the substrate temperature is increased to 400°C to produce a ~1.5 μm thick film with a large grain size.

6.1.2.2 CdS

CdS thicknesses and deposition method have a significant impact in the solar cell performance since the *p-n* junction is formed here. However, these parameters were not the focus of this study, therefore they were kept constant for all the devices that include CdS, and they were based on the literature survey.[8] RF magnetron sputtering was used to deposit 20 nm CdS at 60W, 5mTorr Ar, T_{sub}=200°C.

6.1.2.3 Planar TiO₂

RF magnetron sputtering was used to deposit either 20 or 100 nm TiO_2 at 150 W, 3 mTorr Ar, T_{sub}=25 °C from 3" diameter target.

Thermal TiO_2 ALD was deposited at 160 °C, using titanium (IV) tetraisopropoxide (TTIP) and H_2O as the Ti and O precursors, respectively. Plasma enhanced ALD used the same chemical precursors and 24 W $Ar:O_2$ plasma for 300 and 1200 cycles to grow *ca.* 20 nm and 100 nm thick TiO_2.

6.1.2.4 TiO₂-meso scaffold

TiO_2 mesoporous (TiO_2-*meso*) scaffold was initially optimized on FTO glass (TEC-15), previously cleaned in acetone, ethanol, DI water for 20 min each in an ultrasonic bath. Greatcell Solar® 18NR-T Titania Paste was slot coated using a glass pipette and Scotch® Magic™ tape as template to control the thicknesses of the TiO_2-*meso*. To remove the organic binder in the paste, the films were UV cured using a 365 nm UV LED (2.9 W, 2.2 mm x 2.2 mm Light Emitting Surface in a 7.0 mm x 7.0 mm emitter footprint, LZ4-04UV00/ LED Engin) for 68 h. The distance between the sample and the UV LED was *ca.* 0.5 cm. The TiO_2-*meso* layer was then sintered at 350 °C under constant N_2 flow for 1 h and with a heat rate of 5 °C min $^{-1}$, resulting in a *ca.* 4-6 µm thick, the sample labelled as TiO_2-*meso*(UV).

To compare the physico-chemical properties of the UV cured TiO_2-*meso* films *vs* those prepared by the conventional thermal method (used as control), the TiO_2 paste was slot-coated on FTO in the same manner previously described and then air annealed at 450 °C for 1 h, heat rate of 5 °C min $^{-1}$. The resulting samples were labelled as TiO_2-*meso*(450°C, air).

The same experimental protocol was applied on the top of $Sb_2Se_3/CdS/TiO_2$(S-100nm) photoelectrodes once optimised (samples labelled as $Sb_2Se_3/CdS/TiO_2$(S-100nm)/TiO_2-*meso*).

A $TiCl_4$ treatment was also investigated as an alternative approach to increase the TiO_2 particle interconnectivity,[9] by dipping the samples for 20 min in 40 mM $TiCl_4$ (Titanium(IV) chloride tetrahydrofuran complex, Sigma-Aldrich) at 70 °C before and/or after the UV curing. However, this treatment did not improve the TiO_2-*meso* stability and the films delaminated when Scotch tape was used as template for the doctor-blading. However, it was found that $TiCl_4$ treatment improve the stability of thinner TiO_2-*meso* (< 2 mm thick) films made by only using a glass rod to deposit the titania paste on FTO.

6.1.2.5 Selection Sb₂Se₃ based photocathodes

Close-Spaced Sublimation is technique that allows large-scale thin films production, which is of special interest in solar cell development.[25] For the samples studied here, the Sb_2Se_3 was initially deposited onto 5 x 5 cm Au coated FTO followed by either sputtered CdS/and or the TiO_2. After, the 5 x 5 cm Sb_2Se_3 based device was cut in smaller pieces for the PEC analysis (1 x 1.5 cm). The ohmic contact was made onto Au coated FTO using Ag paste (RS PRO Conductive Lacquer) and a stainless-steel wire. Finally, the sample was encapsulated with epoxy resin (LOCTITE® EA E32 Grey Toughened Epoxy Adhesive). The actual photoelectrode area was 0.5 x 0.5 cm as shown in Figure 104 for a Sb_2Se_3/CdS/TiO_2-meso/Pt sample as an example.
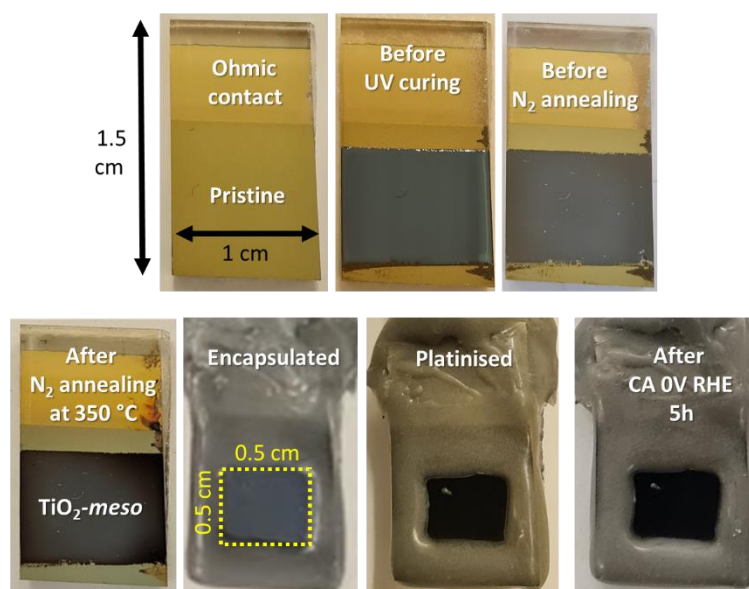

Figure 104 *Process of making Sb₂Se₃/CdS/TiO₂-meso/Pt based photocathodes.*

It is important to point out that significant differences in PEC activity, in terms of photocurrent and onset potential were noticed between samples from different batches. It was later on attributed to the substrate holder in the CSS chamber with the quartz boat giving the best results in spite that a graphite boat provides more homogeneous heat transfer across the 5x5 cm plate. This behaviour was likely associated to the change in the Sb_2Se_3 growth mechanism onto Au layer rather than FTO, process that had been optimised by Dr Jon Mayor group.[25]

Furthermore, differences in PEC activity were found in samples that belong to the same 5 x 5 cm substrate but taken at different positions, the middle or at the edge of the plate as shown in Figure 105 when Pt was used as benchmark catalyst. The LSV and the CA of 3 different Sb_2Se_3 photocathodes are included in panel b and c. Therefore only 6 samples from the centre (indicated in Figure 105a) of the 5x5 cm^2 substrate were further investigated instead of the 20 samples produced within the same batch.
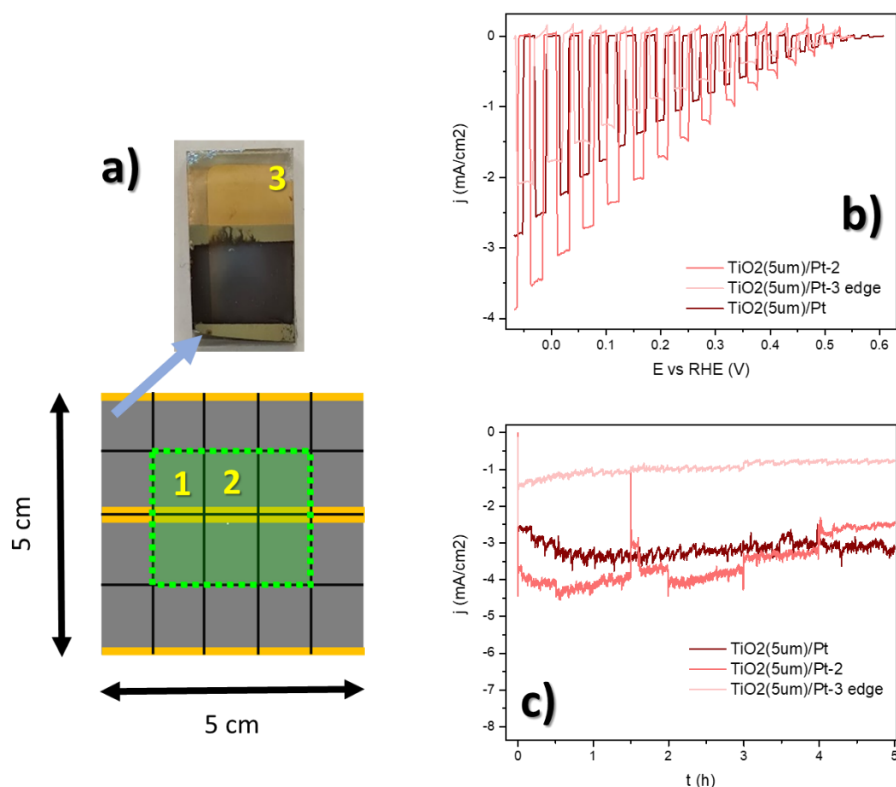

Figure 105. *(a) Sb_2Se_3 films deposited onto 5x5 cm substrate by CSS. PEC activity of Sb_2Se_3/CdS/TiO_2(S-100nm)/TiO_2-meso/Pt depending on the position of the 5x5 cm substrate, (a) LSV at 10 mVs^{-1} and (b) CA test at 0 V vs RHE in 0.1 M H_2SO_4 under N_2.*

6.2 Catalyst immobilization/deposition

6.2.1 NiP

The **NiP** with $[Ni(P_2^{R'}N_2^{R''})_2]^{2+}$ core ($P_2^{R'}N_2^{R''}$ = bis(1,5-R′-diphospha-3,7-R″-diazacyclooctane)), modified with a phosphonic acid pendant arm in the outer coordination sphere catalyst was synthesized according to previously described methods.[10–13] **NiP** immobilization was carried out by soaking the samples in a stationary 0.5 mM **NiP** solution with dry methanol as solvent overnight (16 h) in a dark

vial. Photoelectrodes were then rinsed thoroughly in dry methanol to remove the **NiP** not bound to the TiO$_2$, followed by a vacuum drying process at 60 °C for 2 h in the dark to eliminate the excess of methanol. The same experimental protocol was followed for the **NiP** immobilization in all the samples: planar device (Sb$_2$Se$_3$/CdS/TiO$_2$(S-100nm)), the complete high surface area photoelectrode (Sb$_2$Se$_3$/CdS/TiO$_2$(S-100nm)/TiO$_2$-*meso*), and the bare TiO$_2$-*meso* (without the Sb$_2$Se$_3$/CdS underneath) for the control experiments.

Prior to the **NiP** immobilization, all the (photo-)electrodes were UV cleaned for 4 h using a 365 nm UV LED (2.9 W, 2.2 mm x 2.2 mm Light Emitting Surface in a 7.0 mm x 7.0 mm emitter footprint, LZ4-04UV00/ LED Engin), the sample was *ca.* 0.5 cm apart from the LED. The UV cleaning treatment improved film wettability as the contact angle decreased from 44.65° prior to UV cleaning to 11.07° after (as shown in Figure 106, panel a and b, respectively), which could promote higher catalyst loadings.
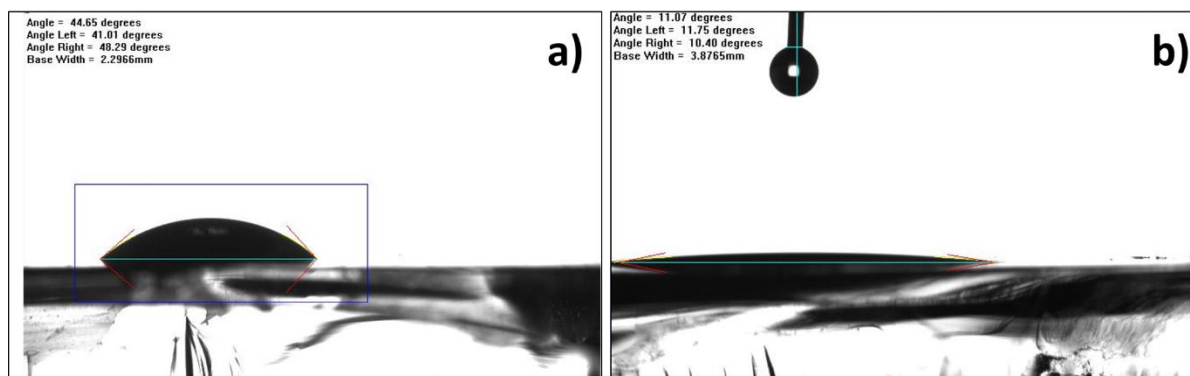

Figure 106 Contact angle measurement (a) before and (b) after the 4 h UV curing on TiO$_2$-meso.

It is important to note that **NiP** is an O$_2$ sensitive molecular catalyst,[14] therefore catalyst handling including storage, once dissolved in dry methanol and immobilization were carried out under Ar. Additionally, the electrolyte for the (photo-)electrochemical measurements was purged with N$_2$ for 30 min to remove oxygen prior the immersion of the **NiP**-based electrode. For H$_2$ quantification, N$_2$ with 1% CH$_4$ as a tracer was used to purge the electrolyte.

To determine the **NiP** loading, the photoelectrodes were soaked in 2 mL of 0.1 M NaOH for 1 h to fully desorb the molecular catalyst. The resultant **NiP** solution was studied using UV/Vis spectroscopy and the concentration calculated by measuring the absorbance at 254.8 nm and through the use of a calibration curve made with known concentrations of **NiP** in 0.1 M NaOH in a 2 mm quartz cuvette. The calibration curve is shown in Figure 50 in Chapter 2.

6.2.2 Ni(cycP)

The **Ni(cycP), cycP** = [(1,4,8,11-tetraazacyclotetradecan-1-yl)methyl] phosphonic acid molecular catalyst was synthesized according to previously described methods.[15,16] The immobilization was carried out by soaking the films (TiO$_2$(S-100 nm), Sb$_2$Se$_3$/TiO$_2$(S-20 nm), and TiO$_2$-*meso*) in 10 mM **Ni(cycP)** ethanolic solution for 48 h, after the samples were thoroughly rinsed with the ethanol to remove the excess catalyst. The immobilization time was increased up to 7 days in an attempt to achieve higher catalyst loadings.

A **Ni(cycP)** solution in H$_2$O and methanol was also studied (10 mM). A fresh-made and 21-day aged solution were used to increase the catalyst content on TiO$_2$-*meso*/Ag, as well as the increase in the immobilization from 48 h to 7 days.

The catalyst loading could not be determined by UV-Vis absorbance due to the low **Ni(cycP)** extinction coefficient ($\varepsilon_{344\ nm}$ = 24 M^{-1} cm^{-1}, $\varepsilon_{533\ nm}$ = 12 M^{-1} cm^{-1}),[16] and no significant change in the absorption peaks were observed in 10 mM **Ni(cycP)** ethanolic solution after the immobilization, not the alkaline solution (1 M NaOH) use for catalyst stripping. Therefore, the **Ni(cycP)** content was determined by ICP after stripping the catalyst off for 72 h in 1 M NaOH.

6.2.3 CoPP

CoPP (Cobalt Protoporphyrin IX, Frontier Scientific) immobilisation was carried out in fresh-made 100 μM **CoPP** ethanolic solution. TiO$_2$-*meso* films were soaked overnight in dark vials (16 h). The catalyst loading was determined by UV-vis spectroscopy considering the UV-vis peak with the highest intensity at 418 nm and a calibration curve with a known **CoPP** concentration.

6.2.4 CoPc

CoPc (Cobalt phthalocyanine, Sigma-Aldrich) was first immobilized on multi wall carbon nanotubes, (CNT) previously acid cleaned in an overnight reflux in 6 M HNO$_3$, then filtered and thoroughly washed with DI water followed by ethanol.[17] **CoPc** was then immobilised on 5 mg CNT overnight in 5 mL of 81 μM of **CoPc** in THF.[17,18] Figure 107 shows a picture of 81 μM of **CoPc** in THF (a) before and (b) after the overnight immobilization on CNT.
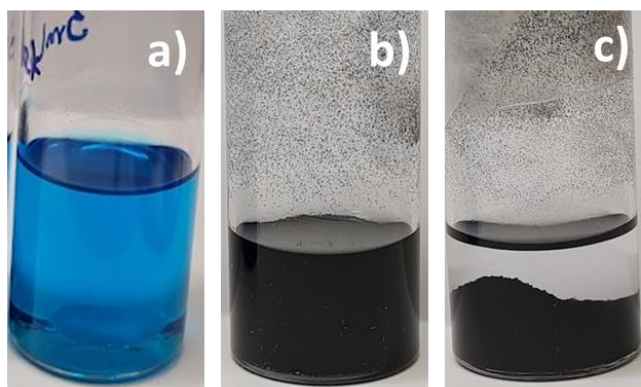
Figure 107 *Picture of 81 μM of CoPc in THF (a) before and (b) after the overnight immobilization on CNT, and (c) once the CoPc@CNT was sedimented*

Then, the active composite **CoPc**@CNT (2 mg) was dispersed in ethanol (950 μL), and 5% Nafion solution (50 μL) to form an ink and 4 μL were drop casted on GC (0.071 cm^2) previously polished with alumina 1.0 μm followed by 0.05 μm, sonicated in DI water for 30 s between the different alumina sizes.

6.2.5 Pt photo-electrodeposition

Pt was photoelectrodeposited according to previous studies[19] by applying a constant current of -30 μA cm^{-2} for 15 min at 100 mW cm^{-2}, λ ≥ 340 nm and a water filter, in 1 mM H_2PtCl_6 (Sigma-Aldrich) and 0.1 M Na_2SO_4. A 3-neck flat glass cell was used for these experiments with magnetic stirring. A constant potential of *ca.* 0.2 V *vs* Ag/AgCl was recorded for the Pt photoelectrodeposition for tha Sb_2Se_3 basesd photocathodes.

6.2.6 Ag electrodepositon

Ag was electrodeposited on TiO_2-*meso* electrodes by applying a constant current of -30 μA cm^{-2} for 10 min (Charge: 0.018 C) in a fresh- made 1 mM $AgNO_3$, 0.1 M KNO_3. A 3-neck flat glass cell was used for these experiments with magnetic stirring. A constant potential of *ca.* -0.05 V *vs* Ag/AgCl was recorded for the Ag electrodeposition.

6.3 Characterisation techniques

6.3.1 Profilometry

Film thicknesses were determined ex situ using an Ambios XP-200 profilometer.

6.3.2 UV-VIS

Transmission and reflectance measurements were taken between 250-1500 nm using a Shimadzu SolidSpec-3700 UV-vis-NIR spectrophotometer to calculate the absorption coefficient, then used to estimate the band gap for CdS, Sb_2Se_3 and TiO_2 thin films according to the Tauc method.[20]

To determine the molecular catalyst loadings, the UV-Vis spectra were recorded using a Shimadzu UV-2600 spectrophotometer using a 2 mm path length quartz cuvette.

6.3.3 Scanning Electron Microscope (SEM)

SEM and elemental analysis were taken on a Hitachi S4800 cold field emission gun (FEG) microscope detecting secondary electrons in the in-column detector. A working distance of 8 mm was used for all imaging. Voltage and gun current were set to 5 kV and 7 µA respectively.

6.3.4 Energy dispersive X-ray spectroscopy (EDX)

Elemental analysis by SEM-EDX was carried out using the same Hitachi S4800 microscope, with an Oxford Instruments AztecOne attachment with a 10 mm^2 silicon drift detector (SDD). A working distance of 15 mm was used for all elemental analysis. A voltage of 20 kV was selected based on the Kα transition energies for Pt and Ni (Pt Lα = 9.441 keV, Ni Kα = 7.471 keV). Gun current was set to 15 µA. The analysis was taken with the aperture completely removed to achieve maximum count rate whilst maintaining dead time <45%.

6.3.5 X-ray Photoelectron Spectroscopy (XPS)

XPS data collection was performed at the EPSRC National Facility for XPS ('HarwellXPS'), operated by Cardiff University and UCL, under contract No. PR16195. XPS data was acquired using a Kratos Axis SUPRA using monochromated Al kα (1486.69 eV) X-rays at 12 mA emission and 12 kV HT (144W) and a spot size/analysis area of 700 x 300 µm. The instrument was calibrated to gold metal Au 4f (83.95 eV) and dispersion adjusted give a BE of 932.6 eV for the Cu 2p3/2 line of metallic copper. Ag 3d5/2 line FWHM at 10 eV pass energy was 0.544 eV. Source resolution for monochromatic Al Kα X-rays is ~0.3 eV. The instrumental resolution was determined to be 0.29 eV at 10 eV pass energy using the Fermi edge of the valence band for metallic silver. Resolution with charge compensation system on <1.33 eV FWHM on PTFE. High resolution spectra were obtained using a pass energy of 20 eV, step size of 0.1 eV and sweep time of 60 s, resulting in a line width of 0.696 eV for Au 4f7/2. Survey spectra were obtained using a pass energy of 160 eV. Charge neutralisation was achieved using an electron

flood gun with filament current = 0.38 A, charge balance = 2 V, filament bias = 4.2 V. Successful neutralisation was adjudged by analysing the C 1s region wherein a sharp peak with no lower BE structure was obtained. Spectra have been charge corrected to the main line of the carbon 1s spectrum (adventitious carbon) set to 284.8 eV. All data was recorded at a base pressure of below 9×10^{-9} Torr and a room temperature of 294 K.

6.3.6 Raman Spectroscopy

Raman analysis was carried out using a Raman microscope (Renishaw InVia) with a 50x objective (Leica). Before measurements, Raman band positions were calibrated *vs* the 520 cm^{-1} silicon peak with a resolution of 1 cm^{-1}. A 532 nm green laser was used with 0.5% laser intensity for 60 s on Sb_2Se_3/CdS/TiO_2-*meso* and 5% laser intensity for 60 s for the sample without the TiO_2-*meso* layer (Sb_2Se_3/CdS/TiO_2). The same conditions were used pre, post N_2 annealing and post Controlled Potential Photoelectrolysis (CPP). To determine the effect of the N_2 annealing on the crystalline structure of the TiO_2 layer made RF magnetron sputtering, 15% laser intensity was used for 60 s.[21]

Table **19** summarise the Raman Shifts used here to assign the peaks.

Table 19 *Raman Shifts used to identify Sb_2Se_3 peaks.* [21]

Compound	Structure	Raman shift (cm^{-1})
Sb_2Se_3	Orthorhombic	80, 120, 151, 189, 210
Sb_2O_3	Cubic	82, 189, 254, 373, 450
Sb_2O_4		72, 142, 199, 255, 400, 463
Se_n (spiral chains)	Trigonal	141, 234, 237
Se_8 (rings)	α-monoclinic	112, 253
Se_6 (rings)	Rhombohedral	67–72, 102, 129, 221, 247
Red Se (rings)	Amorphous	250
Sb	Rhombohedral	110, 150

6.3.7 (Photo)electrochemistry

The (photo)electrochemical studies were carried out using a single compartment three-electrode cell when no gas product needed to be quantified. ZnTe and Sb_2Se_3-based photocathodes were used as working electrode (WE), a Pt mesh worked as counter electrode (CE) and a home-made Ag/AgCl (3 M NaCl) was the reference electrode (RE). The RE was always measured *vs* a master reference electrode (Ag/AgCl (3M NaCl), BASi MF-2052) prior to use.

All the electrolytes were made using Milli-Q water (18.2 MΩ·cm). For the **NiP** study, the pH 3 was adjusted with acetic acid (Sigma-Aldrich). Dissolved oxygen was removed from the electrolytes before all the (photo)-electrochemical experiments by N_2 or Ag purge for 20 min.

For experiments presented in Chapter 4, MeCN (Sigma-Aldrich HPLC, gradient grade ≥99.9%) was the solvent and $TBAPF_6$ the supporting electrolyte (0.1 M, Sigma-Aldrich for electrochemical analysis, ≥99.0%). Ferrocene redox couple was used as the pseudo reference electrode alongside a silver wire, cleaned with 0.1 M HNO_3 (70% Sigma-Aldrich, ACS reagent) prior each experiment. All the potentials were reported vs NHE according to Eq. (5).

$$E \ (V) \ vs \ NHE = E \ (V) \ vs \ Ag_{wire} - E \ (V) \ Fc^+/Fc + 0.63V \qquad (5)$$

The Controlled Potential Photoelectrolysis (CPP) tests for CO_2 photoelectrochemical reduction were carried out in a glass flat cell with nafion deposited a glass frit in the counter sleeve to separate the catholyte and the anolyte. However, it was found that this cell was not gas tight and the gases used to remove the oxygen either N_2 or Ar did not include CH_4 as tracer, nor the CO_2 used to saturate the electrolyte during the CO2 photoelectrochemical reduction, therefore the Faradaic Efficiency of this experiments was not accurated determined.

Electrochemical measurements were carried out using either PalmSens3 or SP-200 BioLogic potentiostat. Chopped light linear sweep voltammetry (LSV) was conducted after the sample was illuminated for 10 s, and starting from the open circuit potential (OCP) in the cathodic direction at 10 mV s^{-1}. The electrochemical potentials were converted to the RHE according to Eq. (6).[19]

$$E \ (V \ vs \ RHE) = E \ (V \ vs \ Ag/AgCl) + 0.059 * pH + 0.209 \qquad (6)$$

Controlled potential photoelectrolysis (CPP) tests were carried out in a gas tight customised H-cell shown in Figure 108, with a Nafion membrane (N117, *ca.* 180 μm thick) between the anode and cathode. For gas product quantification, the customised electrochemical cell was purged for 30 min with N_2 and 1% CH_4 as an internal standard for gas chromatography.
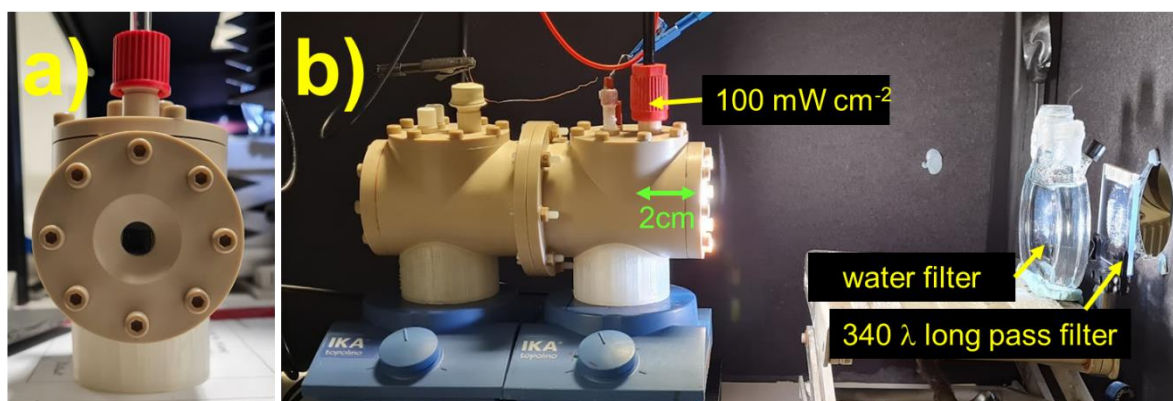

Figure 108 Customized photoelectrochemical cell used for the Controlled Potential Photoelectrolysis (CPP).

The light source was a Xe lamp providing an irradiation of 100 mW cm^{-2} (300 W Xe lamp, LOT Quantum Design) at the front of the electrochemical cell. Schott glass long pass filters were used to limit the output to $\lambda \geq 340$ nm and a water filter removed the infrared component. For low irradiance experiments, a neutral density filter (50 mm x 50 mm UVFS Reflective ND Filter, OD: 1.3) was used to drop the light intensity to 20 mW cm^{-2}. All the photoelectrodes were front illuminated across a quartz window.

Incident photon-to-current efficiency (IPCE) measurements were carried out using 100 W tungsten lamp as a light source coupled with a monochromator (OBB Corp., typically set to 4 nm resolution). The light intensity was measured with a Si-photodiode detector (S120VC) and the IPCE was calculated using equation 7.

$$IPCE \ (\%) = \frac{1240 * J}{\lambda * P} \qquad \text{Eq. (7)}$$

196

Where J is the photocurrent density (mA cm^{-2}) and P is the light power density (mW cm^{-2}) at each wavelength (λ). The IPCE spectra was collected at 0 V *vs* RHE.

6.3.8 Gas chromatography

Gas production was determined using an Agilent 6890N instrument with helium N6 (BOC) as the carrier gas (5 mol min^{-1}), equipped with a 5 Å molecular sieve column (ValcoPLOT, 30 m length, 0.53 mm ID) and a pulsed discharge detector (D-3-I-HP, Valco Vici). Sampling was conducted using a 500 μL gastight syringe with an injection volume of 100 μ L every 30 min.

6.3.9 Transient photocurrent (TPC)

The transient photocurrents decays were measured using part of the slow TAS system at Liverpool University, which contains a Nd:YAG laser (Continuum, Surelite I-10, 6 ns pulse width) operating at 0.33 Hz as the pulsed excitation source, and this system was fully described previously.[22] Here we used the second harmonic (532 nm) to excite the sample. To avoid potential contributions from the fundamental additional beam splitters were employed an optical path to reflect 532 nm and transmits 1064 nm. A liquid light guide transmitted the laser pulse (532 nm, 400 μJ cm^{-2}) to the electrochemical cell. The transient photocurrent was measured by taking the potential drop over an external resistor on a Thomson Ministat with data acquisition making use of a homemade amplifier coupled to both an oscilloscope (Textronix TDS 220) and data acquisition card (National Instruments NI-6221).[22] In all cases, the smallest resistor value possible (to gain sufficient S:N) was chosen to minimise RC time effects on the data.

To study the charge extraction/recombination processes in Sb$_2$Se$_3$/CdS/TiO$_2$(S-100nm)/TiO$_2$-*meso* structure under illumination, a monochromatic bias light 532 CW (constant illumination at 0.8 mW cm^{-2}) was applied in addition to the laser pulse. A 100 W tungsten lamp was used as a light source coupled with a monochromator (OBB Corp., typically set to 4 nm resolution). The light intensity was measured

with a Si-photodiode detector (S120VC). Each transient photocurrent decay shown in Chapter 3 was obtained as an average of 50 individual recordings. A diagram of the actual TPC set up is shown in Figure 109.
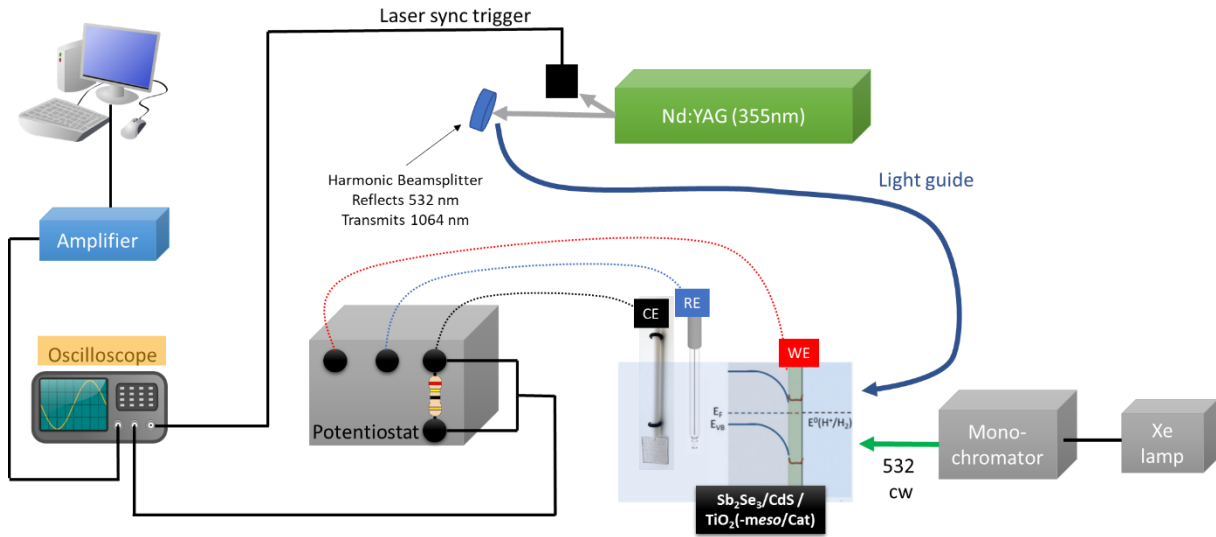

Figure 109 *Scheme of the experimental set up used to measure the transient photocurrent decays of Sb₂Se₃ based photocathodes, adapted from*[22]

Transient photocurrent is technique that enables to measure the current that passes from the working to the counter electrode with a high time resolution by connecting a resistor to the potentiostat and measuring the voltage drop in the oscilloscope.[23] The transient current was calculated by Ohm Law (Eq. 8). Two different resistors were used: 50 and 5.8 Ω. The charge was calculated by the integrated the current according to Eq. (9).

$$I = V/R \qquad \text{Eq (8)}$$

$$q = \int i * dt \qquad \text{Eq (9)}$$

6.3 References

1   E. Palomares, J. N. Clifford, S. A. Haque, T. Lutz and J. R. Durrant, *J. Am. Chem. Soc.*, 2003, **125**, 475–482.

2   I. Ichinose, H. Senzu and T. Kunitake, *Chem. Mater.*, 1997, **9**, 1296–1298.

3   A. R. Balu, V. S. Nagarethinam, A. Thayumanavan, K. R. Murali, C. Sanjeeviraja and M. Jayachandran, *J. Alloys Compd.*, 2010, **502**, 434–438.

4   J. Azevedo, L. Steier, P. Dias, M. Stefik, C. T. Sousa, J. P. Araújo, A. Mendes, M. Grätzel and S. D. Tilley, *Energy Environ. Sci.*, 2014, **7**, 4044–4052.

5   L. Zhang, Z. J. Zhao, T. Wang and J. Gong, *Chem. Soc. Rev.*, 2018, **47**, 5423–5443.

6   M. Forster, R. J. Potter, Y. Ling, Y. Yang, D. R. Klug, Y. Li and A. J. Cowan, *Chem. Sci.*, 2015, **6**, 4009–4016.

7   O. S. Hutter, L. J. Phillips, K. Durose and J. D. Major, *Sol. Energy Mater. Sol. Cells*, 2018, **188**, 177–181.

8   W. Yang, J. H. Kim, O. S. Hutter, L. J. Phillips, J. Tan, J. Park, H. Lee, J. D. Major, J. S. Lee and J. Moon, *Nat. Commun.*, 2020, **11**, 1–10.

9   M. Schreier, J. Luo, P. Gao, T. Moehl, M. T. Mayer and M. Grätzel, *J. Am. Chem. Soc.*, 2016, **138**, 1938–1946.

10   M. A. Gross, A. Reynal, J. R. Durrant and E. Reisner, *J. Am. Chem. Soc.*, 2014, **136**, 356–366.

11   J. J. Leung, J. Warnan, D. H. Nam, J. Z. Zhang, J. Willkomm and E. Reisner, *Chem. Sci.*, 2017, **8**, 5172–5180.

12   T. E. Rosser, T. Hisatomi, S. Sun, D. Antón-García, T. Minegishi, E. Reisner and K. Domen, *Chem. Eur. J.*, 2018, **24**, 18393–18397.

13   M. L. Helm, M. P. Stewart, R. M. Bullock, M. R. DuBois and D. L. DuBois, *Science*, 2011, **333**, 863–866.

14   D. W. Wakerley, M. A. Gross and E. Reisner, *Chem. Commun.*, 2014, **50**, 15995–15998.

15   G. Neri, M. Forster, J. J. Walsh, C. M. Robertson, T. J. Whittles, P. Farrás and A. J. Cowan, *Chem. Commun.*, 2016, **52**, 14200–14203.

16   G. Neri, Thesis, University of Liverpool, 2016.

17   C. Sun, Y. Hou, N. Lüdi, H. Hu, M. de Jesús Gálvez-Vázquez, M. Liechti, Y. Kong, M. Liu, R. Erni, A. v. Rudnev and P. Broekmann, *J. Catal.*, 2022, **407**, 198–205.

18   H. Zhang, Y. Chen, H. Wang, H. Wang, W. Ma, X. Zong and C. Li, *Adv. Energy Mater.*, 2020, **10**, 2002105, 1–9.

19   R. R. Prabhakar, W. Septina, S. Siol, T. Moehl, R. Wick-Joliat and S. D. Tilley, *J. Mater. Chem. A*, 2017, **5**, 23139–23145.

20   J J. Tauc, R. Grigorovici and A. Vancu, *Phys. Status Solidi B*, 1966, **15,** 627-637.

21   A. Shongalova, M. R. Correia, B. Vermang, J. M. V. Cunha, P. M. P. Salomé and P. A. Fernandes, *MRS Commun.*, 2018, **8**, 865–870.

22   M. Forster, Thesis, University of Liverpool. 2017

23   N. Beermann, G. Boschloo and A. Hagfeldt, *J. Photochem. Photobiol. A Chem.*, 2002, **152**, 213–218.

24   V. Pavlishchuk, A. Addison, *Inorganica Chim. Acta*, 2000, **298,** 97 – 102.

25   H. Shiel, Thesis, University of Liverpool, 2021.